Impact of the chemical description on Direct Numerical Simulation and Large Eddy Simulation of turbulent combustion in industrial aero-engines

Benedetta Giulia Franzelli

Réf. CERFACS :
N° d'ordre :

THESE

En vue de l'obtention du

DOCTORAT DE L'UNIVERSITÉ DE TOULOUSE

Délivré par Institut National Polytechnique de Toulouse
Discipline ou spécialité : Energie et Transferts

Par Benedetta Giulia FRANZELLI
Date de soutenance : 19 septembre 2011

IMPACT OF THE CHEMICAL DESCRIPTION ON DIRECT NUMERICAL SIMULATIONS AND LARGE EDDY SIMULATIONS OF TURBULENT COMBUSTION IN INDUSTRIAL AERO-ENGINES

JURY

O. GICQUEL	Professeur - Ecole Centrale de Paris	Rapporteur
H. PITSCH	Professeur - RWTH Aachen University	Rapporteur
W. JONES	Professeur - Imperial College of London	Examinateur
J-F. PAUWELS	Professeur - Université Lille 1	Examinateur
E.S. RICHARDSON	Chercheur - University of Southampton	Examinateur
A. ROUX	Ingénieur - Turbomeca	Invité
B. CUENOT	Chercheur Senior au CERFACS	Directeur de thèse

École doctorale : Mécanique, Energétique, Génie civil, Procédés
Unité de recherche : CERFACS
Directeur de Thèse : Bénédicte CUENOT
Co-encadrant : Eleonore RIBER

Résumé

Le développement de nouvelles technologies pour le transport aérien moins polluant est de plus en plus basé sur la simulation numérique, qui nécessite alors une description fiable de la chimie.
Pour la plupart des carburants, la description de la combustion nécessite des mécanismes détaillés mais leur utilisation dans une simulation numérique de combustion turbulente est limitée par le coût calcul. Des mécanismes cinétiques réduits et des méthodes de tabulation ont été proposés pour surmonter ce problème. Ces descriptions chimiques simplifiées ayant été développées dans le cadre de configurations laminaires, cette thèse propose de les évaluer dans des configurations turbulentes: une DNS de flamme prémélangée méthane/air de type Bunsen et une LES d'un brûleur expérimental. Les mécanismes sont analysés en termes de structure de flamme, paramètres de flamme globaux, longuer de flamme, prediction des concentrations en espèces majoritaires et des émissions polluantes.
Une méthodologie pour évaluer *a priori* la capacité d'un mécanisme à prédire correctement des phénomènes chimiques tridimensionnels est proposée en se basant sur les résultats de flammes laminaires monodimensionnelles non étirées et étirées. Il ressort que, d'une part, pour construire un mécanisme réduit, il est nécessaire de faire un compromis entre coût calcul, robustesse et qualité des résultats. D'autre part, la qualité des résultats de DNS et LES de configurations tridimensionnelles turbulentes peut être anticipée par une analyse du comportement des schémas réduits dans des configurations simplifiées de flammes monodimensionnelles laminaires non étirées et étirées.

Mots-clés : mécanisme cinétique réduit, combustion turbulente, simulation numérique directe, simulation aux grandes échelles.

Abstract

A growing need for numerical simulations based on reliable chemistries has been observed in the last years in order to develop new technologies which could guarantee the reduction of the enviromental impact on air transport.
The description of combustion requires the use of detailed kinetic mechanisms for most hydrocarbons. Their use in turbulent combustion simulation is still prohibitive because of their high computational cost. Reduced chemistries and tabulation methods have been proposed to overcome this problem. Since all these reductions have been developed for laminar configurations, this thesis proposes to evaluate their performances in simulations of turbulent configurations such as a DNS of a premixed Bunsen methane/air flame and a LES of an experimental PRECCINSTA burner. The mechanisms are analysed in terms of flame structure, global burning parameters, flame length, prediction of major species concentrations and pollutant emissions.
An *a priori* methodology based on one-dimensional unstrained and strained laminar flames to evaluate the mechanism capability to predict three-dimensional turbulent flame features is therefore proposed. On the one hand when building a new reduced scheme, its requirements should be fixed compromising the computational cost, the robustness of the chemical description and the desired quality of results. On the other hand, the quality of DNS or LES results in three-dimensional configurations could be anticipated testing the reduced mechanism on laminar one-dimensional premixed unstrained and strained flames.

Keywords: reduced chemistries, turbulent combustion, direct numerical simulation, large eddy simulation.

A Cristina Costarelli

Poca favilla gran fiamma seconda

Dante Alighieri

Contents

Nomenclature

Abreviations

ACARE	Advisory Council for Aeronautics Research in Europe
CFD	Computational Fluid Dynamics
CPU	Central processing unity
DNS	Direct Numerical Simulation
DTFLES	Dynamically thickened flame method for LES
ECCOMET	Efficient and Clean Combustion Experts Training
FPI	Flame Prolongation of ILDM
HIT	Homogeneous isotropic turbulence
ILDM	Intrinsic Low-Dimensional Manifold
ISAT	In Situ Adaptive Tabulation
LES	Large Eddy Simulation
LPM	Lean Pre-Mixed
PAH	Polycyclic Aromatic Hydrocarbons
PCM	Presumed Conditional Moments
PDF	Probability density function
PEA	Pre-Exponential Adjustment
PRECCINSTA	PREdiction and Control of Combustion INSTAbilities for industrial gas turbines
PSR	Perfectly stirred reactor

QSS	Quasi-steady state	
QUANTIFY	Quantifying the Climate Impact of Global and European Transport Systems	
RANS	Reynolds-Averaged Navier-Stokes	
RMS	Root mean square	
TFLES	Thickened flame method for LES	

Greek letters

α_P	Exponent for flame speed dependency on pressure	[$-$]
α_T	Exponent for flame speed dependency on temperature	[$-$]
β_j	Temperature exponent for reaction j	[$-$]
ΔH_j^0	Enthalpy change of reaction j	[J]
$\Delta h_{f,k}^0$	Mass formation enthalpy of species k	[J/Kg]
ΔS_j^0	Entropy change of reaction j	[J/K]
δ	Diffusive flame thickness	[m]
δ_L	Thermal flame thickness	[m]
δ_L^B	Blint flame thickness	[m]
δ_r	Reaction zone thickness	[m]
δ_{ij}	Component (i, j) of the Kronecker delta	[-]
$\dot{\omega}_c$	Reaction rate for the progress variable c	[$1/s$]
$\dot{\omega}_F$	Fuel consumption rate	[$kg/m^3/s$]
$\dot{\omega}_k$	Mass reaction rate of species k	[$kg/m^3/s$]
$\dot{\omega}_T$	Heat release due to combustion	[$J/m^3/s$]
$\dot{\omega}'_T$	Heat release due to combustion	[$J/m^3/s$]
Λ	Flame front length	[m]
λ	Heat diffusion coefficient	[$J/m/K/s$]

$\Lambda^\star$	Reduced flame front length	[−]
Λ_0	Flame front length at the initial time	[m]
μ	Mixture dynamic viscosity	[$Kg/m/s$]
ν	Mixture cinematic viscosity	[m^2/s]
ν''_{kj}	Molar stoichiometric coefficient of species k for the backward reaction j	[-]
ν'_{kj}	Molar stoichiometric coefficient of species k for the forward reaction j	[-]
ϕ	Equivalence ratio	[−]
ρ	Mixture density	[kg/m^3]
ρ_k	Density of species k	[kg/m^3]
Σ	Surface density	[$1/s$]
$\tau_\mathcal{K}$	Kolmogorov time scale	[s]
τ_c	Chemical time scale	[s]
τ_t	Integral time scale	[s]
τ_{ij}	Component (i,j) of the viscous force tensor	[N/m^2]

Non-dimensional numbers

Da	Damköhler number
Ka	Karlovitz number
Ka_r	Karlovitz number based on the reaction zone thickness
Le_F	Fuel Lewis number
Le_k	Lewis number of species k
M_a^c	Markstein number for consumption speed
M_a^d	Markstein number for displacement speed
Pr	Prandtl number
Re	Reynolds number

Re_f	Flame Reynolds number	
Sc_k	Schmidt number for species k	

Roman letters

$[X_k]$	Molar concentration of species k	$[\ mol/m^3\ ]$
$\dot{Q}$	Heat source term	$[\ J/m^3/s\ ]$
$\mathbf{n}$	Flame surface normal	$[\ -\ ]$
$\mathcal{E}$	Efficiency factor	$[\ -\ ]$
$\mathcal{F}$	Thickening factor	$[\ -\ ]$
$\mathcal{J}_i^k$	Component i of the molecular diffusive flux of species k	$[\ Kg/m^2/s\ ]$
$\mathcal{M}_k$	Name of species k	$[\ -\ ]$
$\mathcal{Q}_j$	Progress rate of reaction j	$[\ mole/m^3/s\ ]$
$\overline{k}$	Turbulent kinetic energy	$[\ m^2/s^2\ ]$
$\overline{S}_C$	Flamelet consumption speed	$[\ m/s\ ]$
a	Strain rate	$[\ 1/s\ ]$
A_L	Area of the unwrinkled flame surface	$[\ m\ ]$
A_T	Area of the wrinkled flame surface	$[\ m\ ]$
A_{fj}	Pre-exponential factor for forward reaction j	$[\ cgs\ ]$
c	Progress variable	$[\ -\ ]$
C_{pk}	Specific heat capacity of species k at constant pressure	$[\ J/(Kg\ K)\ ]$
D_k	Molecular diffusivity of species k	$[\ m/s\ ]$
D_{th}	Heat diffusivity	$[\ m/s\ ]$
Ea_j	Activation energy for reaction j	$[\ cal/mol\ ]$
F_i	Component i of the body force	$[\ N/m^2\ ]$
$f_{k,j}$	Component i of the volume force on species k	$[\ N/m^2\ ]$
h_k	Mass enthalpy of species k	$[\ J/Kg\ ]$

$h_{s,k}$	Mass sensible enthalpy of species k	$[\ J/Kg\ ]$
I_0	Burning intensity	$[\ -\ ]$
k	Stretch	$[\ 1/s\ ]$
$k_\mathcal{K}$	Kolmogorov wave number	$[\ 1/m\ ]$
k_e	Integral wave number	$[\ 1/m\ ]$
K_{eq}	Equilibrium reaction constant	$[\ -\ ]$
K_{fj}	Forward reaction constant for reaction j	$[\ cgs\ ]$
K_{rj}	Reverse reaction constant for reaction j	$[\ cgs\ ]$
l	Characteristic domain length	$[\ m\ ]$
$l_\mathcal{K}$	Kolmogorov length scale	$[\ m\ ]$
l_t	Integral length scale	$[\ m\ ]$
l_t	Turbulent length scale	$[\ m\ ]$
m	Mixture mass	$[\ kg\ ]$
m_k	Mass of species k	$[\ kg\ ]$
n	Number of moles	$[\ mol\ ]$
n'_{kj}	Forward order for reaction j and species k	$[\ -\ ]$
n''_{kj}	Backward order for reaction j and species k	$[\ -\ ]$
n_k	Number of moles of species k	$[\ mol\ ]$
p	Pressure	$[\ N/m^2\ ]$
p_k	Partial pressure of species k	$[\ N/m^2\ ]$
q_i	Component i of energy flux	$[\ J/m^2/s\ ]$
R	Perfect gas constant	$[\ J/mol/K\ ]$
s	Mass stoichiometric ratio	$[\ -\ ]$
S_a	Absolute speed	$[\ m/s\ ]$
S_C	Consumption speed	$[\ m/s\ ]$

S_d	Displacement speed	[m/s]
$S_d^\star$	Density-weighted displacement speed	[m/s]
S_L	Propagation speed	[m/s]
S_T	Turbulent flame speed	[m/s]
s_k	Mass entropy of species k	[$J/K/Kg$]
T	Mixture temperature	[K]
u'	root mean square of velocity	[m/s]
$u_\mathcal{K}$	Kolmogorov speed	[m/s]
u_i	Component i of velocity vector	[m/s]
u_p	Turbulent speed	[m/s]
V	Mixture volume	[m^3]
V_i^c	Correction velocity in direction i	[m/s]
$V_{k,i}$	Species diffusion velocity in direction i for species k	[m/s]
W	Mean molecular weight of the mixture	[kg/mol]
W_k	Atomic weight of species k	[kg/mol]
X_k	Molar fraction of species k	[-]
Y_k	Mass fraction of species k	[-]
z	Mixture fraction	[–]
Z_i	Atomic mass fraction	[–]

Introduction

Challenges of combustion in aeronautical engines

Air transport moves over 2.2 billion passengers annually and generates a total of 32 million jobs corresponding to a global economic impact estimated at 3.560 billion of euros. Unfortunately, the fossil fuel combustion typically used in aeronautical engines has a negative impact on climate being characterized by emission of pollutant species:

- **Oxides of carbon** such as the carbon monoxide CO, which is highly toxic combining with hemoglobin and attacking the delivering of oxygen to bodily tissues, and the carbon dioxide CO_2 which is not toxic and it is one of the greenhouse gas responsible for climate change.
- **Oxides of nitrogen** such as the nitric oxide NO and the nitrogen dioxide NO_2 (generally referred as NO_x) and the nitrous oxide N_2O. They have a strong climate impact, i.e. formation of acid rain, and they are greenhouse gases participating in ozone layer depletion.
- **Oxides of sulfur** such as the sulfur dioxide SO_2 and the sulfur trioxide SO_3, precursors of acid rain and atmospheric particulates.
- Highly toxic **soot** having a strongly negative impact on human health.
- **Unburned hydrocarbon** such as alkanes, ketones and alcohols due to an incomplete oxidation of hydrocarbons caused by a low temperature value or a too large heterogeneity of the mixture.

Since 2001 the ACARE[1] establishes the roadmap for aeronautical technology development in the European Union. It aspires at a better technology linked to social

[1]The Advisory Council for Aeronautics Research in Europe (ACARE) is composed by representation from Member States, Commission and stakeholders, i.e. manufacturing industry, airlines, airports

thematic (cleaner environment, safer travel and more security) as well as at the benefits of a more competitive Europe. In the 2008 Addendum to the Strategic Research Agenda, three important areas have been identified for increased priority:

- **Environment**: the transport impact is represented in Fig. 1 in terms of net temperature change for four future times[2]. Even if the aviation contribution is relatively small compared to road transport and producing only 2% of human-induced CO_2 emissions, its emissions have to be controlled since air transport is quickly growing by a factor of 4 – 5% per year and emissions at altitude have an effect on climate change greater than the industry CO_2 emissions alone.

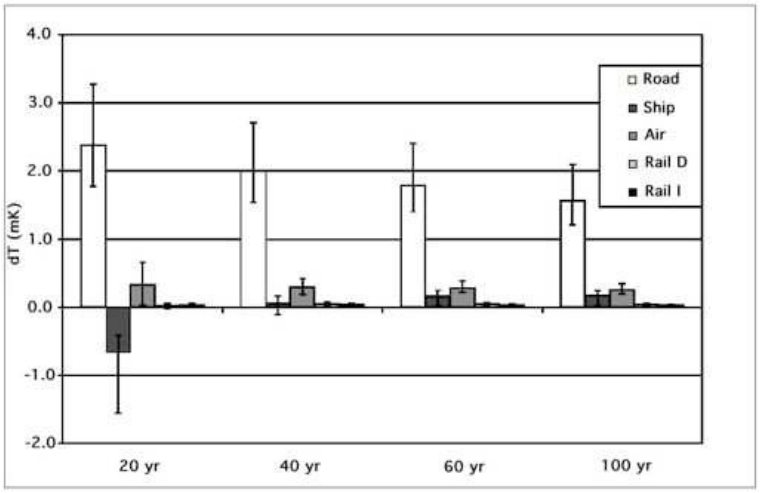

Figure 1 - *Contribution from a one-year pulse of current (year 2000) emissions to net future temperature change (mK) for each transport mode for 4 future times (*20, 40, 60 *and* 100 *years) [22].*

Developing a sustainable aviation system is an urgent thematic concerning global climate change, local noise and air quality. The environmental objectives fixed by the ACARE in the 2020 horizon are:

  - reduction of CO_2 emission by 50% per passenger kilometer (assuming kerosene remains the main fuel in use);
  - perceived noise reduction to one half of the current average levels;
  - reduction of NO_x emissions by 80%;
  - reduction of other emissions: soot, CO, particulates, etc.
  - minimization of the industry impact on the global environment.

[2]Results from the final activity report of the QUANTIFY (Quantifying the Climate Impact of Global and European Transport Systems) project (http://www.ip-quantify.eu).

- **Alternative Fuels**: total energy demand is increasing significantly due to population growth and developing economies whereas the world's reserves of oil are decreasing. The use of new alternative fuels in aviation is not yet a necessity but a study of the specifications of these potential new fuels is required in order to prepare and adapt the aeronautical systems to them. Moreover, their environmental impact has to be carefully analyzed.

- **Security**: measures to increase the security of passengers at airports are also proposed.

Reduction of pollutant emissions is one of the main objectives of the ACARE. The short-term and long-term climate impacts of aviation have been evaluated in the QUANTIFY project including those of long-lived greenhouse gases like CO_2 and N_2O, of ozone precursors and particles, as well as contrail and cirrus cloud impact [22]. Temperature changes due to aviation have been estimated for various years after the emissions with standard emissions and with 20% reduced CO_2 and NO_x emissions (see Fig. 2). Developing new technologies, CO_2 emissions per passenger-kilometer could be reduced and the climate impact would decrease on the long time horizons.

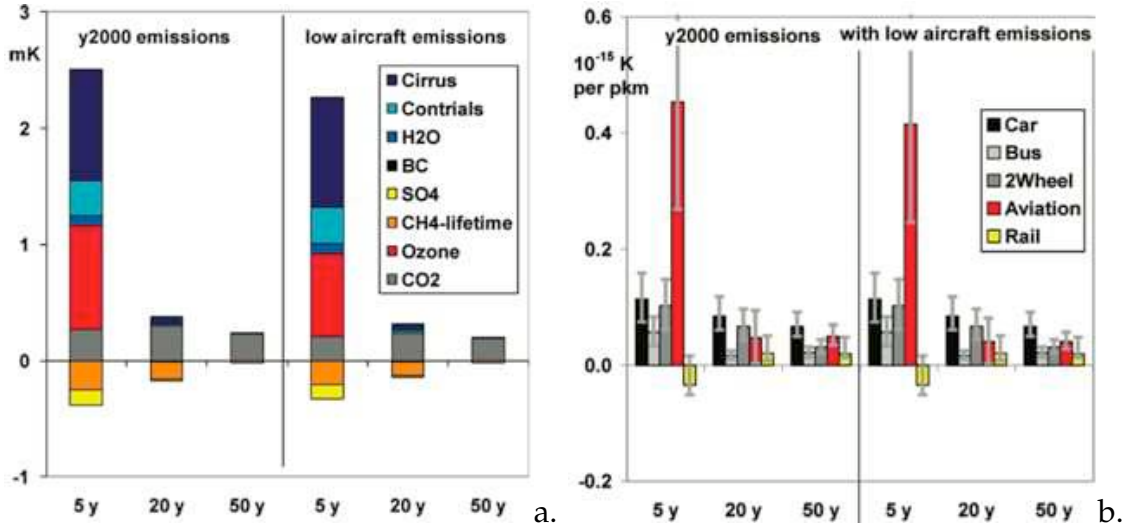

Figure 2 - *Comparison of temperature change for various years after the emissions due to aviation with standard emissions for the year 2000 and with reduced CO_2 and NO_x emissions (−20%) [22]. a) Temperature change per compound and b) specific climate impact of passenger modes per passenger-kilometer.*

The experimental and numerical study of aeronautical engines greatly contributes to the development of new technologies which could guarantee the expected 20% reduction of CO_2 and NO_x emissions. A good knowledge of the **turbulent combustion**

phenomena taking place into the combustion chamber such as the production of pollutants is one fundamental step for minimizing the environmental impact and ensuring the security of the aeronautical systems using alternative fuels.

Turbulent combustion is characterized by multiple aspects: spray dynamics and two-phase flows, radiation effect and wall heat losses, interaction of heat and sound...However, in a very simplified way, it describes the interaction between a turbulent flow and a flame: none of these improvements is useful if the two fundamental bricks, turbulence and chemistry, are not correctly described. Modeling the chemical phenomena and their interaction with turbulence is one of the major problem of combustion.

Chemical description in turbulent combustion

Detailed kinetic mechanisms, comprising hundreds of species and thousands of reactions, are available for most hydrocarbons [148]. They correctly predict multiple aspects of flames over a wide range of cases (i.e. one-dimensional flame structure, gas composition in a stirred reactor, ignition delay, etc...). Unfortunately, using these mechanisms in turbulent combustion simulation is still prohibitive:

- **theoretical difficulties**: in most combustion models, the coupling between turbulence and combustion is generally accounted for through the comparison of a single turbulent time to the characteristic chemical time. Since detailed mechanisms are characterized by very different time scales (i.e. fuel oxidation is governed by fast reactions whereas NO_x production is the result of slow reactions), this coupling is not straightforward.
- **computational costs**: the computational time drastically increases with the number of species to be solved. Moreover, complex schemes are usually very stiff and demand specific (implicit) algorithms to avoid unreasonably small time steps.

Two approaches have been proposed to overcome this problem:

- **Reduced chemistry**: simplification of a detailed mechanism in order to obtain accurate chemical behavior with less species and reactions. They could be classified as:
  - Global or semi-global fitted schemes [171, 63, 144]: they are generally built to correctly reproduce global quantities for premixed flames such as flame speed and burnt gas state. On the one side, these mechanisms are generally easy to build for a wide range of initial conditions, their implementation in

a CFD solver is usually straightforward and they are very robust. On the other side, only global quantities are correctly predicted and all information on intermediate species disappears.

  - Analytical mechanisms [116, 41, 40, 103, 21]: they have been proposed to include more details on the flame such as its structure or the ignition delay. A detailed understanding of the relevant chemistry is required to build this kind of mechanism in order to remove the chemical steps that are useless for specific conditions. These mechanisms provide a physical insight of the chemical processes and some of the intermediate species are correctly described. Unfortunately, their implementation and use in a CFD solver is not easy since they are generally characterized by algebraic relations which are difficult to treat numerically and their computational cost is higher compared to global schemes.

- **Tabulated chemistry**: technique based on the idea that the variables of a chemical mechanism are not independent. The flame structure is studied as function of some few variables (ex. temperature, mixture fraction) used to build a flame database [102, 69, 160, 49]. All the intermediate radicals are available during the computation but their concentrations depend on the information stored into the look-up table, i.e. on the prototype flame chosen to build the table. Handling the table is difficult when simulating complex industrial configurations:

  - its dimension grows rapidly with the number of parameters that have to be taken into account. Solution based on algorithms that dynamically build the table (In Situ Adaptive Tabulation ISAT methods) [126] or on the self-similarities of the flame structure [128, 161, 60] have been proposed;
  - determining the prototype flame to create the table could be a complicated task when the combustion regime is unknown.

A growing need for simulations based on reliable chemistries has been underlined in the last years [77] since restrictions on pollutant emissions motivate request for more accurate results. As a consequence, these simplified chemical descriptions should be carefully used when simulating three-dimensional turbulent complex flames:

- in order to reduce the computational cost, some pieces of information are neglected and accuracy could be affected;
- all these reductions have been developed and evaluated for laminar configurations and their impact on turbulent unsteady flames has not yet been completely evaluated.

A first attempt to characterize the impact of reduced mechanisms on turbulent combustion was proposed by Hilka et al. [78] carrying computations of an interaction between

a vortex pair and a lean methane/air premixed flame with a detailed mechanism (17 species and 52 reactions) and a semi-global scheme (9 species and 4 reactions). Discrepancies between the two mechanisms were underlined on this unsteady configuration for the heat release and the production rates of CO, CO_2 and H_2O species. They were mainly due to the different responses of the mechanisms to strain rate and curvature, and a coupling between chemistry and differential diffusion effects leading to changes in the local composition, and not only to pure kinetics.
At the same time, Baum et al. [13, 14] analyzed the response of a hydrogen/oxygen premixed flame to a homogeneous isotropic turbulent field comparing a simple-step chemistry using constant Lewis numbers with a complete scheme (9 species and 19 reactions) and zeroth-order approximation of the species diffusion velocities. Discrepancies were detected for the flame structure linked to strain rate and curvature response.
The impact of simplified mechanisms has been analyzed on other two-dimensional and three-dimensional configurations [77, 130, 155, 20].

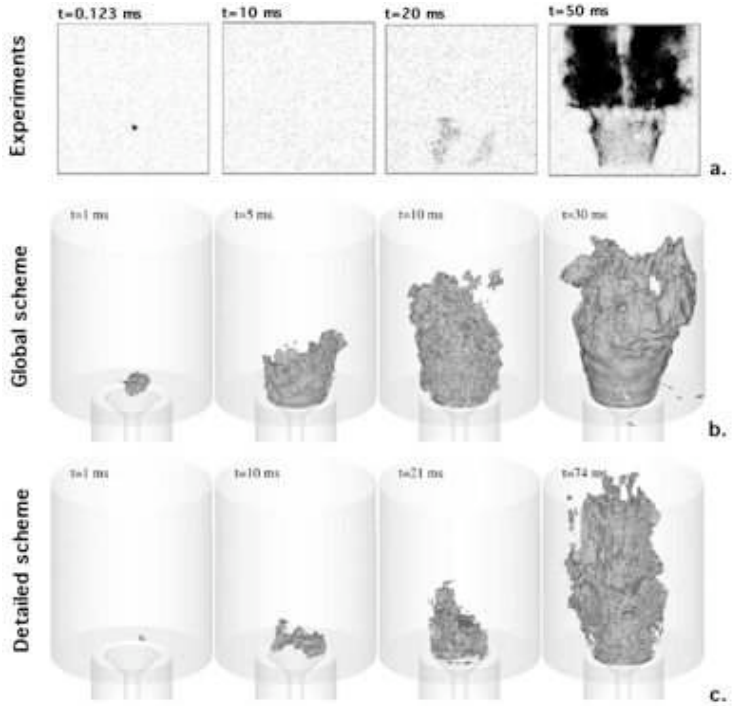

Figure 3 - *Instantaneous pictures of an ignition event for a methane/air flame in a bluff-body configuration. Experimental results by [1] (a.) are compared to numerical results [155] using a global scheme (b.) and a detailed mechanism (c.).*

Simulations of forced ignition of a non-premixed bluff-body methane/air flame by Triantafyllidis et al. [155] showed that a single-step mechanism could reproduce the experimental results [1] with a reasonable accuracy but a better agreement was found

when using a detailed scheme based on 16 species (Fig. 3). Moreover, in [20] it was found that the numerical results of a supersonic hydrogen-air autoignition stabilized flame greatly depend on the simplified mechanism used (Fig. 4).

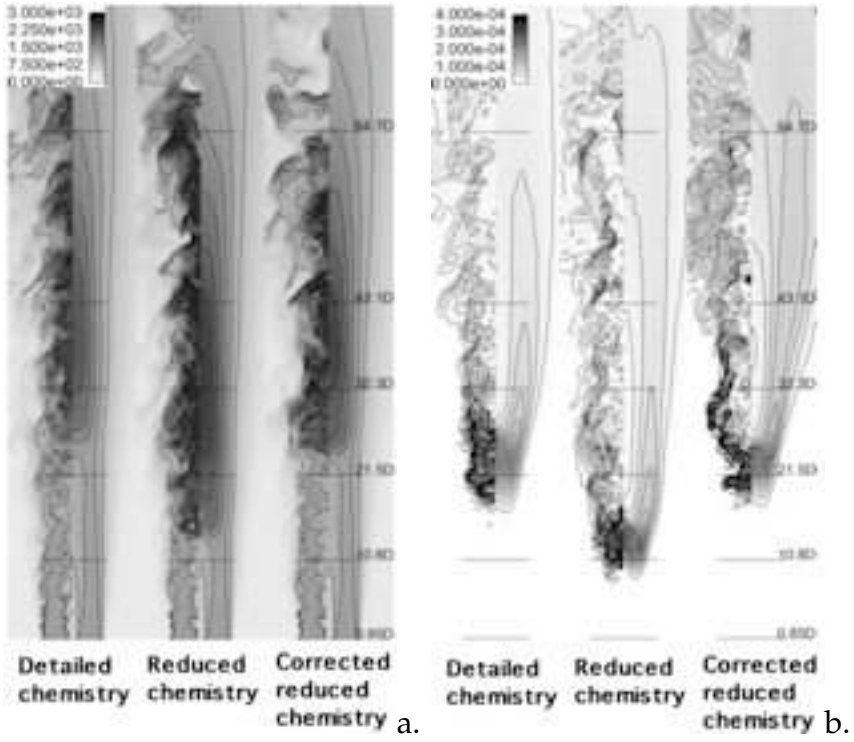

Figure 4 - *Instantaneous and mean a) temperature and b) HO_2 mass fraction in the center plane of the flame for three different chemistries [20].*

Simulations of a side-dump ramjet combustor using a classical one-step scheme and a similar scheme which corrected the flame speed for rich laminar premixed mixture suggested that the chemical scheme not only affects the mean flow field (see Fig. 5) but also the description of thermo-acoustic instabilities [130]. However, no indication was given about the required characteristics of a reduced mechanism to correctly reproduce the main features of the combustion phenomenon.

Finally, Cao and Pope[34] have studied the performance of seven different chemical mechanisms in joint PDF model calculations of the Barlow and Frank [12] non-premixed piloted jet flames D, E and F. A good agreement with experimental results is achieved when using the most complex schemes (called GRI3.0, GRI2.11 and skeletal) whereas the simplest mechanisms (named S5G211, Smooke, ARM1 and ARM2) display significant inaccuracies in term of temperature and species concentrations, causing in some cases an unphysical extinction of the flame (Fig. 6).

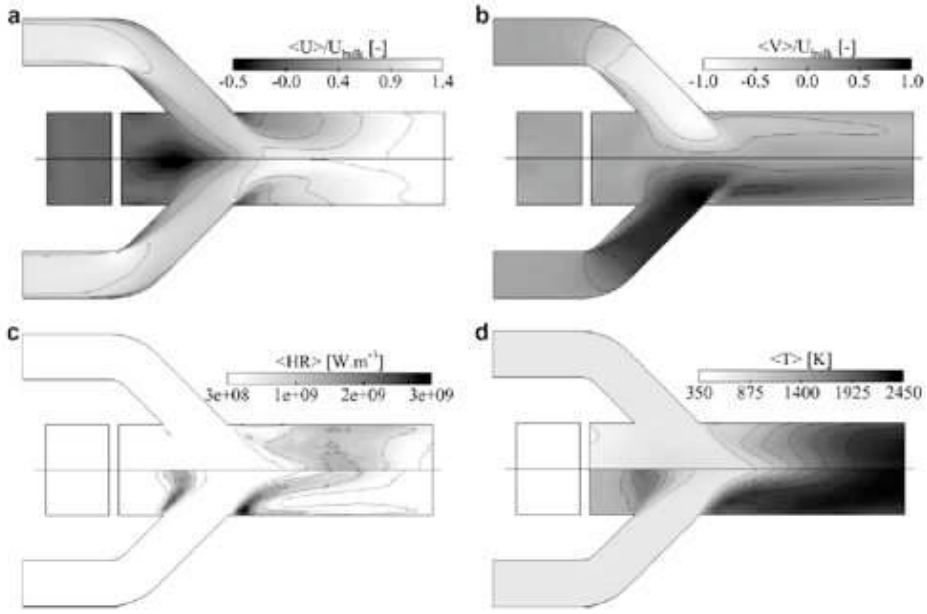

Figure 5 - *Mean flow quantities of the side-dump ramjet combustor calculated by Roux et al. [130]. For each subfigure, top: corrected one-step scheme and bottom: standard one-step scheme. a) Axial velocity, b) radial velocity, c) rate of heat release and d) temperature.*

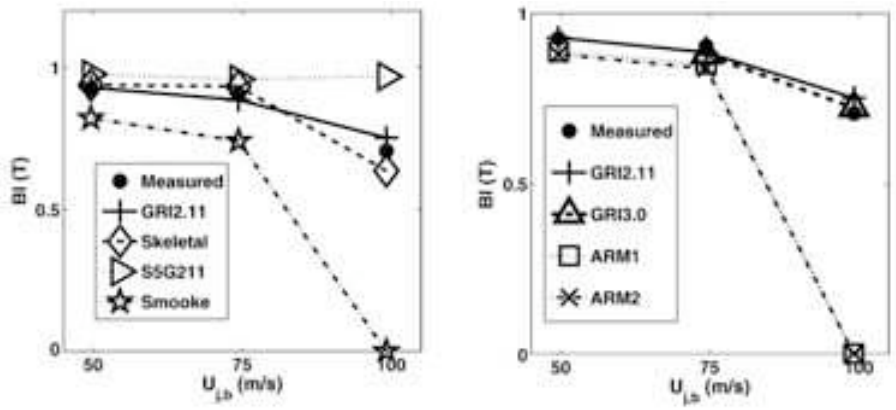

Figure 6 - *Burning indices of temperature versus jet velocity for the Barlow and Frank flames D,E and F [12] calculated by Cao and Pope [34]. Comparison between experimental data and seven chemical mechanisms.*

Even if the importance of a good chemical description has already been underlined in complex configurations, the characteristics of the chemistry model required to correctly reproduce turbulent flames in unsteady calculations have not been completely identified.

Contribution of this thesis

In this thesis, the impact of the chemistry description using reduced kinetic mechanisms is analyzed on turbulent premixed flames in the context of unsteady simulation approaches. Using reduced kinetic mechanisms leads to possible errors on quantities of interest such as major species concentration and temperature, flame structure and its position, its response to turbulence as well as the description of pollutant emissions. Identifying and quantifying these errors are of primary importance for the development of simulation tools.

More precisely, this thesis has two main objectives:

- **The development of a methodology to build semi-global schemes** that correctly predict the flame speed and the burnt gas state for premixed one-dimensional laminar flames on a wide range of pressure, initial temperature and equivalence ratio. This kind of mechanism could be directly implemented and easily used in CFD solvers for the simulation of industrial configurations.
- **Identification of the most impacting characteristics of a reduced mechanism on simulations of a turbulent flame** comparing different chemical descriptions on three-dimensional complex configurations.

The development of a complete experimental database and of detailed mechanisms for the fuels generally used in aeronautical engines such as JET-A, JP10 and biofuels is still in progress [48, 141, 100, 101]. For this reason, the analysis is focused on methane, for which a large set of experimental data as well as various chemical detailed and reduced mechanisms are available. However, conclusions are expected to be valid for most hydrocarbons and could be used to develop new reduced mechanisms for kerosene or biofuel combustion.

Performances of reduced mechanisms are evaluated for both Direct Numerical Simulation (DNS) and Large Eddy Simulation (LES) of turbulent flame [124]. The DNS approach explicitly resolves all the turbulence length and time scales but it is generally confined to academic problems and simple configurations due to its high computational cost. In the LES approach, the computational cost is reduced filtering the flow field equations so that only the largest scales of turbulence are explicitly calculated whereas the smallest turbulent motions are modeled.

Structure of this manuscript

The manuscript is composed by three parts:

- Part 1: General features on turbulent combustion
  - In **Chapter 1**, turbulent premixed combustion is introduced. The conservation equations are generalized to reacting flows and the different combustion regimes are identified. The different approaches for chemistry description in turbulent combustion, i.e. reduced chemistries and tabulation methods, combustion modeling and the different Computation Fluid Dynamics (CFD) tools used in this work are introduced.

- Part 2: Chemistry models for turbulent methane/air combustion
  - In the flamelet regime, the flame front of a turbulent premixed flame is locally modeled by a laminar premixed flame. The general features for laminar premixed methane/air flames are therefore described in **Chapter 2** focusing on the impact of strain rate and simplified transport properties on its structure.
  - In **Chapter 3**, the chemistry for premixed methane/air flame is analyzed. A general methodology is proposed to build a two-step mechanism for premixed flames that correctly predicts the laminar premixed flame and the equilibrium state. This methodology, presented for methane/air flames, could be easily applied to other hydrocarbons and has been successfully used for kerosene/air flames [63]. Five different reduced mechanisms proposed in the litterature are also presented and compared in laminar unstrained and strained flames configuration for two different operating points (corresponding to the three-dimensional numerical configurations analyzed in the third part of this thesis). In order to complete the comparison between the different chemical descriptions, the FPI_TTC tabulation method [164, 9] is presented and evaluated on unstrained premixed flames. The coupling with turbulent combustion modeling is finally addressed as a generalization of the artificially thickened flame method to multi-reactions chemistry.

- Part 3: Validation and impact of chemistry modeling in unsteady turbulent combustion simulations
  - In **Chapter 4** the response to stretch of the different mechanisms analyzed in Chapter 3 is studied in the interaction of a flame with a vortex and with a turbulent homogenous isotropic field in terms of consumption speed and flame structure. From this preliminary analysis, the most performing mechanisms

are identified and used in a DNS of the premixed Bunsen flame calculated by Sankaran et al. [137].

- The different mechanisms are also tested in the LES of the experimental burner named PRECCINSTA (PREdiction and Control of Combustion INSTAbilities for industrial gas turbines [107]) using the artificially thickened flame method in **Chapter 5**. Experimental measurements are available for temperature and major species mass fractions and are used to evaluate the quality of the different mechanisms to predict the structure and the species concentrations of a stable swirled partially premixed flame.
- In **Chapter 6**, the capacity of the simplest mechanism to predict thermo-acoustic instabilities in the PRECCINSTA burner is evaluated. Whereas for one equivalence ratio the flame is stabilized in the chamber, experiments showed that a pulsating flame oscillates at the swirler nozzle for a smaller equivalence ratio. Using a LES, it is possible to predict instabilities even using the simplest chemical scheme.

Three different codes have been used for the numerical simulations. One-dimensional laminar flames have been performed with CANTERA [71], an open-source software package for thermo-chemical problems. DNS results for the Bunsen flame have been obtained using S3D [37], a flow solver developed at CRF/SANDIA to perform DNS of turbulent combustion. LES of the PRECCINSTA burner have been performed with the AVBP code developed at CERFACS/IFPEnergies Nouvelles [140].
This thesis has been financed by the European Union in the framework of the EC-COMET (Efficient and Clean Combustion Experts Training) FP6-Marie Curie Actions.

List of published and submitted articles

- B. Franzelli, E. Riber, M. Sanjosé and T. Poinsot,*A two-step chemical scheme for kerosene-air premixed flames*, Combustion and Flame 157 (7), pp.1364-1373 (2010).
- B.Franzelli, E. Riber , L. Gicquel and T. Poinsot, *"Large-Eddy Simulation of combustion instabilities in a lean partially premixed swirled flame"*, Combustion and Flame, in Press, doi:10.1016/j.combustflame.2011.08.004.

List of honors received

- Zonta International Amelia Earhart Fellowship 2009.
- Zonta International Amelia Earhart Fellowship 2010.

Part I

General features on turbulent combustion

Chapter 1

Turbulent premixed combustion

Combustion implies working with a multi-species and multi-reaction mixture. Each species k is characterized by:

- the mass fraction $Y_k = m_k/m$ defined as the ratio between the mass m_k of species k and the total mass m in a given volume V;
- the density $\rho_k = \rho Y_k$ where ρ is the mixture density;
- the atomic weight W_k;
- the specific heat capacity at constant pressure C_{pk};
- the mass enthalpy $h_k = h_{s,k} + \Delta h^0_{f,k}$ composed by the sensible enthalpy $h_{s,k} = \int_{T_0}^{T} C_{pk} dT$ and the chemical enthalpy equal to the mass enthalpy of formation $\Delta h^0_{f,k}$ at temperature T_0.

The mean molecular weight W of a mixture composed of N species is then given by:

$$\frac{1}{W} = \sum_{k=1}^{N} \frac{Y_k}{W_k}. \tag{1.1}$$

The mole fraction X_k of species k is defined as the ratio between the number of moles n_k of species k and the total number of moles n of the mixture:

$$X_k = \frac{n_k}{n} = \frac{W}{W_k} Y_k. \tag{1.2}$$

The molar concentration of species k is then defined as the moles of species k per unit volume:

$$[X_k] = \rho \frac{Y_k}{W_k} = \rho \frac{X_k}{W}. \tag{1.3}$$

For a mixture of N perfect gases, the total pressure p is the sum of the partial pressures p_k:

$$p = \sum_{k=1}^{N} p_k \quad \text{where} \quad p_k = \rho_k \frac{R}{W_k} T, \tag{1.4}$$

where T is the mixture temperature and R is the perfect gas constant $R = 8.314 J/mol/K$. The state equation is then:

$$p = \sum_{k=1}^{N} p_k = \sum_{k=1}^{N} \rho_k \frac{R}{W_k} T = \rho \frac{R}{W} T \quad \text{where} \quad \rho = \sum_{k=1}^{N} \rho_k. \tag{1.5}$$

Chemical kinetics

During combustion, reactants are transformed into products once a sufficiently high energy is available to activate the reaction. Generally, N species react through M reactions:

$$\sum_{k=1}^{N} \nu'_{kj} \mathcal{M}_k \leftrightharpoons \sum_{k=1}^{N} \nu''_{kj} \mathcal{M}_k \quad \text{for} \quad j = 1, M, \tag{1.6}$$

where $\mathcal{M}_k$ is the symbol for species k, ν'_{kj} and ν''_{kj} are the molar stoichiometric coefficients of species k for reaction j such as:

$$\sum_{k=1}^{N} (\nu''_{kj} - \nu'_{kj}) W_k = \sum_{k=1}^{N} \nu_{kj} W_k = 0 \tag{1.7}$$

to guarantee the mass conservation. Each reaction j contributes to the reaction rate $\dot{\omega}_k$ of species k following its progress rate Q_j:

$$\dot{\omega}_k = W_k \sum_{j=1}^{M} \nu_{kj} Q_j \quad \text{for} \quad k = 1, N. \tag{1.8}$$

The mass species reaction rate per unit volume $\dot{\omega}_k$ describes the rate of production (or destruction if negative) of species k due to reactions. The heat released by combustion is:

$$\dot{\omega}_T = - \sum_{k=1}^{N} \Delta h^0_{f,k} \dot{\omega}_k, \tag{1.9}$$

where $\Delta h^0_{f,k}$ is the mass enthalpy of formation of species k at temperature $T_0 = 0$K. The reaction progress rates Q_j are expressed as:

$$Q_j = K_{fj} \prod_{k=1}^{N} [X_k]^{n'_{kj}} - K_{rj} \prod_{k=1}^{N} [X_k]^{n''_{kj}} \tag{1.10}$$

where n'_{kj} and n''_{kj} are the forward and reverse order of reaction j for species k, K_{fj} and K_{rj} are the forward and reverse reaction constants for reaction j:

$$K_{rj} = K_{fj}/K^j_{eq}. \tag{1.11}$$

The equilibrium constant K^j_{eq} has been defined by Kuo [90]:

$$K^j_{eq} = \left(\frac{p_0}{RT}\right)^{\Sigma_{k=1}^{N} \nu_{kj}} \exp\left(\frac{\Delta S^0_j}{R} - \frac{\Delta H^0_j}{RT}\right), \tag{1.12}$$

where $p_0 = 1$ bar. ΔH^0_j and ΔS^0_j are respectively the enthalpy (sensible + chemical) and the entropy changes for the reaction j:

$$\Delta H^0_j = h(T) - h(0) = \Sigma_{k=1}^{N} \nu_{kj} W_k (h_{s,k}(T) + \Delta h^0_{f,k}) \tag{1.13}$$

$$\Delta S^0_j = \Sigma_{k=1}^{N} \nu_{kj} W_k s_k(T), \tag{1.14}$$

where s_k is the entropy of species k.

In its simplest formulation, the forward reaction constant K_{fj} is generally expressed via an Arrhenius law:

$$K_{fj} = A_{fj} T^{\beta_j} \exp\left(-\frac{Ea_j}{RT}\right). \tag{1.15}$$

From a molecular point of view, it describes the probability that an atom exchange occurs due to molecular collisions. From Eqs (1.10) and (1.15), it could be noticed that this probability depends on:

- the probability that a molecular collision occurs, i.e. the product of the species concentrations $[X_k]$ moduled by n_{kj};
- the activation energy Ea_j, i.e the minimum quantity of collision energy to enhance the reaction. Forward and reverse reactions are characterized by two different activation energies (Fig. 1.1).
- the pre-exponential constant A_{fj} which models the collision frequency, the geometry and the orientation of the molecule during collisions;

- the temperature and its exponent β_j describing the thermal excitation of the molecules.

More complex formulations are available to represent homogeneous reactions with pressure-independent rate coefficients such as third-body reactions [91], the falloff formulation by Lindemann [97] or the Troe falloff function by Gilbert et al. [70]

The characterization of the mass species reaction rates $\dot{\omega}_k$ and, consequently, of the heat release is a central problem of combustion modeling and the main subject of this thesis.

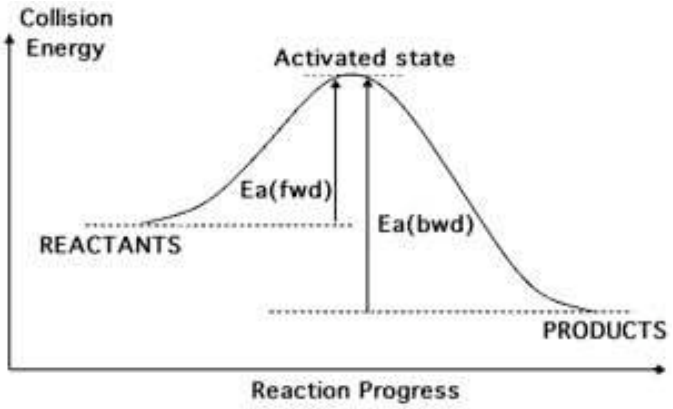

Figure 1.1 - *Sketch of the activation energy [156].*

1.1 Conservation equations for reacting flows

The generalization of the Navier-Stokes equations for a reacting flow is quite straightforward [173]:

- The **continuity and momentum equations** are unchanged:

$$\boxed{\frac{\partial \rho}{\partial t} + \frac{\partial \rho u_j}{\partial x_j} = 0} \tag{1.16}$$

$$\boxed{\frac{\partial \rho u_i}{\partial t} + \frac{\partial \rho u_j u_i}{\partial x_j} = -\frac{\partial p}{\partial x_i} + \frac{\partial \tau_{ij}}{\partial x_j} + F_i} \quad \text{for} \quad i = 1, 2, 3, \tag{1.17}$$

where u_i is the component i of the velocity field. The body force $F_i = \rho \Sigma_{k=1}^{N} Y_k f_{k,j}$ describes the volume force $f_{k,j}$ acting on species k in direction j. The viscous force

tensor τ_{ij} is given by the Newton law [1]:

$$\tau_{ij} = \mu\left(\frac{\partial u_i}{\partial x_j} + \frac{\partial u_j}{\partial x_j}\right) - \frac{2}{3}\mu\delta_{ij}\left(\frac{\partial u_k}{\partial x_k}\right), \tag{1.18}$$

where μ is the mixture dynamic laminar viscosity and δ_{ij} is the Kronecker symbol.

- One **species balance equation** is needed for each species:

$$\boxed{\frac{\partial \rho Y_k}{\partial t} + \frac{\partial \rho u_j Y_k}{\partial x_j} = -\frac{\partial \mathcal{J}_j^k}{\partial x_j} + \dot{\omega}_k} \quad \text{for} \quad k = 1, N, \tag{1.19}$$

where $\mathcal{J}_j^k$ is the molecular diffusive flux of species k comprising the species diffusion velocity $V_{k,j}$ and the correction velocity V_i^c ensuring mass conservation [124]:

$$\mathcal{J}_j^k = -\rho\left(Y_k V_{k,i} - Y_k V_i^c\right) \tag{1.20}$$

with D_k is the molecular diffusion coefficient of species k. Applying the Hirschfelder and Curtiss approximation to species diffusion velocity [79]:

$$Y_k V_{k,i} = -D_k \frac{W_k}{W}\frac{\partial X_k}{\partial x_i}, \tag{1.21}$$

the correction velocity V_i^c is given by:

$$V_i^c = \sum_{k=1}^{N} D_k \frac{W_k}{W}\frac{\partial X_k}{\partial x_i}. \tag{1.22}$$

The species diffusion under temperature gradients (named Soret effect) and molecolar transport due to pressure gradients are neglected in this work. The species diffusion coefficient D_k describes the multi-species molecular diffusion and it is usually characterized in terms of the Schmidt number Sc_k of species k:

$$Sc_k = \frac{\mu}{\rho D_k} = \frac{\nu}{D_k} \tag{1.23}$$

which compares the kinematic viscosity ν of the mixture to the molecular diffusion coefficient D_k of species k.

[1] All fluids are supposed newtonian in the following.

- The **total enthalpy** of the mixture h_t accounts for the sensible, the chemical and the kinetic enthalpy:

$$h_t = h + \frac{1}{2}u_i u_i = \sum_{k=1}^{N} h_k + \frac{1}{2}u_i u_i, \tag{1.24}$$

and its conservation equation is given by:

$$\boxed{\frac{\partial \rho h_t}{\partial t} + \frac{\partial \rho u_i h_t}{\partial x_i} = \frac{\partial p}{\partial t} - \frac{\partial q_i}{\partial x_i} + \frac{\partial}{\partial x_j}\left(\tau_{ij} u_i\right) + \dot{Q} + \rho \sum_{k=1}^{N} Y_k f_{k,i} \left(u_i + V_{k,i}\right),} \tag{1.25}$$

where $\dot{Q}$ is the heat source term, $u_i \tau_{ij}$ and $\rho \sum_{k=1}^{N} Y_k f_{k,i} \left(u_i + V_{k,i}\right)$ denote the power due to viscous forces and the power produced by volume forces f_k on species k respectively. The energy flux q_i is composed by the heat diffusion term (following the Fourier law) and the diffusion between species with different enthalpies:

$$q_i = \underbrace{-\lambda \frac{\partial T}{\partial x_i}}_{\textit{heat diffusion}} + \underbrace{\rho \sum_{k=1}^{N} h_k Y_k V_{k,i}}_{\textit{species enthalpy diffusion}}, \tag{1.26}$$

where λ is the heat diffusion coefficient. The enthalpy diffusion due to mass fraction gradients (Dufour effect) is neglected in this work.

The heat diffusion coefficient is generally compared to the constant pressure specific heat of the mixture $C_p = \sum_k C_{pk} Y_k$ via the Prandtl number:

$$Pr = \frac{\mu C_p}{\lambda}. \tag{1.27}$$

The thermal heat diffusivity D_{th} is defined as:

$$D_{th} = \frac{\lambda}{\rho C_p}, \tag{1.28}$$

and it could be linked to the species diffusion coefficient D_k via the Lewis number Le_k of species k:

$$Le_k = \frac{D_{th}}{D_k} = \frac{Sc_k}{Pr}. \tag{1.29}$$

In simple turbulent flame models, the Lewis number is usually assumed to be equal to unity for each species, i.e. thermal and mass diffusivites are equal, mass and enthalpy balance equations being formally identical. The impact of this assumption in laminar flames is analyzed in Section 2.2. Results are generally not affected by this hypothesis for most hydrocarbons whereas discrepancies could be detected for very light molecules such as H and H_2.

1.1.1 Filtering and Large Eddy Simulation

At present, the full numerical resolution of the instantaneous conservation equations (**Direct Numerical Simulations** or **DNS**) is confined to academic problems or simple configurations since the computational costs to solve all the length scales characterizing a reactive turbulent flow are still very high. The simplest approach to overcome this problem is the **Reynolds-Averaged Navier-Stokes** (**RANS**) modeling. Each quantity Q is decomposed into the mean component $\langle Q \rangle$ and the deviation Q' from the mean:

$$Q = \langle Q \rangle + Q' \quad \text{with} \quad \langle Q' \rangle = 0. \tag{1.30}$$

In the RANS formalism, the balance equations are averaged and only the mean flow field is solved. All effects due to fluctuating motions have to be modeled. **Large Eddy Simulations** (**LES**) are generally preferred since the largest turbulent motions are explicitly calculated and only the smallest length scales of the turbulence are modeled. Moreover in turbulent flows the smallest structures have an universal nature whereas the largest scales generally depend on geometry. As a consequence, the LES approach is more justified compared to RANS since the turbulent models are *a priori* more efficient when describing only the small scales.

In the LES approach, the quantity Q is filtered in the spectral space (when the highest frequencies are suppressed) or the physical space (when a weighted average is applied in a given volume):

$$\overline{Q}(\mathbf{x}) = \int Q(\mathbf{x}^*) F(\mathbf{x} - \mathbf{x}^*) d\mathbf{x}^*, \tag{1.31}$$

where $\overline{Q}$ is a spatially and temporally fluctuating quantity in opposition to the statistically averaged quantity $\langle Q \rangle$ calculated in RANS.

To take into account the fluctuations of density due to thermal heat release a mass-weighted Favre filter is usually introduced when working with reactive flows:

$$\bar{\rho}\widetilde{Q}(\mathbf{x}) = \int \rho Q(\mathbf{x}^*) F(\mathbf{x} - \mathbf{x}^*) d\mathbf{x}^*. \tag{1.32}$$

The resulted filtered instantaneous balance equations are:

$$\frac{\partial \bar{\rho}}{\partial t} + \frac{\partial \bar{\rho}\widetilde{u}_j}{\partial x_j} = 0 \tag{1.33}$$

$$\frac{\partial \bar{\rho}\widetilde{u}_i}{\partial t} + \frac{\partial \bar{\rho}\widetilde{u}_j\widetilde{u}_i}{\partial x_j} = -\frac{\partial}{\partial x_j}\left[\bar{\rho}\left(\widetilde{u_i u_j} - \widetilde{u}_i\widetilde{u}_j\right)\right] - \frac{\partial \bar{p}}{\partial x_i} + \frac{\partial \bar{\tau}_{ij}}{\partial x_j} + \overline{F}_i \quad \text{for} \quad i = 1, 2, 3 \tag{1.34}$$

$$\frac{\partial \bar{\rho}\widetilde{Y_k}}{\partial t} + \frac{\partial \bar{\rho}\widetilde{u_j}\widetilde{Y_k}}{\partial x_j} = -\frac{\partial}{\partial x_i}\left[\bar{\rho}\left(\widetilde{u_i Y_k} - \widetilde{u_i}\widetilde{Y_k}\right)\right] + \frac{\partial \overline{V_{k,i}Y_k}}{\partial x_i} + \overline{\dot{\omega}_k} \quad \text{for} \quad k = 1, N \tag{1.35}$$

$$\frac{\partial \bar{\rho}\widetilde{h_t}}{\partial t} + \frac{\partial \bar{\rho}\widetilde{u_i}\widetilde{h_t}}{\partial x_i} = -\frac{\partial}{\partial x_i}\left[\bar{\rho}\left(\widetilde{u_i h_t} - \widetilde{u_i}\widetilde{h_t}\right)\right] + \frac{\partial \bar{p}}{\partial t} - \frac{\partial \bar{q}_i}{\partial t} + \frac{\partial}{\partial x_j}\left(\overline{u_i \tau_{ij}}\right) + \overline{\dot{Q}}. \tag{1.36}$$

The objective of turbulent combustion and LES modeling is to propose the necessary closures for the unknown quantities:

- **Unresolved Reynolds stresses** $\left(\widetilde{u_i u_j} - \widetilde{u_i}\widetilde{u_j}\right)$ require a subgrid scale turbulence model which reproduces the energy fluxes between resolved and unresolved turbulent scales. Both the interactions between turbulent structures of different sizes and the interactions between structures of comparable size must be taken into account. These models are generally based on turbulence modeling developed for non-reacting flows such as the Smagorinsky model [127], the dynamic Smagorinsky model [67], the Wale model [54] or the Sigma model [114].
- **Unresolved species** $\left(\widetilde{u_i Y_k} - \widetilde{u_i}\widetilde{Y_k}\right)$ **and enthalpy fluxes** $\left(\widetilde{u_i h_t} - \widetilde{u_i}\widetilde{h_t}\right)$ are modeled in an analogous manner to the unresolved Reynolds stresses [110].
- **Filtered laminar diffusion fluxes** for species and enthalpy may be neglected since they are small compared to turbulent transport once a sufficiently large turbulence level is reached, or modeled through a simple gradient assumption such as:

$$\overline{V_{k,i}Y_k} = -\bar{\rho}\overline{D}_k\frac{\partial \widetilde{Y_k}}{\partial x_i} \quad \text{and} \quad \overline{\lambda\frac{\partial T}{\partial x_i}} = \overline{\lambda}\frac{\partial \widetilde{T}}{\partial x_i}. \tag{1.37}$$

- **Filtered chemical reaction rates** $\overline{\dot{\omega}_k}$ modeling is a key point in turbulent combustion theory. It is discussed in Section 1.2.3.

1.2 Turbulent premixed combustion

The transition from a laminar flow to a turbulent flow is characterized by the Reynolds number comparing inertia to viscous forces:

$$Re = \frac{|u|l}{\nu} \tag{1.38}$$

where l and u are reference dimension and velocity respecitvely characterizing the flow.

A turbulent flow is characterized by significant variations of the velocity field in space and time which present a continuous spectrum of vortical structures, called

eddies, convected by the mean flow. Eddies strongly interact with each other through a cascade process which enhances the transfer of mass, momentum and heat compared to a laminar flow. The energetic density spectrum $E(k)$ of the turbulent eddies in an homogeneous isotropic turbulence is displayed in Fig. 1.2 as a function of the wave number k proportional to the inverse of the eddy length scale.

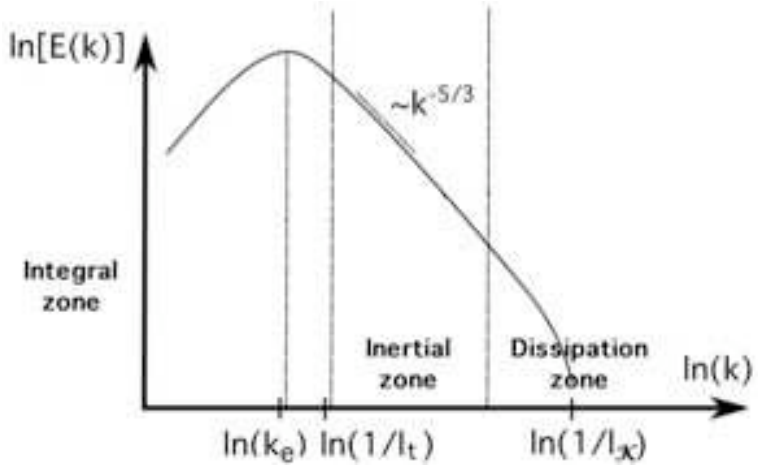

Figure 1.2 - *Sketch of energy density spectrum E(k) in an homogeneous isotropic turbulence. Distinction between integral, inertial and dissipation zones. The abscissa of the integral (l_t) and Kolmogorov ($l_\mathcal{K}$) length scales are indicated [127].*

Three different zones may be identified [127]:

- **Integral zone**: it is characterized by the lowest frequencies and it is centered on the wave number k_e. It contains the biggest and most energetic structures related to the integral length scale l_t, fixed by the production conditions of turbulence, and to the turbulent speed u_p. The resolved turbulent kinetic energy $\bar{k}$ characterizing this region is given by:

$$\bar{k} = \frac{\overline{u_i'^2}}{2} = \frac{3u_p^2}{2}, \tag{1.39}$$

  where u_p is the turbulent speed defined as the mean standard deviation of velocity.

  The length scale and velocity of the integral zone structures are comparable to the quantities used to define the Reynolds number of the flow field and are not affected by viscous effects.

- **Dissipation zone**: it is characterized by the highest frequencies and it is centered on the Kolmogorov wave number $k_\mathcal{K}$. It contains the smallest structures called

Kolmogorov scales which length $l_\mathcal{K}$ and speed $u_\mathcal{K}$ are estimated as [153]:

$$l_\mathcal{K} = \left(\frac{\nu^3}{\epsilon}\right)^{1/4} \quad \text{and} \quad u_\mathcal{K} = (\nu\epsilon)^{1/4}, \tag{1.40}$$

where ϵ is the dissipation which converts the turbulent kinetic energy $\bar{k}$ into heat due to the mixture kinematic viscosity ν.

- **Inertial zone**: in this zone, the large eddies become unstable and break down into smaller eddies via a "cascade" process. No eddy dissipation is detected and the energy is transfered from the biggest to the smallest structures following a $k^{-5/3}$ law for isotropic steady turbulence.

1.2.1 Combustion regimes

Building a turbulent combustion model generally requires a classification of the different combustion regimes classically based on the characteristic dimensions of turbulence and chemistry. The chemical phenomena are characterized by the chemical time:

$$\tau_c = \frac{\delta_L}{S_L}, \tag{1.41}$$

where δ_L and S_L are respectively the thickness and flame speed of a laminar premixed flame.[2] On the contrary, turbulent combustion involves very different lengths, velocities and times and the flame interacts at the same time with the most energetic turbulent structures characterized by the turbulence time scale $\tau_t = l_t/u_p$, and with the turbulence smallest scales characterized by the Kolmogorov time scale $\tau_\mathcal{K} = l_\mathcal{K}/u_\mathcal{K}$:

- The characteristic turbulence time scale τ_t is compared to the chemical time scale τ_c via the **Damköhler number**:

$$\boxed{Da = \frac{\tau_t}{\tau_c} = \frac{l_t}{\delta_L}\frac{S_L}{u_p}.} \tag{1.42}$$

  For high Damköhler number $Da >> 1$, the internal thin structure of the flame is not strongly affected by turbulence although the flame surface is wrinkled, stretched and convected by the turbulent flow. The reaction zone can be modeled by a laminar flame element named "**flamelet**". In the limit of small Damköhler number $Da << 1$, reactants and products are mixed by turbulence before reacting via a slow chemical reaction like in a perfectly stirred reactor. In pratical applications,

[2] Details on the characterization of laminar flames are provided in Chapter 2.

both regimes are usually found: fuel oxidation usually corresponds to a fast chemical reaction ($Da >> 1$), whereas pollutant formation (CO oxidation or NO formation) are slower.

- The **Karlovitz number** identifies the different interactions between turbulence small scales and flame:

$$\boxed{Ka = \frac{\tau_c}{\tau_\mathcal{K}} = \frac{\delta_L}{l_\mathcal{K}} \frac{u_\mathcal{K}}{S_L}.} \tag{1.43}$$

The relation $S_L \approx \nu/\delta_L$ [124] leads to a unity flame Reynolds number[3]:

$$Re_f = \frac{\delta_L S_L}{\nu} \approx 1. \tag{1.44}$$

Using Eqs. (1.40) and (1.44) the Karlovitz number is rewritten as:

$$Ka = \left(\frac{u_\mathcal{K}}{S_L}\right)^{3/2} \left(\frac{l_\mathcal{K}}{\delta_L}\right)^{-1/2} = \left(\frac{\delta_L}{l_\mathcal{K}}\right)^2. \tag{1.45}$$

Thus, the Karlovitz number compares the flame length scale to the smallest turbulence structure.

Since the Reynolds, Damköhler and Karlovitz numbers are related through $Re = Da^2 Ka^2$ the transition between the different combustion regimes is completely defined by two of them (Fig. 1.3).

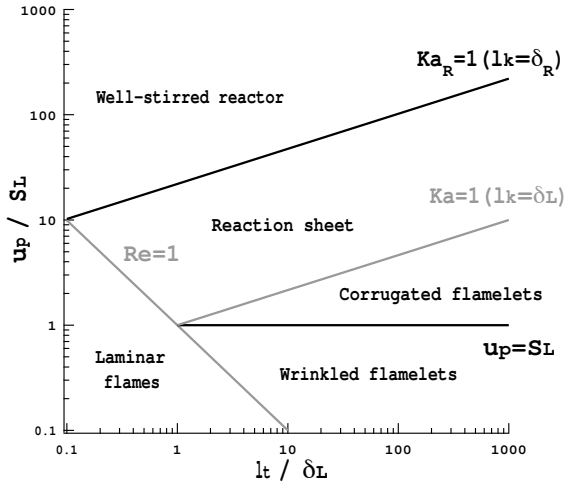

Figure 1.3 - *Regime diagram for premixed turbulent combustion [117].*

[3]From [173] and [90] the flame Reynolds number is usually assumed constant and approximately equal to $Re_f = (\delta_L S_L)/\nu \approx 4$.

To distinguish the turbulence effects on the flame inner structure, i.e. the reaction zone, from the turbulence effect on the whole flame comprising also the preheating and the postflame zones, one additional Karlovitz number is defined using the reaction zone thickness δ_r [117]:

$$Ka_r = \left(\frac{\delta_r}{l_k}\right)^2 = \left(\frac{\delta_r}{\delta_L}\right)^2 \left(\frac{\delta_L}{l_k}\right)^2 \approx \frac{1}{100}\left(\frac{\delta_l}{l_k}\right)^2 \approx \frac{Ka}{100}. \tag{1.46}$$

Five different regimes have been defined by Peters [117] (Fig. 1.4):

- **Laminar flame regime** ($Re_t < 1$): the flow is laminar and the flame is slightly wrinkled.
- **Wrinkled flamelet regime** ($Re_t > 1$, $Ka < 1$, $u_p/S_L < 1$): when $Ka < 1$, the flame thickness is smaller than the Kolmogorov scale. The flame element can be associated to a laminar flame and its surface is only slightly wrinkled by the vortex passage due to $u_p/S_L < 1$ (Fig. 1.4). The interaction between turbulence and flame is limited.
- **Corrugated flamelet regime** ($Re_t > 1$, $Ka < 1$, $u_p/S_L > 1$): the flamelet regime is still valid but, since $u_p/S_L > 1$, the flame surface is more curved and stretched with the formation of pockets of size similar to the eddy size.
- **Reaction-sheet regime** ($Re_t > 1$, $Ka > 1$, $Ka_r < 1$): the smallest eddies of length l_k are smaller than the flame thickness δ_L ($Ka > 1$) and they can interact with the preheat zone of the flame enhancing heat and mass transfers. The preheat zone is then thickened whereas the reaction zone, that is thinner than the Kolmogorov length scale ($Ka_r < 1$), is not affected and keeps its laminar nature.
- **Well-stirred reactor regime** ($Re_t > 1$, $Ka > 1$, $Ka_r > 1$): the Kolmogorov scale l_k is smaller than the reaction zone thickness δ_r ($Ka_r > 1$) and both preheat and reaction zones are affected by turbulent motions. The smallest eddies penetrate into the reaction zone, increasing diffusion and heat transfer rate to the preheat zone. The flow behaves like a well-stirred reactor without any distinct laminar structure.

The distinction of the different combustion regimes based on the Reynolds and Karlovitz numbers is only qualitative since:

- the homogenous and isotropic turbulence is supposed unaffected by heat release, which is not true for combustion systems;
- unsteady and curvature effects which play an important role [121] are neglected;

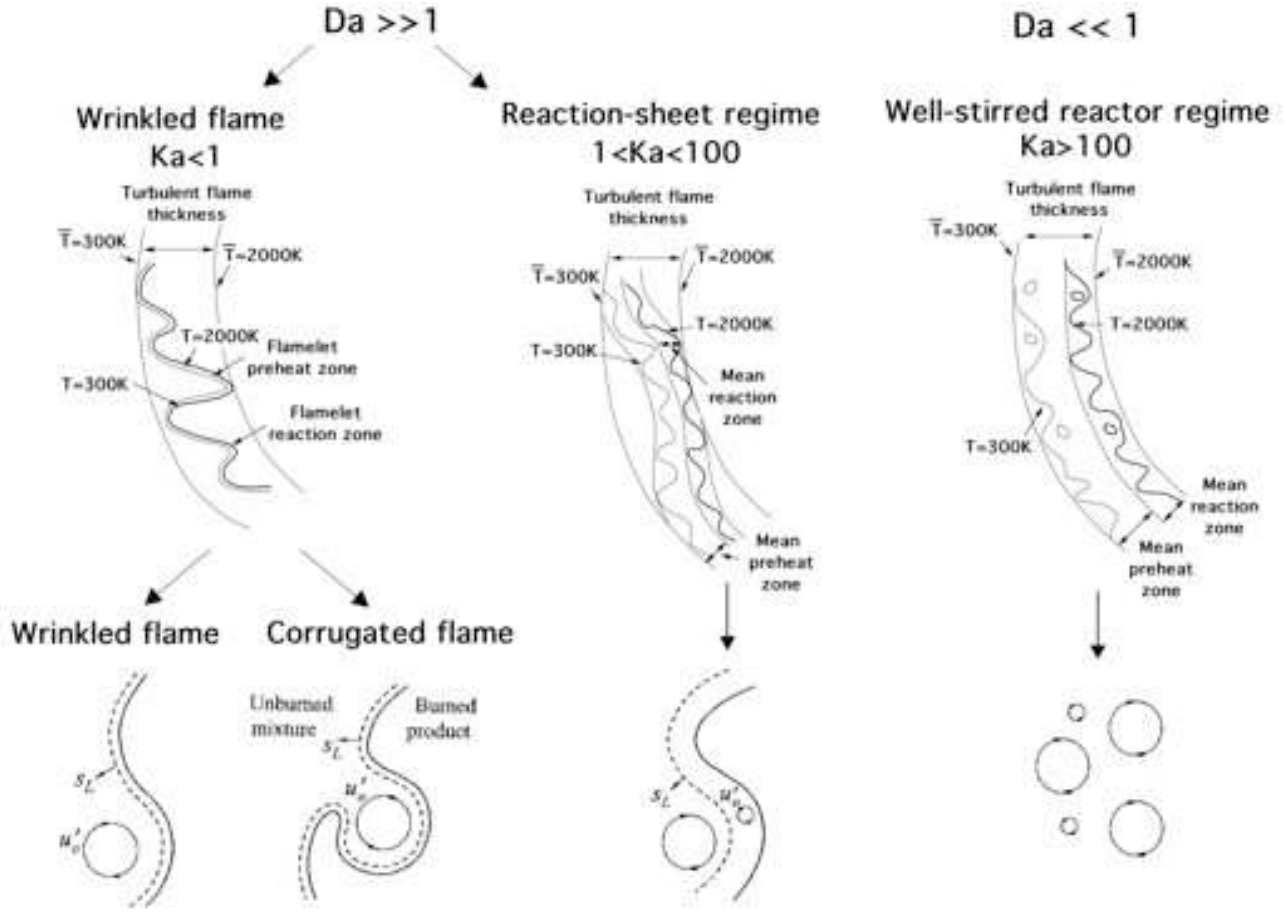

Figure 1.4 - *Turbulent premixed combustion regimes illustrated in a case where the fresh and burnt gas temperatures are* 300 *and* 2000 *K respectively [124, 91].*

- the entire analysis is based on order of magnitude estimations, i.e. the flamelet regime limit could correspond to $Ka = 0.1$ or $Ka = 10$ [31, 42];
- there is no experimental verification that eddies actually enter the flamelet and increase diffusivity [52];
- a one-step irreversible reaction chemistry has been assumed for this classification. Combustion is generally characterized by multiple species and reactions with consequently very different chemical time scales.

Most of combustion applications belong to the flamelet regime ($Da >> 1$). An example of corrugated flame regime is the interaction between a pair of vortices and a flame analyzed in Section 4.1 whereas the reaction-sheet regime characterizes the flame interaction with a homogeneous isotropic turbulence (HIT) and the Bunsen flame studied in Sections 4.2 and 4.3 respectively.

1.2.2 Turbulent flame speed

In the flamelet regime, the turbulent flame front can be locally modeled by a laminar premixed flame which is stretched and deformed by turbulence.
The main effect of turbulence on combustion is the flame front wrinkling [15], by the large turbulent scales, augmenting its effective area A_T (Fig. 1.5).

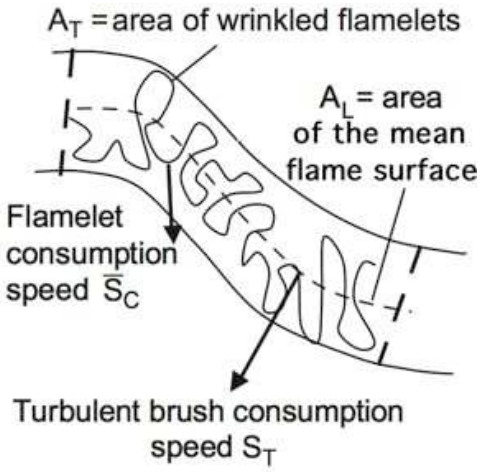

Figure 1.5 - *Sketch of the wrinkled area A_T and of the mean flame surface A_L. The flamelet consumption speed $\overline{S}_C$ and the turbulent brush local consumption speed S_T are also labeled [52].*

As a consequence, the rate of reactant consumption increases, augmenting the propagation speed of the mean front. For the flamelet regime, it is supposed that the front locally propagates at the laminar velocity S_L. The turbulent flame is then propagating with a **turbulent speed** S_T equal to the laminar flame speed weighted by the ratio of the wrinkled instantaneous front area A_T and the projected unwrinkled area A_L [52]:

$$\boxed{\frac{S_T}{S_L} = \frac{A_T}{A_L} I_0,} \tag{1.47}$$

where $I_0 = \overline{S}_C / S_L$ is the burning intensity defined as the ratio between the time average of the flamelet consumption speed $\overline{S}_C$ and the local laminar speed. The typical behavior of the turbulent velocity S_T/S_L is represented in Fig. 1.6 as a function of u_p for various pressures. The turbulent speed S_T increases with the turbulence intensity as well as with pressure. A gradually decreasing slope for high turbulence intensities is detected denoting that beyond a certain level the impact of turbulence intensity on turbulent flame is reduced.

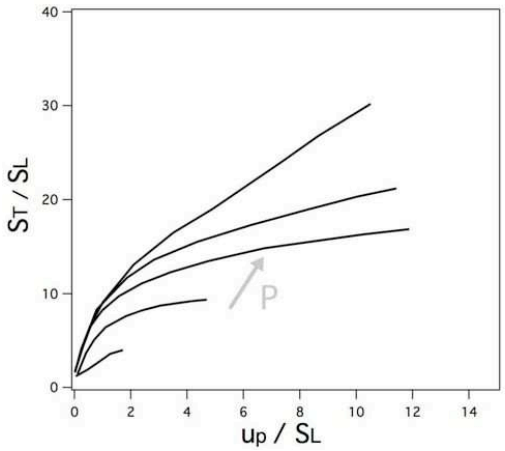

Figure 1.6 - *Experimental turbulent burning velocity as function of turbulence intensity and pressure for methane-air mixture at equivalence ratio $\phi = 0.9$ [89]. The investigated pressure values are $P = 0.1, 0.5, 1.0, 2.0, 3.0$ MPa.*

1.2.3 Combustion modelling for LES

Different models have been proposed to approximate the filtered species reaction rates $\overline{\dot{\omega}_k}$ for turbulent premixed combustion of Eq.(1.35) using the LES approach [76, 10]. They may be separated into two main categories:

- **Models assuming an infinitely thin reaction zone**: the turbulent premixed flame is modeled by fresh reactants and burnt products separated by an infinitely thin reaction zone. The local structure of the flame is assumed equal to a laminar flame for which the inner structure is not affected by turbulence (flamelet assumption). The Bray-Moss-Libby (BML) models [28], the flame surface density models [74, 108], the flame wrinkling description [170] and G-equation models [117, 53, 119, 112] are some of the most common examples.
  In the **BML** model, the progress variable $c(\mathbf{x}, t)$ is the only quantity defining the thermochemical state of the mixture. All other mean quantities are described in terms of a probability density function $P(c, \mathbf{x})$ which represents fresh reactants, burnt products and a partially burned mixture with probability $\alpha(\mathbf{x})$, $\beta(\mathbf{x})$ and $\gamma(\mathbf{x})$ respectively, where $\gamma(\mathbf{x}) \ll 1$. The mean values of quantities such as species mass fractions only depend on $\alpha(\mathbf{x})$ and $\beta(\mathbf{x})$.
  In the **coherent flamelet model** (or flame surface density model) the mean chemical reaction rate is expressed in terms of the flame surface density where conditions are favorable for reaction. The balance equation required for the flame surface density accounts for average stretch rate and extinction.
  In the **level set approach** (or G-equation approach), a function $G(\mathbf{x}, t)$ is defined such as $G(\mathbf{x}, t) = G_0$ identifies the flame surface, whereas for $G > G_0$ burnt gases

are found and the fresh reactants are located where $G < G_0$. A transport equation is solved for the function $G(\mathbf{x}, t)$ based on kinematic considerations.

- **Models describing the reaction zone thickness**: the turbulent premixed flame is characterized by a finite thin reaction zone that could interact with the turbulent flow and often behaves as a stretched laminar flame. Some examples are the Probability Density Function (PDF) models [6, 51] and the artificially thickened flame (TF) models [8, 7, 93].
  In the **Probability Density Function model**, mean values and correlations of quantities of interest are extracted by the use of a probability density function, based on statistical properties of a scalar field such as the progress variable c.
  The **artificially thickened flame approach** is the one used in this study and is detailed below.

Artificially thickened flame model for LES (TFLES)

The flame thickness δ_L is usually smaller than the LES filter size Δ. The artificially thickened flame approach for LES (TFLES) has been proposed in order to resolve the flame front on a LES grid [8, 7, 93].

The whole TFLES method is based on a simple change of the spatial and temporal variables:

$$x \mapsto \mathcal{F} x \quad \text{and} \quad t \mapsto \mathcal{F} t, \tag{1.48}$$

which corresponds to a thickening of the flame thickness by a factor $\mathcal{F}$. The filtered species and thermal reaction rates are:

$$\overline{\dot{\omega}_k} = \frac{\dot{\omega}_k}{\mathcal{F}} \quad \text{and} \quad \overline{\dot{\omega}_T} = \frac{\dot{\omega}_T}{\mathcal{F}}. \tag{1.49}$$

Following the theory of laminar premixed flames [173], the flame speed S_L is consequently modified:

$$S_L \propto \frac{D_{th}}{\delta_L} \mapsto \frac{D_{th}}{\mathcal{F}\delta_L}. \tag{1.50}$$

In order to maintain the same flame speed, the thermal and species diffusivities are also multiplied by F:

$$D_{th} \mapsto \mathcal{F} D_{th} \quad \text{and} \quad D_k \mapsto \mathcal{F} D_k, \tag{1.51}$$

so that

$$S_L \mapsto \frac{\mathcal{F} D_{th}}{\mathcal{F}\delta_L} = \frac{D_{th}}{\delta_L}. \tag{1.52}$$

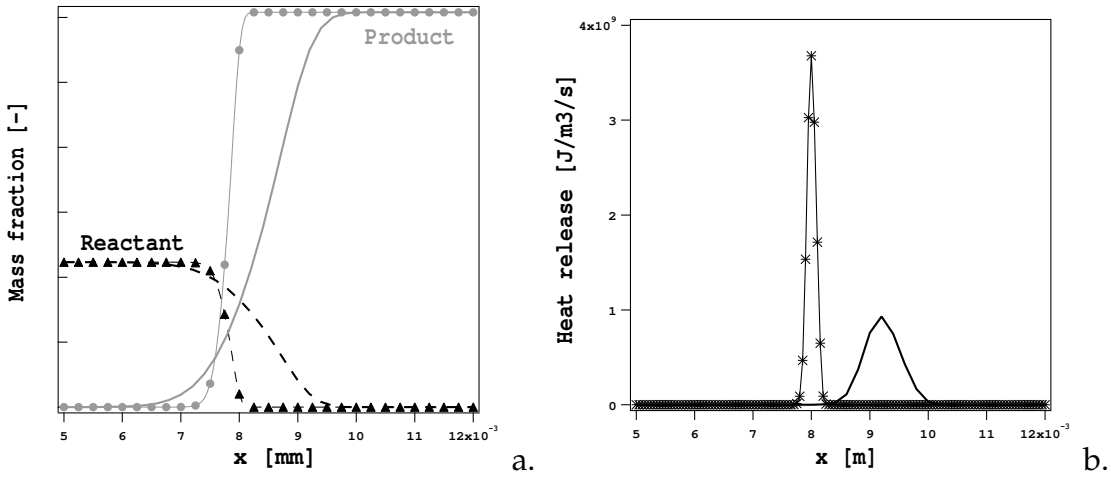

Figure 1.7 - *Results for a flame thickened by a factor $\mathcal{F} = 4$ (lines) compared to the reference solution of a laminar unthickened flame (symbols).*

Results for a laminar premixed flame are shown in Fig. 1.7 using a thickening factor $\mathcal{F} = 4$. The gradient profiles are decreased allowing the use of a coarse grid. The maximum values of reaction rates and heat release are reduced by a factor $\mathcal{F} = 4$. However, the integrals of reaction rates are conserved and consequently the laminar flame speed is conserved too.

When a turbulent flame is artificially thickened, the flame front is less wrinkled by the turbulent eddies and the time scale ratio between turbulence and chemistry is modified. The so-called efficiency function $\mathcal{E}$ [46, 36] has been proposed to properly account for the wrinkling effect on the flame front:

$$D_{th} \mapsto \mathcal{E}\mathcal{F} D_{th} \quad \text{and} \quad D_k \mapsto \mathcal{E}\mathcal{F} D_k \tag{1.53}$$

$$\overline{\dot{\omega}_k} = \frac{\mathcal{E}\dot{\omega}_k}{\mathcal{F}} \quad \text{and} \quad \overline{\dot{\omega}_T} = \frac{\mathcal{E}\dot{\omega}_T}{\mathcal{F}}, \tag{1.54}$$

so that:

$$S_L \mapsto \frac{\mathcal{E}\mathcal{F} D_{th}}{\mathcal{F}\delta_L} = S_T. \tag{1.55}$$

This model has been first developed for perfectly premixed combustion. The implementation of the TFLES method in a numerical code and its extention to partially premixed combustion and multi-reactions chemistries are presented in Chapter 3.

1.3 Chemistry for turbulent combustion

Chemical kinetic models are used to describe the transformation of reactants into products at the molecular level. Different detailed mechanisms characterizing the combustion phenomena of alkanes, alkynes and aromatics species are available [148]. These mechanisms characterized by hundreds of species and thousands of reaction are supposed to accurately and reliably describe all kinds of combustion phenomena over all possible ranges of the thermodynamic parameters such as pressure, initial composition and temperature. Nevertheless, this kind of mechanism is computationally expensive due to the large number of species and reactions. Moreover, numerical problems often occur when solving the stiff system of conservation equations involving different chemical time scales [91] (Fig. 1.8). For these reasons, different methods of mechanism reduction have been developed.

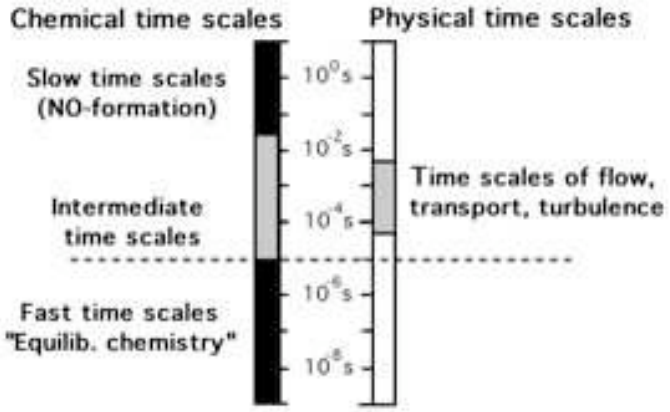

Figure 1.8 - *Range of chemical time scales [166].*

In this section, different approaches to approximate the species reaction rates $\dot{\omega}_k$ defined in Eq. (1.8) are presented:

- mechanism reduction by elimination of redundant species and reactions (skeletal and reduced mechanisms);

- dimension reduction of the phase space by the generation of a lower-dimensional manifold involving only $P < N$ parameters, N being the number of species. The thermochemical system generally evolves in a space of $2+N$ dimension (pressure, enthalpy and mass fraction of N species), but follows much lower-dimensional paths in this phase-space.

1.3.1 Skeletal mechanisms

Starting from a detailed mechanism, a so-called skeletal mechanism is obtained by eliminating species and reactions which have a negligible effect on the phenomena of interest. Useful methods for species elimination include the systematic reaction rate analysis [158], the Jacobian analysis [154] and the theory of directed relation graph proposed by Lu and Law [99]. The computational singular perturbation method [106, 85] and the sensitivity analysis [166] may also be used to decrease the number of reactions.

Although information on the redundant species is completely lost, the reaction rates of the relevant species are not greatly affected and different combustion phenomena (premixed and diffusion combustion, reponse to stretch, ignition delay, dilution effect, etc..) are naturally described. Unfortunately, skeletal mechanisms are usually still too expensive to be used in CFD but they can be used as reference to build more reduced mechanisms or to generate a reduced manifold.

1.3.2 Reduced chemical mechanisms

The reduced chemical mechanisms are highly simplified versions of the true chemistry, but are built to reproduce a minimum of flame features. The number of species and reactions is drastically reduced to decrease the computational cost (i.e. the species considered are generally fewer than fifteen). Depending on its complexity, a reduced mechanism correctly reproduces some characteristics of laminar flames. The simplest global or semi-global schemes only predict the laminar flame speed S_L, linked to the fuel consumption rate, and the burnt gas state of a premixed flame. When increasing the number of species and reactions, more details are introduced about the flame structure and its response to stretch.
Two different approaches exist to build reduced mechanisms: the fitting method and the analytical approach.

Fitted mechanisms

Global and semi-global mechanisms [171, 82, 4, 63] are generally 'ad hoc' schemes with fitted reaction parameters on the flame properties of interest. A general methodology to build a fitted two-step scheme that correctly reproduces the flame speed and the equilibrium state for a premixed flame on a wide range of initial temperature and pressure is described in: *B. Franzelli, E. Riber, M. Sanjosé and T. Poinsot ,"A two-step chemical scheme for kerosene-air premixed flames", Combustion and Flame 157, 2010*. The complete article is proposed in Appendix A, and a summary is presented in

Chapter 3, illustrated with a two-step mechanism (2S_CH4_BFER) for methane/air flames. For comparison purposes, a more complex fitted mechanism is also presented in Chapter 3 (JONES scheme [82]) based on the experimental species profiles of laminar premixed and diffusion flames. Genetic self-adaptive algorithms have also been used to automatically fit the reaction parameters in order to correctly reproduce the global required quantities [55, 105].

The validity of the fitted mechanisms is quite limited: since the reaction rates have been built to fit global characteristics, they do not contain any 'real' physical information and their extension to other cases, for example strained flames, is not straightforward and needs validation. This is the objective of Chapter 3.

Analytical mechanisms

Based on skeletal schemes, analytical mechanisms [94, 135, 21] use the quasi-steady state approximation (QSS) for some species and partial equilibrium assumption for some reactions.

Whenever the creation rate of a give species k is slow compared to its destruction rate, the produced concentration is quasi-instantly consumed. The species k can be then assumed in a quasi-steady state and its net rate may be considered as equal to zero: $\dot{\omega}_k \approx 0$. Using Eq. (1.8), this leads to a relation between the involved species concentrations:

$$\dot{\omega}_k = \sum_{j=1}^{M} \nu_{kj} Q_j = \sum_{j=1}^{M} \nu_{kj} \left[K_{fj} \prod_{k=1}^{N} [X_k]^{n'_{kj}} - K_{rj} \prod_{k=1}^{N} [X_k]^{n''_{kj}} \right] = 0. \tag{1.56}$$

The concentration of species k is then computed from Eq. (1.56) and not anymore from its conservation equation, reducing the size of the system of equations.
The system may be further simplified using the partial equilibrium hypothesis for a given reaction j. This simplification can be assumed whenever both the forward and the backward components of reaction j are fast compared to all other reactions. The reaction j is then in a partial equilibrium condition:

$$Q_j = K_{fj} \prod_{k=1}^{N} [X_k]^{n'_{kj}} - K_{rj} \prod_{k=1}^{N} [X_k]^{n''_{kj}} = 0. \tag{1.57}$$

The PETERS [116], the SESHADRI [39] and the LU [98] mechanisms presented in Chapter 3 are analytical schemes, expressing species production/consumption rates as functions of the reaction rates of a skeletal mechanism for methane/air flames.

1.3.3 Manifold generation methods

In the manifold generation methods, the state space of size $N + 2$ is reduced to a lower-dimensional subset of $P < N$ parameters. Following a chemical approach, the phase space is reduced to P slow species whereas the species involved in fast chemical processes are expressed as functions of the manifold parameters. From a mathematical point of view, the eigenvalues of the equation system for the state vector (pressure, fresh gas enthalpy, species mass fractions) are used to estimate the characteristic time scales and to built an Intrinsec-Low-Dimensional-Mainfold (ILDM) [102] neglecting the fast chemical processes.

From a physical point of view, the combustion is described as a family of flame prototypes which represent the combustion mode. Each flame prototype is computed using a detailed mechanism and is then projected in the manifold identified by a couple of controlling parameters. Different types of flame prototype and controlling parameters are identified for different combustion mode [163]:

- **Premixed flames**: information on one-dimensional laminar premixed flames is recorded in a database defining a manifold based on the progress variable describing the progress of the reaction, and the mixture fraction identifying the equivalence ratio of the flame. Two classical methods based on premixed flames are the Flame Prolongation of ILDM (FPI) [69] and the Flame Generated Manifold (FGM) [160, 49]. An extension to non-adiabatic flames has been proposed [59] introducing enthalpy as an ulterior controlling parameter.
- **Steady non-premixed flames** [117]: diffusion flames are computed and store as function of the mixture fraction and of the strain rate.
- **Perfectly stirred reactor** (PSR) [57, 84] are used to describe autoignition adding the residence time.

A major issue associated to tabulation methods is their extension to cases where the number of parameters which must be taken into account increases drastically: for example, in a piston engine, tabulating chemistry requires to account for heat losses, fresh gas temperature and pressure, dilution by recirculating gases... In a gas turbine, the combustion may be fed by more than one stream (for example fuel, cold air and heated air), requiring more than one passive scalar to describe mixing. Generating and handling the lookup table can become difficult in such situations. First, the dimension of the lookup table grows very rapidly and can lead to memory problems on massively parallel machines where the table must be duplicated on each core. A solution is then to use self-similarities in the flame structure [128, 161, 60] or to use in-situ tabulated methods [126]. Second, determining which prototype flame should be used for combustors where the combustion regime is unknown can be a complicated task:

if the turbulent burner has multiple inlets and can feature flame elements which are premixed or not, autoignite or not, choosing the right laminar configuration to tabulate chemistry becomes almost impossible. On the contrary, some reduced mechanisms are able to reproduce these multiple phenomena since the trajectory of their reaction rates are not confined to evolve in a predefined manifold.

In this work, performances of the FPI_TTC* tabulation method [164] are evaluated on a LES of the experimental PRECCINSTA burner (Chapter 5).

1.4 CFD tools

Three different softwares have been used to perform the simulations presented in this thesis:

- the **CANTERA** code efficiently reproduces one-dimensional flame behavior using detailed chemistry and complex transport properties;
- the **S3D** code is a perfectly scaling code for DNS of turbulent combustion in academic configurations;
- the **AVBP** code is dedicated to LES of turbulent combustion on academic and industrial geometries.

CANTERA

CANTERA is an object-oriented, open source suite of software tools for reacting flow problems involving detailed chemical kinetics, thermodynamics and transport processes [71]. It can be used to perform kinetics simulations with large reaction mechanisms, compute chemical equilibrium, evaluate thermodynamic and transport properties of mixtures, evaluate species chemical production rates and create process simulators using networks of stirred reactors. An adaptative mesh-refining algorithm is used to refine the mesh in the reaction zone of laminar flames where strong gradients are detected, drastically reducing the calculation time while preserving results accuracy. Simplified transport properties and the different reduced schemes presented in Chapter 3 have been integrated in CANTERA to allow comparison with the AVBP code.
All equilibrium calculations and simulations of one-dimensional premixed flames presented in this manuscript have been performed with CANTERA.

S3D

S3D is a massively parallel DNS solver developed at Sandia National Laboratories [37]. It solves the full compressible Navier-Stokes equations coupled with detailed chemistry and transport. The governing equations are supplemented with additional constitutive relationships, such as the ideal gas equation of state, and models for reaction rates, molecular transport and thermodynamic properties. S3D is based on a high-order accurate, non-dissipative numerical scheme. The governing equations are solved on a structured three-dimensional cartesian mesh. The solution is advanced in time through a six-stage fourth-order explicit Runge–Kutta method [87]. The solution is spatially discretized using an eighth-order central differencing scheme and a tenth-order filter is used to remove any spurious high-frequency fluctuations in the solution [88]. The DNS of the Bunsen flame by Sankaran [137] (Chapter 4) have been performed using S3D.

AVBP

AVBP is a parallel CFD code which solves the three-dimensional compressible Navier-Stokes on unstructured and hybrid grids [139, 133, 46, 83, 144, 149, 132, 68, 113, 157, 143, 23, 145]. It is dedicated to the prediction of unsteady reacting flow in combustor configurations based on the LES approach. The data structure of AVBP employs a cell-vertex finite-volume approximation [113, 45, 47] and the numerical methods are based on a Lax-Wendroff or a Finite-Element type low-dissipation Taylor-Galerkin discretization in combination with a linear-preserving artificial viscosity model. AVBP is highly portable to most standard platforms including PCs, work stations and mainframes and has proven to be efficient on most parallel architectures [151]. An Arrhenius law reduced chemistry model and the FPI_TTC tabulation method are available to investigate combustion for complex configurations. The interaction between chemical kinetics and turbulence is modeled by the Dynamically Thickened Flame (TFLES) model [46]. All the LES presented in this manuscript have been performed with the AVBP code (Chapters 5 and 6).

Part II

Chemistry models for turbulent combustion

Chapter 2

Major properties of laminar premixed methane/air flames

In the flamelet regime, the turbulent flame front could be modeled by small laminar premixed flames which are stretched and deformed by the turbulent flow. A correct description of the basic element of the flame front, i.e. the laminar premixed flame, is then fundamental to characterize the flame front and its interaction with turbulence. Two generic configurations are used to study turbulent flames: unstrained flames, needed to preliminary validate the chemical description, and strained flames, used to model in a very simplified way the turbulence interaction with the flame whose main effect is the stretching of the flame front.

In this Chapter, the main features of the methane oxidation is presented and the behavior of laminar premixed flames is illustrated for different operating conditions in the physical space and in the phase space based on the progress variable c. Experimental results are presented for classical methane/air flames and completed with numerical results obtained with the software CANTERA [71] using the detailed GRI3.0 mechanism [65] composed by 53 species and 300 reactions.

2.1 Oxidation of methane

Some similarities between the most important reactions for hydrocarbon fuels have been identified [91]:

- The most important reactions in a combustion process are:

$$H + O_2 \;=>\; O + OH \tag{2.1}$$
$$CO + OH \;=>\; CO_2 + H, \tag{2.2}$$

  which are common to oxidation of all hydrocarbons and do not depend on the fuel studied.

- The initial fuel breakdown is fuel specific, but its rate is in general too fast to limit the overall rate of combustion. Moreover, the initial fuel breakdown always leads to C_1, C_2 and C_3 fragments.

- Since combustion processes can take place for different ranges of conditions, the dominant reactions could vary. For examples, the importance of a family of reactions could depend on temperature:

  - low temperature reactions ($T < 800\ K$): slow reactions characterized by a small release of heat;
  - high temperature reactions ($T > 1000\ K$): essential reactions for the description of flames releasing the most of heat;
  - intermediate temperature reactions ($750\ K < T < 950\ K$): reactions describing the auto-ignition phenomenon.

  The chemistry for high temperature is activated once auto-ignition has taken place and is generally easier than oxidation chemistry for low temperatures.

The chain reaction for hydrocarbons flames has been largely studied and characterized by different steps [166]:

- the first radicals responsible for the reaction initiation are produced by the **initiation reactions**;
- the **chain-branching reactions** multiply the radicals necessary for the combustion;
- reactants are burnt and intermediates and products are created by the **chain-carrying reactions**;
- radicals are then consumed by the **termination reactions**.

The main pathways in methane/air flame are analyzed in the following (Fig. 2.1). Compared to auto-ignition mechanism, the flame chemistry is characterized by the presence of H, O and OH radicals required for fuel consumption which is supplied through back diffusion from the reaction zone. As a consequence, no initiation reaction

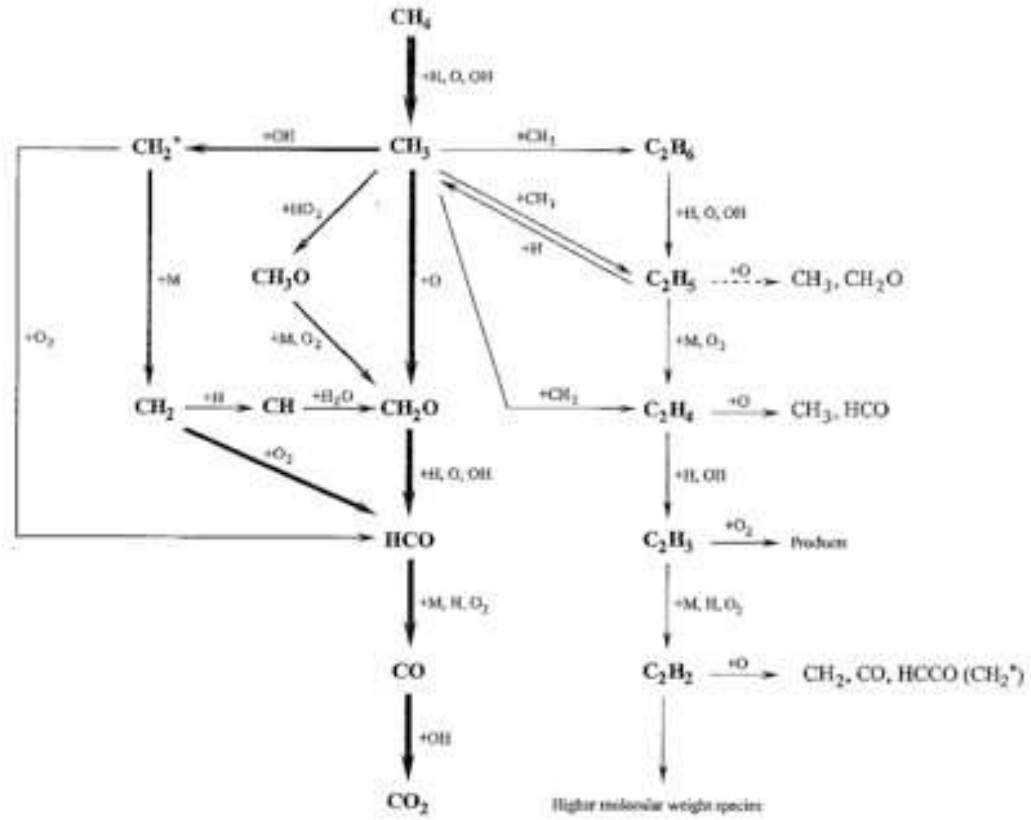

Figure 2.1 - *Reaction pathways in methane/air flames [165]. The thickness of the arrows indicates the relative importance of individual pathways.*

is necessary and the methane is directly consumed by H, O and OH species through the following chain-carrying reactions:

$$CH_4 + H \;=>\; CH_3 + H_2 \tag{2.3}$$
$$CH_4 + O \;=>\; CH_3 + OH \tag{2.4}$$
$$CH_4 + OH \;=>\; CH_3 + H_2O, \tag{2.5}$$

producing the methyl radical which reacts with O and OH:

$$CH_3 + O \;<=>\; CH_2O + H \tag{2.6}$$
$$CH_2O + OH \;<=>\; HCO + H_2O. \tag{2.7}$$

The highly active formyl radical HCO is finally consumed and CO species is formed:

$$HCO + M \;<=>\; H + CO + M \tag{2.8}$$
$$HCO + O_2 \;<=>\; CO + HO_2. \tag{2.9}$$

The CO oxidation into CO_2 is achieved by the following reactions:

$$CO + OH \Rightarrow CO_2 + H \tag{2.10}$$
$$CO + HO_2 \Rightarrow CO_2 + OH \tag{2.11}$$
$$CO + O + M \Rightarrow CO_2 + M. \tag{2.12}$$

and it does not involve the specific hydrocarbon fuel. Predicting the CO concentration is not straightforward since the CO species is produced in the reaction zone and is recombined into CO_2 in the postflame zone and Reactions (2.9)-(2.12) have to be taken into account in the mechanism.
Some of the neglected pathways of the methane oxidation are more important for rich mixtures and should be taken into account in a detailed chemical mechanism. Moreover, auto-ignition of methane requires more complex pathways and is therefore more difficult to reproduce using a simplified chemistry. Different detailed mechanisms characterizing the combustion phenomena of alkanes, alkynes and aromatics species are available [148]. For methane oxidation, the detailed **GRI3.0 mechanism** [65] has been chosen as reference. It is a compilation of 325 elementary chemical reaction and associated rate coefficient expressions and thermochemical parameters for the 53 species involved in them. The conditions for which GRI3.0 mechanism was optimized roughly correspond to initial temperature 1000 to 2500 K, pressure from 0.01 to 10 atm, and equivalence ratio from 0.1 to 5 for premixed systems choosing methane and natural gas as fuel.

Pollutant formation

Five principal pollutants are produced from fossil fuel combustion:

- **Oxides of carbon**: The most important reaction of CO oxidation into CO_2 is given by Eq. (2.10). It is usually slow compared to the fuel oxidation and it rules the formation and destruction of CO species.
- **Oxides of nitrogen** such as nitric oxide NO, nitrogen dioxide NO_2 and nitrous oxide N_2O. Nitric oxide can be formed from atmospheric N_2 through three different mechanisms [91]:
  - Thermal NO mechanism: it consists of three reactions referred as the Zel'dovich mechanism:

$$N_2 + O \Rightarrow NO + N \tag{2.13}$$
$$O_2 + N \Rightarrow NO + O \tag{2.14}$$
$$N + OH \Rightarrow NO + H. \tag{2.15}$$

    It is usually considered unimportant at temperatures below 1800 K.

  - Prompt NO mechanism: NO formation in the colder part of premixed hydrocarbon flames is due to a sequence of reactions involving N_2, CH and CH_2 species. In opposition to thermal NO, the prompt NO is created even at low temperatures ($T \approx 1000\ K$) but it is generally irrelevant compared to the concentration built by the thermal NO mechanism.
  - NO_2 mechanism [109]: the formation of NO through the N_2O route follows a sequence requiring the O atom and a three-body recombination reaction which is favored by an increasing of air concentration and pressure.

- **Oxides of sulfur** such as the sulfur dioxide SO_2 and the sulfur trioxide SO_3.
- **Soot**: it is not a uniquely defined chemical substance. It contains mostly carbon with an atomic C/H ratio of about 8 to 1. The physical and chemical coalescence of polycyclic aromatic hydrocarbons (PAH) is responsible for the inception of soot. Acetylene (C_2H_2) is the main precursor of PAH and the formation and growth of soot particles are linked to it [75].
- **Unburned hydrocarbon** such as alkanes, ketones and alcohols.

Radical species like OH, H, O have a fundamental role in the formation of oxides of carbon and nitrogen as well as acetylene and benzene species are precursors to the soot formation. One of the most important issue for combustion is the correct prediction and description of pollutants since precise detailed chemical mechanisms and accurate models are required.

2.2 Unstrained premixed flames

The planar laminar premixed flame is one of the basic academic configurations when studying combustion (Fig. 2.2). Fresh fuel and oxidizer are supplied from the left side (identified with the index f) and are separated to combustion products (located in the right zone identified with the index b) by a thin region characterized by a high temperature gradient. This region generally consists of three layers [118]:

- a chemically inert **preflame zone** where no reaction takes place and fresh gases are preheated due to thermal fluxes;
- a thin **reaction zone**, or fuel consumption layer, of thickness δ where fuel reacts with radicals (like H) forming secondary fuels like CO and H_2;
- a **postflame zone**, or oxidation layer, of thickness ϵ where the secondary fuels are converted into products such as CO_2 and H_2O.

The reaction zone is characterized by a high heat release and, consequently, a strong gradient of temperature. Intermediate species, such as CO, and radicals like OH and H are produced in this region characterized by fast reactions. In comparison, the postflame region is characterized by slower reactions recombining intermediate species into the final products of combustion like CO_2 and NO_x. Since the fuel consumption is much faster than the recombination reaction, it is expected that $\delta \ll \epsilon \ll 1$.

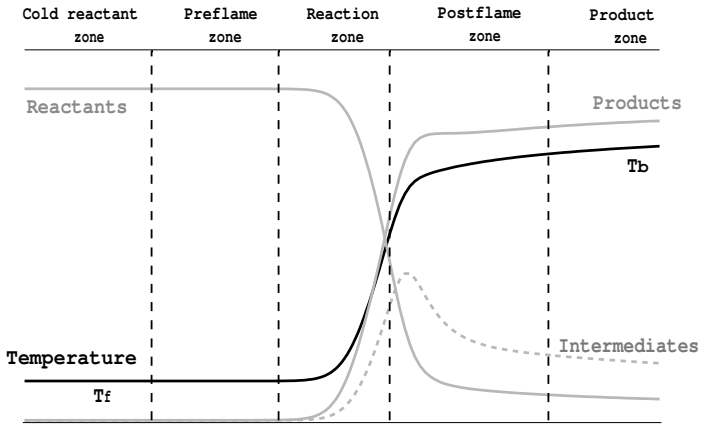

Figure 2.2 - *Sketch of a laminar premixed flame.*

Different factors contribute at the same time to combustion in a premixed flame: the temperature gradient generates a thermal flux which preheats the fresh gases in the preflame zone, the radicals needed for fuel consumption are supplied through back diffusion from the oxidation layer, and fresh gases start to burn: the flame propagates then towards fresh gases.
When the flame is steady, i.e. the reference frame of the flame is chosen, the balance equations can be simplified as follows [124]:

$$\frac{\partial \rho u}{\partial x} = 0 \quad \text{or} \quad \rho u = \text{constant} = \rho_f S_L \tag{2.16}$$

$$\frac{\partial}{\partial x}\left(\rho(u + V_K)Y_k\right) = \dot{\omega}_k \quad \text{for} \quad k = 1, N \tag{2.17}$$

$$\rho C_p u \frac{\partial T}{\partial x} = \dot{\omega}'_T + \frac{\partial}{\partial x}\left(\lambda \frac{\partial T}{\partial x}\right) - \frac{\partial T}{\partial x}\left(\rho \sum_{k=1}^{N} C_{p,k} Y_k V_k\right), \tag{2.18}$$

where S_L is the propagation speed of the wave from burnt to fresh gases and $\dot{\omega}'_T$ is the heat release due to combustion:

$$\dot{\omega}'_T = -\sum_{k=1}^{N} h_k \dot{\omega}_k = -\sum_{k=1}^{N} h_{sk} \dot{\omega}_k - \sum_{k=1}^{N} \Delta h^0_{f,k} \dot{\omega}_k. \tag{2.19}$$

Definition of the progress variable

For a one-step irreversible chemical scheme written as:

$$\nu'_F F + \nu'_O O \rightarrow Products, \tag{2.20}$$

a premixed flame is usually represented using the progress variable c defined as:

$$c = \frac{T - T_f}{T_b - T_f} \quad \text{or} \quad c = \frac{Y_F - Y_F^f}{Y_F^b - Y_F^f}, \tag{2.21}$$

which describes the progression from fresh gases ($c = 0$) to burnt gases ($c = 1$). The fuel mass fraction and temperature are Y_F^f and T_f respectively in the fresh gases and Y_F^b and T_b in the burnt gases.

The typical evolution of the progress variable c based on temperature is represented

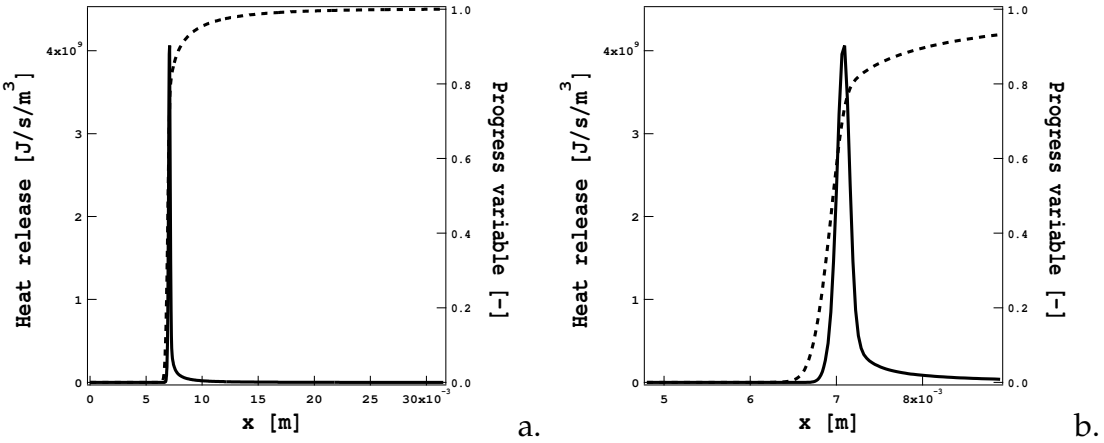

Figure 2.3 - *a) Evolution of the progress variable c (dashed line) and of heat release (solid line) in a stochiometric premixed methane/air flame at ambient temperature and atmospheric pressure. b) Same profiles zoomed in the reaction zone.*

in Fig. 2.3 for a stochiometric premixed methane/air flame at ambient temperature and atmospheric pressure. The fresh gas zone is identified by $c = 0$ and the final equilibrium state is reached at $c = 1$.

The gradient of the progress variable $|\nabla c|$ represented in Fig. 2.4 characterizes the different flame zones:

- first, c slightly increases in the preheat region;
- a high gradient of c then occurs, identifying the reaction zone;

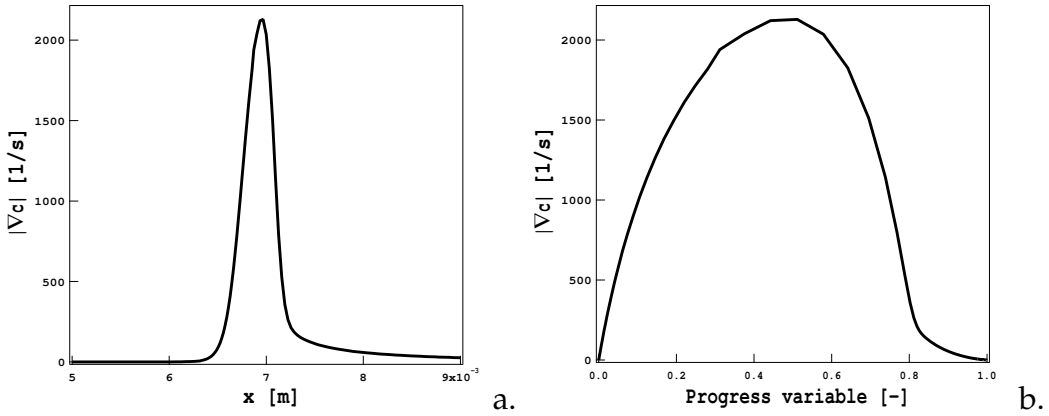

Figure 2.4 - *Gradient of the progress variable in (a.) the physical space (zoomed in the reaction zone) and (b.) the phase space.*

- finally, a small gradient of c represents the postflame region.

Under the unity Lewis number and adiabaticity assumptions, the two definitions of Eq. (2.21) are equivalent and a single **balance equation for the progress variable** is sufficient to describe a steady flame:

$$\boxed{\frac{\partial \rho u c}{\partial x} = \frac{\partial}{\partial x}\left(\rho D \frac{\partial c}{\partial x}\right) + \dot{\omega}_c,} \tag{2.22}$$

where $\dot{\omega}_c$ is the reaction rate in Eq. (2.20). When working in the phase space based on the reduced temperature or the reduced mass fraction, the flame structure is easily analyzed (Fig. 2.5). An iso-c surface (for example for the value of c corresponding to the maximum of heat released) may be used to localize the flame front.

Flame speed

Equation (2.22) may be rewritten in a propagative form [35] (here proposed in a three-dimensional formulation):

$$\mathbf{u} \cdot \nabla c = \underbrace{\frac{1}{\rho}\left[\frac{\nabla \cdot (\rho D \nabla c) + \dot{\omega}_c}{|\nabla c|}\right]}_{\text{displacement speed } S_d} |\nabla c| = S_d \, |\nabla c| \,, \tag{2.23}$$

where S_d is the displacement speed of the iso-c surface measured relatively to the flow. Defining the unity normal vector $\mathbf{n}$ to the iso-c surface pointing towards the fresh gases:

$$\mathbf{n} = -\frac{\nabla c}{|\nabla c|}, \tag{2.24}$$

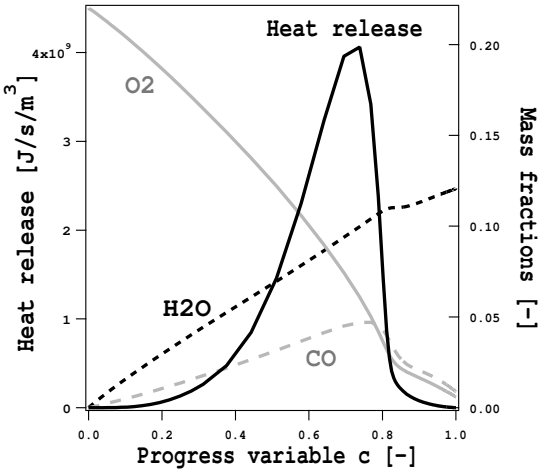

Figure 2.5 - *Premixed laminar flame represented in the c-phase space: O_2 (grey solid line), H_2O (black dashed line), CO (grey dashed line) and heat release (black solid line).*

the displacement speed S_d may be decomposed into three contributions:

$$S_d = S_n + S_t + S_r \tag{2.25}$$

$$= \frac{1}{\rho\,|\nabla c|}\mathbf{nn} : \nabla\left(\rho D \nabla c\right) - D\nabla\cdot\mathbf{n} + \frac{1}{\rho\,|\nabla c|}\dot{\omega} \tag{2.26}$$

$$= \frac{1}{\rho\,|\nabla c|}\frac{\partial}{\partial n}\left(\rho D \nabla c\right) - D\nabla\cdot\mathbf{n} + \frac{1}{\rho\,|\nabla c|}\dot{\omega}, \tag{2.27}$$

where S_n is the normal molecular diffusion component, S_t is the tangential diffusion component depending on the local mean curvature $\nabla\cdot\mathbf{n}$ of the iso-c surface, and S_r is the reaction rate component.

In order to compare the displacement speed S_d to the propagation speed S_L, the density expansion has to be taken into account and the density-weighted displacement speed $S_d^\star$ is generally preferred [81]:

$$S_d^\star = \frac{\rho S_d}{\rho_f}. \tag{2.28}$$

To summarize, the different definitions of flame speed are:

- **Propagation speed $\mathbf{S_L}$**: the propagation speed of the flame wave for laminar premixed flame defined in Eq. (2.16).
- **Absolute speed $\mathbf{S_a}$**: the flame front speed relative to a fixed reference frame. When studying a steady premixed laminar flame, the reference frame coincides with the flame front and $S_a = 0$.

- **Displacement speed S_d**: the flame front speed relative to the flow defined in Eq. (2.25): $S_a = u + S_d$. When studying a steady premixed unstretched laminar flame, the displacement speed is equal to the flow velocity $S_d = u$. To account for the flow dilatation, the speed $S_d^\star$ is introduced (Eq. (2.28)).

- **Consumption speed S_C**: the speed at which reactants are consumed. For lean flames, it is equal to the integral of the fuel consumption rate $\dot{\omega}_F$ in the direction normal to the flame:

$$S_C = -\frac{1}{\rho_f Y_F^f} \int_{-\infty}^{\infty} \dot{\omega}_F d\mathbf{n}. \tag{2.29}$$

The consumption speed has a global definition whereas the other definitions have a local nature since they are calculated at the flame front. For this reason, the use of consumption speed is usually preferred [43]. For an unstretched laminar premixed flame ($\rho u = \rho_f S_L = constant$) the relation between the different flame speed is:

$$S_a = 0 \quad \text{and} \quad S_L = S_C = S_d^\star = \frac{\rho}{\rho_1} S_d. \tag{2.30}$$

Flame thickness

Before computing a flame, a correct estimation of the flame thickness is required to discretize the flame front with a sufficient number of points. Different definitions exist for the hot gas layer based on *a priori* or *a posteriori* estimations:

- **Thermal thickness** δ_L [124] is the thickness of the hot gas layer estimated from the gradient of temperature:

$$\delta_L = \frac{T_b - T_f}{\max\left(\left|\frac{\partial T}{\partial x}\right|\right)}. \tag{2.31}$$

  To estimate this quantity, the temperature profile is required from computation or experiment.

- **Diffusive thickness** δ [124] is an *a priori* estimation based on the thermal diffusion of fresh gases $\delta = D_{th}^f / S_L$. Its computation is easy but it is generally less accurate than δ_L and usually too small.

- **Blint thickness** δ_L^B [17] is an improved a priori estimation using equilibrium thermochemistry: $\delta_L^B = 2\delta(T_b/T_f)^{.0.7}$ It is generally close to the thermal thickness δ_L.

A definition of thickness based on the reaction layer is also necessary:

- **Reaction zone thickness** $\delta_\mathbf{r}$ [91] is the thickness of the reaction zone, i.e. the region where heat is released. Generally, it is smaller than the thermal thickness δ_L by one order of magnitude.

Whenever the temperature profile is available, the thermal thickness δ_L should be used. If no initial profile is available, the Blint definition $delta_L^B$ offers a good estimate of the thermal flame thickness.

Equivalence ratio and mixture fraction

In a premixed flame, fuel and oxidizer are mixed at the molecular level. The obtained mixture is characterized by an equivalence ratio ϕ:

$$\phi = s\frac{Y_F}{Y_O} = \left(\frac{Y_F}{Y_O}\right) / \left(\frac{Y_F}{Y_O}\right)_{st}, \tag{2.32}$$

where s is the mass stoichiometric ratio:

$$s = \left(\frac{Y_O}{Y_F}\right)_{st} = \frac{\nu'_O W_O}{\nu'_F W_F}. \tag{2.33}$$

Ideally, for a mixture in stoichiometric proportion ($\phi = 1.0$), both fuel and oxidizer are completely converted into products. The mixture is considered lean when the fuel is the limiting reactant ($\phi < 1$) and rich when the oxidizer is the limiting reactant ($\phi > 1.0$).

The mixture fraction z defined by Bilger on the atomic mass fraction [16]:

$$z = \frac{2Z_C + \frac{1}{2}Z_H + \left(Z_O^O - Z_O\right)}{2Z_C^F + \frac{1}{2}Z_H^F + Z_O^O} \tag{2.34}$$

may be used to identify the local fuel/oxidizer ratio since it gives information on the local fuel/oxidizer ratio going from pure fuel (z=1) to pure oxidizer (z=0). The superscripts F and O indicate pure fuel and air respectively.
The atomic mass fraction Z_i of atom i is defined as:

$$Z_i = \sum_{k=1}^{N} \frac{n_k^i Y_k}{W_k} \tag{2.35}$$

where n_k^i is the number of atom i in species k.
In the unity Lewis hypothesis, the mixture fraction z is conserved in a premixed flame

and it could be used to identify the flame equivalence ratio using the following definition:

$$z = \frac{sY_F - Y_O + Y_O^0}{sY_F^0 + Y_O^0} = \frac{1}{\phi + 1}\left(\phi\frac{Y_F}{Y_F^0} - \frac{Y_O}{Y_O^0} + 1\right) \tag{2.36}$$

where Y_F^0 and Y_O^0 are the fuel and oxidizer mass fractions in pure fuel and pure oxidizer streams respectively. It is a conserved scalar since it changes because of diffusion and convection but it does not see the chemical reaction:

$$\boxed{\frac{\partial \rho z}{\partial t} + \frac{\partial}{\partial x_i}(\rho u_i z) = \frac{\partial}{\partial x_i}\left(\rho D \frac{\partial z}{\partial x_i}\right),} \tag{2.37}$$

where D is the species diffusion coefficient assumed equal for all species.

Impact of initial composition, temperature and pressure

The laminar flame speed S_L depends on the chemical parameters determining the fuel consumption rate $\dot{\omega}_F$, and on the transport properties of the mixture. The flame speed varies with the initial composition (i.e. the equivalence ratio), the initial temperature T_f and the pressure P.

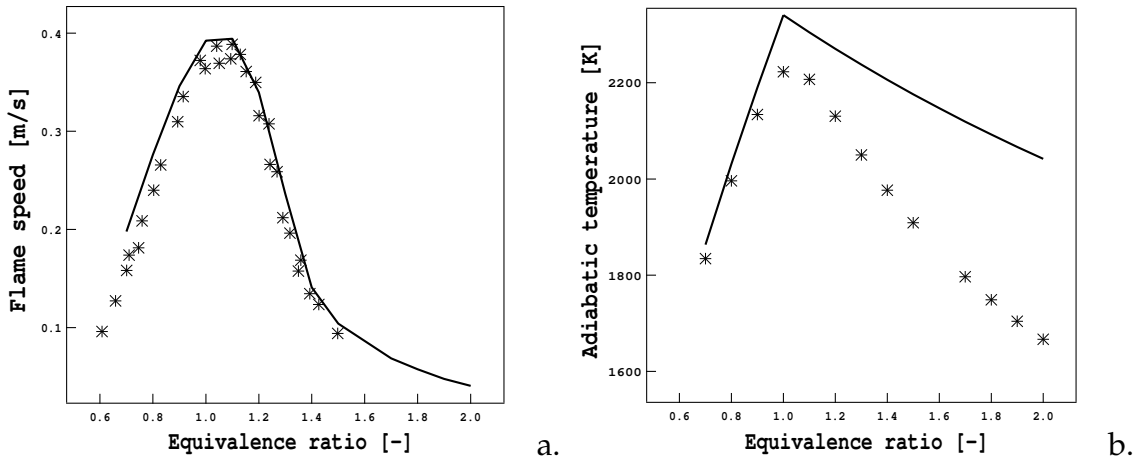

Figure 2.6 - *a) Flame speed as a function of the equivalence ratio: experimental data by Vagelopoulos [159] (symbols) and numerical results (line). b) Adiabatic temperature as a function of the equivalence ratio: comparison between the 53 species mixture of the detailed GRI3.0 mechanism (symbols) and 5 species mixture (line).*

A typical variation of flame speed with equivalence ratio is shown in Fig. 2.6a where experimental data for methane/air flames provided by Vagelopoulos [159] at ambient

temperature (T_f = 300 K) and atmospheric pressure are compared to numerical results obtained with the detailed GRI3.0 mechanism. The highest values of flame speed S_L are found for near-stoichiometric mixtures ($\phi \approx 1$) for which $\dot{\omega}_F$ reaches its maximum value. For the leanest or richest flames, the limiting reactant is almost insufficient to activate the reactions and the flame speed approaches zero.

The burnt gas temperature and composition are controlled by thermochemistry, i.e. the species formation enthalpies $\Delta h^0_{f,k}$ and the species heat capacities $C_{p,k}$. The adiabatic flame temperature is shown in Fig. 2.6b as a function of the equivalence ratio. To show the effect of composition, two calculations have been made to obtain the thermochemistry equilibrium of a mixture composed of 5 species (CH_4, CO_2, H_2O, O_2 and N_2) and of 53 species (those used in the GRI3.0 mechanism). It is important to notice that results for the adiabatic temperature could be affected when neglecting some important species such as CO or H_2, especially for rich regimes. As for the flame speed, the maximum value of T_b is found for a near-stoichiometric mixture.

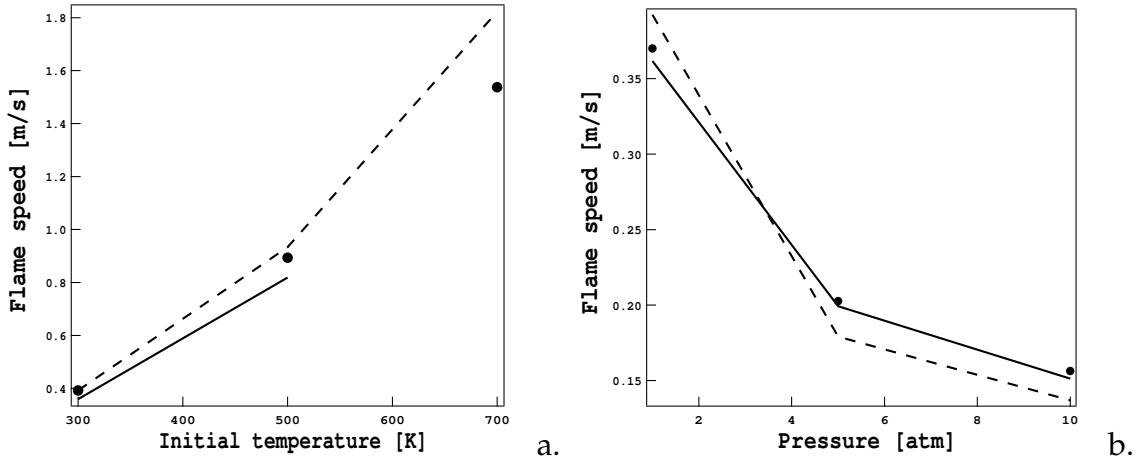

Figure 2.7 - *Flame speed versus pressure at T = 300 K (a.) and versus temperature at P = 1 atm (b.). Comparison between experimental data (continous line) [73], numerical results (dashed line) and the experimental correlations (symbols) [73].*

To describe the variations of flame speed with initial temperature and pressure, experimental polynomial functions are generally used:

$$S_L(P, T_1) = S_L(P^0, T_f^0)\left(\frac{P}{P^0}\right)^{\alpha_P}\left(\frac{T_f}{T_f^0}\right)^{\alpha_T}, \tag{2.38}$$

where T_f^0 and P^0 are the reference initial temperature and pressure. The dependency coefficients for pressure α_P and temperature α_T are deduced from experiments or from numerical results. The numerical flame speed values are compared to experimental

results of Gu et al. [73] for a stoichiometric methane/air premixed flame in Fig. 2.7. The experimental correlations proposed by Gu et al. [73] are also added to Fig. 2.7:

$$S_L = 0.360 * \left(\frac{P}{1\ bar}\right)^{-0.374} \left(\frac{T_f}{300\ K}\right)^{1.612} \tag{2.39}$$

Since $\alpha_P = -0.374$ and $\alpha_T = 1.612$ the flame speed decreases with pressure and rapidly increases with temperature.

Impact of simplified transport properties

Transport properties are simplified in most turbulent combustion models. First of all, Prandtl and Schmidt numbers are assumed constant along the flame. As shown in Fig. 2.8 using complex thermodynamic and transport properties, the Prandtl and Schmidt numbers only slightly vary in the reaction zone and small discrepancies are found between fresh and burnt gases. Aa a consequence, results for a premixed flame will be little affected by the assumption of constant Prandtl and Schmidt numbers.

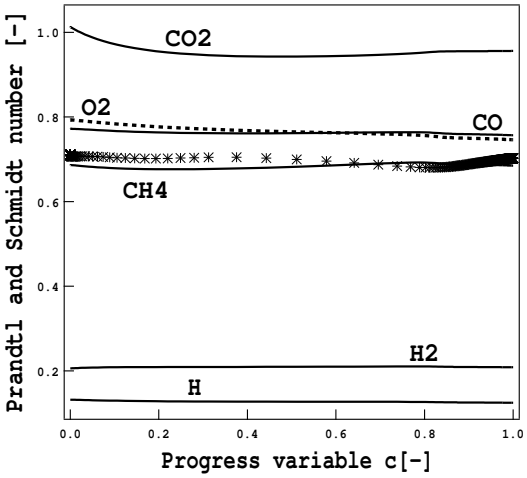

Figure 2.8 - *Prandtl number (symbols) and species Schmidt numbers (lines) in a premixed flame.*

On the contrary the unity Lewis number hypothesis, i.e. species Schmidt numbers equal to the Prandtl number, assumed in most combustion models has a larger impact. First of all, it can be noticed in Fig. 2.8 that the Schmidt numbers greatly vary between species, i.e. between hydrocarbons as CH_4 and the lightest species H and H_2. Secondly when unity Lewis numbers are assumed, the flame structure is modified as shown in Fig. 2.9a. which compares the profiles of species mass fractions in the phase space obtained with detailed and with simplified transport properties. Again, the hydrocarbon

species are less affected by the simplified transport than the lightest species H_2 and H. The impact of simple transport properties is shown on the laminar flame speed S_L in Fig. 2.9b: unity Lewis numbers lead to an underestimated flame speed with a maximum error of about 25% for stoichiometry.

The unity Lewis number hypothesis greatly impact the performances of detailed mechanisms in terms of flame speed, whereas reduced mechanisms and tabulation methods are generally fitted or corrected to predict the expected flame speed values.

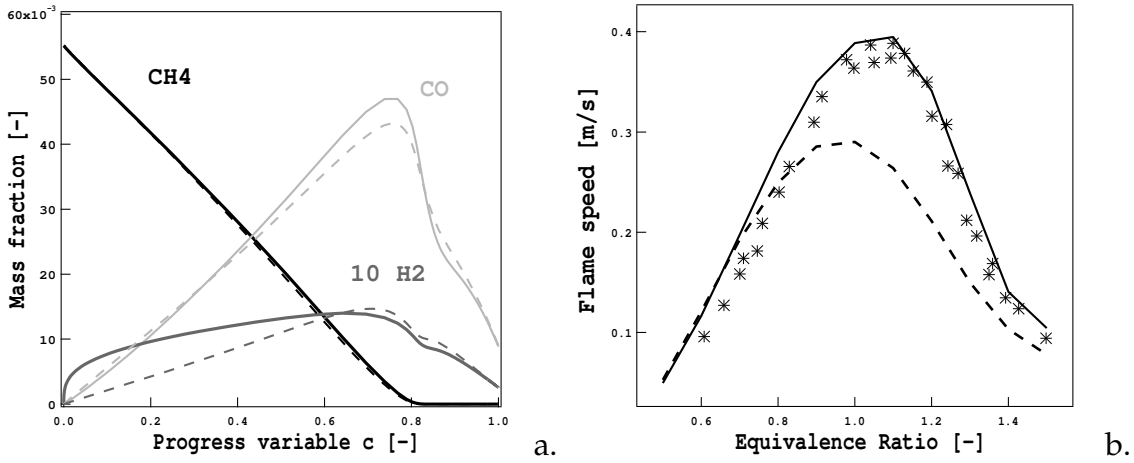

Figure 2.9 - *Effect of the unity Lewis number assumption on a) the flame structure and b) the flame speed. Comparison between GRI3.0 mechanism with complex transport (solid line) and with simple transport (dashed line). Experimental data by Vagelopoulos [159] are added to the flame speed results (symbols).*

2.3 Strained premixed flames

In the strained premixed flame sketched in Fig. 2.10 a fresh premixed methane/air mixture is injected on the left side and combustion products are injected on the right side. The injection velocities could vary to modify the global strain rate $a = (|u^f|+|u^b|)/d$, where d is the distance between the two jets.
The flame front velocity $\mathbf{w}$ is given by the sum of the unburned gas velocity $\mathbf{u}$ and the displacement speed S_d defined in Eq. (2.25):

$$\mathbf{w} = \mathbf{u} + S_d\mathbf{n}. \tag{2.40}$$

The flame is characterized by the presence of a stagnation plane where the flow velocity is zero. Stagnation point flames are stationary, which means that they do not propagate

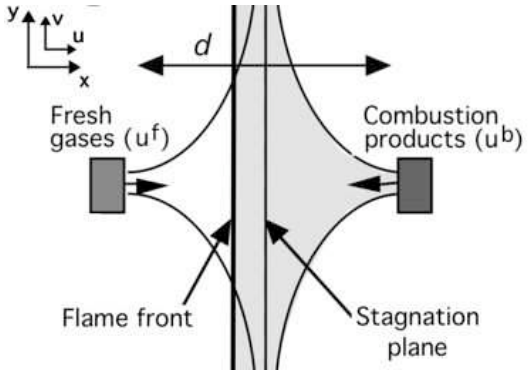

Figure 2.10 - *Sketch of a premixed strained flame.*

along its normal direction **n**: $\mathbf{w} \cdot \mathbf{n} = 0$, even if a velocity exists in the plane tangent to the flame. As the flow velocity is not uniform, the flame displacement speed is difficult to measure and the global consumption speed defined in Eq. (2.29) is usually preferred to quantify the flame speed [43].

Definition of stretch

The total flame stretch k is defined in [173] as the time derivative of the fractional rate of a flame surface element A:

$$k = \frac{1}{A}\frac{dA}{dt}. \tag{2.41}$$

It may be decomposed into a strain rate term (related to the non-uniformity of the flow) and a term which accounts for effects of the flame front curvature [124]:

$$\boxed{k = \underbrace{\left(\delta_{ij} - n_i n_j\right)\frac{\partial u_i}{\partial x_j}}_{\textit{strain rate}} + \underbrace{S_d \frac{\partial n_i}{\partial x_i}}_{\textit{curvature}} = a + S_d \nabla \cdot \mathbf{n},} \tag{2.42}$$

where S_d is the displacement speed, a is the strain rate and **n** is the normal vector defined in Eq. (2.24). For a stagnation point flame $\mathbf{u} \cdot \mathbf{n} = -S_d$ and the stretch is composed only by the tangential strain rate:

$$k = a = \nabla_t \cdot \mathbf{u}_t = \frac{\partial v}{\partial y}, \tag{2.43}$$

where $\nabla_t \cdot \mathbf{u}_t = -\mathbf{nn} : \nabla \mathbf{u}_t + \nabla_t \cdot \mathbf{u}_t$.

Impact of strain rate

The different flame speeds (S_L, S_d and S_C) assume different values for a stretched flame and their evaluation is not straightforward neither experimentally nor numerically. Under the conditions of validity of the asymptotic theory, i.e. small strain rate and curve terms, the flame structure is controlled only by the stretch k [32, 29, 44]. Moreover, the displacement speed on the fresh gas side and the consumption speed have a linear response to stretch:

$$\frac{S_d}{S_L} = 1 - M_a^d \frac{k\delta}{S_L} \quad \text{and} \quad \frac{S_C}{S_L} = 1 - M_a^c \frac{k\delta}{S_L}, \tag{2.44}$$

where $k\delta/S_L^0$ is a reduced Karlovitz number based on the diffusive thickness δ. The Markstein numbers for the displacement and the consumption speeds, respectively M_a^d and M_a^c, are proportional to the fuel Lewis number ($Le_F - 1$). The stability of the flame front depends on the sign of the displacement Markstein number: natural intrinsic instabilities of the flame front are found for negative Markstein numbers [173, 26].

The typical asymptotic behavior of the consumption speed for stagnation flames are reproduced in Fig. 2.11 as a function of the stretch k for different values of the fuel Lewis number Le_F:

- For $Le_F = 1$, species and temperature gradients increase in the same proportion when increasing the stretch. As a consequence, the flame is thinner but the consumption speed is not affected, at least for small strecth values.
- For $Le_F < 1$, the consumption Markstein number is negative and the consumption speed linearly increases when the stretch increases, at least for low values.
- For $Le_F > 1$, the consumption speed decreases when stretch increases. In general for an adiabatic flame, quenching can be observed only for very large values of the stretch. When heat loss is taken into account, sudden extinctions could occur for lower stretch levels.

For high stretch values above the crucial stretch, the asymptotic theory is not valid anymore.
The above analysis was performed assuming one-step irreversible chemistry. To illustrate the effect of stretch in complex chemistry flames, the response of a stoichiometric methane/air strained flame is numerically studied using the detailed GRI3.0 mechanism, for which the Lewis number for reactants are $Le_{CH_4} \approx 0.98$ and $Le_{O2} \approx 1.06$. As already said, for this configuration the only contribution to stretch k is the strain rate a. Contrary to the asymptotic analysis, the consumption speed decreases when

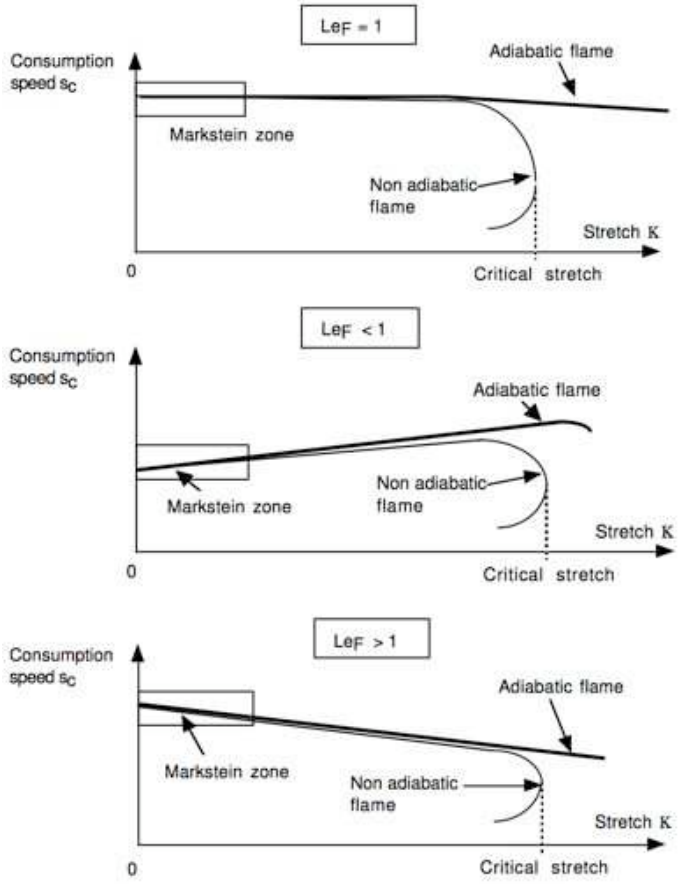

Figure 2.11 - *Asymptotic response of consumption speed to strain rate for different Lewis numbers [124].*

strain rate increases as shown in Fig. 2.12a, showing that in complex chemistry the fuel Lewis number is not sufficient to predict the response to strain rate. In order to validate the numerical results on the consumption speed, experimental results for the normalized displacement speed obtained by Gu et al. [73] for the same flame are proposed in Fig. 2.12b. Even if the consumption speed S_C does not coincide with the displacement speed S_d on a laminar strained flame, the response of both S_C and S_d to strain rate is qualitatively the same and in contrast with the asymptotic analysis.

The flame structure is also generally modified by strain rate. Profiles of species mass fractions for an unstrained flame are compared to mass fraction profiles for a strained flame ($a = 1000\ s^{-1}$) in Fig. 2.13 as a function of the progress variable c. The largest discrepancies are found for intermediate species (CO and OH) in the reaction zone for which maximum values are reduced by strain. This may have an important impact on flame emissions.

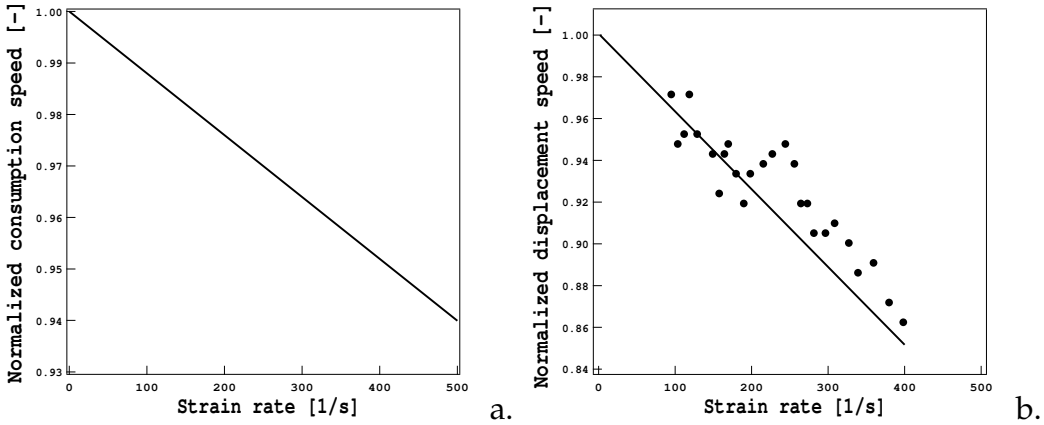

Figure 2.12 - *a) Numerical results of the normalized consumption speed as function of strain rate for a premixed flame. b) Experimental results by Gu et al. [73] of the displacement speed as function of strain rate for a premixed flame.*

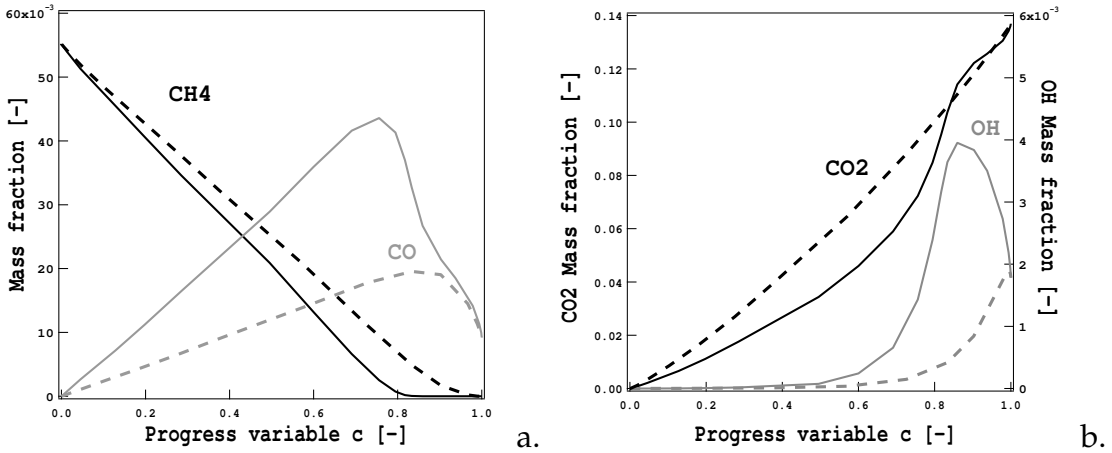

Figure 2.13 - *Effect of the strain on the flame structure: an unstrained premixed flame (solid line) is compared to a strained premixed flame with* $a = 1000\,s^{-1}$ *(dashed line).*

Chapter 3

Chemistry for premixed methane/air flames

The use of simplified chemical descriptions guarantees a reduction of the computational cost but the impact on result accuracy has to be validated. A preliminary estimation of the performances of reduced chemical descriptions could be performed on laminar unstrained and strained premixed flames, which are the fundamental bricks in the modeling of turbulent premixed flames in the flamelet combustion regime.

In this chapter, different reduced mechanisms for premixed methane/air flames are presented and the technique to implement and use them in CFD tools such as CANTERA, AVBP and S3D is explained (Section 3.1). A comparison with results of a detailed scheme is proposed for laminar unstrained and strained flames in terms of flame speed, equilibrium state, flame thickness and flame structure (Section 3.2). The FPI_TTC tabulation method is then discussed in Section 3.3 for laminar unstrained premixed flames. In order to use the presented reduced schemes for turbulent combustion, an extension of the TFLES method to multi-species reversible chemistry is proposed for partially premixed flames in Section 3.4.

3.1 Reduced mechanisms for laminar premixed flame

In this section, different reduced mechanisms from the literature for methane/air combustion are presented from the simplest to the most complex one:

- **2S_CH4_BFER**: two-step mechanism by Franzelli et al. [62]: main steps for its derivation are summarized in Section 3.1.2.

- **JONES**: four-step mechanism by Jones and Lindstedt [82];
- **PETERS**: analytical scheme based on Peters work [116];
- **SESHADRI**: analytical scheme by Seshadri and Peters [39];
- **LU**: the most complex mechanism based on the work of Lu and Law [98].

The reduced mechanisms are tested on laminar unstrained and strained premixed flames for the two operating points corresponding to the DNS and LES calculations presented in the third Part of this work (Table 3.1):

1. **BUNSEN** operating point: the DNS of a turbulent premixed flame is performed at initial temperature (T_f = 800 K), equivalence ratio ϕ = 0.7 and atmospheric pressure (Chapter 4).
2. **PRECCINSTA** operating point: the LES of a non perfectly premixed swirled turbulent flame at ambient temperature (T_f = 320 K), global equivalence ratio ϕ = 0.83 and atmospheric pressure is studied in Chapters 5 and 6.

Results are compared to the detailed GRI3.0 mechanism [65] in order to evaluate their performances on unstrained and strained flames.

Table 3.1 - *Operation points for DNS and LES of Chapters 4, 5 and 6.*

	Initial temperature T_f	Pressure	Equivalence ratio ϕ
BUNSEN	800 K	1 atm	0.7
PRECCINSTA	320 K	1 atm	0.83

3.1.1 Simplified transport properties

All calculations presented in this section have been performed using CANTERA [71]. Since simplified transport properties are used in most combustion models, such properties have been implemented in CANTERA to test the impact of these simplifications on the performances of reduced mechanisms. When simplified transport properties are used, Prandtl and Schmidt numbers are assumed constant but the Lewis numbers are not necessarily equal to unity. Several formulations for the molecular viscosity μ have been implemented in CANTERA:

- μ is independent from temperature and constantly equal to μ_0,

- μ follows a Sutherland law:

$$\mu = \mu_0 \frac{T^{3/2}}{T + c_2} \frac{T_0 + c_2}{T_0^{3/2}}, \tag{3.1}$$

  where T_0 is the temperature of reference, μ_0 is the reference viscosity at temperature T_0 and c_2 is the second Sutherland constant.

- μ follows a power law in temperature:

$$\mu = \mu_0 \left(\frac{T}{T_0} \right)^{\alpha}, \tag{3.2}$$

  where α is the power law constant.

In the following, the dynamic viscosity is described by a power law for all reduced mechanisms, whereas complex transport properties are used for the reference detailed GRI3.0 mechanism. Parameters for the power law have been fitted on results for a stoichiometric methane/air mixture using the detailed GRI3.0 mechanism as well as detailed transport properties at initial temperature $T_0 = 300\ K$ and atmospheric pressure [124]. The **dynamic viscosity** of reference is $\mu_0 = 1.8405 \times 10^{-5}\ kg/m/s$ and $\alpha = 0.6759$ enables to fit the dependence on temperature over the whole range of considered temperature (Fig 3.1). The **Prandtl number** $Pr_0 = 0.7$ is also assumed

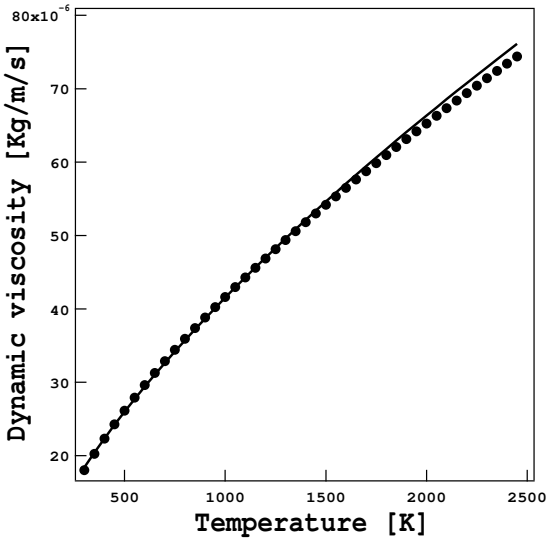

Figure 3.1 - *Dependance of the dynamic viscosity on temperature. Results obtained with detailed transport properties (symbols) are fitted using a power law (continous line).*

constant and equal to the Prandtl number in the burnt gases of a stoichiometric mixture

at initial temperature $T_0 = 300\ K$. Finally, the **Schmidt numbers** are assumed constant but not necessarily equal for each species. Their values correspond to the species Schmidt numbers in burnt gases. It has been already shown that these simplifications do not greatly affect results for laminar premixed flames (Section 2.2).

3.1.2 The two-step mechanisms: 2S_CH4_BFER and 2S_CH4_BFER*

Several approaches have been proposed to build two-step schemes. Li et al. [94] and Sanchez et al. [135] use the so-called slow CO oxidation limit of premixed combustion [30] which is valid for lean and stoichiometric mixtures to derive a CO oxidation reaction from detailed chemistry. Fuel oxidation in H_2O and CO_2 is described by two global reactions which take place in two different layers of the flame. First, fuel is attacked by radicals and totally oxidized in a thin layer, producing both CO and H_2O. Second, downstream from this thin layer, no fuel is left and radicals maintain a steady state, allowing a slow oxidation of CO into CO_2 to take place in this second layer which is thicker than the first one (Fig. 3.2). This approach provides an accurate description of the chemical flame structure for lean mixtures. However in aeronautical or piston engines, large values of equivalence ratio can be found locally and the slow CO oxidation limit is too restrictive to be used in the context of LES in such configurations.

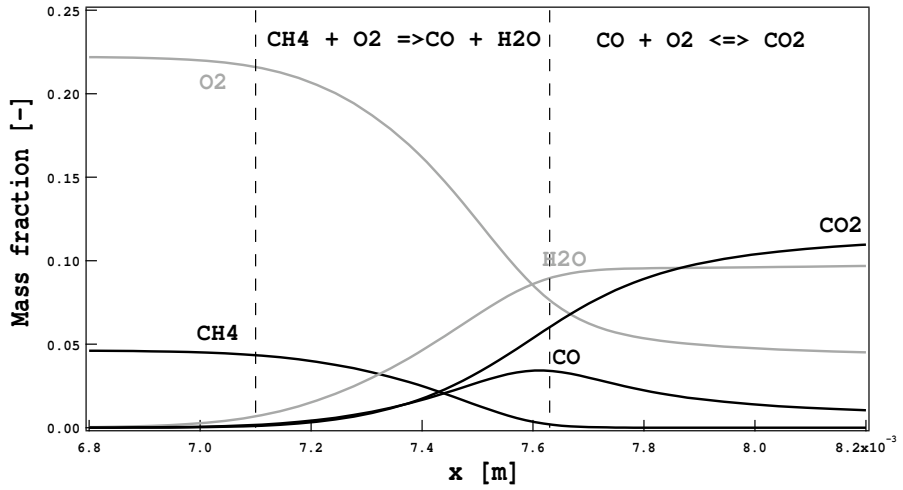

Figure 3.2 - *Sketch of the reaction and recombination zones for a premixed flame at* $\phi = 0.83$, $T_f = 320\ K$ *and* $P = 1\ atm$.

Westbrook et al. [171] build a classical two-step mechanism by choosing the appropriate reaction parameters to fit flame speed measurements. This method has two disadvantages. First, it has more difficulties to reproduce the flame structure for lean mixtures than methods based on the CO oxidation limit [94, 135]. Second, it requires negative

and/or small reaction exponents to correctly reproduce laminar flame speeds for rich mixtures. These exponents may lead to a very unstable numerical behavior and should be avoided.

The methodology proposed by Franzelli et al. [63] to build a reduced mechanism on a wide range of equivalence ratio ϕ, pressure P and initial temperature T_f is based on parameter best fitting and may be viewed as an optimisation technique. It has been applied to methane/air flames and is briefly detailed hereafter. The 2S_CH4_BFER (or BFER) mechanism correctly predicts the flame speed and the equilibrium state of a premixed laminar methane/air flame for a wide range of equivalence ratio ($\phi \in [0.6; 1.6]$), pressure ($P \in [1; 10]$ *atm*) and fresh gas temperature ($T_f \in [300; 800]$ *K*). To be consistent with the TFLES model for turbulent combustion [124] unity Lewis numbers are assumed for all species.

Equilibrium state

As discussed in Section 2.2 , the burnt gas state is controlled by thermochemistry, i.e. the species formation enthalpies and the heat capacities. The quality of a mechanism to correctly reproduce the equilibrium temperature T_b is strictly linked to the species composing the mixture. As shown in Fig. 3.3 when describing methane/air combustion, the adiabatic temperature is greatly overestimated for near-stoichiometric and rich mixtures if only five species (CH_4, O_2, CO_2, H_2O et N_2) are taken into account. When including CO, i.e. taking into account six species, the burnt gas temperature is correctly reproduced up to $\phi = 1.4$. Consequently, the 2S_CH4_BFER mechanism accounts for six species (CH_4, O_2, CO_2, CO, H_2O et N_2) and two reactions:

$$CH_4 + 1.5\ O_2 \quad => \quad CO + 2\ H_2O \tag{3.3}$$

$$CO + 0.5\ O_2 \quad <=> \quad CO_2. \tag{3.4}$$

The first irreversible reaction describes the oxidation of CH_4 into CO and H_2O, while the second reversible reaction rules the recombination between CO and CO_2.

Pressure and initial temperature dependence

The analysis of detailed methane and methanol schemes has clarified the flame speed dependence on temperature and pressure variations [172]. When increasing the fresh gas temperature, the fuel consumption and the heat release are accelerated by an increase in the elementary reaction rates which generally depends on temperature. Moreover, the maximum radical concentrations which are responsible for the fuel consumption and flame propagation become larger. The pressure dependence is linked to

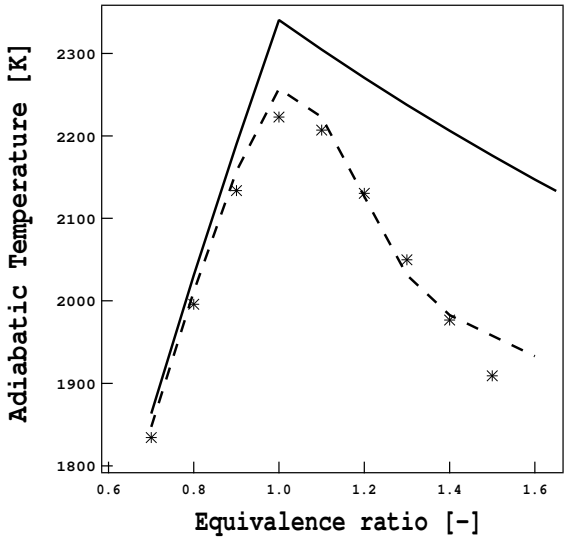

Figure 3.3 - *Adiabatic temperature as a function of the equivalence ratio for a mixture initially at temperature T_f = 320 K: comparison between 5 (solid line), 6 (dashed line) and 53 (symbols) species.*

the pressure-dependent radical recombination reactions that, by removing free radicals, inhibit the flame.

For a one-step scheme and lean combustion, a relation exists between the **pressure exponent** α_P (defined in Eq. (2.38)) and the reaction orders [124]:

$$\alpha_P = \frac{n_F + n_O - 2}{2}\,, \tag{3.5}$$

where n_F and n_O are respectively the reaction order for fuel and oxygen. This relation has been derived for one-step scheme and the flame speed dependency does not necessarily follow a power law in pressure when using a detailed mechanism. The numerical estimations of the pressure exponent for different initial values of temperature and pressure obtained with the GRI3.0 mechanism are presented in Table 3.2. The flame speed does not obey a simple power-law expression over the whole pressure range [172]. Discrepancies are expected when fixing a constant value for α_P. However, in the 2S_CH4_BFER scheme the reaction orders $n_{CH_4} = 0.5$ and $n_{O_2,1} = 0.65$ have been chosen to obtain $\alpha_P \approx -0.425$ which minimizes the errors for the flame speed on a wide range of initial temperatures and pressures.

It is more difficult to anticipate a relation between the **temperature exponent** α_T and the reaction parameters, and theoretical evaluations of α_T for single-step schemes are usually inaccurate [124]. Generally, the flame speed dependence on temperature is governed by the totality of the reaction parameters and can not be estimated *a priori*. Fixing the temperature coefficient $\beta_2 = 0.7$ of the recombination reaction (Eq. (3.4)), a correct description of the temperature dependence of the flame speed has been guaranteed.

Table 3.2 - *Numerical estimation of the pressure exponent α_P for different temperatures and pressures with $P_0 = 1$ atm and $T_0 = 300$ K. Extreme values are indicated in bold.*

Temperature	300 *K*		500 *K*		700 *K*	
Pressure	3 *atm*	10 *atm*	3 *atm*	10 *atm*	3 *atm*	12 *atm*
$\phi = 0.8$	−0.445	−0.488	−0.411	−0.453	−0.355	−0.410
$\phi = 1.0$	−0.421	−0.457	−0.358	−0.402	−0.295	−0.362
$\phi = 1.2$	−0.495	**−0.527**	−0.393	−0.451	**−0.294**	−0.373
$\phi = 1.5$	−0.320	−0.256	−0.362	−0.308	−0.390	−0.323

Flame speed

Once the reaction orders and the temperature exponents have been chosen to correctly reproduce the pressure and the temperature dependences, the pre-exponential factor and the activation energy could be fitted to predict the flame speed for the reference temperature T_0 and pressure P_0. The flame speed for a given temperature T and pressure P is automatically described since α_P and α_T are correctly reproduced.

Reduced one- or two-step schemes guarantee proper flame predictions only for lean combustion and greatly overestimate the laminar flame speed in the rich regime [130]. To overcome this problem, the Pre-Exponential Adjustement (PEA) method, where the rate constants are allowed to vary with equivalence ratio, has been proposed [24, 92, 56]. The reaction rates of Eqs. (3.3) and (3.4) are written in the classical Arrhenius form:

$$k_{f,1} = A_1 \, f_1(\phi) \, \exp^{(-E_{a,1}/RT)} \, [CH_4]^{n_{CH_4}} \, [O_2]^{n_{O_2,1}} \, , \tag{3.6}$$

$$k_{f,2} = A_2 \, f_2(\phi) \, T^{0.7} \, \exp^{(-E_{a,2}/RT)} \, [CO]^{n_{CO}} \, [O_2]^{n_{O_2,2}} \, , \tag{3.7}$$

where A_j is the pre-exponential factor of reaction j, $E_{a,j}$ is the activation energy and $n_{k,j}$ is the reaction exponent for species k in reaction j. Reaction parameters fitted to match the flame speed in the lean regime at the reference temperature $T_0 = 300$ *K* and pressure $P_0 = 1$ *atm*. They are summarized in Table 3.3.

Both reaction rates are then multiplied by a correction function $f_j(\phi)$ of the equivalence

Table 3.3 - *Activation energy E_a, pre-exponential factor A, and reaction exponents n_k for the 2S_CH4_BFER mechanism. Units are: mol, s, cm^3 and cal/mol.*

	CH_4 oxidation		CO-CO_2 equilibrium	
Activation energy	3.55×10^4		1.2×10^4	
Pre-exponential factor	4.9×10^9		2×10^8	
Reaction exponents (-)	n_{CH_4}	0.50	n_{CO}	1.00
	$n_{O_2,1}$	0.65	$n_{O_2,2}$	0.50

ratio:

$$f_1(\phi) = \frac{2}{\left[1+\tanh\left(\frac{\phi_{0,1}-\phi}{\sigma_{0,1}}\right)\right] + B_1\left[1+\tanh\left(\frac{\phi-\phi_{1,1}}{\sigma_{1,1}}\right)\right] + C_1\left[1+\tanh\left(\frac{\phi-\phi_{2,1}}{\sigma_{2,1}}\right)\right]}, \quad (3.8)$$

$$\begin{aligned} f_2(\phi) &= \frac{1}{2}\left[1+\tanh\left(\frac{\phi_{0,2}-\phi}{\sigma_{0,2}}\right)\right] + \frac{B_2}{2}\left[1+\tanh\left(\frac{\phi-\phi_{1,2}}{\sigma_{1,2}}\right)\right] \\ &+ \frac{C_2}{2}\left[1+\tanh\left(\frac{\phi-\phi_{2,2}}{\sigma_{2,2}}\right)\right] \times \left[1+\tanh\left(\frac{\phi_{3,2}-\phi}{\sigma_{3,2}}\right)\right]. \end{aligned} \quad (3.9)$$

The correction functions are built to recover the correct flame speed for rich mixtures and to quickly reach the equilibrium state for a laminar premixed flame at the reference fresh gas temperature $T_0 = 300\ K$ and atmospheric pressure. Their parameters are summarized in Table 3.4 and the shape of such correction functions is illustrated in Fig. 3.4: while f_1 first increases just above stoichiometry and later decreases to slow down the combustion, f_2 goes very fast to zero to accelerate the evolution towards equilibrium.

For lean combustion, no correction is required on the flame speed and $f_1(\phi)$ remains

Table 3.4 - *Coefficients for the two correction functions $f_1(\phi)$ and $f_2(\phi)$ in the 2S_CH4_BFER scheme.*

	$\phi_{0,j}$	$\sigma_{0,j}$	B_j	$\phi_{1,j}$	$\sigma_{1,j}$	C_j	$\phi_{2,j}$	$\sigma_{2,j}$	$\phi_{3,j}$	$\sigma_{3,j}$
$j=1$	1.1	0.09	0.37	1.13	0.03	6.7	1.6	0.22	-	-
$j=2$	0.95	0.08	$2.5\ 10^{-5}$	1.3	0.04	0.0087	1.2	0.04	1.2	0.05

constant and equal to one. The methodology first determines $f_2(\phi)$ then adjusts $f_1(\phi)$ to match the flame speed for rich combustion. The two correction functions $f_1(\phi)$ and $f_2(\phi)$ do not depend on pressure or temperature. Flame speed results obtained with the 2S_CH4_BFER are displayed in Fig. 3.5 for three different initial temperatures ($T_f = 300, 500, 700\ K$) and pressures ($P = 1, 3, 10\ atm$) over the flammability range

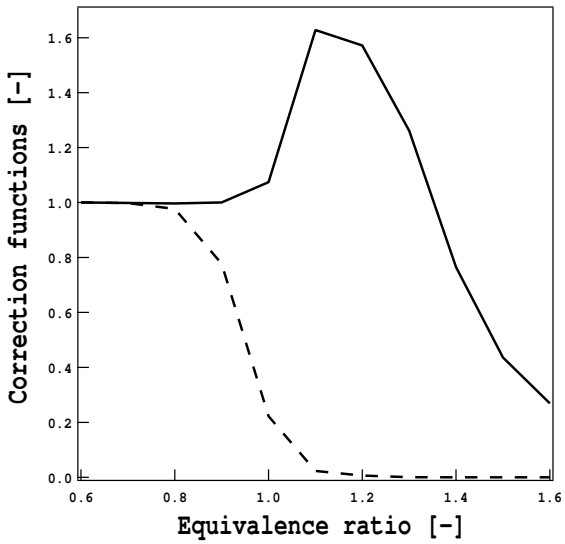

Figure 3.4 - *Evolution of the correction functions f_1 (continous line) and f_2 (dashed line) versus equivalence ratio.*

($\phi = 0.6 - 1.6$). For the whole range of pressures and fresh gas temperatures, the 2S_CH4_BFER scheme predicts a laminar flame speed in agreement with the GRI 3.0 mechanism. The largest discrepancies occur for $T_f = 300\ K$, $P = 10\ atm$ (up to 32%) due to the variation of the pressure dependency coefficient α_P observed at these conditions (Table 3.2). The temperature dependency is well preserved everywhere.

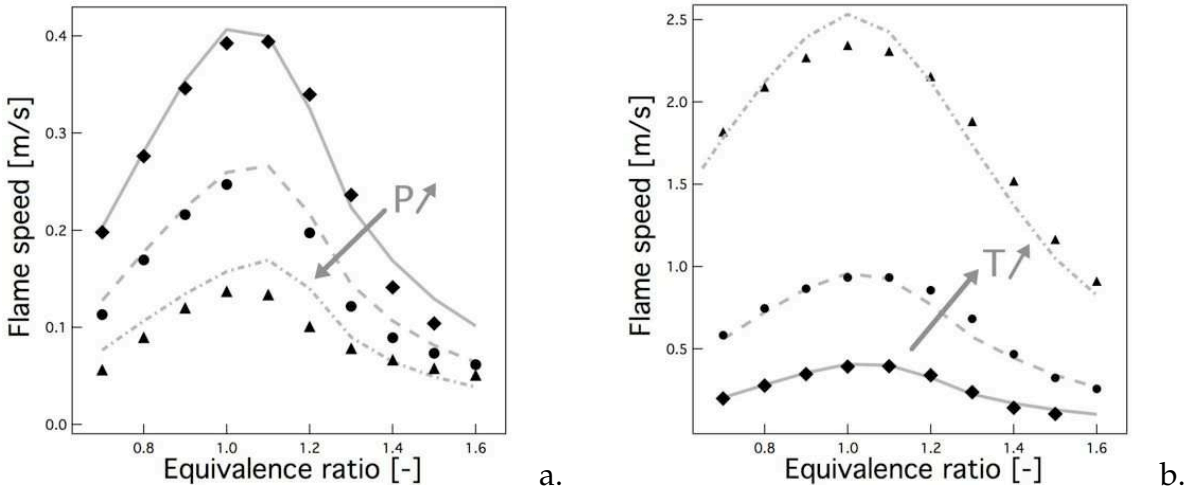

Figure 3.5 - *a) Pressure dependence of the flame speed for $T_f = 300\ K$ and $P = 1, 3, 10\ atm$. b) Temperature dependence of flame speed for $P = 1\ atm$ and $T_f = 300, 500, 700\ K$. Comparison between GRI3.0 (black symbols) and 2S_CH4_BFER (grey lines) mechanisms.*

Strained flames: the 2S_CH4_BFER* scheme

Response to strain is a key point in turbulent combustion. The flame response to strain is known to be strongly affected by the Lewis numbers [124]. In the original 2S_CH4_BFER scheme, unity Lewis numbers assumption is used for all species, but they can be adjusted to improve the response to strain of the mechanism in terms of consumption speed. This is done in the 2S_CH4_BFER* (or BFER*) mechanism having the same parameters than the previous two-step scheme but using Lewis numbers fixed to $Le_K = 1.65$. The pre-exponential factor A_1 for Eq. (3.3) is accordingly reduced to $A_1 = 3.96 \times 10^9$ in order to reproduce the correct flame speed. Parameters for the pressure and temperature dependence are kept unchanged.

This modified 2S_CH4_BFER* scheme is first tested on laminar unstrained and strained flames at the two operating points of interest (Sections 3.2.1 and 3.2.2), before being applied to turbulent flames (Chapters 4 and 5) to study the impact of flame response to strain on the global flame behavior.

3.1.3 The four-step mechanisms: JONES and JONES*

The JONES mechanism presented in [82] is composed of seven species (CH_4, O_2, CO_2, CO, H_2O, H_2 et N_2) and takes into account four reactions:

$$CH_4 + 0.5\ O_2 \quad => \quad CO + 2\ H_2 \tag{3.10}$$

$$CH_4 + \ H_2O \quad => \quad CO + 3\ H_2 \tag{3.11}$$

$$CO + \ H_2O \quad <=> \quad CO_2 + H_2 \tag{3.12}$$

$$H_2 + 0.5\ O_2 \quad <=> \quad H_2O. \tag{3.13}$$

It is based on a flame structure comprising two reaction zones: a first reaction zone where methane oxidation into CO and H_2 occurs (reactions (3.10) and (3.11)) and a second reaction zone where CO_2 and H_2O are produced (reactions (3.12) and (3.13)). Each reaction follows an Arrhenius law whose parameters have been chosen in order to correctly describe the flame structure of both premixed and diffusion flames for ambient temperature and atmospheric pressure (Table 3.5).

Two formulations for the forward reaction rate of reaction (3.13) were proposed by Jones and Lindstedt [82]

$$k_f = 0.25 \times 10^{17}\ \exp^{(-40000/RT)}\ T^{-1}\ [H_2]^{0.5}\ [O_2]^{2.25}\ [H_2O]^{-1}\ , \tag{3.14}$$

$$k_f^\star = 0.68 \times 10^{17}\ \exp^{(-40000/RT)}\ T^{-1}\ [H_2]^{0.25}\ [O_2]^{1.50}\ . \tag{3.15}$$

Equation (3.15) is usually preferred to avoid the singularity caused by the negative order for H_2O species although it reduces the scheme accuracy in the fuel lean region.

Table 3.5 - *Activation energy E_a, pre-exponential factor A, temperature exponent β ,and reaction exponents n_k for the JONES mechanism. Units are: kmol, s, m^3 and cal/mol.*

	Reaction (3.10)		Reaction (3.11)		Reaction (3.12)		Reaction (3.13)	
Activation energy	3.00×10^4		3.0×10^4		2.0×10^4		4.0×10^4	
Pre-exponential factor	4.4×10^{11}		3.0×10^9		2.75×10^9		2.5×10^{16}	
Temperature exponent	0		0		0		-1	
Reaction exponents (-)	$n_{CH_4,1}$	0.50	$n_{CH4,2}$	1.00	$n_{CO,3}$	1.00	$n_{H_2,4}$	0.50
	$n_{O_2,1}$	1.25	$n_{H_2O,2}$	1.00	$n_{H_2O,3}$	1.00	$n_{O_2,4}$	2.25
							$n_{H_2O,4}$	-1

In the present work the use of Eq. (3.14) is preferred to preserve the quality of the mechanism, and particular attention is given to its implementation in CFD tools such as CANTERA or AVBP (Section 3.1.7), since negative species order are found not only for the forward reaction rate but also for the reverse reaction rate of reaction (3.13):

$$k_r = 0.178 \times 10^{14} \exp^{(-93000/RT)} T^{-1} [H_2]^{-0.5} [O_2]^{1.75} . \quad (3.16)$$

Species Lewis numbers are assumed constant but different for each species (cfr. Table 3.6).
Figures 3.6a and 3.6b show respectively the flame speed dependence on pressure and temperature for the JONES mechanisms. The pressure exponent of Jones et Lindstedt [82] is greatly underestimated $\alpha_P \approx -0.125$, and, as a consequence, the flame speed is too high when increasing the pressure (Fig. 3.6a.). However, it was shown in [156] that the four-step mechanism could be adapted to different operation points adjusting the pre-exponential factor of Eqs. (3.10) and (3.13), at least for lean mixtures.
The temperature dependence is better described (Fig. 3.6b), at least for $T < 500\ K$, but it is greatly overestimated for $T_f = 800\ K$, i.e. the BUNSEN operating point.

Table 3.6 - *Species Lewis numbers for the JONES scheme*

CH_4	O_2	CO_2	CO	H_2O	H_2	N_2
0.967	1.0557	1.35	1.07	0.777	0.29	1.036

A correction is then proposed, introducing a new mechanism named JONES* by adjusting the parameters of the reactions (3.10) and (3.13) governing the flame speed. Their pre-exponential factors are now $A_1^* = 0.5A_1$ and $A_4^* = 0.3A_4$ improving the flame speed prediction especially for the equivalence ratio of interest $\phi = 0.7$ (Fig. 3.7, dashed line). For the PRECCINSTA operating point ($T_f = 320\ K$), the original JONES mechanism will be used.

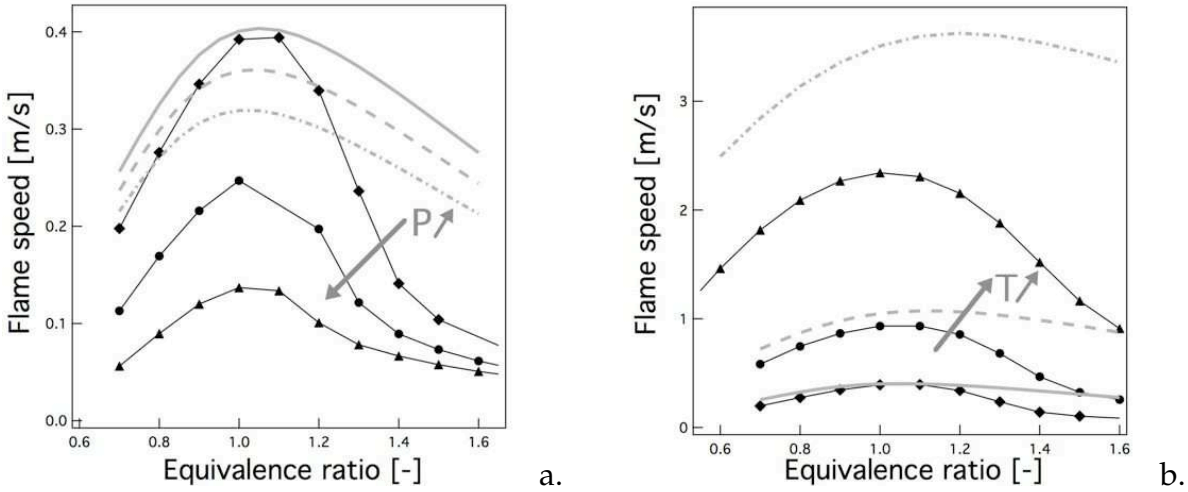

Figure 3.6 - *a) Pressure dependence of the flame speed for $T_f = 300$ K and $P = 1, 3, 10$ atm. b) Temperature dependence of flame speed for $P = 1$ atm and $T_f = 300, 500, 700$ K. Comparison between GRI3.0 (black symbols) and JONES (grey lines) mechanisms.*

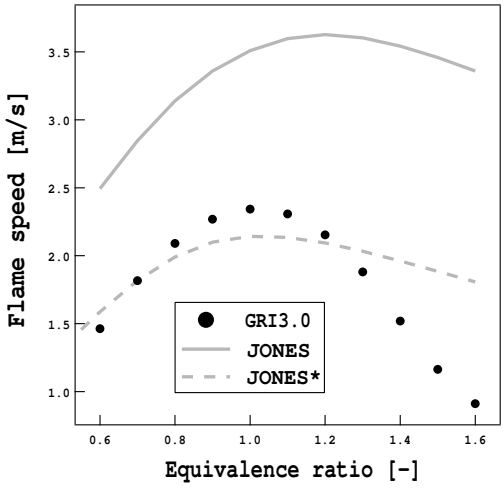

Figure 3.7 - *Flame speed of a premixed unstrained methane/air flame at $T_f = 800$ K and $P = 1$ atm. Comparison between reduced the JONES and JONES* mechanisms and the GRI3.0 detailed scheme.*

3.1.4 The analytical mechanisms: PETERS and PETERS*

The PETERS mechanism presented in [116] accounts for eight species (CH_4, O_2, CO_2, CO, H_2O, N_2, H_2 and H) and four reactions:

$$RI: \quad CH_4 + 2\,H + H_2O \quad => \quad CO + 4\,H_2 \tag{3.17}$$
$$RII: \quad CO + H_2O \quad <=> \quad CO_2 + H_2 \tag{3.18}$$
$$RIII: \quad 2\,H + M \quad <=> \quad H_2 + M \tag{3.19}$$
$$RIV: \quad 3\,H_2 + O_2 \quad <=> \quad 2\,H + 2\,H_2O. \tag{3.20}$$

It is based on a skeletal mechanism for lean methane/air flames composed by 18 reactions and 13 species:

$$R1: \quad CH_4 + H \quad => \quad CH_3 + H_2 \tag{3.21}$$
$$R2: \quad CH_4 + OH \quad => \quad CH_3 + H_2O \tag{3.22}$$
$$R3: \quad CH_3 + O \quad => \quad CH_2O + H \tag{3.23}$$
$$R4: \quad CH_2O + H \quad => \quad CHO + H_2 \tag{3.24}$$
$$R5: \quad CH_2O + OH \quad => \quad CHO + H_2O \tag{3.25}$$
$$R6: \quad CHO + H \quad => \quad CO + H_2 \tag{3.26}$$
$$R7: \quad CHO + M \quad => \quad CO + H + M \tag{3.27}$$
$$R8: \quad CHO + O_2 \quad => \quad CO + HO_2 \tag{3.28}$$
$$R9: \quad CO + OH \quad <=> \quad CO_2 + H \tag{3.29}$$
$$R10: \quad H + O_2 \quad <=> \quad OH + O \tag{3.30}$$
$$R11: \quad O + H_2 \quad <=> \quad OH + H \tag{3.31}$$
$$R12: \quad OH + H_2 \quad <=> \quad H_2O + H \tag{3.32}$$
$$R13: \quad OH + OH \quad <=> \quad H_2O + O \tag{3.33}$$
$$R14: \quad H + O_2 + M \quad <=> \quad HO_2 + M \tag{3.34}$$
$$R15: \quad H + OH + M \quad <=> \quad H_2O + M \tag{3.35}$$
$$R16: \quad H + HO_2 \quad => \quad OH + OH \tag{3.36}$$
$$R17: \quad H + HO_2 \quad => \quad H_2 + O_2 \tag{3.37}$$
$$R18: \quad OH + HO_2 \quad => \quad H_2O + O_2. \tag{3.38}$$

where M is a third body whose concentration is given by: $[X_M] = [X_H] + [X_{H_2}] + 0.4\,[X_{O_2}] + 6.5\,[X_{H_2O}] + 0.75\,[X_{CO}] + 1.5\,[X_{CO_2}] + 6.54\,[X_{CH_4}]$.

The fundamental reactions which cannot be eliminated are listed: reactions R1 and R2 (Eqs. (3.21) and (3.22)) determine fuel consumption, reaction R9 (Eq. (3.29)) describes the oxidation of CO, reaction R10 (Eq. (3.30)) determines the consumption of

O_2 and reaction R14 (Eq. (3.34)) is the only reaction taking into account a third body recombination. In order to reduce the computational time, six intermediate species (OH, O, HO_2, CH_3, CH_2O and CHO) are assumed to be in "quasi steady state" (QSS), i.e their production/consumption rates are supposed equal to zero $\dot{\omega}_k \approx 0$ and at least six reaction rates are eliminated from the system. Eliminating the fast reactions and recombining the different reaction rates, the global rate of reactions RI - RIV (Eqs. (3.17)-(3.20)) are given in terms of eight elementary reactions:

$$\begin{aligned} Q_I &= Q_1 + Q_2 && (3.39)\\ Q_{II} &= Q_9 && (3.40)\\ Q_{III} &= Q_6 + Q_8 + Q_{14,f} + Q_{15,f} && (3.41)\\ Q_{IV} &= Q_{10} && (3.42)\\ & && (3.43) \end{aligned}$$

where $Q_{j,f}$ and Q_j are respectively the forward and the net reaction rates of reaction Rj. Imposing a steady state for species CH_3 ($\dot{\omega}_{CH_3} \approx 0$) an algebraic relation is deduced for the concentration of species CHO necessary for the calculation of reaction rates Q_6 and Q_8:

$$[X_{COH}] = \frac{K_1 [X_{CH_4}] [X_H] + K_2 [X_{CH_4}] [X_{OH}]}{K_6 [X_H] + K_7 [X_M] + K_8 [X_{O_2}]}. \tag{3.44}$$

To further simplify the chemical mechanism, a partial equilibrium is assumed for reactions R11-R13 (Eqs. (3.31)-(3.33)) whose reaction rates are large compared to the other reaction rates in the high temperature region of the flame. Two algebraic relations result for species OH and O:

$$[X_{OH}] = [X_H] \frac{[X_{H_2O}]}{K_{12}^{eq} [X_{H_2}]} \quad , \quad [X_O] = \frac{[X_H] [X_{OH}]}{K_{11}^{eq} [X_{H_2}]}. \tag{3.45}$$

Note that the use of these relations could be numerically difficult when a small H_2 concentration is detected (Section 3.1.7).

Progress reaction rates (3.39)-(3.42) are then calculated using the rate coefficients recommended in [167]. Constant Lewis numbers are assumed as described in Table 3.7.

Table 3.7 - *Species Lewis numbers for the PETERS and SESHADRI schemes.*

CH_4	O_2	CO_2	CO	H_2O	H_2	N_2	H
0.967	1.0557	1.35	1.07	0.777	0.29	1.036	0.243

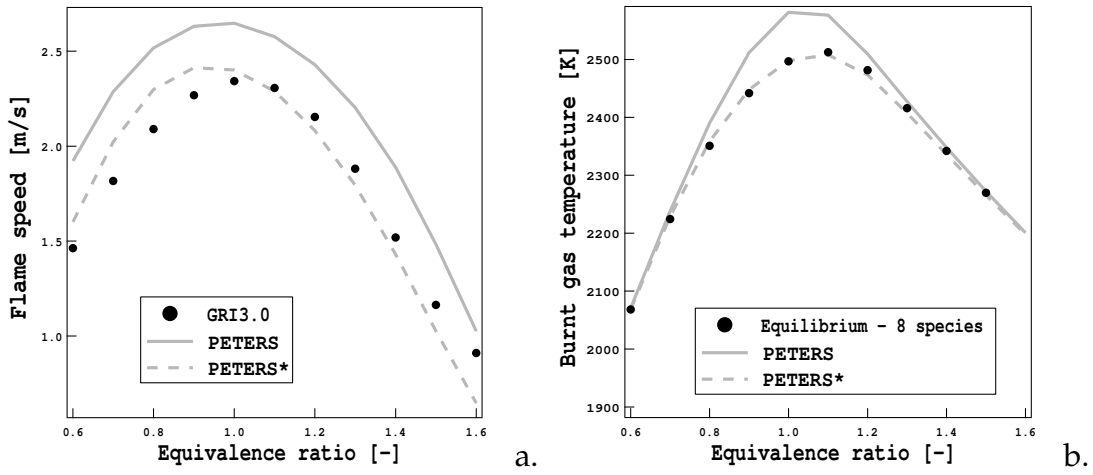

Figure 3.8 - *Flame speed (a.) and burnt gas temperature (b.) for a premixed unstrained methane/air flame at T_f = 800 K and P = 1 atm. Comparison between reduced PETERS and PETERS* mechanisms and the GRI3.0 detailed scheme for the flame speed and the equilibrium state (8 species) for the burnt gas temperature.*

This scheme describes the basic features of the skeletal mechanism, i.e. the flame structure of premixed and diffusion flames, but the assumed QSS and equilibrium state hypothesis are valid only for fresh gas temperatures lower than T_f = 500 K.
Indeed the reverse path of reaction R15 of the skeletal mechanism (Eq. (3.35)) greatly affects results for $T_f > 500$ K so that the PETERS mechanism, where it is missing is not able to describe the equilibrium state at T_f = 800 K (Fig. 3.8b, solid line).
To improve the scheme performance, the reverse path of reaction R15 is reintroduced in the calculation of the rate of progress of reaction RIII (Eq. (3.19)) leading to:

$$Q^*_{III} = Q_6 + Q_8 + Q_{14,f} + Q_{15,f} - Q_{\mathbf{15,r}} \tag{3.46}$$

Moreover, the reaction parameters are extracted from a more recent detailed scheme for methane/air flames named SanDiego [174]. This new mechanism is named PETERS*. Figure 3.8 (dashed line) shows how PETERS* scheme recovers the flame speed and the equilibrium temperature at T_f = 800 K for the whole range of equivalence ratio. In the following, the PETERS and PETERS* schemes will be validated and used for calculations at T_f = 320 K (Chapter 5) and T_f = 800 K (Chapter 4) respectively.

3.1.5 The SESHADRI and SESHADRI* mechanisms

The four-step reduced mechanism SESHADRI by Seshadri and Peters [39] has been derived by using a computer program for optimization and reduction of detailed mechanisms [38]. It takes into account the same species (CH_4, O_2, CO_2, CO, H_2O, N_2,

H_2 and H) and reactions used by the PETERS mechanism:

$$CH_4 + 2\,H + H_2O \;=>\; CO + 4\,H_2 \tag{3.47}$$
$$CO + H_2O \;<=>\; CO_2 + H_2 \tag{3.48}$$
$$2\,H + M \;<=>\; H_2 + M \tag{3.49}$$
$$3\,H_2 + O_2 \;<=>\; 2\,H + 2\,H_2O. \tag{3.50}$$

As for the PETERS scheme, the global reaction rates are based on a reduction of a skeletal mechanism of 25 reactions using the QSS assumption and the equilibrium hypothesis. Algebraic relations are given for OH, O, CH_3, CH_3O, CH_2O, HCO, HO_2 and H_2O_2 species. The same constant Lewis numbers as for the PETERS scheme are used (Table 3.7).

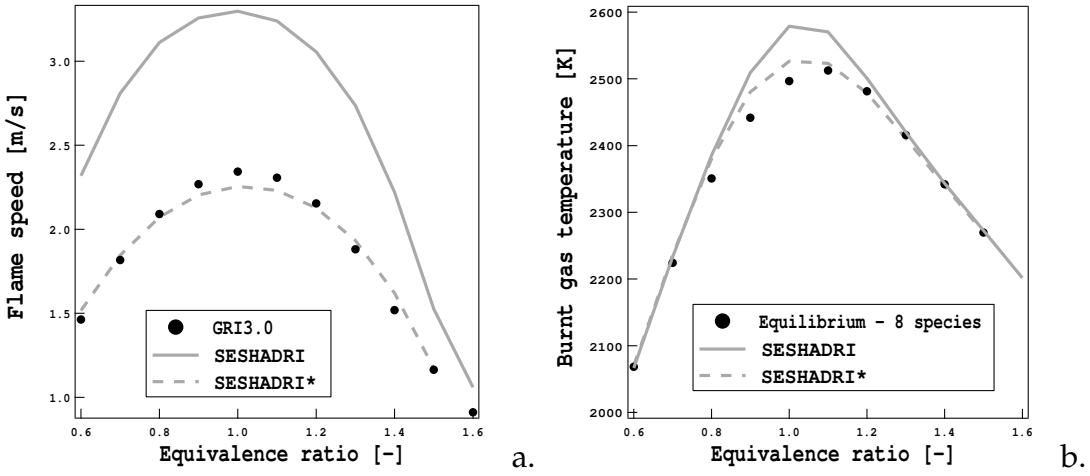

Figure 3.9 - *Flame speed (a.) and burnt gas temperature (b.) for a premixed unstrained methane/air flame at T_f = 800 K and P = 1 atm. Comparison between reduced SESHADRI and SESHADRI* mechanisms and the GRI3.0 detailed scheme for the flame speed and the equilibrium state (8 species) for the burnt gas temperature.*

The SESHADRI scheme correctly reproduces the structure of premixed and diffusion flames for ambient temperature and atmospheric pressure [39]. At T_f = 800 K, this mechanism shows the same problem in describing the equilibrium state as the PETERS scheme (Fig.3.9b, solid line). Again, its behavior is incorrect because the reverse path of reaction $H + OH + M$ <=> $H_2O + M$ is neglected when calculating the reaction rate of Eq. (3.49). The SESHADRI* scheme is therefore proposed also accounting for the reverse reaction rate of $H + OH + M$ <=> $H_2O + M$. Moreover, the SESHADRI scheme largely overestimates the flame speed. The pre-exponential factor of reaction $H + O2$ <=> $OH + O$ is reduced by a facto 0.7 since governing the production of radical species, it mainly controls the flame speed. This adjustment is not systematic and the

SESHADRI* mechanism is no more an analytical scheme.
Figure 3.9 shows that the SESHADRI* scheme behaves better than the SESHADRI scheme at $T_f = 800$ although some discrepancies are still detected near stoichiometry. The SESHADRI* mechanism is then used to compute the Bunsen configuration.

3.1.6 The LU mechanism

The LU mechanism corresponds to the reduced chemical scheme used by Sankaran et al. [137, 136] in the DNS of the Bunsen flame and is based on the work of Lu and Law [98]. It takes into account 13 resolved species (CH_4, O_2, CO_2, CO, H_2O, N_2, H_2, H, OH, O, HO_2, CH_3 and CH_2O), 4 QSS species (CH_2, CH_2S, HCO and CH_2OH) and 73 elementary species. The detailed mechanism GRI1.2 is reduced applying the directed relation graph method, the sensitivity analysis and the computational singular perturbation approach [98]. QSS is assumed for various species in order to obtain algebraic expressions. The quality of this scheme is evaluated on lean premixed methane/air flames, perfectly stirred reactor for $T_f = 300\ K$ and auto-ignition configurations from 1000 K to 1800 K [136]. Simplified transport properties are assumed and the constant Lewis numbers are summarized in Table 3.8.

Table 3.8 - *Species Lewis numbers for the LU scheme*

CH_4	O_2	CO_2	CO	H_2O	H_2	N_2	H	O	OH	HO_2	CH_3	CH_2O
0.967	1.0557	1.35	1.07	0.777	0.29	1.036	0.17	0.69	0.7	1.07	0.97	1.25

The agreement between the LU mechanism and the detailed scheme are satisfactory for both operating points (Fig. 3.10) and in the following it will be used as the reference mechanism representing the behavior of complex chemistry.

3.1.7 Implementation of reduced mechanisms in CFD tools

Using the reduced mechanisms presented in Section 3.1 in a CFD code is not straightforward for two reasons:

- Thermo-chemical codes such as CANTERA [71] support different types of reactions including Arrhenius law, third-body and fall-off reactions whereas in CFD tools such as AVBP only Arrenhius and third-body reactions are generally used.

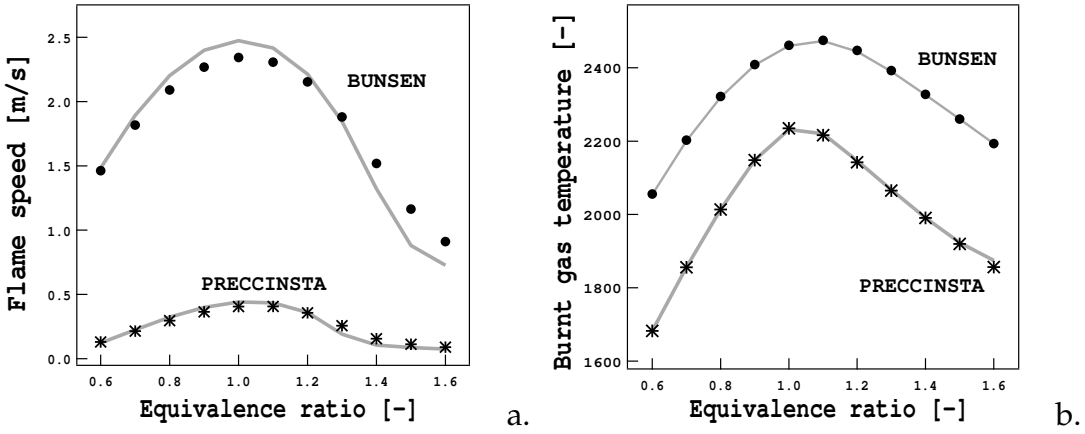

Figure 3.10 - *Flame speed (a.) and burnt gas temperature (b.) for both BUNSEN and PRECCINSTA operating points. Comparison between reduced LU mechanism (solid lines) and the GRI3.0 detailed scheme (symbols) for the flame speed and the equilibrium state (13 species) for the burnt gas temperature.*

Negative species orders are not admitted and there is no automatic way to implement a custom mechanism or to express reaction rates in an algebraic formulation. As a consequence, the JONES mechanism and all analytical schemes can not be directly used and they require hard-coding in the kernel of the code.

- Numerical difficulties could be encountered when implementing and using the analytical mechanisms due to the algebraic expressions in the denominator of the reaction rates and of the species in the QSS. Clipping on species mass fraction has therefore been implemented to overcome this problem. Moreover, negative reaction orders have to be carefully treated and specific algorithms could be necessary to avoid unreasonable small time steps due to the stiffness of some reaction rates.

The method to implement and use the reduced mechanisms avoiding numerical singularity is presented in the following for all reduced mechanisms.

The two-step mechanisms 2S_CH4_BFER

The reaction rates of the two-step mechanisms 2S_CH4_BFER and 2S_CH4_BFER* have a classical Arrhenius law formulation with pre-exponenential constants that are functions of the equivalence ratio. In practice, no modification is required for a perfectly premixed combustion calculation at fixed equivalence ratio. In that case, the pre-exponential constants are adjusted in advance when defining the reactions in the input file. Whenever the equivalence ratio varies in the calculation domain, the pre-

exponential constants need to be locally modified and the implementation of the PEA method is thus necessary. In CANTERA, AVBP and S3D at each grid point a local equivalence ratio is evaluated from the mixture fraction based on the conservation of carbon atoms. The correction PEA functions are then applied to the pre-exponential constants when computing the reaction rates.
Generally, this kind of mechanism is quite robust and does not present any pathologic singularity, i.e. the reaction orders are positive and larger than 0.5. No numerical problem is detected neither in laminar nor in turbulent premixed flame calculations.

The JONES scheme

In JONES/JONES* schemes, the negative species order for species H_2 and H_2O in the reversible reaction (3.13) is an important difficulty:

$$H_2 + 0.5\ O_2 \quad <=> \quad H_2O \tag{3.51}$$

whose progress rate is given by 3.14 and 3.16:

$$Q = K_f \left[[H_2]^{0.5} [H_2]^{2.25} [H_2O]^{-1} - \frac{1}{K_{eq}} [O_2]^{1.75} [H_2]^{-0.5} \right]. \tag{3.52}$$

The reaction rate may tend to infinity whenever the H_2O or the H_2 concentrations approach to zero and must be limited. When calculating the reaction rate, the mass fractions of the H_2 and H_2O species are not allowed to decrease below their clipping values ϵ_{H_2} and ϵ_{H_2O} (in this work, equal to 1% of the maximum mass fraction values for H_2 and H_2O species respectively). The stability is thus guaranteed but the scheme behavior may be altered and clipping must be used with caution.
Particular attention has to be paid to preserve the equilibrium state for which the progress rate is supposed equal to zero $Q = 0$. From Eq. (3.52) the equilibrium constant is given by:

$$K_{eq} = \frac{[O_2]^{1.75} [H_2]^{-0.5}}{K_f [H_2]^{0.5} [H_2]^{2.25} [H_2O]^{-1}}. \tag{3.53}$$

In order to preserve the equilibrium state and to avoid numerical instabilities, the progress rate is modified as follows:

- if $Y_{H_2O} > \epsilon_{H_2O}$ and $Y_{H_2} > \epsilon_{H_2}$: the progress rate (3.52) may be used without any problem;
- if $Y_{H_2O} < \epsilon_{H_2O}$ and $Y_{H_2} > \epsilon_{H_2}$: the H_2O concentration is not taken into account in the forward path and it is added to the reverse path in order to preserve the equilibrum state:

$$Q* = Q \times [H_2O]; \tag{3.54}$$

- similarly if $Y_{H_2O} > \epsilon_{H_2O}$ and $Y_{H_2} < \epsilon_{H_2}$: when the H_2 concentration is too small it is not taken into account in the reverse path but appears in to the forward progress rate to guarantee a correct description of the equilibrium state:

$$Q* = Q \times [H_2]^{0.5}; \tag{3.55}$$

- if $Y_{H_2O} < \epsilon_{H_2O}$ and $Y_{H_2} < \epsilon_{H_2}$: both H_2 and H_2O concentrations are deleted to the denominators and added to the numerator of the forward and reverse path respectively:

$$Q* = Q \times [H_2O] \times [H_2]^{0.5}; \tag{3.56}$$

This modification is not active in the reaction zone, characterized by H_2 and H_2O concentrations bigger than the clipping values, and it does not affect the description of the flame.

Analytical schemes (PETERS, SESHADRI and LU)

Some numerical difficulties may be expected when implementing and using the analytical mechanisms due to the algebraic expressions in the denominators of the reaction rates and of the species in the QSS [115]. When the denominators go to zero, the reaction rates go to infinity and a control on these terms is necessary to avoid singularities, then a clipping on the species mass fraction is used:

$$\text{if} \quad 0 < Y_k < \epsilon : \quad Y_k = \epsilon, \tag{3.57}$$

where the clipping parameter ϵ is small enough to avoid unphysically high values of the reaction rates (in this work $\epsilon = 1.0e^{-10}$). It should be noticed that the species mass fractions are modified only in the calculation of the reaction rates but are otherwise unchanged. One consequence is that the reaction rates are always non-zero. Since H_2 is the species that activates the reactions, its mass fraction is used to inhibit them:

$$\text{if} \quad Y_{H_2} < \epsilon_{H_2} : \quad Q = 0, \tag{3.58}$$

where ϵ_{H_2} has been chosen in this work equal to 0.1% of the maximum mass fraction value for species H_2. However it is not possible to generalize the clipping procedure and some trials are necessary when implementing new analytical mechanisms.

3.2 Comparison between reduced mechanisms

In this Section, the performances of the reduced mechanisms are evaluated on laminar premixed unstrained and strained flames for the operating points of the DNS and LES of Chapters 4 and 5. The preliminary results on unstrained flames discussed in Section 3.1 are completed with results on the flame structure and on the response of the flame to strain rate.

3.2.1 Comparison between reduced mechanisms on unstrained flames

The quality of different reduced mechanisms is compared on unstrained flames at the two different points of interest (PRECCINSTA and BUNSEN) in terms of flame speed, burnt gas temperature and flame structure.

Flame characteristics

In Fig. 3.11, the flame speed obtained with the reduced schemes are compared to the detailed GRI3.0 mechanism. The behavior of the simplified mechanisms is the same for both operating points. For lean and stoichiometric mixtures, all mechanisms correctly reproduce the flame speed. The agreement with the detailed GRI3.0 scheme is satisfactory for the equivalence ratio of interest ($\phi = 0.83$ and $\phi = 0.7$ for $T_f = 320\ K$ and $T_f = 800\ K$ respectively). For rich mixtures, the decrease in flame speed is well predicted by all mechanisms except the JONES and JONES* schemes which greatly overpredict it.

The introduction of additional species in the JONES, PETERS, SESHADRI, LU mechanisms and their modified versions improves the description of the burnt gas temperature (Fig. 3.12), only overestimated for very rich flames ($\phi > 1.4$) by the two-step schemes. High discrepancies are also detected for near-stoichiometric flames for the highest initial temperature $T_f = 800\ K$. The most complex reduced LU scheme is the only one which correctly predicts the burnt gas temperature on the whole range of equivalence ratio which means that 13 species are required to correctly reproduce the burnt gas temperature at both operating points. For the composition of interest ($\phi = 0.7$ and $\phi = 0.83$), the two-step schemes predict the flame speed and burnt gas temperature with an error smaller than 8% and 1% respectively. The largest error for the flame speed is produced by the SESHADRI scheme (about 15%) whereas the error on the burnt gas temperature is less than 1% for all the schemes. All mechanisms are valid in terms of S_L and burnt gas temperature for the two operating points (see Tables 3.9 and 3.10).

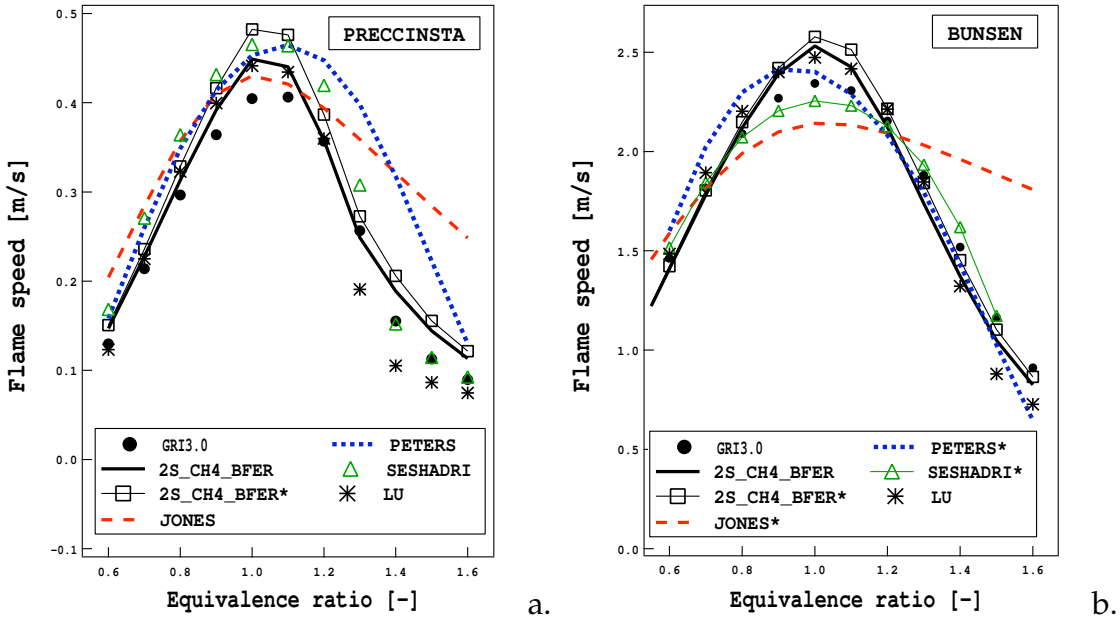

Figure 3.11 - *Flame speed for a premixed unstrained methane/air flame at initial temperature a) T_f = 320 K and b) T_f = 800 K and atmospheric pressure. Comparison between the reduced mechanisms and the GRI3.0 detailed scheme.*

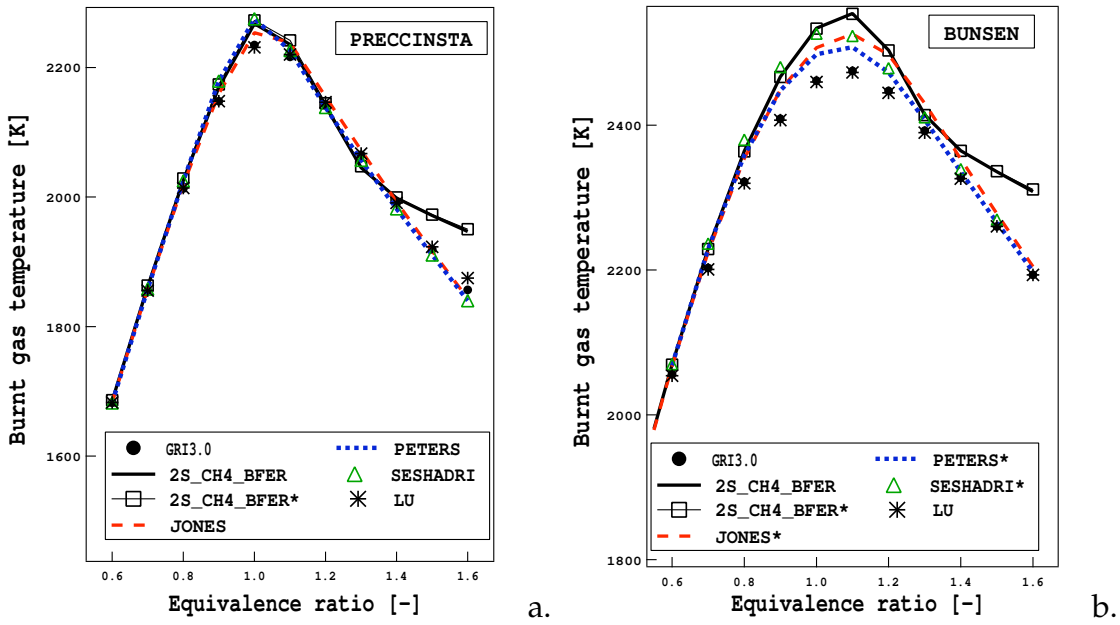

Figure 3.12 - *Burnt gas temperature for a premixed unstrained methane/air flame at initial temperature a) T_f = 320 K and b) T_f = 800 K and P = 1 atm. Comparison between the reduced mechanisms and the GRI3.0 detailed scheme.*

Table 3.9 - *Flame speed, burnt gas temperature and flame thickness for the different mechanisms at* $\phi = 0.83$, $T_f = 320$ *K and* $P = 1$ *atm.*

	GRI3.0	**BFER**	**BFER***	**JONES**	**PETERS**	**SESHADRI**	**LU**
$S_l\ [m/s]$	0.329	0.339	0.355	0.378	0.371	0.388	0.351
$T_b\ [K]$	2056.68	2072.03	2072.47	2068.78	2072.99	2071.11	2057.75
$\delta_L\ [m]$	5.056e-4	3.906e-4	3.732e-4	3.769e-4	4.475e-4	4.644e-4	4.610e-4
$\tau_c\ [s]$	1.536e-3	1.152e-3	1.052e-3	0.997e-3	1.207e-3	1.198e-3	1.313e-3

Table 3.10 - *Flame speed, burnt gas temperature and flame thickness for the different mechanisms at* $\phi = 0.7$, $T_f = 800$ *K and* $P = 1$ *atm.*

	GRI3.0	**BFER**	**BFER***	**JONES***	**PETERS***	**SESHADRI***	**LU**
$S_l\ [m/s]$	1.817	1.782	1.806	1.793	2.023	1.845	1.893
$T_b\ [K]$	2202.8	2229.38	2229.7	2224.56	2228.9	2236.34	2200.8
$\delta_L\ [m]$	3.375e-4	2.2846e-4	2.231e-4	3.072e-4	3.092e-4	3.859e-4	3.451e-4
$\tau_c\ [m]$	1.857e-4	1.282e-4	1.235e-4	1.713e-4	1.528e-4	2.092e-4	1.823e-4

Flame thickness

An important variable in turbulent combustion modeling is the progress variable. Its definition is however not straightforward for complex reduced chemistry. The progress variable c is defined on the O_2 species as proposed by Sankaran et al. [137]:

$$c = \frac{Y_{O_2} - Y^f_{O_2}}{Y^b_{O_2} - Y^f_{O_2}}. \tag{3.59}$$

It indicates the progression of the reaction from fresh to burnt gases.

The ability of a reduced mechanism to reproduce the correct flame thickness is very important as it affects the interaction with turbulence. Moreover, if a simplified scheme strongly underpredicts the flame thickness, the computational grid has to be refined (at least five grid points are necessary in the reaction zone to correctly describe the flame) and the computational cost increases. Its gradient $|\nabla c|$ is displayed in Fig. 3.13 for both operating points and all reduced mechanisms. It could be used to represent the flame thickness: the highest is $|\nabla c|$ the thinner is the flame. This quantity is very helpful when analyzing turbulent flames for which the definition of thermal thickness cannot be easily applied.

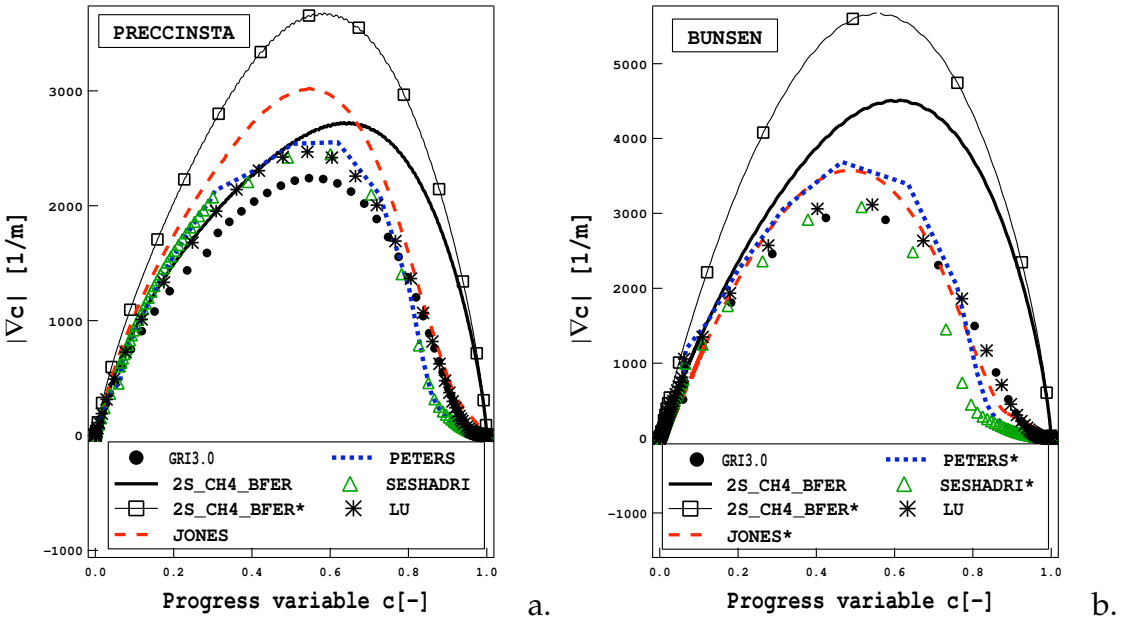

Figure 3.13 - *Gradient of the progress variable |∇c| for a premixed unstrained methane/air flame at initial temperature a) T_f = 320 K and b) T_f = 800 K and P = 1 atm. Comparison between the reduced mechanisms and the GRI3.0 detailed scheme.*

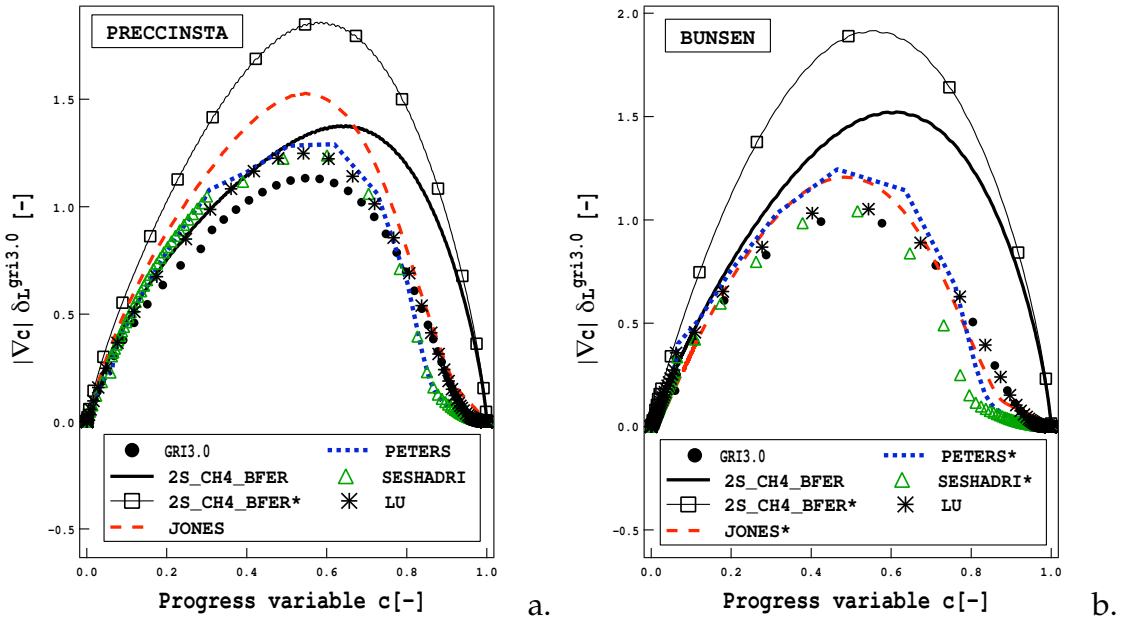

Figure 3.14 - *Magnitude of the progress variable gradient normalized by the laminar flame thickness $\delta_L^{GRI3.0}$ for a premixed unstrained methane/air flame at initial temperature a) T_f = 320 K and b) T_f = 800 K and atmospheric pressure. Comparison between the reduced mechanisms and the GRI3.0 detailed scheme.*

The behavior of the reduced mechanisms is similar for both operating points. The two-step schemes generally overestimate $|\nabla c|$, i.e. the flame is thinner, as also predicted by the thermal thickness in Tables 3.9 and 3.10. The agreement between all other reduced mechanisms and the detailed scheme is satisfactory, with the JONES less performant in the PRECCINSTA case.

The progress variable gradient $|\nabla c|$ may be normalized by the laminar thermal thickness predicted by the detailed mechanism $\delta_L^{GRI3.0}$ (Tables 3.9 and 3.10). Results are displayed in Fig. 3.14 for both operating points and all reduced mechanisms. The normalized flame gradient magnitude is not exactly equal to one for the detailed mechanism since its Lewis number differs to one. In this work, the normalized formulation of the progress variable gradient is used to analyzed the flame thickness of turbulent flames.

Species profiles

Spatial profiles of CH_4, CO_2 and CO species representing respectively reactants, products and intermediate species for the reduced schemes are compared to the GRI3.0 scheme at $\phi = 0.83$, $T_f = 320\ K$ and $P = 1\ atm$ in Fig. 3.15 and $\phi = 0.7$, $T_f = 800\ K$ and $P = 1\ atm$ in Fig. 3.16. The visualization in the physical space is zoomed in the reaction zone and the equilibrium state could only be evaluated looking at the flame state at $c = 1$ in the progress variable space.

A first difference is that the **concentration of CH_4** predicted by the two-step mechanisms is non-zero for all values of c except $c = 1$, while for all other mechanisms (including the GRI3.0 scheme) the CH_4 is totally burnt close to $c \approx 0.80$ while temperature still increases due to recombination in the post-flame zone.
The **CO_2 spatial profile** predicted by the GRI3.0 scheme shows two different zones: a first reaction zone, characterized by a high gradient, and a second post-flame zone where recombination takes place and CO_2 increases slowly. Again, the two-step mechanisms are not able to reproduce the slower recombination zone and equilibrium is reached too quickly. The JONES/JONES* results are in good agreement with the detailed mechanism but better results are obtained with all other reduced mechanisms.
A correct description of the **CO concentration** is necessary when predicting pollutants but reproducing the maximum value of CO species is a hard task since it is first produced then oxidized into CO_2. The two-step schemes predict an unphysical monotonous profile and greatly underestimate its maximum value, but its value at equilibrium is correctly described. The JONES/JONES* provide profiles in good agreement with the detailed mechanism, with correct maximum levels for CO and H2 species even if the equilibrium in the post flame region is reached slightly too rapidly.
The PETERS/PETERS*, SESHADRI/SESHADRI* and LU mechanisms predict almost perfectly the flame structure: the maximum levels of CO and H2 species are well cap-

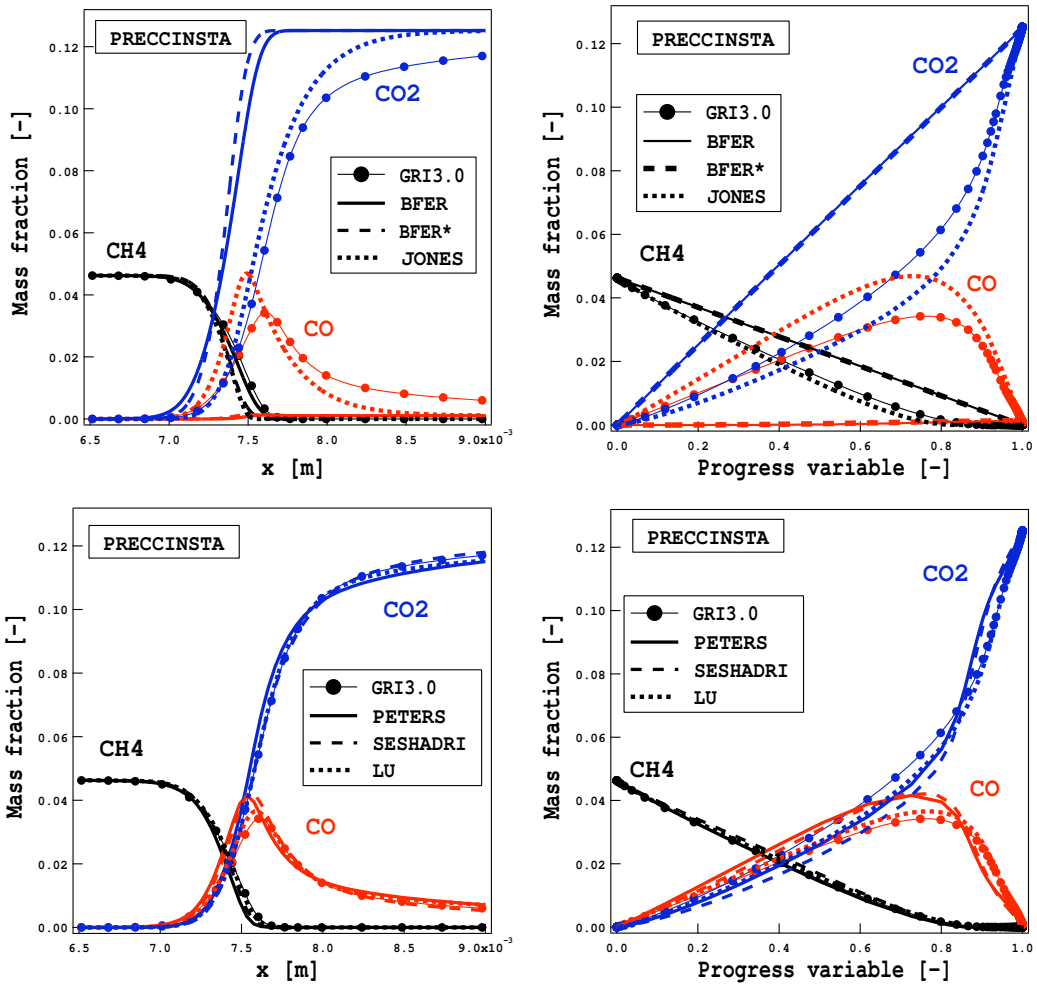

Figure 3.15 - *Species profiles for* $\phi = 0.83$, $T_f = 320$ *K and* $P = 1$ *atm.*

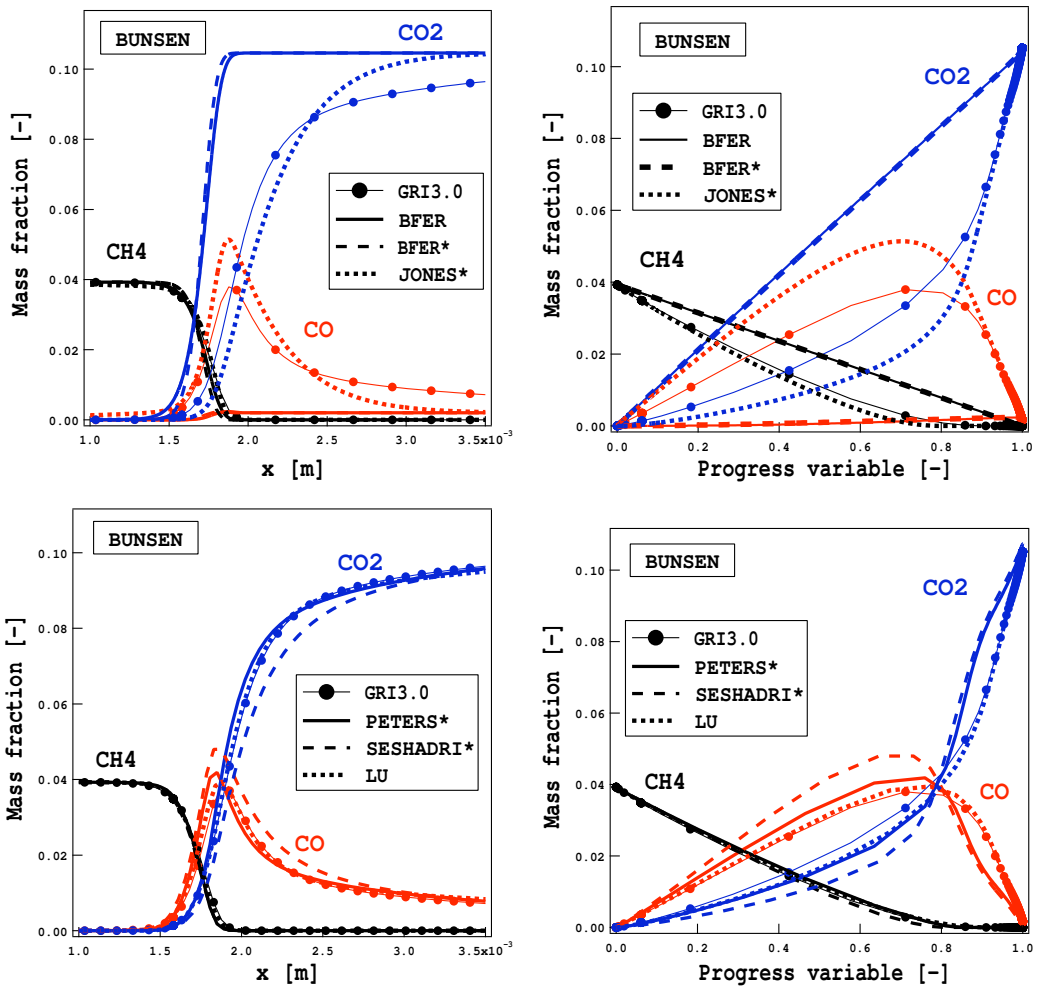

Figure 3.16 - *Species profiles for* $\phi = 0.70$, $T_f = 800\ K$ *and* $P = 1\ atm$.

tured and the equilibrium is slowly reached since the analytical mechanisms explicitly include reactions :

$$H + O_2 \;=>\; O + OH \tag{3.60}$$
$$CO + OH \;=>\; CO_2 + H. \tag{3.61}$$

As already discussed in Section 2.2, a correct description of radical species such as OH, H and O is necessary to predict oxides of nitrogen via the Zel'dovich mechanism. Although the prediction of NO_x emissions is not the purpose of this thesis, the computation of premixed flames using the different reduced schemes provides interesting information in this topic. Figure 3.17 compares the profile of H_2, H, OH and O mass fractions versus progress variable obtained with analytical schemes and the GRI3.0 scheme at the two operating points. As expected, the LU mechanism correctly reproduces the profiles for H, OH and O radicals. Although the analytical schemes use a quasi-steady assumption, OH and O results for PETERS/PETERS* and SESHADRI/SESHADRI* schemes are qualitatively in agreement with the detailed mechanism.

3.2.2 Comparison between reduced mechanisms on strained flames

The response to strain rate is evaluated for all reduced mechanisms on strained one-dimensional premixed flames (see configuration sketch in Fig. 2.10). A global approximation of the strain rate a_g is based on the injection velocity magnitude of fresh u_f and burnt gases u_b and the distance d between the two jets:

$$a_g = \frac{\left|u^f\right| + \left|u^b\right|}{d}. \tag{3.62}$$

This approximation has no meaning in three-dimensional turbulent flames and the local strain rate calculated from Eq. (2.42) is preferred:

$$a = \frac{\partial v}{\partial y}. \tag{3.63}$$

It is evaluated in the reaction zone estimated at progress variable $c = 0.65$. As the mass flow rate increases the flame is more strained by the velocity field: it is generally thinner and its structure is modified.

Flame thickness

The flame thickness is linked to the gradient magnitude of the progress variable $|\nabla c|$, usually normalized by the laminar flame thickness $\delta_L^{GRI3.0}$. Its value in the reaction zone

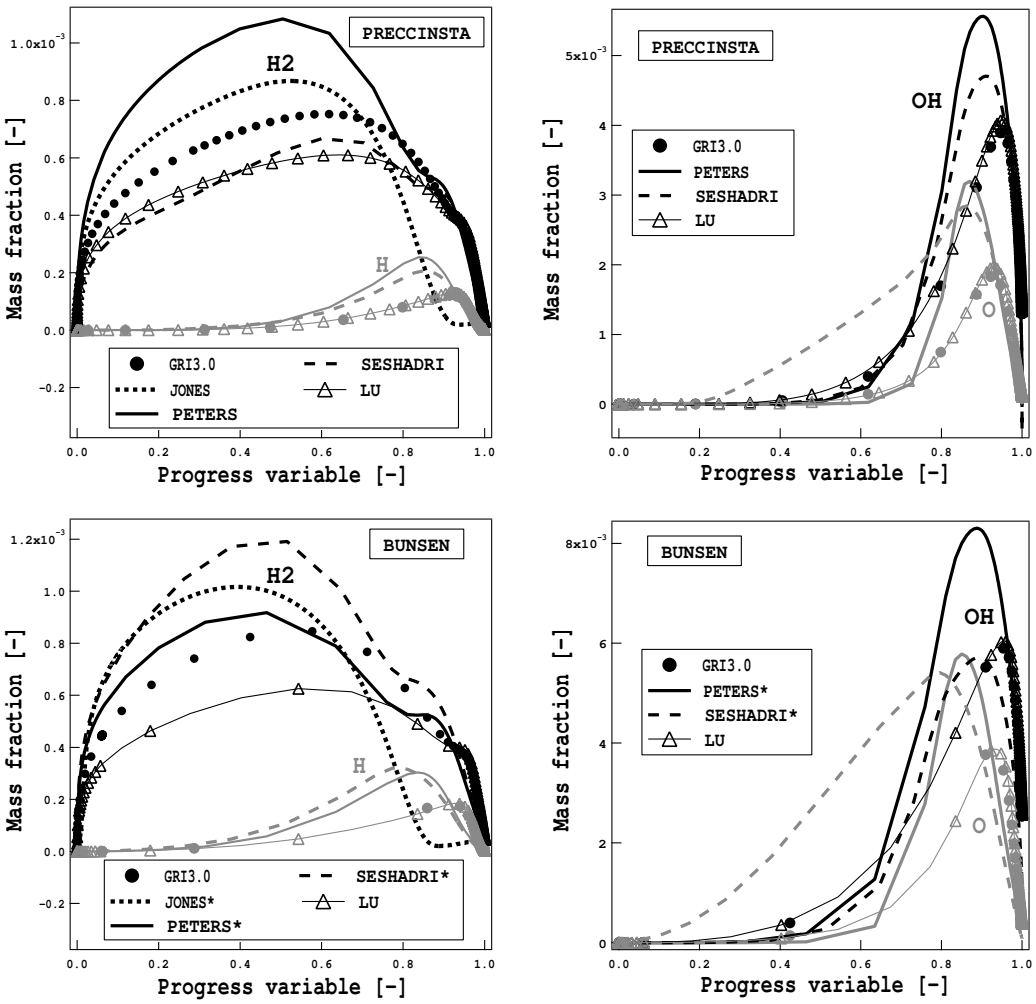

Figure 3.17 - *Radicals profiles for the PRECCINSTA and BUNSEN operating points.*

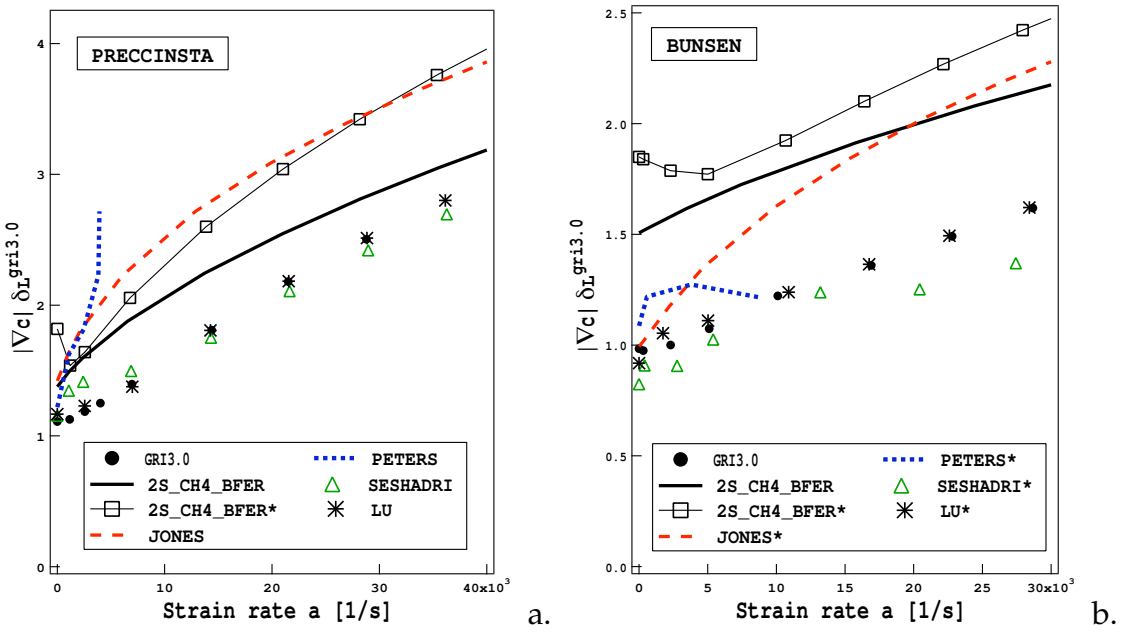

Figure 3.18 - *Gradient magnitude of the progress variable normalized by the laminar flame thickness* $\delta_L^{GRI3.0}$ *versus local strain ratio in the reaction zone* ($c = 0.65$) *for strained methane/air flames at initial temperature (a)* $T_f = 320\ K$ *and (b)* $T_f = 800\ K$. *Comparison between the reduced mechanisms and the GRI3.0 detailed scheme.*

(at $c = 0.65$) is shown in Fig. 3.18 as a function of the local strain rate for all reduced mechanisms at both operating points. First of all, it should be noticed that the flame predicted by the PETERS/PETERS* scheme is quenched for high strain rates and results for these schemes are then presented only for $a < 10.0e^{+3}1/s$. All the reduced schemes, except 2S_CH4_BFER* and PETERS* mechanisms, are able to qualitatively describe that the flame gradient magnitude increases with strain, i.e. the flame is thinner. The behavior of the 2S_CH4_BFER* scheme must be related to the Lewis numbers: since $Le = 1.65$, the diffusion is sowed down and the flame is thickened for low strain rates. Concerning the 2S_CH4_BFER/2S_CH4_BFER* and JONES/JONES* schemes, the error already noted for an unstrained flame is amplified on strained flames: the flame thickness is greatly underestimated for high strain rate values. The analytical SESHADRI and LU schemes are in good agreement with the detailed mechanism.

Local consumption speed

The response of the reduced mechanisms is displayed in Fig. 3.19 for different local strain rate values in terms of consumption speed. The two analyzed operating points show a similar behavior.
On the one hand, the simplest mechanism, 2S_CH4_BFER, is not sufficiently affected

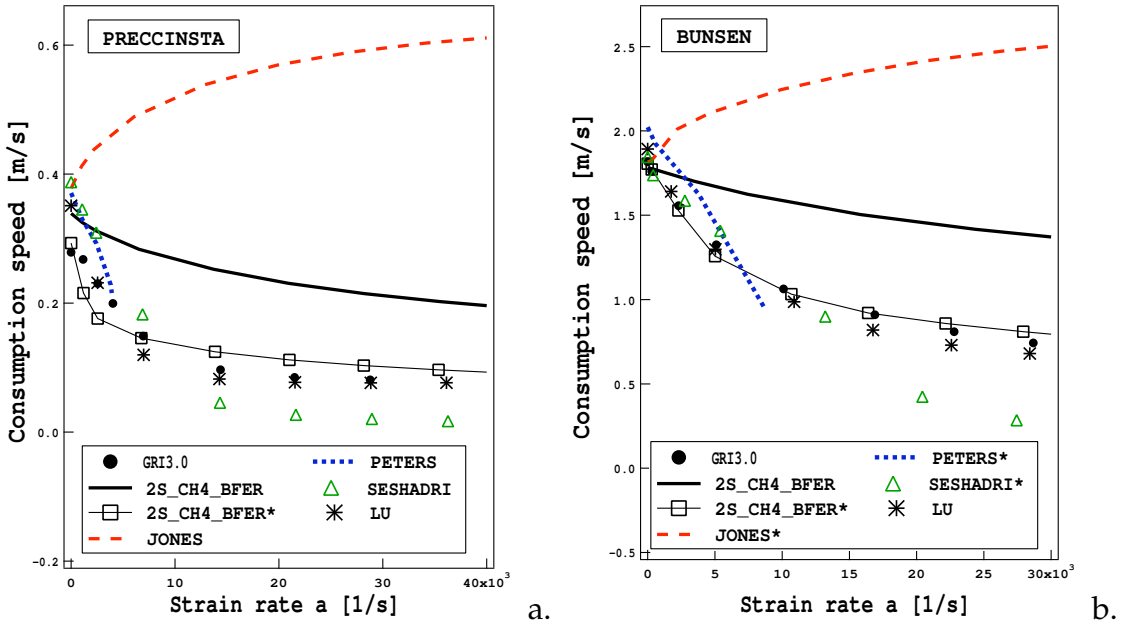

Figure 3.19 - *Consumption speed for a premixed strained methane/air flame as a function of local strain rate at (a) T_f = 320 K and (b) T_f = 800 K. Comparison between the reduced mechanisms and the GRI3.0 detailed scheme.*

by the strain rate and too high values of the consumption speed are found even for really high strain rates. On the other hand, both the JONES/JONES* and the PETERS/PETERS* mechanisms are too much affected by the strain rate. Even worse, the JONES/JONES* mechanism increases the consumption speed with the strain rate while all other schemes decrease it. The response to strain rate in terms of consumption speed is correctly predicted by the SESHADRI/SESHADRI* mechanisms, at least for relatively small strain rate values, and the LU scheme.
The modified two-step 2S_CH4_BFER* mechanism shows a great improvement compared to the 2S_CH4_BFER scheme and is now satisfactory.
This impact of transport properties is expected for all reduced mechanisms: if the response to the strain rate is not affected by the hypothesis of simplified transport properties, it depends on the values chosen for the species Lewis numbers (not shown). However, the complex formulation of the reaction rates in JONES and PETERS made impossible to fit both the strain rate response and the flame speed of the unstrained flame for these schemes by modifying only the Lewis numbers.

Flame structure

The maximum value of the CO mass fraction is studied in Fig. 3.20. It is a good indication of the impact of the strain rate on the flame structure since intermediates

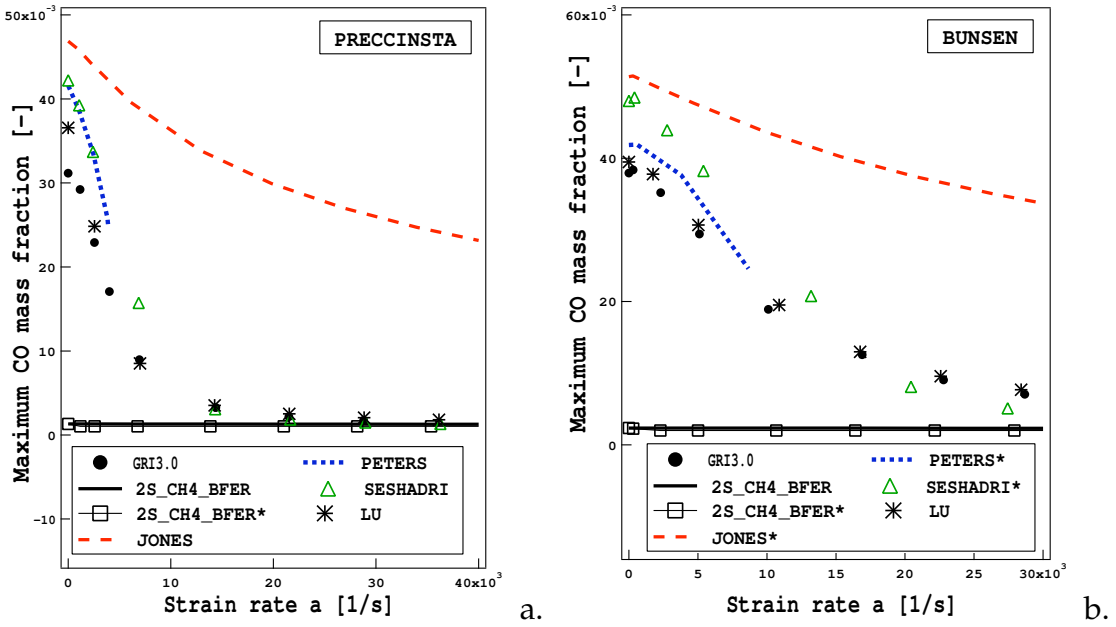

Figure 3.20 - *Maximum value for CO mass fraction for a premixed strained methane/air flame as a function of local strain rate in the reaction zone at (a) T_f = 320 K and (b) T_f = 800 K. Comparison between the reduced mechanisms and the GRI3.0 detailed scheme.*

species and radicals are more affected by strain. The two-step mechanisms being unable to predict the CO concentration in the reaction zone for unstrained flames, the response to strain rate in terms of *CO* mass fraction is completely lost. All other mechanisms show the same tendency, i.e. as the strain rate increases, the *CO* mass fraction in the reaction zone decreases. More specifically, the JONES/JONES* schemes greatly overestimated the CO mass fraction in the reaction zone and this error increases with strain rate. The maximum value of *CO* is however correctly predicted by the PETERS/PETERS* mechanism, at least for low strain rates, and by the SESHADRI/SESHADRI* and the LU schemes for the whole range of strain rates tested.
Figures 3.21 and 3.22 show species profiles versus progress variable for small and high strain rates ($a = 2000s^{-1}$ and $a = 20000s^{-1}$) are displayed in for the two operating points. Confirming results on unstrained flames, the analytical mechanisms by Seshadri and Lu correctly reproduce the flame structure even for high strain values. Note that results for PETERS/PETERS* scheme are shown only for low strain values since the flame is quenched for high strain rate values. The flame structure predicted by the JONES/JONES* scheme is not greatly affected by the strain rate, i.e. the species profiles are slightly modified, as well as the 2S_CH4_BFER/2S_CH4_BFER* mechanism. The LU scheme is able to correctly reproduce the radicals *OH* and *O*, required for the NO_x prediction. Results obtained with the analytical schemes are qualitatively correct at least for low strain rate values.

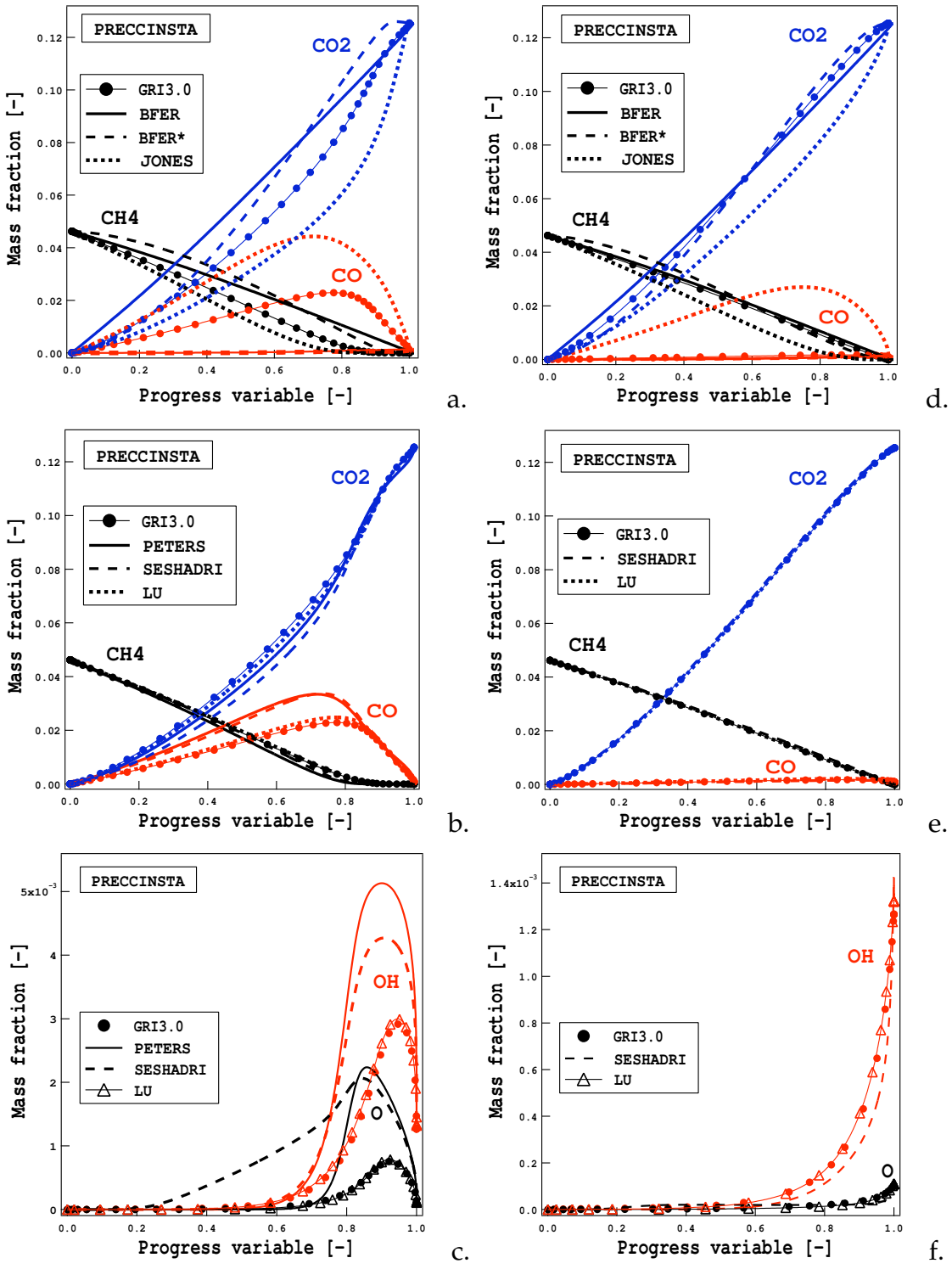

Figure 3.21 - *Species profiles for a premixed strained methane/air flame at* $\phi = 0.83$, $T_f = 320$ *K and* $P = 1$ *atm for (a-c)* $a = 2000s^{-1}$ *and (d-f)* $a = 20000s^{-1}$ *. Comparison between the reduced mechanisms and the GRI3.0 detailed scheme. Profiles of radical species are provided for the analytical mechanisms only.*

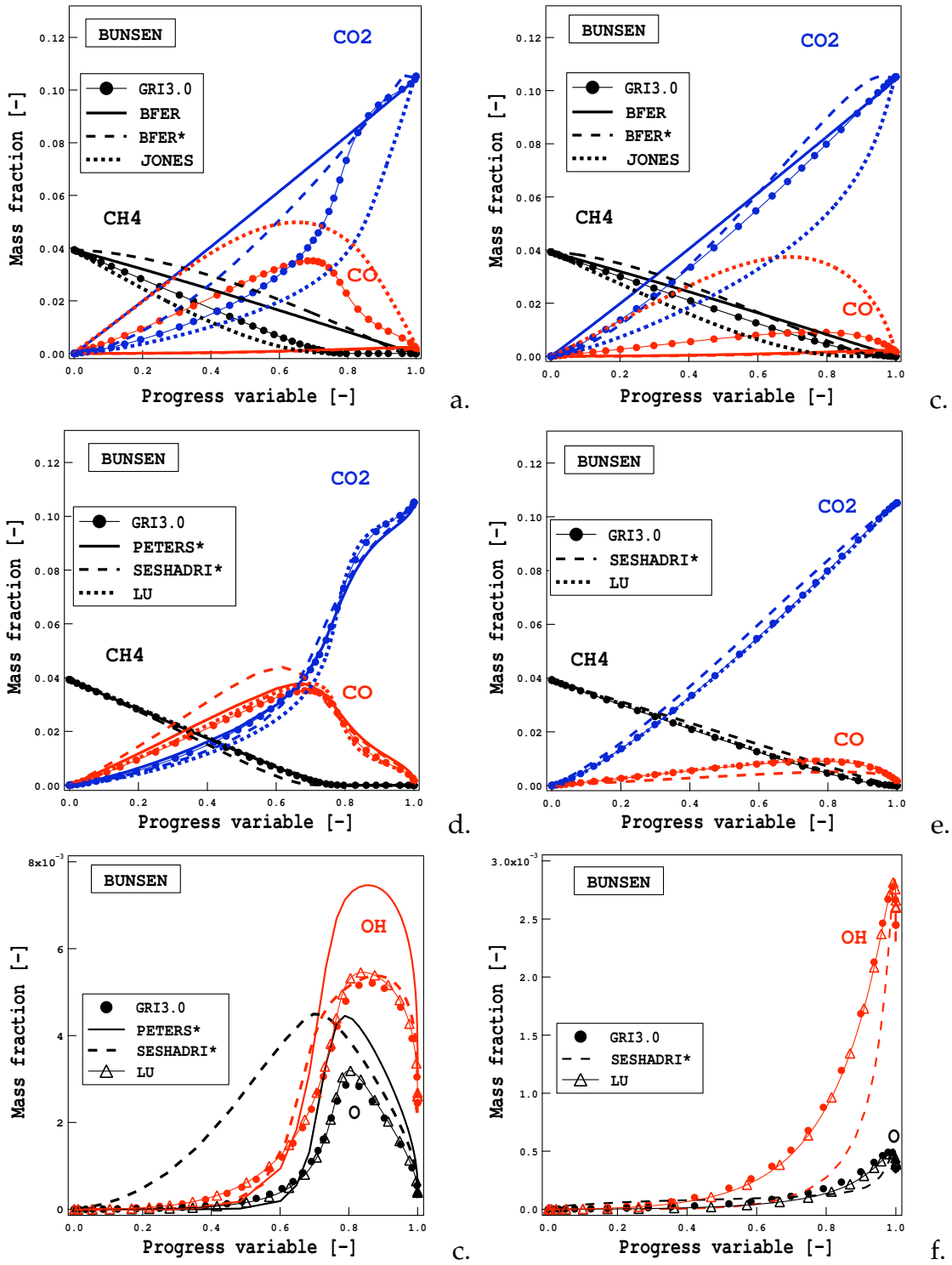

Figure 3.22 - *Species profiles for a premixed strained methane/air flame at* $\phi = 0.7$, $T_f = 800$ *K and* $P = 1$ *atm for (a-c)* $a = 2000s^{-1}$ *and (d-f)* $a = 20000s^{-1}$ *. Comparison between the reduced mechanisms and the GRI3.0 detailed scheme. Profiles of radical species are provided for PETERS*, SESHADRI* and LU mechanisms only.*

3.3 The FPI_TTC tabulation method

Tabulation methods are a recent and promising alternative to reduced mechanisms [11, 120, 152, 86, 19, 129]. A deep validation of this approach is out of the objectives of this work, but it is introduced for completeness of the analysis performed in Chapter 5. The basic idea of such method consists in assuming that the chemical evolutions can be described by a reduced manifold. More specifically in the FPI_TTC [164] method used in this work, the chemical phenomena are parameterized by:

- the **mixture fraction** z^{fpi}: a conserved passive scalar transported by convection and diffusion. The N_2 concentration is a good candidate to build such a variable flame whenever unity Lewis number is assumed for all species. The mixture fraction then yields:

$$z^{fpi} = \frac{Y_{N_2} - Y^F_{N_2}}{Y^O_{N_2} - Y^F_{N_2}}, \tag{3.64}$$

  where $Y^F_{N_2}$ and $Y^O_{N_2}$ are the N_2 mass fractions in fuel and air streams feeding the burners respectively.

- the **normalized progress variable** c^{fpi}: it is based on the progress variable Y_c^{fpi} classically defined for methane-air combustion as [59]:

$$Y_c^{fpi} = Y_{CO} + Y_{CO_2} \tag{3.65}$$

  and is normalized by the value at equilibrium $Y_c^{eq}(z)$:

$$c^{fpi} = \frac{Y_c^{fpi}}{Y_c^{eq}(z)}. \tag{3.66}$$

  In this work, since the CO species in not correctly predicted by all reduced mechanisms, the progress variable on the O_2 mass fraction (Eq. (3.59) is preferred in the post-processing analysis for all chemical descriptions, whereas the progress variable c^{fpi} defined in Eq. (3.66) is used for building the look-up table.

These two variables z^{fpi} and Y_c^{fpi} are solved in the system instead of the species mass fractions reducing the computational cost. The flame structure is recovered from a look-up table, built from results of unstrained laminar flames. For each value of the mixture fraction z^{fpi}, the equilibrium value $Y_c^{eq}(z^{fpi})$ is recorded together with the following information tabulated as function of the progress variable c^{fpi}:

- **Source term**: $\dot{\omega}_{Y_c}(c^{fpi}, z^{fpi})$ of the progress variable.

- **Thermodynamic properties**: the mixture molar mass $W^{tab}(c^{fpi}, z^{fpi})$, the heat capacity at constant pressure $C_p^{tab}(c^{fpi}, z^{fpi})$ and the heat capacity at constant volume $C_v^{tab}(c^{fpi}, z^{fpi})$.

- **Transport properties**: the detailed dynamic viscosity $\mu^{tab}(c^{fpi}, z^{tfpi})$ and the thermal conductivity $\lambda^{tab}(c^{fpi}, z^{fpi})$. As done in [163], unity Lewis numbers are assumed for all species.

- **Temperature**: the temperature $T^{tab}(c^{fpi}, z^{fpi})$ and the total energy $e^{tab}(c^{fpi}, z^{fpi})$ are tabulated to approximate the temperature as:

$$T = T^{tab}(c^{fpi}, z^{fpi}) + \frac{e - e^{tab}(c^{fpi}, z^{fpi})}{C_v^{tab}(c^{fpi}, z^{fpi})}, \tag{3.67}$$

  where e is the computational total energy.

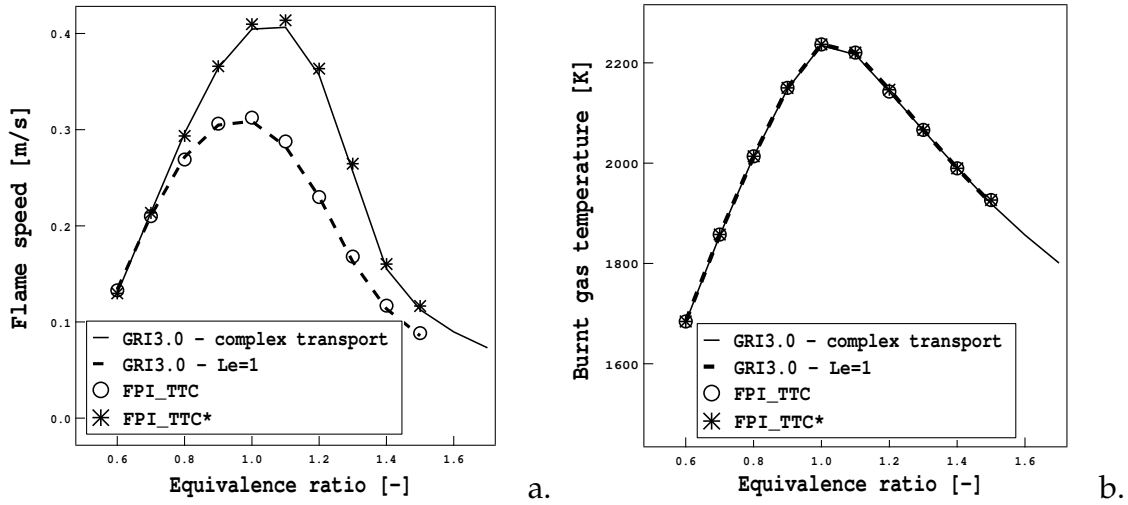

Figure 3.23 - *a) Flame speed and b) burnt gas temperature as a function of the equivalence ratio for an unstrained laminar premixed flame at atmospheric pressure and ambient temperature (T_f = 320 K). Comparison between the GRI3.0 mechanism using detailed transport properties (solid line), the GRI3.0 mechanism with unity Lewis number (dashed line), the FPI_TTC method (circle) and the FPI_TTC* method (star).*

The tabulation method may be generalized parametrizing the problem on additional parameters [163, 10].

The quality of the results depends on the table resolution for the mixture fraction and the progress variable. In this thesis, the FPI_TTC method has been evaluated on laminar unstrained premixed flames for the PRECCINSTA operating point (T_f = 320 K and P = 1 atm) using a 2000 × 1000 points table for the mixture fraction and the progress variable respectively. The table has been built from solutions obtained with

the detailed GRI3.0 mechanism using CANTERA and imposing $Le_k = 1$ for all species ($Sc_k = Pr = 0.7$).
Since the look-up table is based on unstrained flames, the FPI_TTC method correctly reproduces the flame speed and burnt gas temperature predicted by the detailed GRI3.0 mechanism with unity Lewis numbers (Fig. 3.23). Results are also compared to the GRI3.0 scheme with complex transport properties. As shown in Section 2.2, the simplification of the transport properties impacts the flame speed but does not change the burnt gas temperature, which only depends on the thermodynamic properties of the mixture. The tabulation method is affected by the assumption of the unity Lewis number underestimating the flame speed of about 25% for a near-stoichiometric flame. In order to correct this natural overestimation of the flame speed, both the tabulated term source of the progress variable $\dot{\omega}_{Y_c}^{fpi}$ and the tabulated thermal diffusivity λ^{fpi} have been multiplied by an artificial correction function (Fig. 3.23a. The correction function is given by the ratio between the flame speed values for the detailed mechanism using detailed transport properties and values obtained using simplified transport properties. Thus, it varies with the equivalence ratio (Fig. 3.24). Correcting the thermal diffusivity, the Prandt number is modified whereas the Schmidt numbers are equal to 0.7 for all species. In the following, the tabulation method using the corrected table is called FPI_TTC*.

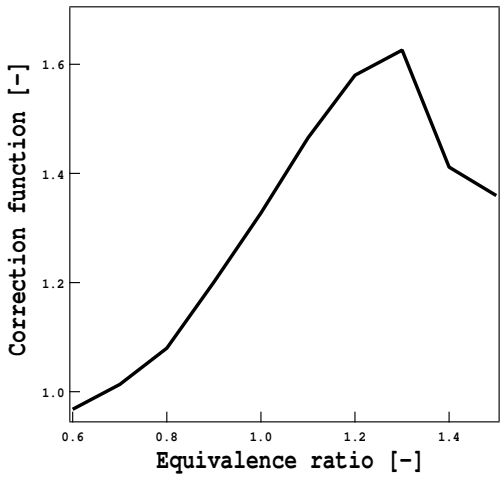

Figure 3.24 - *Correction function for the FPI_TTC* method.*

Figure 3.25 compares the profiles of CH_4, CO and CO_2 species obtained with the FPI_TTC* method and the detailed GRI3.0 scheme as a function of the spatial variable (Fig. 3.25a.) and the progress variable c (Fig. 3.25b.). The tabulation method perfectly recovers the flame structure of the detailed mechanism with equal Schmidt number, which is slightly different from results when using complex transport properties. Even if a method to take into account detailed transport properties has been proposed [9], in the following the equal Schmidt numbers are assumed for all species when using the

FPI_TTC* method. The FPI_TTC* method has been implemented in AVBP in 2011 by P. Auzillon [9].

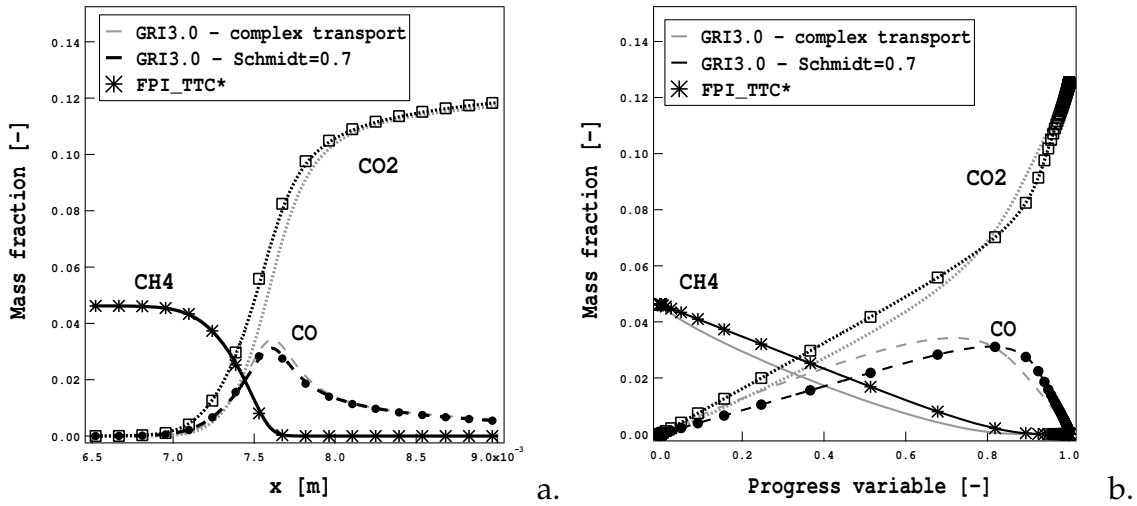

Figure 3.25 - *Species mass fractions as a function of a) spatial abscissa and b) progress variable for an unstrained laminar flame at the PRECCINSTA operating point ($P = 1$ atm, $\phi = 0.83$ and $T_f = 320$ K). Comparison between the GRI3.0 mechanism using detailed transport properties (grey lines), GRI3.0 scheme with $Sc_k = 0.7$ number (black lines) and the FPI_TTC* method (symbols).*

3.4 Towards turbulent combustion: generalization of the thickened flame method

In the context of Large Eddy Simulation, the thickness δ_L of a premixed flame is generally smaller than the mesh size Δx used for LES and a model is required. Among a variety of models, the Thickened Flame (TFLES) model has been developed so as to resolve the flame fronts on a LES mesh. The laminar flame thickness δ_L is thickened by a factor $\mathcal{F}$, modifying the interaction of the flame with turbulence, as small vortices can not anymore wrinkle the flame front. As the flame surface is reduced, the flame consumption is underestimated. In order to correct this effect, an efficiency function $\mathcal{E}$ has been developed from DNS results and implemented in AVBP [46] allowing to recover a correct turbulent flame burning.

Applying a uniform thickening in the whole domain accelerates diffusion in non reactive zones, where the thickening is not necessary. A dynamically thickening procedure depending on the flame position and the local resolution is therefore preferred (DTFLES method). A local thickening is controlled by a sensor $\mathcal{S}$ based on reaction

rates, and its maximum value depends on the local resolution:

$$\mathcal{F} = \mathcal{F}_{max} S = -n \frac{\delta_L}{\Delta x} S, \tag{3.68}$$

where n is the number of grid points in the flame front. Typically, $n = 5$ guarantees a good behavior.

The sensor S for the thickening model is defined as:

$$S = \tanh\left(\beta' \frac{\Omega}{\Omega_0}\right), \tag{3.69}$$

where β' is a constant equal to 50, Ω is a sensor function detecting the presence of a reaction front and Ω_0 corresponds to its maximum value. For an irreversible one-step reaction chemistry, the sensor function depends on both the local temperature and the reactant mass fractions:

$$\Omega = Y_F^{n_F} Y_O^{n_O} \exp\left(-\Gamma \frac{E_a}{RT}\right). \tag{3.70}$$

The coefficient Γ is used to extend Ω beyond the reaction zone ($\Gamma < 1$).
A generalization for partially premixed combustion is necessary when working with reduced multi-step chemistries.

Sensor for reversible reactions

The sensor must be generalized to reversible reactions. At the equilibrium state, the progress rate is equal to zero, leading to:

$$1 - \frac{1}{K_{eq}} \frac{\Pi_{k=1}^{N} [X_k]^{n_k''}}{\Pi_{k=1}^{N} [X_k]^{n_k'}} = 0. \tag{3.71}$$

A second term is then added to the sensor for a reversible reaction which accounts for the backward reaction and guarantees a sensor equal to zero in the equilibrium state, considered as a non reactive zone:

$$\Omega = \Pi_{k=1}^{N} Y_k^{n_k'} \exp\left(-\Gamma \frac{E_a}{RT}\right) \left[1 - \frac{1}{K_{eq}} \frac{\Pi_{k=1}^{N} [X_k]^{n_k''}}{\Pi_{k=1}^{N} [X_k]^{n_k'}}\right]. \tag{3.72}$$

Working with this sensor is not straightforward when using a multi-step chemical scheme since the reaction used to evaluate the sensor function Ω must be selected. Generally, both the reaction and the post-flame zones have to be thickened but each region is characterized by different reactions and scales, and using a specifically single reaction is not sufficient. The only exception is the 2S_CH4_BFER scheme, designed so that both fuel oxidation and $CO - CO_2$ recombination take place in the same region, and a sensor based on the recombination reaction is sufficient. However, for all other reduced mechanisms a new sensor function is required.

Sensor for multi-step chemistries

The sensor for multi-step chemistry is based on the consumption/production rate $\dot{\omega}_k$ for species k:

$$\mathcal{S}^{multi} = \min\left(\frac{|\dot{\omega}_k|}{|\dot{\omega}_k^0|}, 1\right), \tag{3.73}$$

where $\dot{\omega}_k^0$ corresponds to the maximum value of the species consumption/production rate in a premixed laminar flame. To capture the preheat zone the sensor is widen combining clipping:

$$\text{if} \quad \mathcal{S}^{multi} > 0.1 : \quad \mathcal{S}^{multi} = 1 \tag{3.74}$$

with five consecutive filtering operations (Fig. 3.26). This procedure is repeated two times to obtain a smooth filter correctly located in the high gradient zones generated by reactions.

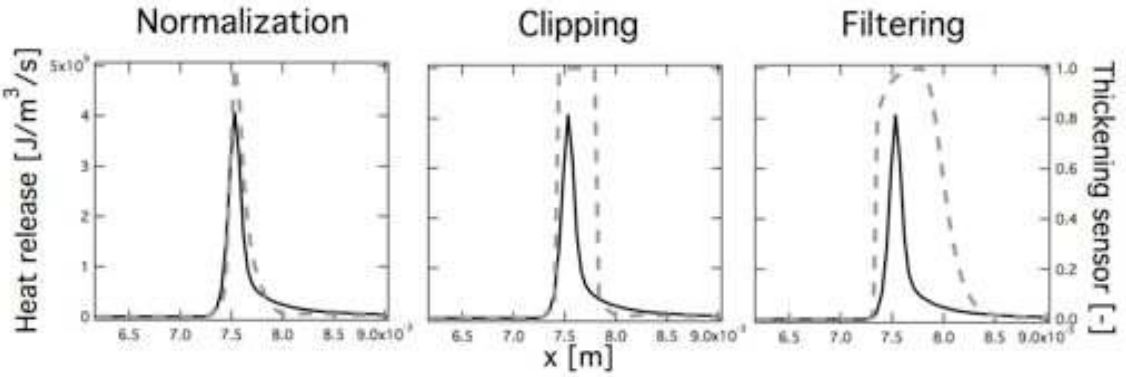

Figure 3.26 - *Sketch of the construction of the sensor S^{multi} for multi-step chemistries. The heat release and the thickening sensor are displayed in black and grey respectively.*

As example, the classical sensor S has been applied to reaction R1 (Eq. (3.17)) of the PETERS mechanism, whereas the new sensor S^{multi} has been built on $\dot{\omega}_{CO}$ for a premixed flame at the PRECCINSTA operating point. Both sensors are displayed in Fig. 3.27 together with the heat release. Considering the species reaction rate for CO both the reaction zone, where CO is created, and the post-flame zone, where CO recombines into CO_2, are taken into account and thickened when using the S^{multi} sensor whereas the sensor S does not thicken the recombination zone leading to numerical difficulties.

This sensor function can also be used with the FPI tabulation working with the term source for the progress variable $\dot{\omega}_{Y_c}$ and, in Chapter 5, is applied to all reduced mechanisms.

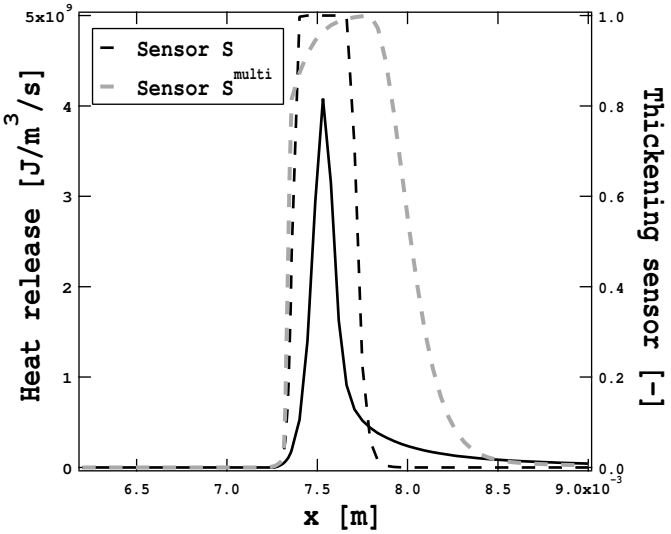

Figure 3.27 - *Comparison between the sensor S (black dashed line) applied to reaction R1 (Eq. (**??**) and the sensor S^{multi} (grey dashed line) applied to $\dot{\omega}_{CO}$ for the PETERS mechanism. The heat release is also plotted (solid black line).*

Sensor for partially premixed combustion

Finally the sensor was adapted to partially premixed combustion. In the Dynamically Thickened Flame method, parameters such as $\delta_L(\phi)$, $\Omega_0(\phi)$ or $\dot{\omega}_k^0(\phi)$ have been preliminary calculated for a laminar premixed flame on a wide range of equivalence ratio ϕ for the operating point of interest and are recorded in a database. At each point of the computational domain, a local equivalence ratio (based on the number of carbon atoms) is evaluated and the local values of $\delta_L(\phi)$, $\Omega_0(\phi)$ and $\dot{\omega}_k^0(\phi)$ are extracted from the database. The same method is used to evaluate the laminar flame speed $S_L^0(\phi)$ for the efficiency function. In this way, the thickening is optimized on the whole range of the equivalence ratio and the correction of the efficiency function is correctly estimated.

3.5 Conclusions

In this chapter, six reduced mechanisms for methane/air premixed combustion have been presented and their performances have been compared to results of the detailed GRI3.0 scheme on laminar unstrained flames in terms of flame speed, burnt gas temperature, flame thickness, flame structure and predictions of *CO* and radical species. A modified version of these mechanisms has been proposed when necessary to correctly predict the flame speed and burnt gas temperature for the two operating points corresponding to the DNS and LES calculations proposed in Chapters 4 and 5. The

response of the reduced mechanisms to strain rate has also been evaluated looking at consumption speed, flame structure, flame thickness and *CO* mass fraction in the reaction zone for unstrained premixed flames. Moreover, the implementation of simplified transport properties in CFD tools and their impact on results have been discussed. The different features of the reduced mechanisms from a numerical point of view, i.e. computational cost, implementation and robustness, have also been treated. To complete the comparison between different chemical descriptions, the FPI_TTC tabulation method has been presented and evaluated on premixed unstrained flames. Finally, the coupling with turbulent combustion modeling has been addressed as a generalization of the artificially thickened flame method to multi-reaction chemistries and partially premixed combustion.

Conclusions are expected to be valid for most hydrocarbons mechanisms:

- **Two-step fitted mechanisms** such as the 2S_CH4_BFER correctly predict the flame speed and the burnt gas state for unstrained laminar flames on a wide range of pressure, initial temperature and equivalence ratio. The flame structure is not captured since equilibrium is reached too quickly and, for the same reason, the *CO* mass fraction is strongly underestimated in the reaction zone as well as the flame thickness. These mechanisms could be easily implemented and used in a CFD tool and they are the least expensive reduced schemes. Moreover they could be easily modified to better predict the consumption speed of strained flames (2S_CH4_BFER*) but results for the flame structure of strained flames are not accurate.

- **Four-step fitted mechanisms** (JONES/JONES*) better work on unstrained flames, but their response to strain rate is in contrast with GRI3.0 results. The consumption speed wrongly increases with strain rate and the *CO* mass fraction may be largely overestimated for high strain rate values. The use of this kind of mechanisms requires a particular attention due to the presence of negative reaction orders in their reaction rates.

- **Eight-species mechanisms** (PETERS/PETERS* and SESHADRI/SESHA- DRI*) correctly describe unstrained and strained flames, at least for small values of strain rate. Result accuracy depends on the number of species and reactions taken into account in the reference skeletal scheme. The implementation of this mechanism in a CFD code is not straightforward but it is quite robust.

- **Analytical thirteen-species scheme** (LU) quasi-perfectly reproduces the quantities of interest for unstrained and strained flames. The agreement with the detailed GRI3.0 mechanism is really satisfactory. In the following, the LU mechanism is chosen as the reference mechanism correctly reproducing the main combustion phenomena.

- **Tabulation method** (FPI_TTC/FPI_TTC*) has been validated on laminar unstrained flames. As expected, the agreement with the GRI3.0 results is excellent, but no validation of this method on strained flames has been performed.

The quality of the different chemical descriptions has been analyzed in detail for laminar mono-dimensional test cases, but their performances in describing three-dimensional turbulent flames need to be evaluated. This is the objective of the third part of this manuscript.

Part III

Validation and impact of chemistry modeling in unsteady turbulent combustion simulations

Chapter 4

Impact of reduced chemistry on turbulent combustion: Direct Numerical Simulation of a perfectly premixed methane/air flame

DNS is a powerful tool to study the interaction of combustion with turbulence but due to its high computational cost it is classically confined to small academic configurations. Only recently DNS of a real premixed methane/air Bunsen flame has been performed [137], allowing to detailed study of the turbulence impact on chemistry.
Using reduced chemical mechanisms in DNS may be considered in order to drastically decrease the computational cost and to apply DNS to more complex flows, provided that the accuracy of results is preserved.
The objective of this chapter is to analyze DNS of perfectly premixed methane/air flames using the reduced mechanisms of Chapter 3 in order to identify their impact and to propose a satisfactory compromise between computational cost and result accuracy. Three different configurations are presented in this chapter, two simple academic configurations and a complex real Bunsen flame. In a first step, the flame/vortex configuration (Section 4.1) allows to study the complex interaction between a flow field and the flame. Viewing turbulence as a collection of vortices of different time and length scales, the results from the flame/vortex simulation (characterized by a single flow scale) may be directly related to the 3D turbulent flame simulation. A three-dimensional flame interacting with a homogeneous isotropic turbulent (HIT) field is then studied in Section 4.2. Finally from the conclusions on laminar and academic configurations, the best performing mechanisms are identified and used in Section 4.3 for the DNS of the Sankaran Bunsen flame [137] allowing a comparison between mechanism performances when simulating a complex perfectly premixed flame.

In all configurations, the performances of the reduced mechanisms are evaluated in terms of flame length, consumption speed, flame thickness and flame structure. Results are compared to the LU mechanism which has been chosen as reference: since it correctly reproduces the behavior of laminar unstrained and strained flames obtained with the detailed GRI3.0 mechanism while remaining computationally affordable.
The behavior of the FPI_TTC* method is not studied in this chapter.

4.1 Flame/vortex interaction

Studying the flame response to isolated deterministic vortices is a classical preliminary approach to understand the interaction between the turbulence and the flame front [124, 104, 35]. The objective of this section is to analyze the flame front response to an aerodynamic perturbation and to study the impact of the different chemical mechanisms presented in Chapter 3.

4.1.1 Numerical configuration

A two-dimensional simulation of the interaction between a methane/air flame and a pair of vortices has been performed using the different schemes of Chapter 3. The operating point corresponds to the BUNSEN conditions specified in Chapter 3: initial temperature $T_f = 800\ K$, equivalence ratio $\phi = 0.7$ and atmospheric pressure.
Each chemical scheme predicts a different flame structure. In order to guarantee the same initial position of the flame for all calculations, the field has been initialized with a laminar unstrained flame solution in such a way that the iso-contour of temperature $T = 1000\ K$ is located at $x = 1.2e^{-3}\ m$ for all mechanisms (Fig. 4.1).

A pair of Oseen vortices [104] is then superimposed to the field. Their characteristics, summarized in Table 4.1, have been chosen as follows:

- diameter $D = 2 \times \delta_L^{GRI3.0} \approx 6.86e^{-4}\ m$, where $\delta_L^{GRI3.0}$ is the flame thickness at $\phi = 0.7$ obtained for a laminar unstrained flame with the detailed GRI3.0 scheme;
- vortex strength $\Psi = 6.71e^{-2}$ which corresponds to a maximum velocity induced by the vortex pair $u' = 11 \times S_L^{GRI3.0} \approx 19.69\ m/s$, where $S_L^{GRI3.0}$ is the laminar flame speed at $\phi = 0.7$ obtained with the detailed GRI3.0 scheme;
- total length r, which characterizes the size of the perturbation, equal to $r \approx 6 \times \delta_L^{GRI3.0} \approx 2.058e^{-3}\ m$;

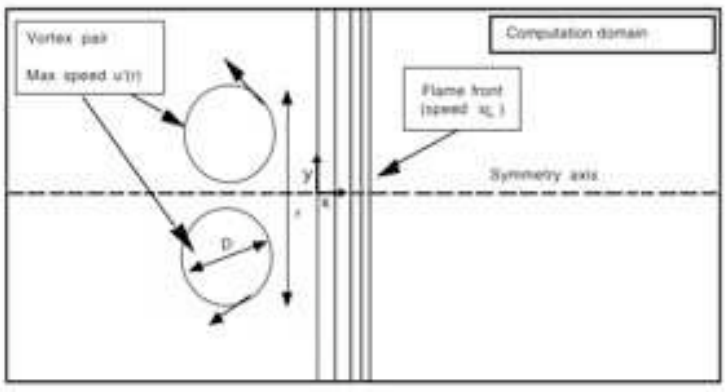

Figure 4.1 - *Classical configuration for DNS of a flame/vortex interaction.*

- initial position for the vortex center sufficiently far from the flame front: $x_0 = -1.66e^{-3}\ m$ and $y_0 = 6.85^{-4}\ m$.

Such characteristics place the flow/flame interaction in the corrugated flamelet regime (Fig. 1.4): the vortices are bigger than the flame thickness and, as a consequence, they could not penetrate into the flame ($Ka < 1$). Since $u' > S_L$, the flame surface is curved and stretched by the vortex passage forming pockets of size r.

Table 4.1 - *Oseen vortex characteristics.*

Diameter D	Strength Ψ	Maximum velocity u'	Length scale r	Initial position (x_0, y_0)
$2 \times \delta_L^{GRI3.0}$	-	$11 \times S_L^{GRI3.0}$	$6 \times \delta_L^{GRI3.0}$	-
$6.86e^{-4}\ m$	$6.71e^{-2}$	$19.69\ m/s$	$2.058e^{-3}\ m$	$(-1.66e^{-3}\ m, 6.85^{-4}\ m)$

Since the configuration is totally symmetric on axis $y = 0\ mm$, only the upper half-side of the configuration is simulated and a symmetric boundary condition is imposed at the symmetry axis. Navier-Stokes Characteristic Boundary Conditions (NSCBC) [123] are used to impose the inflow/outflow conditions. On the left side, a fresh gas mixture of methane/air at $\phi = 0.7$ and initial temperature $T_f = 800\ K$ is injected with a velocity equal to the laminar flame speed. The burnt gases are located on the right side, where an imposed pressure outlet boundary condition is applied [72]. The computational domain is large enough to suppose that results are not affected by boundaries (Table 4.2). It is meshed with about 500,000 triangular cells with a refined zone where vortex and flame are located and where the characteristic cell size $\Delta x \approx \delta_L^{GRI3.0}/11 \approx 3.0e^{-5}\ m$ guarantees at least eight points in the thinnest initial flame

front (δ_L^{bfer*}) and five points in the thinnest laminar strained flame front.

The Finite-Element type low-dissipation Taylor-Galerkin discretization [113, 45, 47] is used in AVBP for the numerical integration. The simulated physical time is 0.9 *ms* and an instantaneous solution is recorded each 10μs. In the following, the flame front is identified by the iso-contour of the progress variable $c = 0.65$ based on the O_2 species[1].

Table 4.2 - *Computational domain characteristics.*

x_{min}	x_{max}	y_{min}	y_{max}	cell numbers
-0.02 m	0.015 m	0.0 m	0.015 m	500,000

4.1.2 Stretch rate

An example of results is plotted in Fig. 4.2 where temperature isocontours obtained with the 2S_CH4_BFER mechanism are shown at six increasing different times ($t = 0.3, 0.4, 0.5, 0.6, 0.7$ *ms*). The flame is stretched and curved by the vortex pair which induces the formation of a fresh gas pocket downstream of the flame at $t > 0.6$ *ms*. As already discussed in Section2.3, the total flame stretch k may be decomposed into a

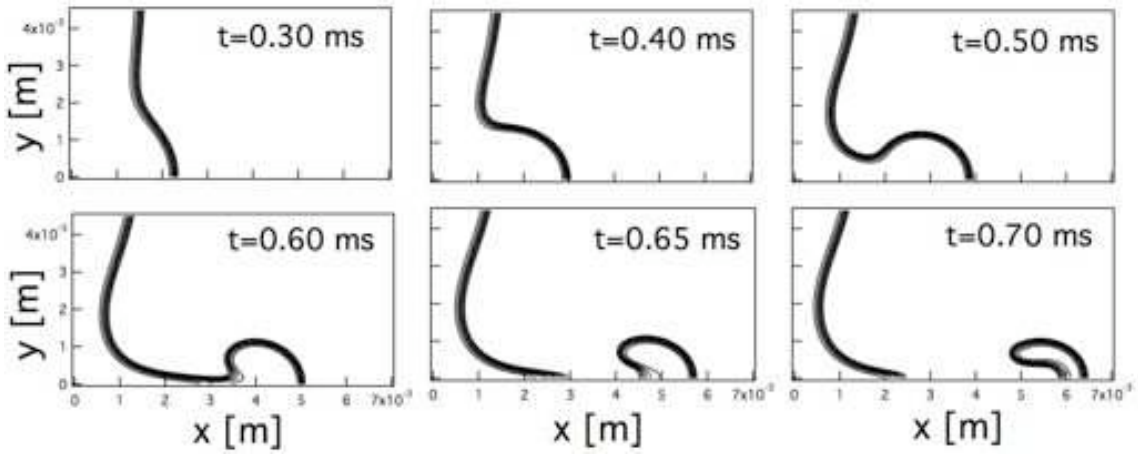

Figure 4.2 - *Time series of temperature isoclines for the flame/vortex interaction obtained with the 2S_CH4_BFER mechanism. Contour lines are plotted every* 200 *K from* 1000 *K to* 2000 *K.*

[1]Results slightly vary when modifying the value of c used to detect the flame front. However, qualitative conclusions on the behavior of the different mechanisms are expected not to depend on the chosen value of c once it belongs to the inner reaction zone ($0.4 < c < 0.85$).

strain rate term (related to the non-uniformity of the flow) and a term which takes into account the flame front curvature:

$$k = \underbrace{\left(\delta_{ij} - n_i n_j\right)\frac{\partial u_i}{\partial x_j}}_{\textit{strain rate}} + \underbrace{S_d \frac{\partial n_i}{\partial x_i}}_{\textit{curvature}} = a + S_d \nabla \cdot n, \tag{4.1}$$

where S_d is the front displacement speed and $\mathbf{n}$ is the unity vector normal to the flame surface pointing towards the fresh gases:

$$\mathbf{n} = -\frac{\nabla c}{|\nabla c|}. \tag{4.2}$$

As usual, the flame surface is identified by an iso-line of the normalized progress variable $c = 0.65$ based on the mass fraction of O_2 species. The displacement speed S_d of the flame surface is calculated from the density-weighted displacement speed $S_d^\star$[81]:

$$S_d^\star = \frac{\rho S_d}{\rho_f} = -\left[\frac{\dot{\omega}_c}{\rho_f |\nabla Y_c|} + \frac{\frac{\partial}{\partial x_j}\left(\rho D_c \frac{\partial Y_c}{\partial x_j}\right)}{\rho_f |\nabla Y_c|}\right], \tag{4.3}$$

where $D_c = D_{O_2}$ represents the local mass diffusivity of the progress variable c and ρ_f is the fresh gas density.

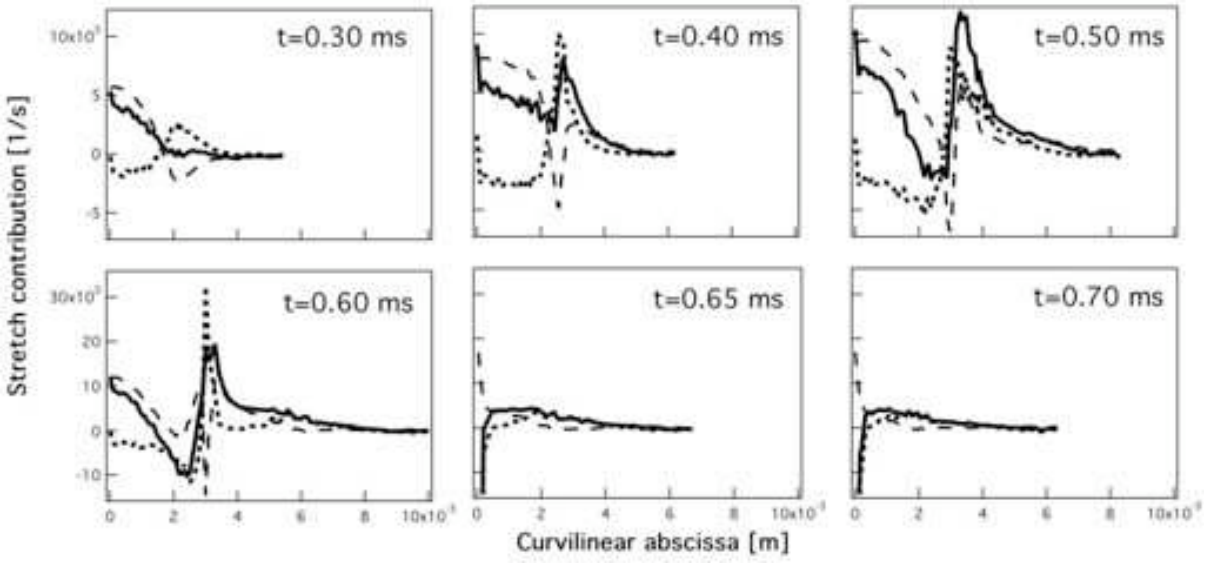

Figure 4.3 - *Contribution of the tangential strain (– – –) and the curvature (·····) to the total stretch (——) along the c = 0.65 isoline at six different times.*

The tangential strain rate, the curvature and the total stretch along the isoline $c = 0.65$ are represented in Fig. 4.3 as a function of the curvilinear abscissa along the flame (starting at the symmetric axis) for six increasing times. At $t = 0.3$ ms and small abscissa, i.e. near the symmetry axis, the curvature effect is small and negative (since the flame has a concave curvature). In this region the stretch is mainly due to the positive strain rate term. For higher abscissa, the flame has a convex curvature, making the curvature contribution positive. Advancing in time, the flame is more and more strained and curved. As a consequence, curvature and strain rate increase drastically. However, curvature on the symmetry axis is close to zero, except after the pocket detachment. At this point the effect of strain only may be studied. Note that the flame inner structure and flamelet regime are always preserved. At $t = 0.6$ ms, the stretch reaches its highest value at $x \approx 3.5$ mm and $y = 0.27$ mm leading to local extinction. The flame front is broken and a fresh gas pocket is formed. The flame front is subsequently highly deformed at the symmetry axis and the curvature contribution is very high (not visible on the graphs), whereas the tangential strain stays low. The pocket of fresh gases is rapidly convected downstream and extinguished by lack of fresh gases.

4.1.3 Comparison of the different reduced mechanisms

Temporal evolution

As already said, the flame curvature is close to zero near the symmetric axis and, as a consequence, the only effect of strain rate could be studied. The temporal evolution of the strain rate a, consumption speed S_C (from Eq. (2.29)) and normalized gradient of the progress variable $|\nabla c|\delta_L^{GRI3.0}$ along the symmetry axis is displayed in Fig. 4.4. On the one side, the strain rate detected at the flame front ($c = 0.65$) is the same for all mechanisms indicating that the same flow perturbation is imposed to all reduced mechanisms (Fig. 4.4a.). On the other side, the flame response to this perturbation, i.e. the consumption speed, depends on the used chemical scheme (Fig. 4.4b.). Results are in agreement with the laminar behavior (Section 3.2.2): the 2S_CH4_BFER is almost insensitive to strain rate, whereas the response of the JONES* scheme is qualitatively incorrect as the consumption speed increases with strain rate. The PETERS* and SESHANDRI* mechanisms and the 2S_CH4_BFER* scheme are generally too affected by strain rate compared to the reference LU mechanism.
The flame front is slightly thinned by the strain rate (Fig. 4.4c.) at the flame front ($c = 0.65$) except when using the 2S_CH4_BFER* scheme. Discrepancies on the normalized gradient of the progress variable are mainly due to the different laminar flame thickness for unstrained flames predicted by the chemical schemes (Section 3.2.1). Moreover, the time evolution of the reduced flame length $\Lambda^\star = \Lambda/\Lambda_0$ is reproduced in Fig. 4.5 for the different reduced mechanisms. The reduced flame length $\Lambda^\star$ is the length of the flame front Λ , i.e. of the $c = 0.65$ contour, normalized by its value at the initial time

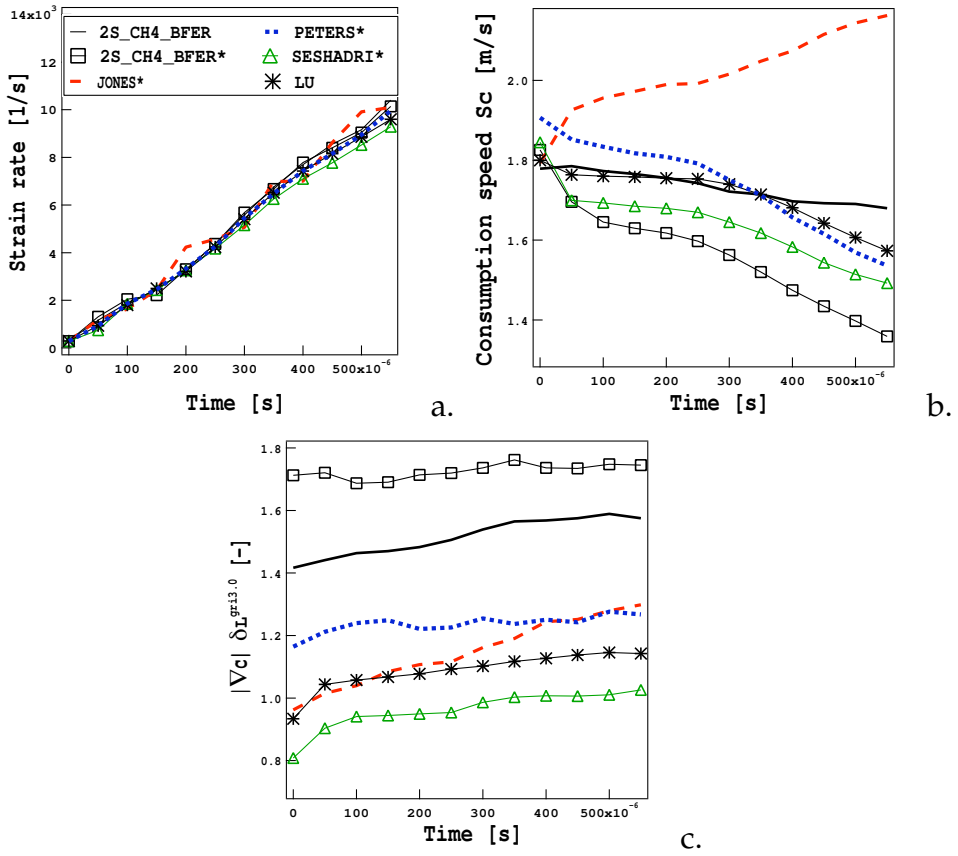

Figure 4.4 - *Temporal evolution of (a.) strain rate for the flame front ($c = 0.65$), (b.) consumption speed and (c.) normalized gradient of the progress variable for the flame front ($c = 0.65$) at the symmetry axis ($x = 0$ mm) for the different mechanisms.*

Λ_0. It increases with time since the flame is curved and deformed by the vortices. No relevant discrepancies are detected between the different mechanisms for this quantity indicating that the vortices modify the flame front in the same way for all chemical schemes. This is expected as the flame wrinkling is the result of the ratio u'/S_L and r/δ_L, which are similar for all schemes.

Flame thickness

Discrepancies are detected in terms of thermal thickness as shown by iso-lines of temperature for all mechanisms at $t = 0.5$ *ms* in Fig. 4.6. As already observed on laminar flames, the two-step schemes highly reduce the post-flame region characterized by the highest temperatures compared to the LU mechanism. The inner reaction zone identified by the highest gradient of temperature is similar for all reduced schemes, although some discrepancies appear at the highest flame curvature.

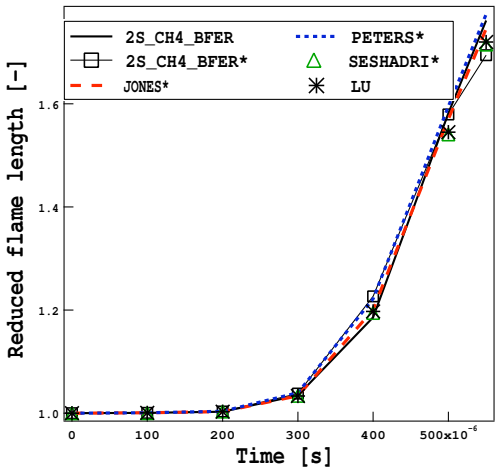

Figure 4.5 - *Time evolution of reduced flame length* $\Lambda^\star$.

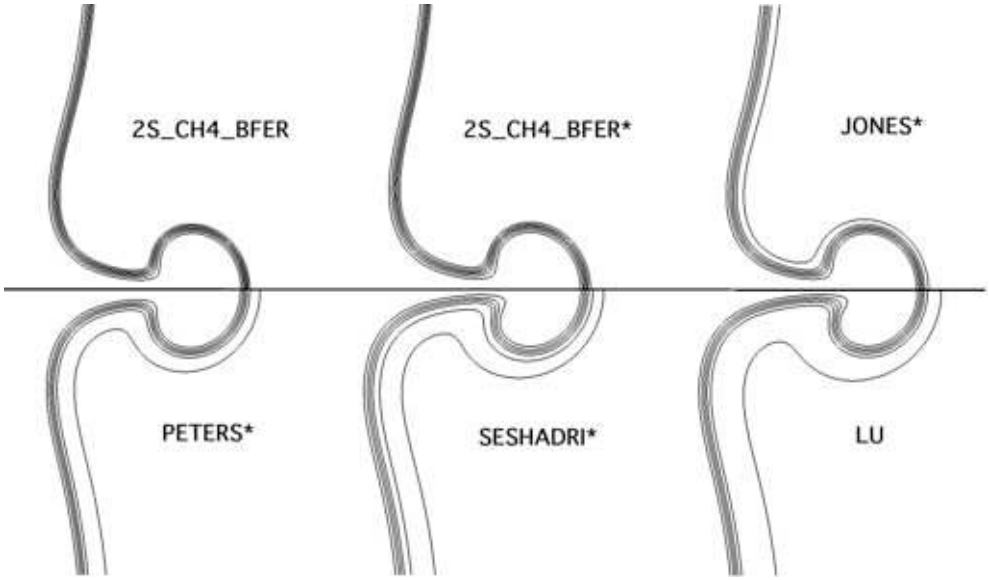

Figure 4.6 - *Temperature iso-contours for all reduced mechanisms at* $t = 0.55$ *ms. Contour lines are plotted every* 200 *K from* 1000 *K to* 2000 *K.*

The impact of the vortex passage on flame thickness is displayed in Fig. 4.7 where the instantaneous magnitude of the progress variable gradient normalized by the flame thickness $\delta_L^{GRI3.0}$ of the detailed GRI3.0 mechanism is analyzed as function of c at $t = 0.55$ *ms*. The laminar results of Section 2.2 are also added. Globally, the flame thickness is smaller, i.e. $|\nabla c|$ increases, compared to laminar results for all values of the progress variable except for the 2S_CH4_BFER* scheme. The effect is emphasised in the reaction zone ($0.5 < c < 0.8$) and the flame is less affected in the preheated ($c < 0.3$) and postflame zones ($c > 0.85$). This behavior is typical of the corrugated flamelet regime: the flame

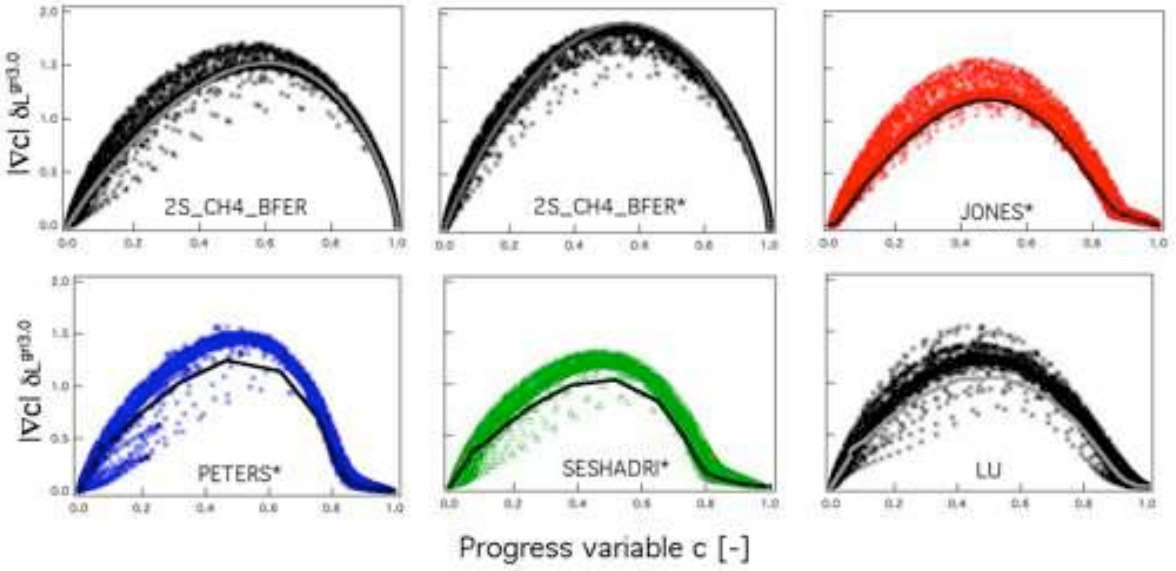

Figure 4.7 - *Instantaneous magnitude of progress variable gradient normalized by the laminar flame speed $\delta_L^{GRI3.0}$ of the detailed GRI3.0 mechanism for the flame/vortex configuration at $t = 0.55$ ms. Comparison between the reduced mechanisms. Lines correspond to results for an unstrained laminar flame. (Section 3.2.2)*

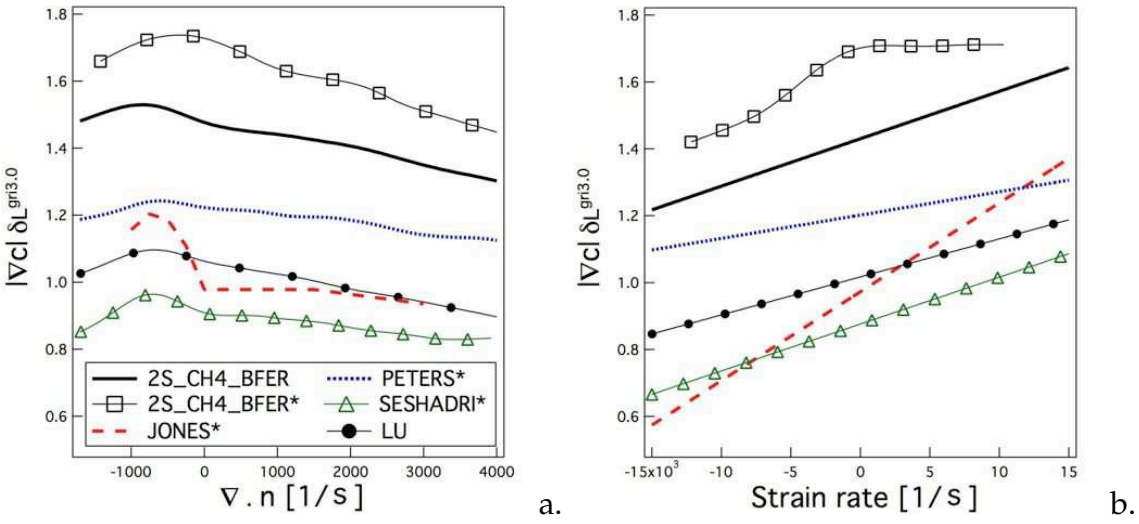

Figure 4.8 - *Mean magnitude of the progress variable gradient normalized by $\delta_L^{GRI3.0}$ as function of (a) curvature and (b) strain for the different mechanisms obtained averaging along the flame surface ($c = 0.65$) for ten different instantaneous solutions ($t = 0.05, 0.1, 0.15, 0.20, 0.25, 0.30, 0.35, 0.40, 0.45, 0.50$ ms).*

front is thinned due to strain rate.

Only the 2S_CH4_BFER* mechanism shows the flame thickness which is increased by the vortices. This behavior should be related to the Lewis numbers increased to $Le = 1.65$ to correctly predict the consumption speed which slows down diffusion and consequently decreases the flame thickness.

The mean response of the flame thickness to curvature and strain rate is shown in Fig. 4.8 for different mechanisms at $c = 0.65$. It has been obtained averaging the normalized $|\nabla c|$ along the flame surface ($c = 0.65$) for ten different instantaneous solutions ($t = 0.05, 0.1, 0.15, 0.20, 0.25, 0.30, 0.35, 0.40, 0.45, 0.50\ ms$).
Although the different schemes lead to different thickness, the tendency is qualitatively the same for all mechanisms: the flame is thickened when curvature increases, i.e. $|\nabla c|$ decreases when the magnitude of $\nabla \cdot \mathbf{n}$ increases. Moreover, as predicted by the strained one-dimensional flames, the flame thickness reduces when increasing the strain except for the 2S_CH4_BFER* scheme.

Local consumption speed

Section 2.3 has shown that the correlation between consumption flame speed S_C and tangential strain a strongly depends on the chemical mechanism in strained laminar premixed flames. The instantaneous correlation between the local consumption speed and the flame stretch is shown in Fig. 4.9 for the different mechanisms along the $c = 0.65$ isoline at four different times $t = 0.3, 0.4, 0.5, 0.55\ ms$. As in the laminar case, the consumption speed values of the 2S_CH4_BFER scheme do not depend on the flame stretch, i.e. the points are homogeneously distributed around the laminar flame speed line. On the contrary, results of the 2S_CH4_BFER* scheme, also in accordance with the laminar flame results, show the decrease of S_C with stretch. The maximum consumption speed, much higher than the laminar speed S_L for high stretch, is obtained for the JONES* mechanism. Surprisingly, results for the PETERS* mechanism are not in agreement with the laminar results of Section 2.3. Although a strong negative correlation between consumption speed and stretch was expected, a quite homogenous distribution around the laminar flame speed is observed and high values of S_C are detected at the largest stretches. The SESHADRI* and LU results are quite in agreement with the one-dimensional calculations: most values are smaller than the laminar speed S_L for high stretch values.
Discrepancies with the one-dimensional results may be caused by curvature effects since results at the symmetry axis, where curvature is quasi zero, are in agreement with laminar analysis (Fig. 4.4b.). The two contributions are better displayed in Figs. 4.10 and 4.11 where the impacts of strain rate and curvature on the consumption speed are respectively shown. Observations made on the one-dimensional results are confirmed when looking at Fig. 4.10: a negative correlation between S_C and the strain

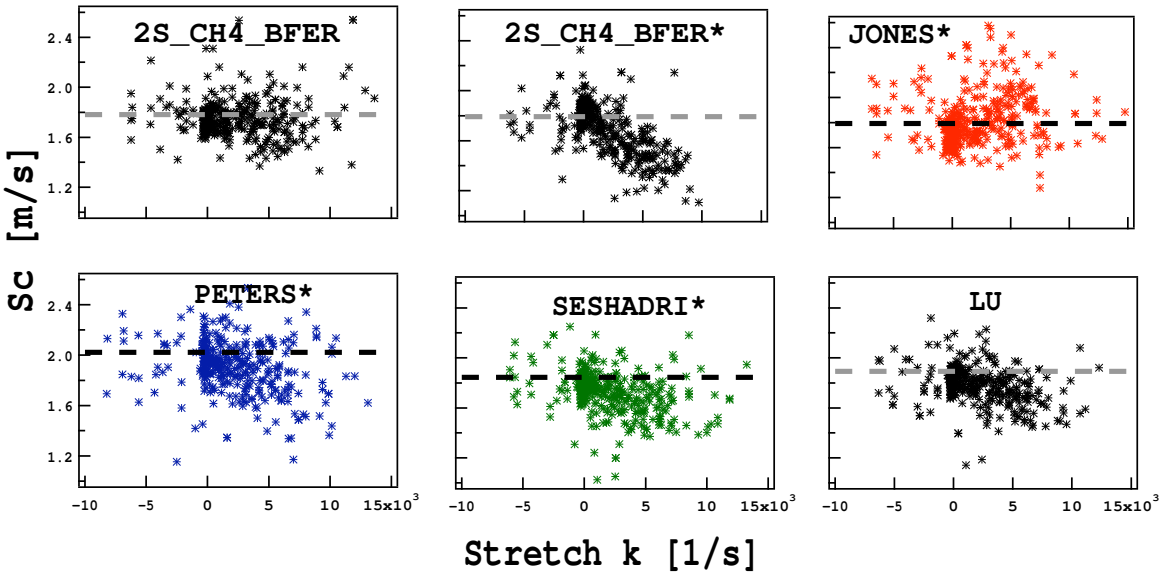

Figure 4.9 - *Instantaneous correlation between consumption speed and flame stretch along the isoline* $c = 0.65$ *obtained at four different times* ($t = 0.30, 0.40, 0.50, 0.55$ *ms). Horizontal line indicates the flame speed for a laminar unstrained flame (Section 3.2.1).*

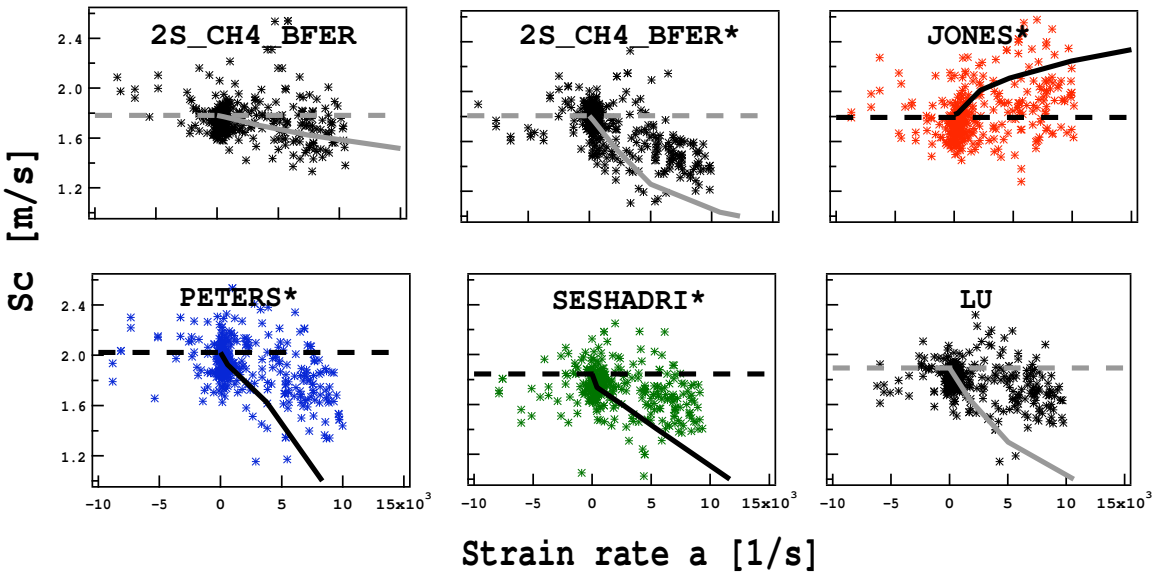

Figure 4.10 - *Instantaneous correlation between consumption speed and strain rate along the isoline* $c = 0.65$ *obtained at four different times* ($t = 0.30, 0.40, 0.50, 0.55$ *ms). Results for one-dimensional strained premixed flame of Section 2.3 are added. Horizontal line indicates the flame speed for a laminar unstrained flame (Section 3.2.1).*

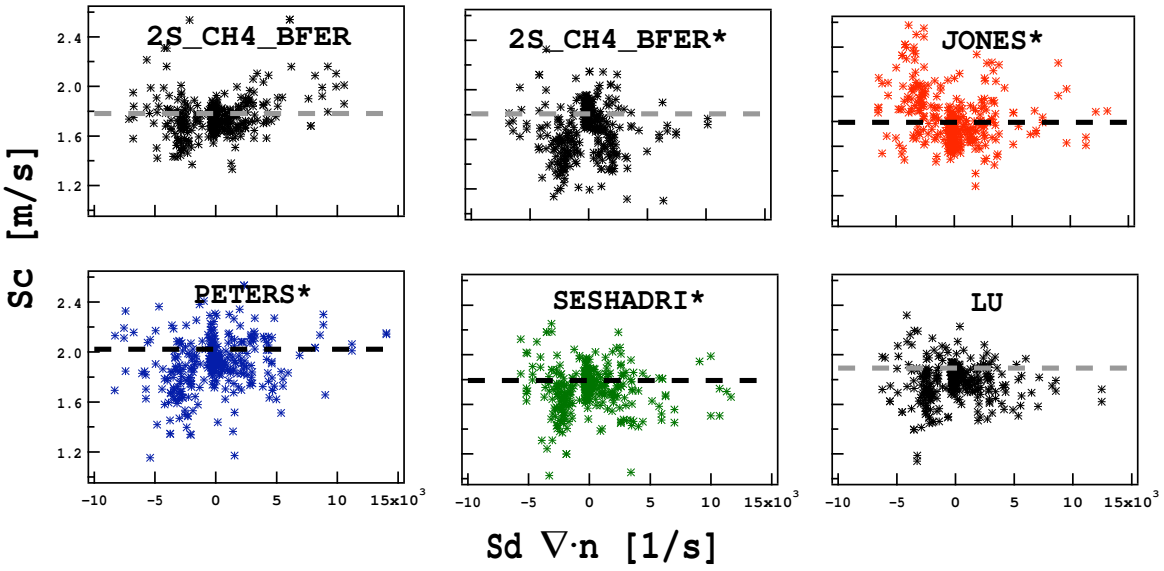

Figure 4.11 - *Instantaneous correlation between consumption speed and curvature along the isoline* $c = 0.65$ *obtained at four different times* ($t = 0.30, 0.40, 0.50, 0.55$ *ms). Horizontal line indicates the flame speed for a laminar unstrained flame (Section 3.2.1).*

rate a is found for the PETERS*, SESHANDRI*, LU and 2S_CH4_BFER* mechanisms. Moreover, a positive correlation is obtained when using the JONES* scheme whereas the 2S_CH4_BFER scheme is quite insensitive to strain rate. The curvature effect on consumption speed is represented in Fig. 4.11: the JONES* and the PETERS* schemes present a response to curvature that is qualitatively opposed to the response to strain rate. Globally, a strong correlation has been identified between the consumption speed and the strain rate whereas no relevant dependence on curvature is detected. It seems that in this configuration the strain rate is the most impacting contribution affecting the flame front.

Local flame stucture

The **CO_2 and CO mass fractions** are displayed in Figs. 4.12 and 4.13 as a function of the progress variable at the initial time, i.e. laminar flame, and at $t = 0.55$ *ms* (black and grey symbols respectively) for the different mechanisms.

For PETERS*, SESHADRI* and LU schemes, higher values of CO_2 are detected for $0.5 < c < 0.8$ at $t = 0.55$ *ms*. This tendency is in agreement with results for strained laminar flames: the flame is highly stretched and, as a the consequence, not only the flame is thinner but its structure is modified according to results for strained laminar flames. This behavior is not found with the two-step schemes that are not sensitive to

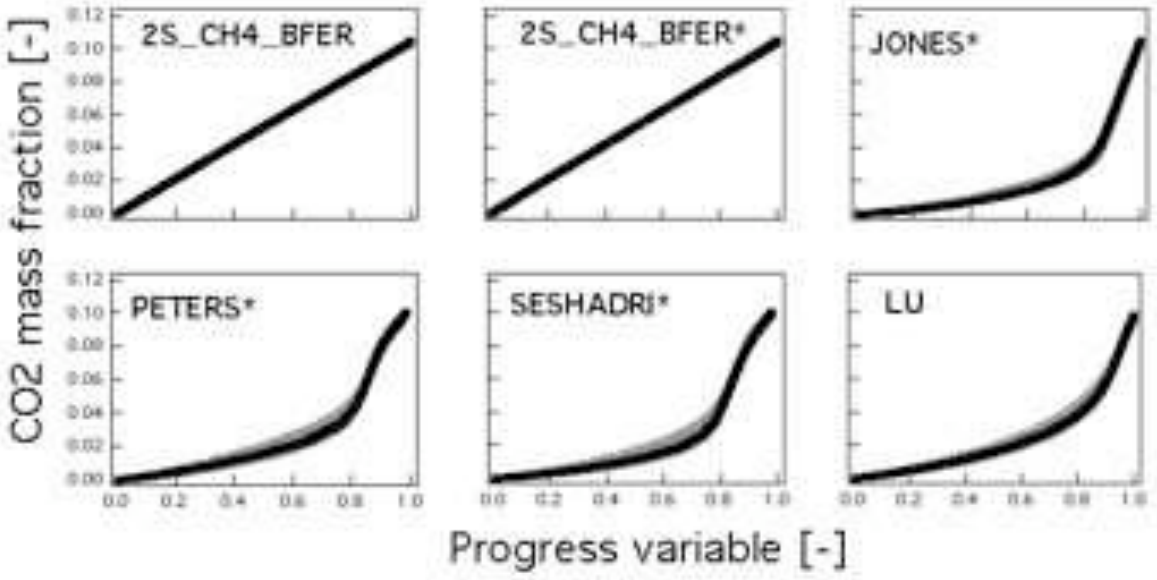

Figure 4.12 - *CO mass fraction as function of the progress variable. Instantaneous results at the initial time $t = 0$ s (black) and the time $t = 0.55$ μs (grey).*

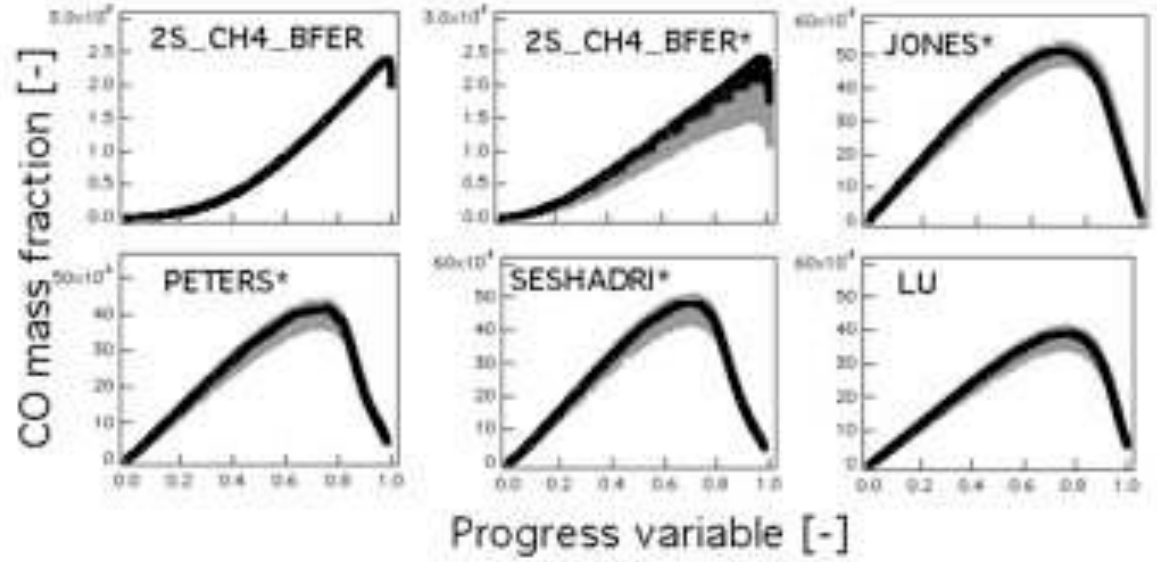

Figure 4.13 - *CO mass fraction as function of the progress variable. Instantaneous results at the initial time $t = 0$ s (black) and the time $t = 55$ μs (grey).*

strain in terms of species profiles (Section 2.3).
More important differences between laminar and stretched flames are found for the *CO* mass fraction since intermediate species and radicals are greatly affected by strain rate as shown in Section 2.3.

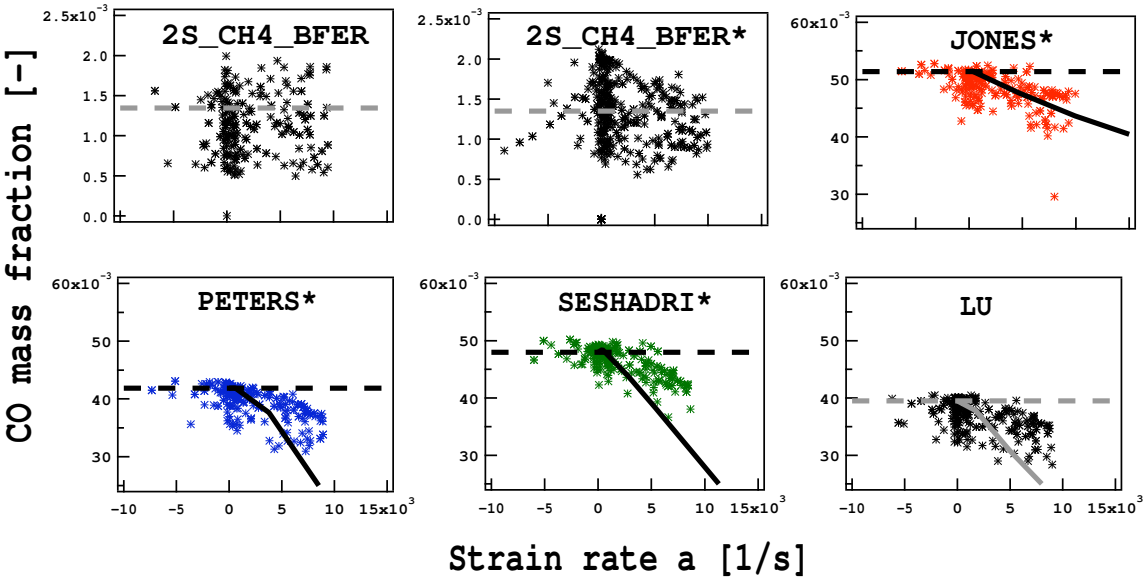

Figure 4.14 - *Instantaneous correlation between CO mass fraction and strain rate along the* $c = 0.65$ *isoline obtained for* $t = 0.55$ *ms. Results for one-dimensional strained premixed flame are added (Section 3.2.2). Horizontal line indicates the flame speed for a laminar unstrained flame (Section 3.2.1).*

To better underline the impact of strain rate and curvature on the **CO mass fraction**, its value at $c = 0.65$ is represented as a function of strain rate and curvature in Figs.4.14 and 4.15 respectively. On the one side, the two-step schemes greatly underestimate the *CO* mass fraction compared to the LU mechanism and no relevant conclusion could be drawn. On the other side, results for the most complex schemes are in agreement with the LU mechanism and with the prediction of strained laminar flames. The *CO* mass fraction in the reaction zone decreases when the strain rate increases. On the contrary, the *CO* mass fraction increases with curvature.

4.2 DNS of homogeneous isotropic turbulent field with flame

The flame response to turbulence may be studied in the generic configuration of homogenous isotropic turbulence [25, 18, 134, 13, 14]. In this section the impact of different reduced mechanisms on a flame strained and curved by such a turbulent field is evaluated in terms of flame surface, consumption speed, flame thickness and flame structure, as already done for the flame/vortex configuration in Section 4.1.

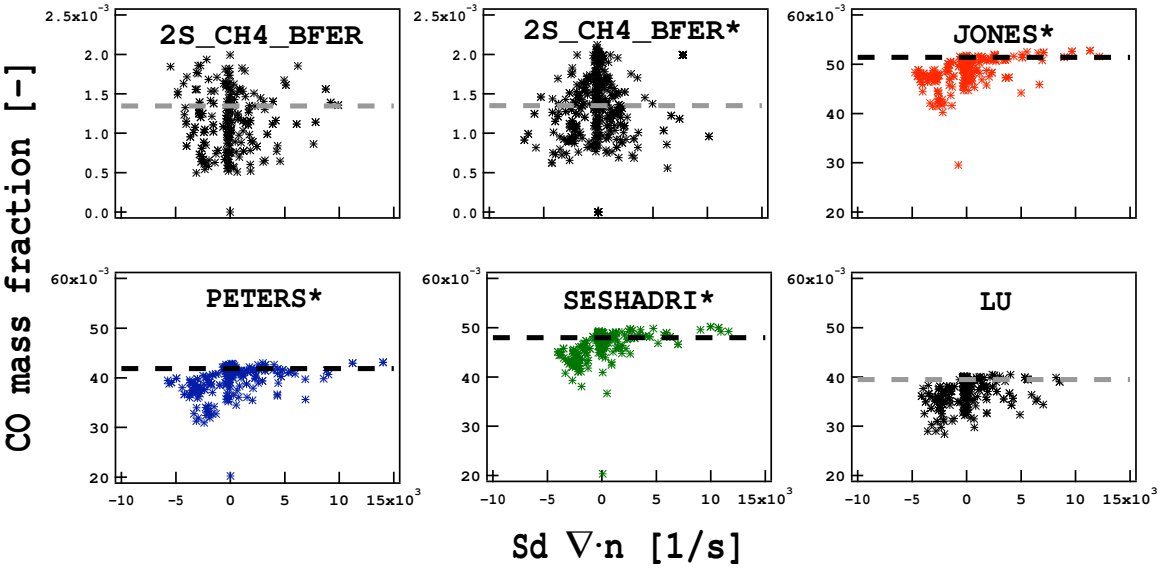

Figure 4.15 - *Instantaneous correlation between CO mass fraction and curvature along the* $c = 0.65$ *isoline obtained for* $t = 0.55$ *ms. Horizontal line indicates the flame speed for a laminar unstrained flame (Section 3.2.1).*

4.2.1 Numerical configuration and initialization of the HIT field

A three-dimensional DNS of a premixed flame interacting with an HIT field has been performed using the six different kinetic mechanisms introduced in Section 3.1. A laminar premixed flame is superimposed to the HIT field, preliminary initialized in a cube of $N^3 = 384^3$ points. Note that the turbulent structures appear only in the fresh gas zone, since the burnt gas higher viscosity dissipates them (see Fig. 4.16).

The HIT field is generated by an energetic Passot-Pouquet spectrum $E(k)$ [25] characterized by an initial turbulent speed u_p, an integral length l_t and an initial turbulent Reynolds number:

$$Re_t = \frac{u_p l_t}{\nu}. \tag{4.4}$$

Non reflecting inlet and outlet NSCBC conditions [121] are applied in the x-direction normal to the initial laminar flame imposing the operating conditions for the Bunsen flame ($T_f = 800\ K$, $\phi = 0.7$ and $P = 1\ atm$). All other boundaries are periodic. Using the Finite-Element type low-dissipation Taylor-Galerkin discretization [113, 45, 47], 0.42 *ms* are simulated with AVBP and an instantaneous solution is recorded every 10 μs.

Mesh and turbulence parameters have been chosen in order to guarantee the following criteria [25]:

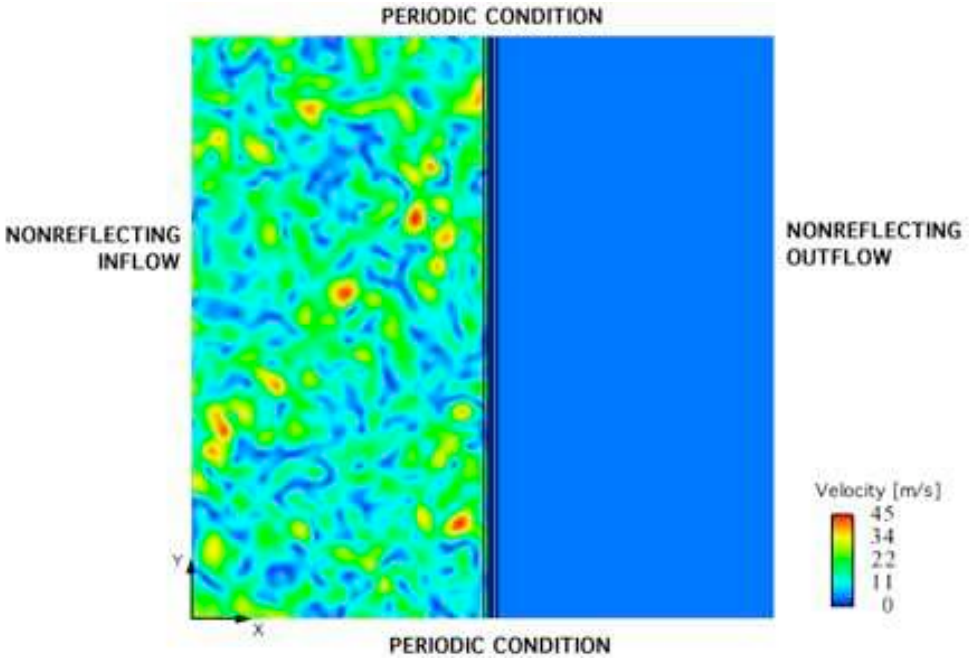

Figure 4.16 - *Two-dimensional cut of the velocity field for the initial solution. The flame position is identified by black iso-lines of temperature.*

- **Chemistry description:** the flame front must be accurately solved, i.e. at least seven points in the flame front are required for the smaller flame thickness δ_L^{bfer*} (cfr. Table 3.10):

$$\Delta x = 3.0e^{-5}m \leq \delta_L^{bfer*}/7 \approx 3.2e^{-5}m. \tag{4.5}$$

  The cell size has been chosen equal to $\Delta x \approx \delta_L^{GRI3.0}/11 = 3.0e^{-5}m$ and the domain length is consequently equal to $L = N \times \Delta x = 1.152e^{-2}m$.

- **Turbulence description:** The biggest structures must be completely solved in the half computational domain of size L where the HIT field is located:

$$l_t = 7.52e^{-4}m \leq \frac{L}{2C_1} \approx 7.67e^{-4}m \quad \text{with} \quad C_1 \approx 7.5. \tag{4.6}$$

  Moreover, the dissipation structures characterized by a length l_d must be solved at least on five cells:

$$l_d \approx 10\, l_\mathcal{K} = 2.56e^{-4}m \geq C_2 \Delta x \approx 1.5e^{-4}m \quad \text{with} \quad C_2 \approx 5, \tag{4.7}$$

  where $l_\mathcal{K}$ is the Kolmogorov length scale. The values of constants C_1 and C_2 have been indicated in [25]. The maximum turbulent Reynolds number is then:

$$Re_t = \left[\frac{l_t}{l_\mathcal{K}}\right]^{4/3} \leq \left[\frac{10N}{2C_1C_2}\right] \approx 175, \tag{4.8}$$

which limits the initial turbulent speed u_p to 10.11 $m/s \approx 5 \times S_L^{GRI3.0}$. These turbulent characteristics guarantee that the flame/flow interaction belongs to the reaction-sheet regime since $Da \approx 100$ (Fig. 1.4 in Section 1.2): the smallest vortices may interact with the preheat zone of the flame, but its inner structure is preserved.

The energetic density spectrum $E(k)$ used to initialize the HIT field is displayed in Fig. 4.17 and its parameters are summarized in Table 4.3.

Table 4.3 - *Characteristics of the energetic density spectrum and of the computational mesh.*

l_t	$l_\mathcal{K}$	u_p	Re_t	N	Δx	L
$7.52e^{-4}$ m	$2.56e^{-5}$ m	10.11	91	384	$3.0e^{-5}$ m	$1.152e^{-2}m$

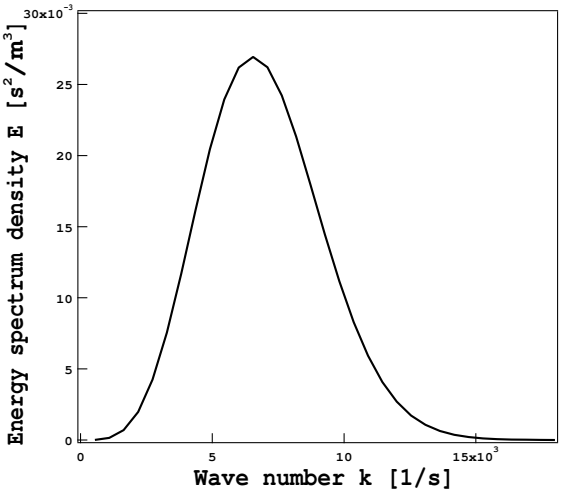

Figure 4.17 - *Passot-Pouquet energy density spectrum $E(k)$ used to initialize the HIT field.*

4.2.2 Temporal evolution

Interacting with a three-dimensional HIT field, the initial laminar flame is highly stretched and deformed. The temporal evolution of the flame surface identified by the isosurface of progress variable $c = 0.65$ is displayed in Fig. 4.18 for the 2S_CH4_BFER scheme. The flame surface is colored by the stretch k and the velocity field is displayed in the bottom plane.

The two contributions to stretch, i.e. strain rate a and curvature $S_d \nabla \cdot \mathbf{n}$, spatially averaged over the flame surface are shown in Figs. 4.19a and 4.19b together with their

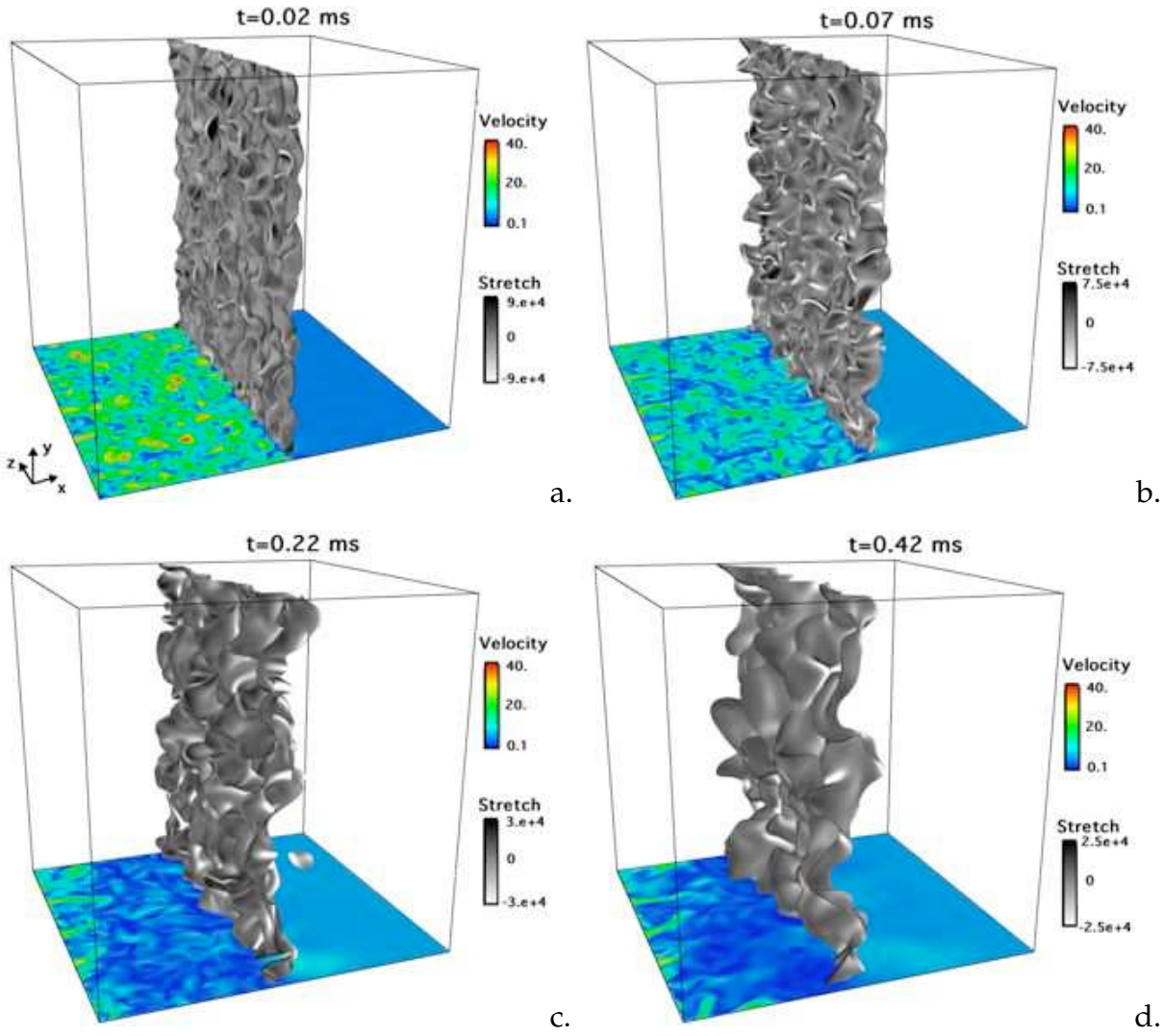

Figure 4.18 - *DNS of a premixed flame interacting with a three-dimensional HIT using the 2S_CH4_BFER mechanism at four increasing times: a)t = 0.020 ms, a) t = 0.070 ms, a) t = 0.220 ms and a) t = 0.420 ms. The isosurface of progress variable c = 0.65 identifying the flame surface is colored by stretch. The velocity field is displayed in the bottom plane.*

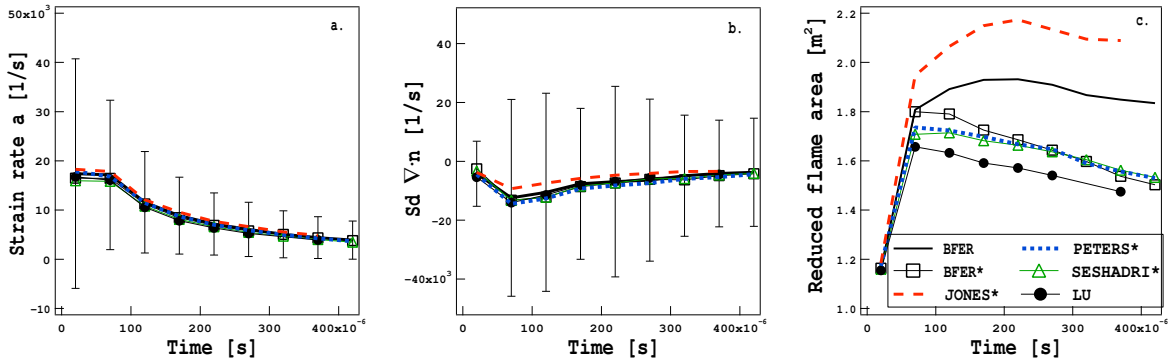

Figure 4.19 - *Temporal evolution of mean strain rate (a.), mean curvature* $Sd\ \nabla \cdot \mathbf{n}$ *(b.) and reduced area of the flame surface (c.) for different chemical mechanisms. Error-bars indicate the RMS values.*

root-mean-square (RMS) as function of time. Moreover, the temporal evolution of the reduced flame area $\tilde{A}$, i.e. the ratio between the instantaneous flame front area and the initial flame front area, is plotted in Fig. 4.19c for the six chemical mechanisms.

At $t = 0.02$ *ms* the velocity field is characterized by highly-energetic vortices that interact with the flame, inducing the maximum stretch which is mostly due to strain rate a and slightly curving the flame front. The reduced flame area slightly increases at the beginning ($t = 0.02$ *ms*), then drastically increases at $t = 0.07$ *ms* when the flame is highly wrinkled by stretch. The mean curvature reaches its maximum as well as its RMS denoting the presence of highly convex and concave zones, i.e. greatly wrinkled front.
After 0.07 *ms*, vortices are slowly dissipated by viscosity and induce smaller stretch values on the flame front. The strain rate a decreases with time as well as its RMS and the mean curvature, but high RMS values for the curvature remain for a long time. As a consequence, the flame front is less and less wrinkled and finally its reduced area decreases with time.

The evolution of the strain rate a and the curvature averaged on the flame front is the same for all reduced mechanisms (see Figs. 4.19a and 4.19b). On the contrary, the evolution of the reduced flame area varies with the chemical schemes (Fig. 4.19c). Results for the PETERS* and SESHADRI* schemes are in good agreement with the LU mechanism whereas the flame is more wrinkled when using the 2S_CH4_BFER and JONES* schemes. The 2S_CH4_BFER* mechanism predicts a flame wrinkling in better agreement with the LU scheme compared to the 2S_CH4_BFER scheme. Since each mechanism has a different response to strain rate and curvature, the flame wrinkling could be differently predicted by the six mechanisms.

4.2.3 Comparison of the different reduced mechanisms

The following analysis on strain rate, curvature, local consumption speed, flame thickness and flame structure has been performed in the central plane (x, y) at $z = 5.76mm$.

Strain rate and curvature

The probability density function of the strain rate and the curvature contribution are plotted in Fig. 4.20 at the final time ($t = 0.420$ ms) for the different chemical mechanisms. Results confirm the findings of earlier studies [14, 134]: the maximum probability is found for a small positive strain rate, negative strain rates are less likely to be seen compared to positive ones whereas convex and concave curvatures are detected with the same probability. This behavior does not depend on the chemical description used.

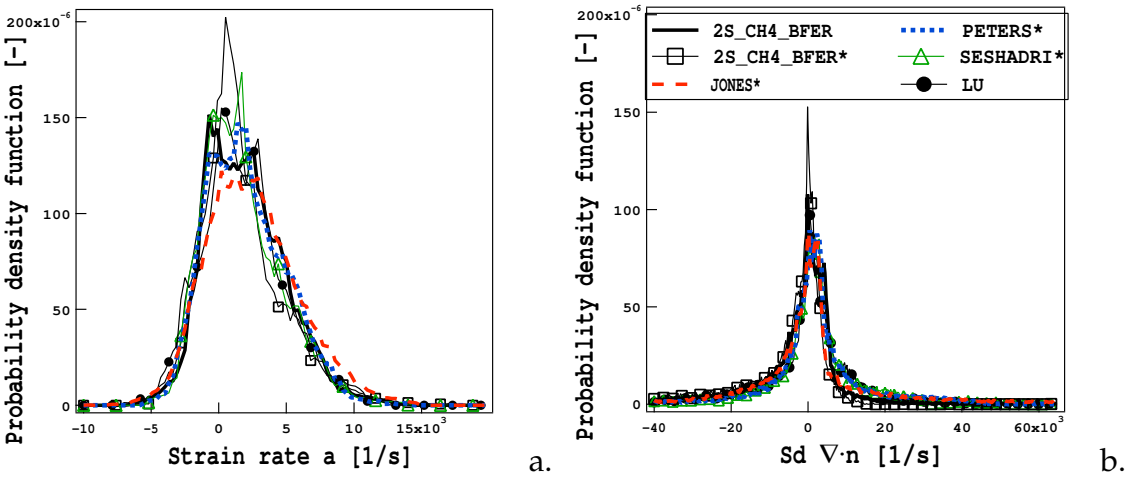

Figure 4.20 - *Probability density function of a) strain rate a and b) curvature term* $Sd\ \nabla \cdot \mathbf{n}$ *at the final time* $t = 420$ μs *for the six chemical mechanisms.*

Local consumption speed

The local fuel consumption rate $\dot{\omega}_F$ is displayed in Fig. 4.21 in the (x, y) plane at four increasing times ($t = 0.02$ ms, $t = 0.070$ ms, $t = 0.220$ ms and $t = 0.420$ ms) for the different reduced mechanisms. For $t = 0.020$ ms the flame is only slightly deformed by vortices and no relevant discrepancies are detected between the chemical schemes. For higher time values ($t \geq 70$ μs), the flame front is wrinkled and the fuel consumption rate assumes different values depending on the reduced mechanisms. As usual,

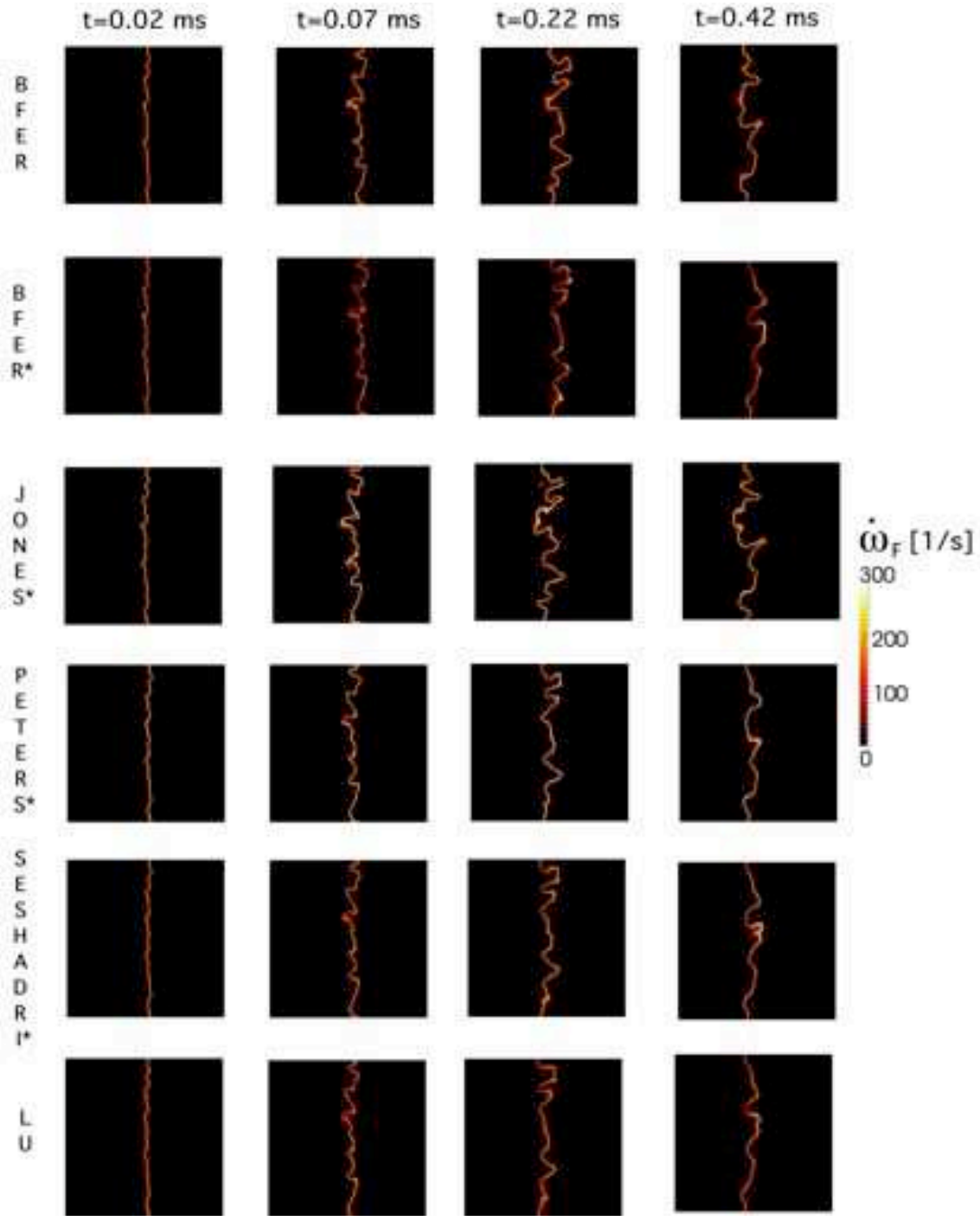

Figure 4.21 - *Instantaneous fuel consumption rate* $\dot{\omega}_F$ *in the* (x, y) *plane at four increasing times* ($t = 0.02$ *ms*, $t = 0.070$ *ms*, $t = 0.220$ *ms and* $t = 0.420$ *ms) for different reduced mechanisms.*

results of the LU scheme are expected to better describe the behavior of complex chemistry and are taken as reference. With the PETERS* and SESHANDRI* schemes, the consumption rate profile varies in agreement with the LU results. Profiles of $\dot{\omega}_F$ are only slightly affected by the flame wrinkling when using the 2S_CH4_BFER scheme, while results of the modified 2S_CH4_BFER* scheme are qualitatively in agreement with the LU mechanism. The fuel consumption rate $\dot{\omega}_F$ predicted by the JONES* scheme highly varies with stretch.

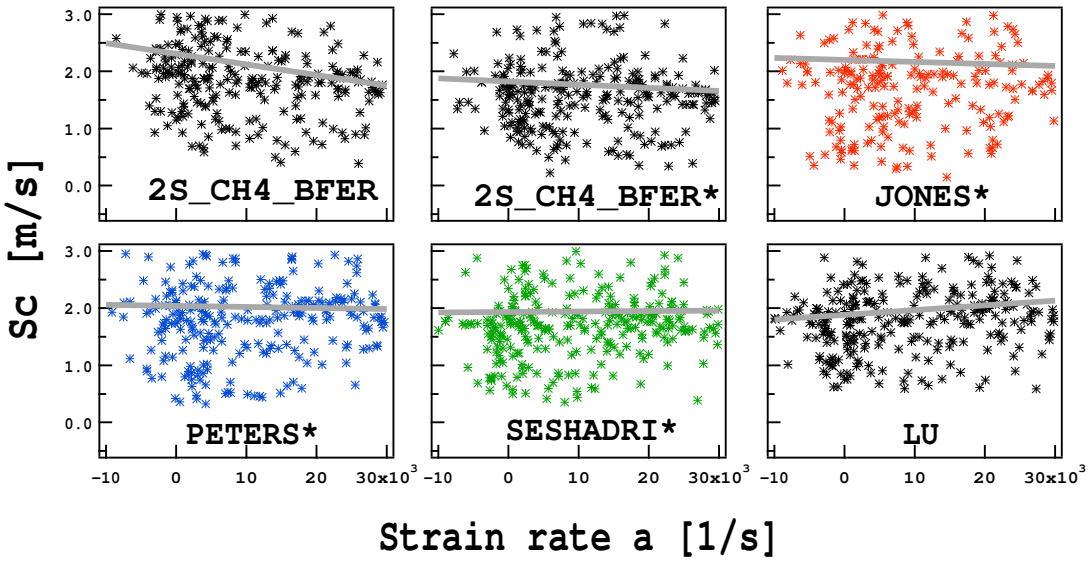

Figure 4.22 - *Correlation between consumption speed and strain rate from four instantaneous solutions ($t = 0.02, 0.07, 0.22, 0.42$ ms) along the flame front ($c = 0.65$). Lines represent the mean correlation obtained with the linear least square method.*

In Fig. 4.22, the local consumption speed S_C has been evaluated integrating the fuel consumption rate in the direction normal to the flame surface from instantaneous solutions at four times ($t = 0.02, 0.07, 0.22, 0.42$ *ms*) along the flame surface ($c = 0.65$):

$$S_T = \frac{1}{\rho Y_{O_2}} \int \overline{\dot{\omega}}_{O_2} d\mathbf{n}. \tag{4.9}$$

To ensure not to neglect an important contribution in the z direction when working in the (x, y) plane only points of the iso-contour such as $\sqrt{n_x^2 + n_y^2} > 0.95$ are considered, where $\mathbf{n} = \nabla c / |\nabla c|$. In such points, the variation of the progress variable in z direction is negligible compared to the two other directions and the local consumption speed could be accurately approximated considering only the (x, y) plane. The mean correlations are calculated via the linear least square method from four instantaneous solutions. Only

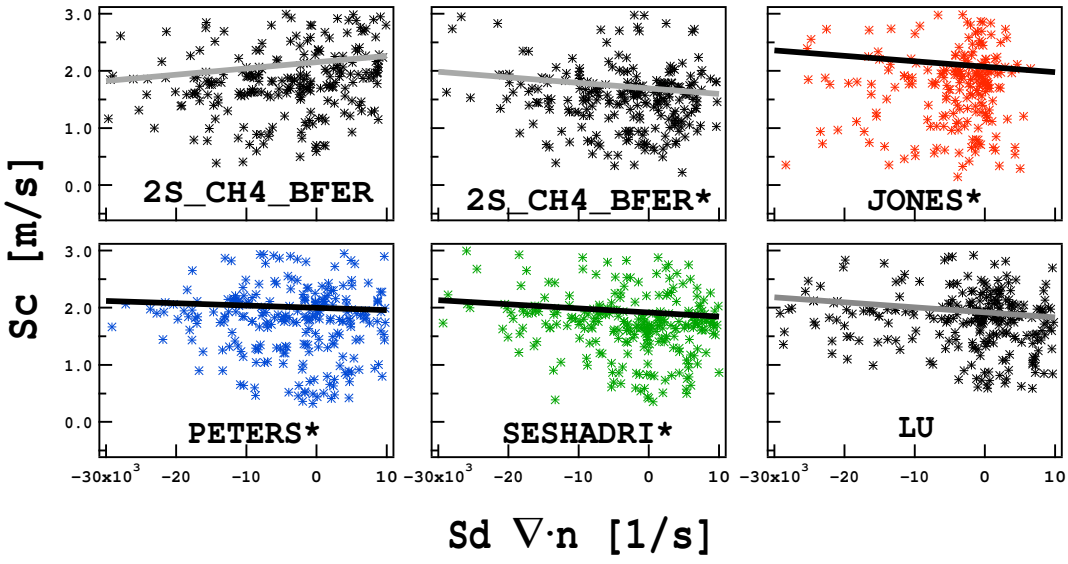

Figure 4.23 - *Correlation between consumption speed and curvature from four instantaneous solutions ($t = 0.02, 0.07, 0.22, 0.42$ ms) along the flame front ($c = 0.65$). Lines represent the mean correlation obtained with the linear least square method.*

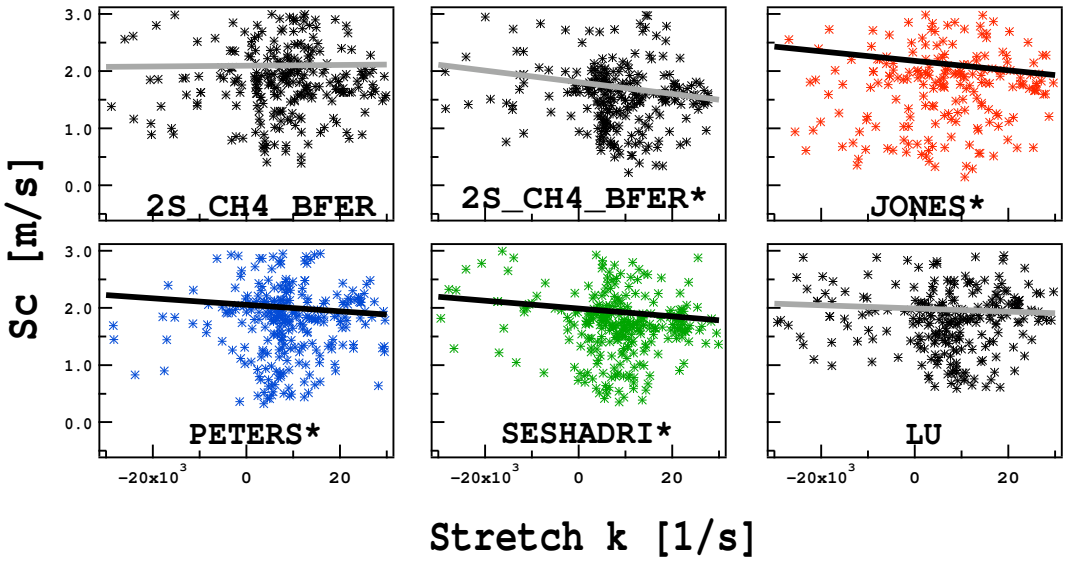

Figure 4.24 - *Correlation between consumption speed and stretch from four instantaneous solutions ($t = 0.02, 0.07, 0.22, 0.42$ ms) along the flame front ($c = 0.65$). Lines represent the mean correlation obtained with the linear least square method.*

the 2S_CH4_BFER, the 2S_CH4_BFER* and the JONES* schemes predict a negative correlation of consumption speed with strain rate whereas SESHADRI* and LU schemes show a positive correlation. The local consumption speed is also affected by curvature as shown in Fig. 4.23. A negative correlation is identified with all chemical schemes expect for the 2S_CH4_BFER mechanism whose consumption speed increases with the flame curvature. The response of the different reduced mechanisms to stretch, adding the strain rate and the curvature contributions, is displayed in Fig. 4.24. The local consumption speed decreases when stretch increases for the LU scheme. The same behavior is predicted by the JONES*, PETERS* and SESHADRI* mechanisms, whereas the 2S_CH4_BFER has a positive correlation. The modified 2S_CH4_BFER* scheme allows to recover a good behavior. From the laminar and the flame/vortex results, the consumption speed is expected to decrease when the strain rate increases for the most complex schemes. Since the consumption speed is affected by strain rate and curvature at the same time, it is not straightforward to identify the impact of each contribution to the local consumption speed since no strong correlation has been identified for the consumption speed neither with the strain rate nor with the curvature in this configuration.

Flame thickness

The interaction of vortices with the flame modifies the flame thickness as shown in Fig. 4.25. It has been obtained spatially averaging the normalized instantaneous gradient of the progress variable in the (x, y) plane.
The normalized gradient of the progress variable is analyzed as function of the progress variable c for two different times ($t = 0.070$ ms and $t = 0.420$ ms), comparing it with results for the laminar flame. At $t = 0.070$ ms the LU flame is characterized by high wrinkling and stretch values. On the one side, the reaction zone ($0.5 < c < 0.8$) is thinned by the interaction with the large scale structures as observed in the flame/vortex configuration. On the other side, the preheat zone ($c < 0.3$) is thickened since small eddies enhance mixing in this region. This behavior is characteristic of the reaction-sheet regime. At $t = 0.420$ ms the stretch has reduced and, as a consequence, the reaction zone is less thinned by strain rate, going back to laminar results. On the contrary, the preheat zone is still thickened by turbulence. The PETERS* and SESHADRI* schemes behave in agreement with the LU mechanism: the preheat zone is usually thickened by turbulence and the reaction zone is thinned by large scale structures according to the strain rate values. Since the PETERS scheme is the most sensitive mechanism to strain rate, the reaction zone is highly thinned even at $t = 420$ μs. The two-step scheme 2S_CH4_BFER is quite insensitive to stretch and consequently the flame is not thickened in the reaction zone. Except for the preheat zone which is slightly thickened by the interaction with small eddies, profiles for the 2S_CH4_BFER scheme mostly coincide with laminar results. The behavior of the flame predicted by the modified

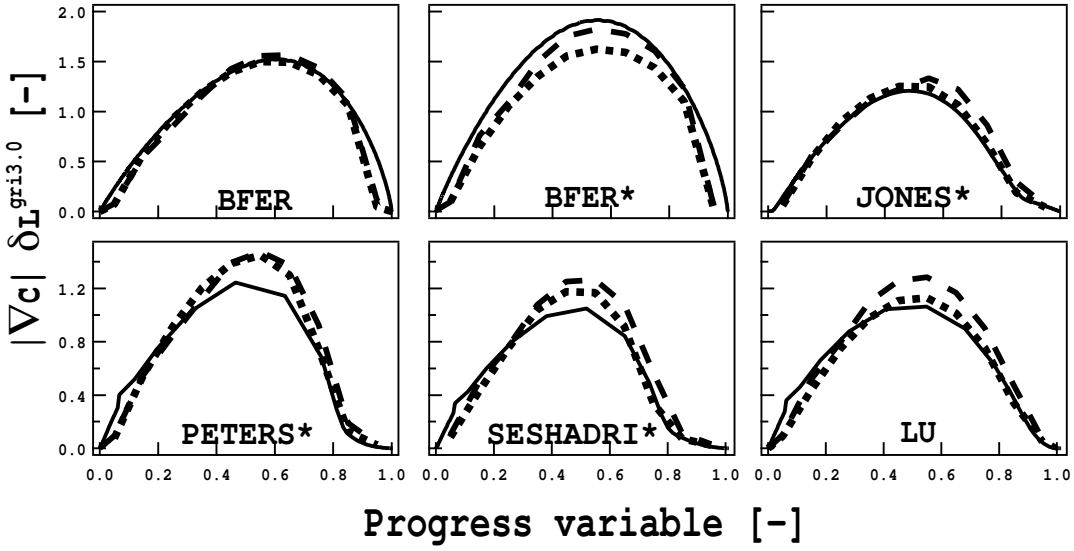

Figure 4.25 - *Spatially averaged gradient of progress variable normalized by the laminar flame speed* $\delta_L^{GRI3.0}$*. Comparison between laminar results (solid line), DNS results at* $t = 0.07$ *ms (dashed line) and at* $t = 0.42$ *ms (dotted line) for the six reduced mechanisms. Note that visualization scales are different between results.*

2S_CH4_BFER* scheme is in opposition with the LU results: the flame is thickened not only in the preheat zone but also in the reaction zone in agreement with the laminar and flame/vortex results. The JONES* scheme is in agreement with the LU mechanism: the flame is thickened in the preheat zone whereas it is thinned in the reaction zone.

The response of the flame thickness in the reaction zone to curvature and strain rate is shown in Fig. 4.26. The normalized gradient of the progress variable has been averaged along the flame front ($c = 0.65$) for four increasing times ($t = 0.02, 0.07, 0.22, 0.42$ *ms*). Results are coherent with the observations for the flame/vortex configuration: the flame is thickened when the curvature increases and the flame thickness reduces when strain rate increases for all reduced mechanisms.

Flame structure

Finally, the instantaneous CO mass fraction as function of the progress variable is displayed in Fig. 4.27 at $t = 0.07$ *ms*. The two-step schemes greatly underestimate the *CO* concentration in the reaction zone ($0.2 < c < 0.8$) as already seen in laminar calculations. The PETERS* and SESHADRI* schemes correctly reproduce the *CO* mass fraction whereas the JONES* mechanism globally overestimates its maximum value as observed in laminar flames. For all mechanisms, the response to stretch is qualitatively

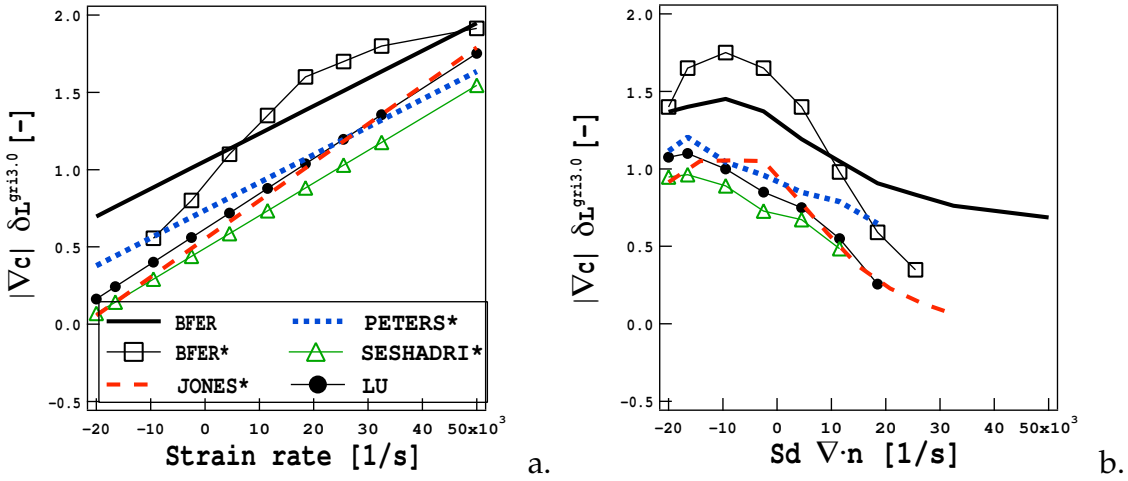

Figure 4.26 - *Mean gradient of the progress variable in the reaction zone ($c = 0.65$) as function of a) strain and b) curvature for four increasing times ($t = 0.02, 0.07, 0.22, 0.42$ ms). Comparison between the six reduced mechanisms.*

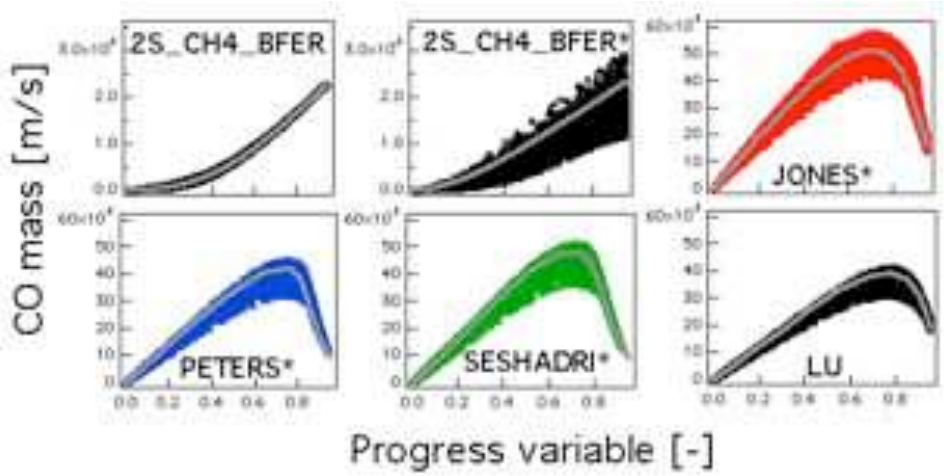

Figure 4.27 - *Instantaneous CO mass fraction as a function of progress variable at $t = 0.07$ ms. Comparison between the six reduced mechanisms. Solid lines correspond to results for an unstrained laminar flame.*

the same as in the flame/vortex configuration: at $t = 0.07$ *ms* the flame is highly wrinkled and smaller concentrations of *CO* mass fraction are found in the reaction zone compared to laminar unstrained flames. Smaller values of *CO* mass fraction are characteristic of strained flames and their impact of strain rate and curvature is identified in Figs.4.28 and 4.29. Results of the two-step schemes are not really significant since they highly underestimate the *CO* concentration. All other chemical schemes show a negative correlation between the *CO* mass fraction and the strain rate in agreement with the laminar results which are also plotted. Results of the impact of curvature on the *CO*

mass fraction are in agreement with the flame/vortex conclusions: the *CO* concentration tends to increase with the curvature flame.

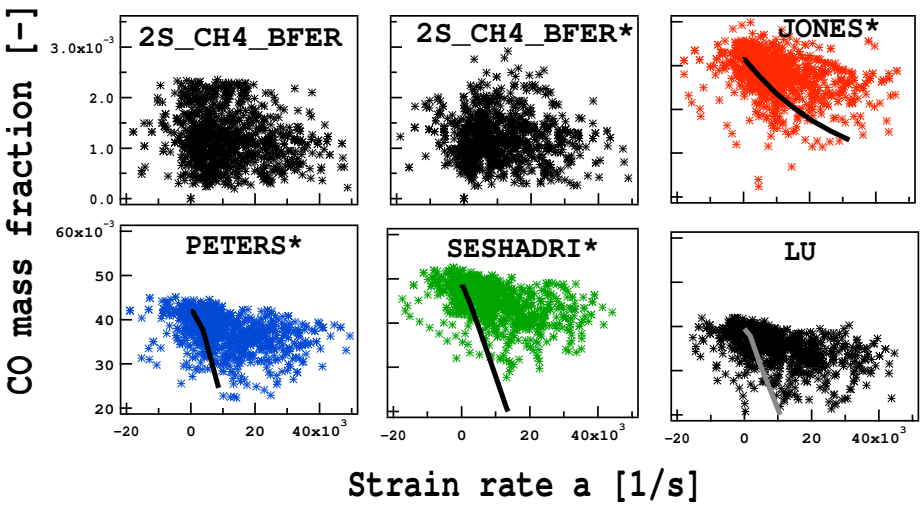

Figure 4.28 - *Instantaneous CO mass fraction along the flame front ($c = 0.65$) at $t = 0.07$ ms. Comparison between the six reduced mechanisms. Solid lines correspond to results for strained laminar flames.*

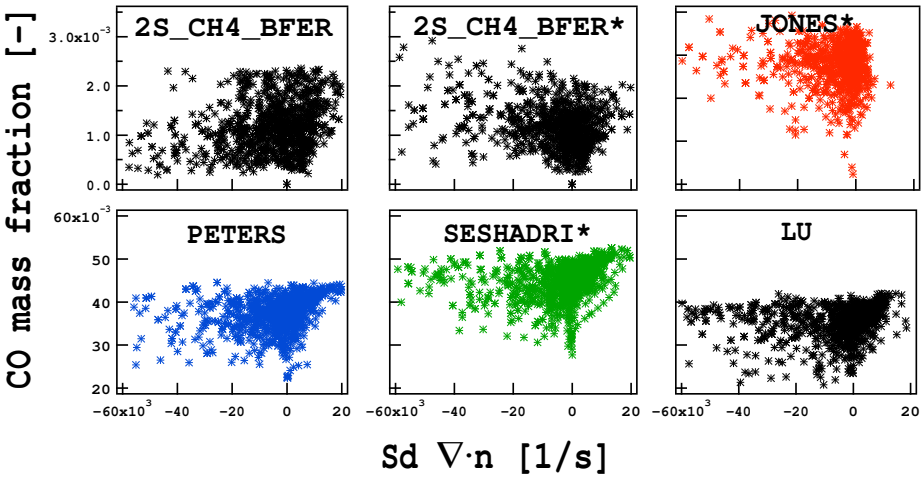

Figure 4.29 - *Instantaneous CO mass fraction along the flame front ($c = 0.65$) at $t = 0.07$ ms. Comparison between the six reduced mechanisms.*

4.2.4 Preliminary conclusions on academic configurations

The reduced mechanisms have been compared to the LU scheme in terms of flame thickness, flame wrinkling A', consumption speed S_C and CO mass fraction for the flame/vortex and the flame/HIT configurations (Table 4.4).
The **flame thickness** depends more on the characteristics of the flame and of the flow, i.e. on the combustion regime, than on the reduced mechanisms themselves. It generally increases with the absolute value of the curvature and it decreases when the strain rate increases. All schemes correctly reproduce the impact of strain rate and curvature on the flame thickness except the 2S_CH4_BFER* scheme due to the Lewis number $Le = 1.65$ assumption.
The **consumption speed** S_C of turbulent flames generally decreases when strain rate increases and this behavior is reproduced only by the chemical mechanisms which correctly work on laminar strained flames, i.e. 2S_CH4_BFER*, PETERS* and SESHADRI* schemes.
The **flame wrinkling** A' represents the first effect of turbulence on the flame front and it is linked to the turbulent speed. This quantity is generally overestimated by the 2S_CH4_BFER and JONES* schemes which incorrectly predict the consumption speed.
The **CO mass fraction** in the reaction zone depends on the strain rate values and it is correctly predicted only by the PETERS* and SESHADRI* schemes since the two-step schemes and the JONES* mechanism are not able to describe CO mass fraction on laminar strained flames.

Table 4.4 - *Performances of the reduced mechanisms compared to the LU scheme.*

	BFER	**BFER***	**JONES***	**PETERS***	**SESHADRI***
Flame thickness	√	× $Le = 1.65$	√	√	√
Consumption speed	× wrong lam. strained flames	√	× wrong lam. strained flames	√	√
Flame wrinkling	× wrong S_C	√	× wrong S_C	√	√
CO mass fraction	× wrong lam. unstrained flames	× wrong lam.r unstrained flames	× wrong lam. strained flames	√	√

The different mechanisms are characterized by a different **computational cost** mostly depending on the number of resolved species (Table 4.5). The two-step schemes are the

less expensive since only six species are taken into account. For the HIT calculation, adding one or two species (JONES and PETERS*/SESHADRI* schemes) increases the computational cost by about 15 – 25%. The LU mechanism is the most accurate scheme but is 60% more expensive than the two-step mechanisms. However, it should be noticed that instantaneous solutions are written very frequently, which impacts the computational cost since for example LU solutions are twice as big as 2S_CH4_BFER solutions. Reducing the output operations, i.e. the number of written solutions, will decrease the normalized computational cost for the most expensive mechanism.

Table 4.5 - *Normalized computational time per physical second for the HIT calculation.*

2S_CH4_BFER	**2S_CH4_BFER***	**JONES***	**PETERS***	**SESHADRI***	**LU**
1.0	1.0	1.16	1.26	1.26	1.68

Three different reduced mechanisms will be further tested in the DNS of the Bunsen flame in Section 4.3. The two-step 2S_CH4_BFER scheme is very attractive since its computational is reduced by up to 60% compared to LU calculation. Unfortunately, preliminary tests have revealed an incorrect response to stretch which has to be evaluated in complex flame configurations: if result accuracy is satisfactory, this kind of mechanism represents a good compromise between cost and quality. The 2S_CH4_BFER* scheme is also retained for DNS in order to verify that the modifications based on laminar tests really improve the quality of results for complex turbulent flames. On the contrary, bad performances of the JONES* mechanism make it no relevant for further tests. Globally, the PETERS* and SESHADRI* schemes have a similar behavior and a good agreement with the LU results on preliminary tests have been highlighted. The SESHADRI* scheme is chosen for further testing in DNS of real flames for the following reasons:

- the SESHADRI* mechanism is numerically more robust compared to the PETERS* scheme;
- results for laminar strained flames are in agreement with GRI3.0 and LU mechanisms also at high strain rates;
- the response of flame thickness to turbulence in a flame/HIT configuration is better described compared to PETERS* scheme.
- using the SESHADRI* scheme computational cost is reduced by about 20% compared to the LU mechanism, while preserving the same level of accuracy.

4.3 DNS of stationary lean premixed Bunsen flame

A Direct Numerical Simulation of the stationary lean premixed Bunsen flame by Sankaran et al. [137, 136] is performed using the three reduced mechanisms selected in the flame/vortex and flame/HIT configurations: the 2S_CH4_BFER, the 2S_CH4_BFER* and the SESHADRI* schemes. Results are compared to the solutions obtained with the reference LU mechanism from [137].

This configuration represents a pilot flame classically used in experiments [58]. It consists of a central turbulent jet of premixed methane/air mixture injected at equivalence ratio $\phi = 0.7$, initial temperature $T_f = 800\ K$ and atmospheric pressure, surrounded by a heated coflow having both the temperature and the composition of the combustion products of the reactant jet. The instantaneous flame surface identified by the iso-surface of the progress variable $c = 0.65$ based on the O_2 mass fraction is displayed in Fig. 4.30a.

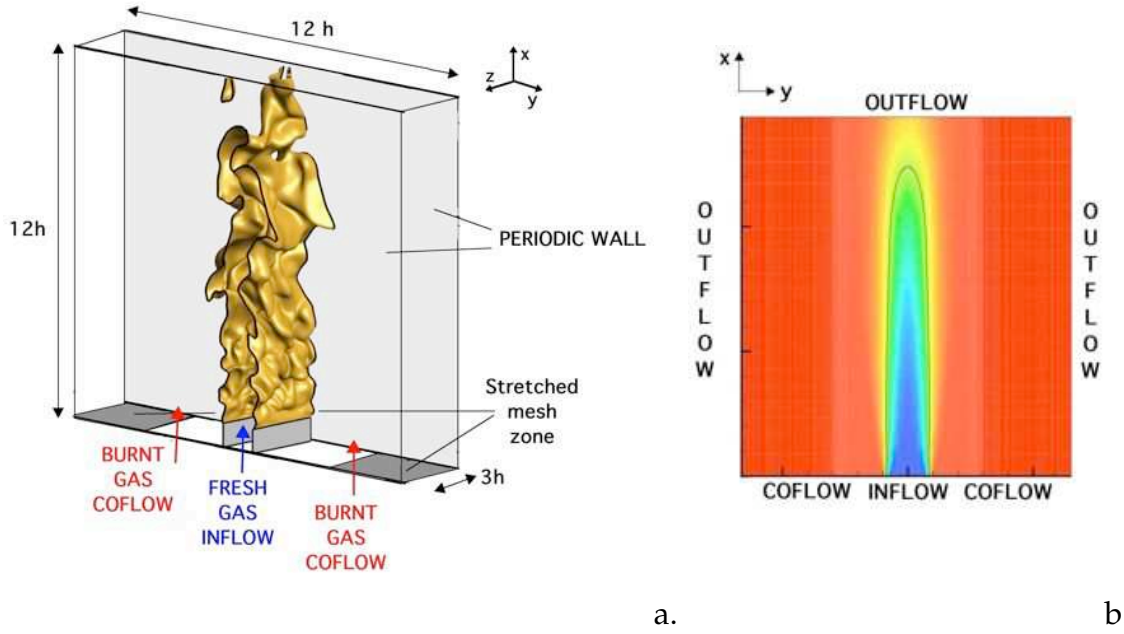

a. b.

Figure 4.30 - *(a.) Instantaneous flame surface identified by the isosurface of progress variable c = 0.65. (b.) Mean progress variable c shown as a pseudocolor plot (blue=0, red=1), the solid line represents the iso-contour of c = 0.65. Results obtained with the LU mechanism [137].*

The impact of the reduced mechanisms on the description of complex flames is evaluated performing DNS of the Bunsen flame with the S3D code [37], which was the code used by Sankaran, in collaboration with E. Richardson (University of Southampton) and J. Chen (Sandia National Laboratories).

4.3.1 Numerical configuration

The same numerical configuration calculated by Sankaran et al. [137] is used for the present simulations with the 2S_CH4_BFER, the 2S_CH4_BFER* and the SESHADRI* schemes.

The mesh presents a uniform spacing of 20 μm in the streamwise $x-$ and spanwise $z-$directions. In the crosswise $y-$direction, a uniform grid spacing of 20 μm extends over a region of $6mm$ in width in the center of the domain. In the outer part of the domain, the mesh is stretched using an algebraical function [137], which guarantees a grid spacing ratio smaller than 2%. The resultant mesh size is $L_x \times L_y \times L_z = 12h \times 12h \times 3h$, where $h = 1.2\ mm$ is the slot width, discretized on $N_x \times N_y \times N_z = 720 \times 400 \times 180$ points. The parameters are summarized in Table 4.6 and the mesh stretching zone is sketched in Fig. 4.30a.

Table 4.6 - *Mesh parameters for the Bunsen configuration.*

Slot width (h)	Domain size	Grid points
1.2 mm	$12h \times 12h \times 3h$	52 Million

A central jet of methane/air premixed mixture is injected imposing the mean and fluctuating velocity profiles represented in Fig. 4.31 via a NSCBC [123] non-reflecting boundary inlet condition [136]. At the jet inlet centerline, the mean velocity is equal to $U = 60\ m/s$ and the fluctuating velocity is equal to $u' = 18\ m/s$. The jet Reynolds number, based on the centerline mean velocity and the slot width, is equal to $Re = 840$.

Table 4.7 - *Inlet parameters for the Bunsen configuration.*

Jet centerline mean velocity	Jet centerline fluctuating velocity	Coflow velocity	Jet Reynolds number
$60m/s$	$18m/s$	$15m/s$	840

A heated coflow is also injected with a laminar velocity of 15 m/s. Non-reflecting outlet conditions are imposed on the transverse $y-$direction whereas a periodicity hypothesis is assumed for walls in the spanwise $z-$direction (Fig. 4.30). The turbulent field is characterized by the length scale and the magnitude of the velocity fluctuations defined in Table 4.8. The turbulent Reynolds number is equal to $Re_t = 14$ and the

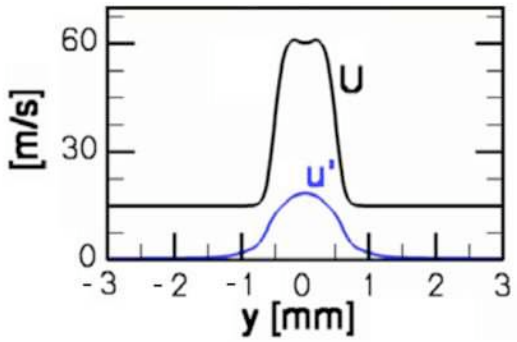

Figure 4.31 - *Mean and fluctuating velocity profiles at the inlet [136].*

flame/flow interaction is governed by a Karlovitz number $Ka \approx 100$ corresponding to the reaction-sheet flame regime (see Fig. 1.4 in Section 1.2).

Table 4.8 - *Parameters for turbulence.*

u'	l_t	Re_t	Ka
5.4	$2.1e^{-3}$	14	100

All statistical quantities are computed using data from solutions at 60 different time instants which are equally spaced (by 4 μs) over 1 flow through time (0.24 ms). Moreover, when quantities are conditionally average at $c = 0.65$, the range $0.63 < c < 0.67$ is actually considered.

4.3.2 Results

The mean progress variable $\tilde{c}$ based on O_2 species is shown in Fig. 4.32a., where the flame surface is identified by the isoline $c = 0.65$ as done in [137]. The SESHADRI* and the 2S_CH4_BFER* schemes are in a satisfactory agreement with the LU mechanism whereas the flame shape predicted by the 2S_CH4_BFER scheme seems slightly too wide in the half-domain region.The fields of heat release shown in Fig. 4.32b localize the reaction zone. The 2S_CH4_BFER scheme leads to a more intense flame compared to the 2S_CH4_BFER* and SESHADRI* mechanisms, which are both in good agreement with the LU results. Moreover, the flame obtained with the 2S_CH4_BFER scheme has a shorter core compared to the LU results while the flame length estimated by the isoline $c = 0.65$ is larger.

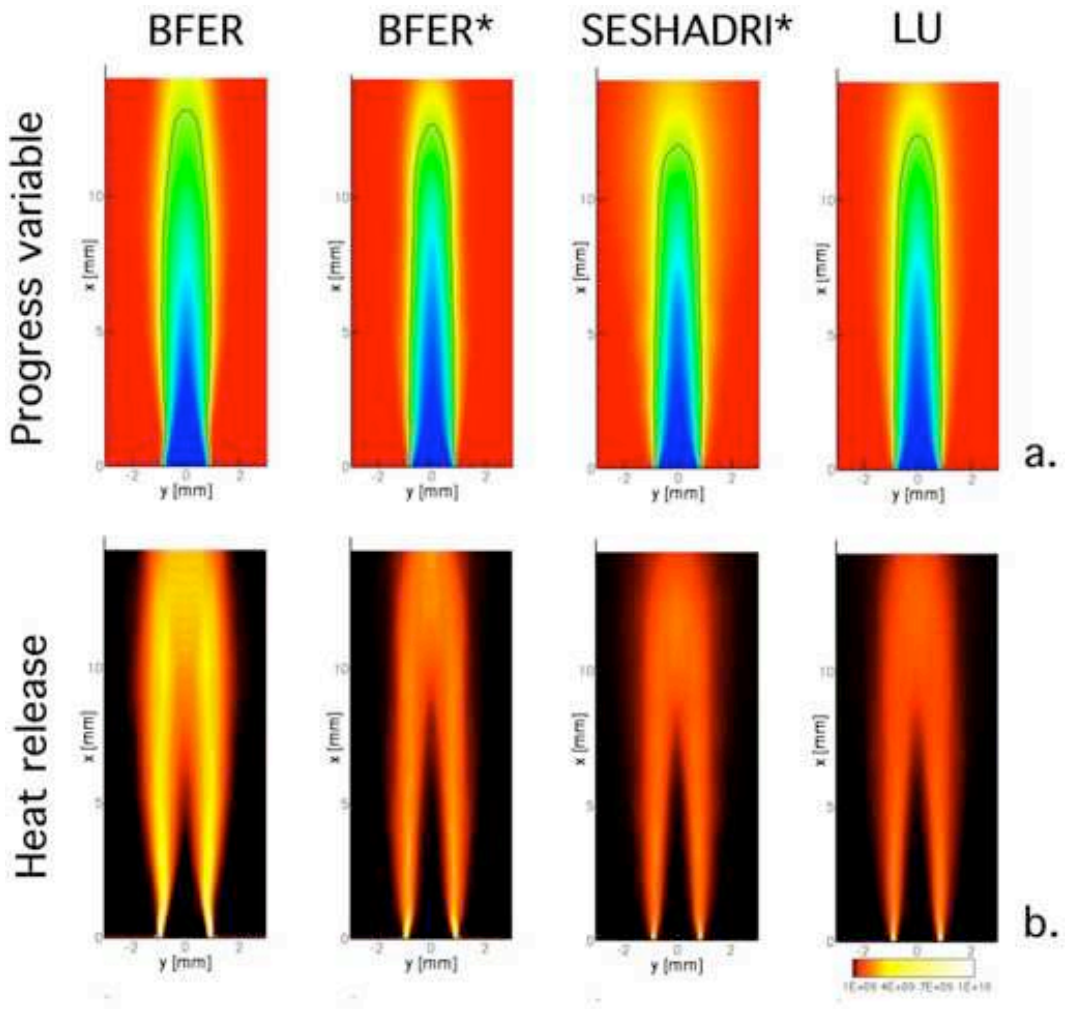

Figure 4.32 - *a) Mean progress variable $\tilde{c}$ shown as a pseudocolor plot (blue=0, red=1); the solid line represents the isoline of $c = 0.65$. b) Mean heat release. Comparison for different reduced mechanisms from left to right: 2S_CH4_BFER (left), 2S_CH4_BFER*, SESHADRI* and LU (right).*

Flame thickness

From the flame/vortex and the flame/HIT analysis in Sections 4.1 and 4.2, the interaction of turbulence with the flame is expected to modify the flame thickness. The mean normalized gradient of the progress variable is displayed in Fig. 4.33 for the four chemical mechanisms at the half of the domain height. High discrepancies on the maximum value are found for both two-step schemes which are mainly due to the underestimation of the laminar unstrained flame thickness (cfr. Section 3.2.1).
These results are compared with the laminar behavior in Fig. 4.34 (DNS results - dashed line and laminar results - solid line). The preheat zone ($c < 0.3$) is generally thickened due to the presence of small eddies interacting with this region as in the HIT configura-

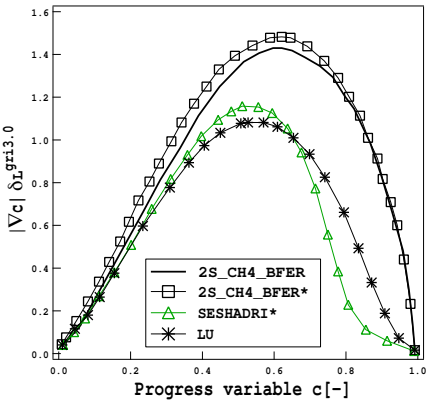

Figure 4.33 - *Mean gradient of normalized progress variable as function of the progress variable at half of the domain length in the streamwise direction. Comparison between the different reduced mechanisms.*

tion. But, as also seen for the flame/HIT configuration, some discrepancies are detected in the reaction zone ($0.6 < c < 0.8$): the SESHADRI* and LU flames are slightly thinned by the large length scale structures whereas the reaction zone is thickened when using a two-step scheme. The postflame zone is relatively unchanged for all mechanisms.

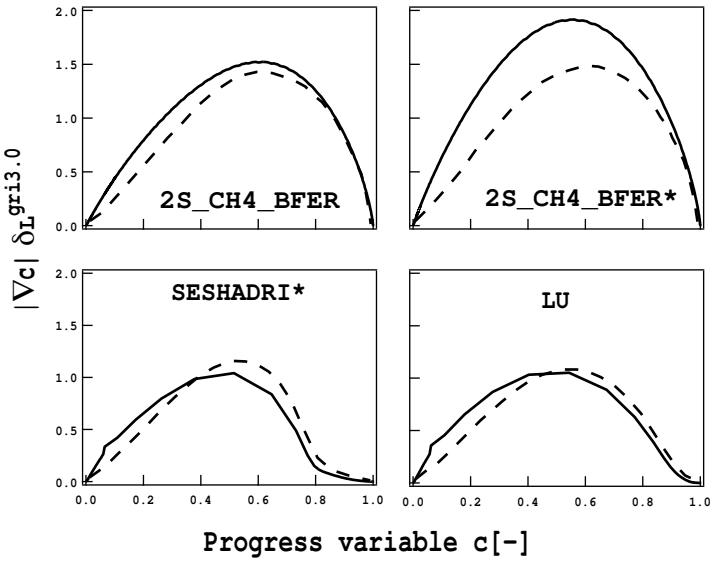

Figure 4.34 - *Mean normalized gradient of progress variable $|\nabla c|\delta_L^{GRI3.0}$ (dashed line) as function of the progress variable at half of the domain length in the streamwise direction. Comparison with laminar results (solid line) for the four reduced mechanisms.*

The impact of stretch on the thickness of the reaction zone, i.e. at $c = 0.65$, is investigated in Fig. 4.35 in terms of flame curvature and tangential strain rate. Results

are similar for all mechanisms and coherent with the observations on laminar and academic configurations. The thickness of the reaction zone decreases when the tangential strain rate increases (Fig. 4.35a.) whereas it increases with the curvature absolute value (Fig. 4.35b.).

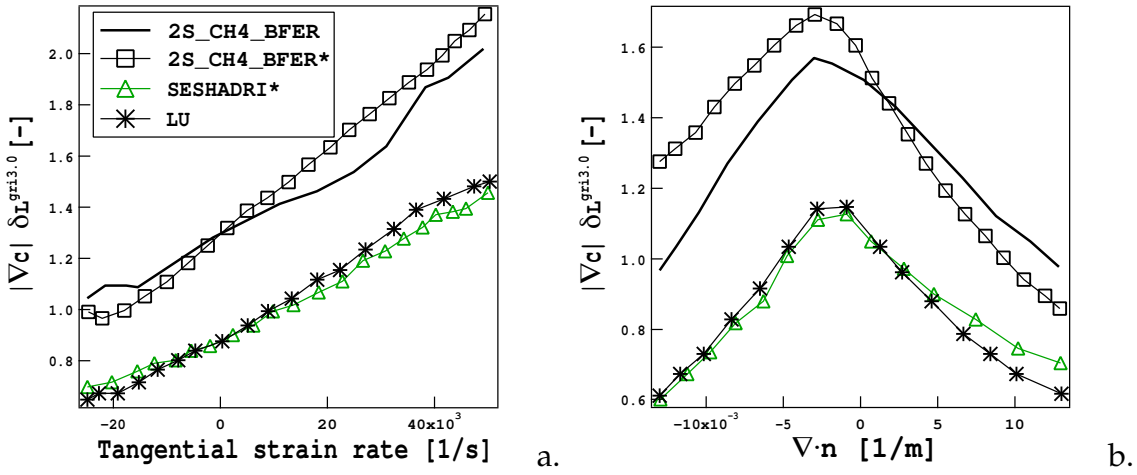

Figure 4.35 - *Mean normalized progress variable magnitude as a function of a) tangential strain rate and b) flame curvature at isoline $c = 0.65$ at half of the domain length in the streamwise direction. Comparison between the four reduced mechanisms.*

Strain rate and curvature

The probability density function of the **tangential strain rate** conditioned by the flame surface ($c = 0.65$) at half of the domain length is displayed in Fig. 4.36a. The distribution for tangential strain rate obtained with the 2S_CH4_BFER* and the SESHADRI* mechanisms are in very good agreement with the reference LU scheme, whereas small discrepancies are outlined for the 2S_CH4_BFER mechanism (cfr Fig. 4.36a). The maximum probability for the tangential strain rate is positive for all mechanisms and extremely high strain rates have a quasi-zero probability to occur. The maximum probability occurs for an higher tangential strain rate when using the 2S_CH4_BFER scheme. More than half of the probability belongs to positive strain rate denoting that negative strain rate is less likely to be seen.
The probability density function of **flame curvature** conditioned on the flame surface at half of the domain length is reproduced in Fig. 4.36b. Its distribution is correctly described with all three tested mechanisms. Very high negative curvatures are less likely to be seen compared to very high positive values but convex and concave curvatures roughly have the same probability to occur. However, the maximum probability is found for a small negative curvature.

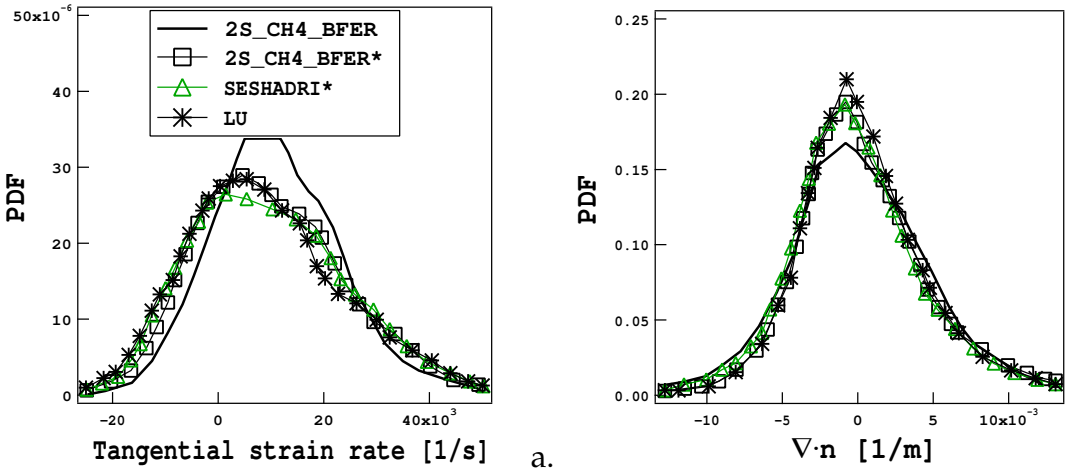

Figure 4.36 - *a) Tangential strain rate PDF and b) curvature PDF conditioned by $c = 0.65$ at half of the domain length. Comparison between the four reduced mechanisms.*

Global burning parameters

To further analyze the behavior of the reduced mechanisms, global burning parameters are studied in the following. As already discussed in Section 1.2, the wrinkled flame area A_T, here defined as the instantaneous area of the iso-surface $c = 0.65$ (plotted in Fig. 4.32), is supposed to be linked to the turbulent combustion speed S_T (Eq.(1.47)):

$$S_T = \frac{A_T}{A_L} I_0 S_L = \frac{A_T}{A_L} \overline{S}_C = A' \overline{S}_C, \tag{4.10}$$

where A' is the flame wrinkling, I_0 is the burning intensity, $\overline{S}_C$ is the mean local flamelet consumption speed (Fig. 1.5 in Section 1.2.2) and S_L is the reference laminar flame speed $S_L = S_L^{GRI3.0} = 1.817$ for the unstrained premixed flame obtained with the detailed GRI3.0 mechanism at the BUNSEN operating point. The turbulent burning velocity is then:

$$\frac{S_T}{S_L^{GRI3.0}} = A' I_0 \tag{4.11}$$

which is related to the mean surface density $\overline{\Sigma}$ [27]:

$$\frac{S_T}{S_L^{GRI3.0}} = I_0 \int_{-\infty}^{+\infty} \Sigma d\mathbf{n} \quad \text{and} \quad A_T = \int_{-\infty}^{+\infty} \Sigma dV = \int_{-\infty}^{+\infty} \Sigma A_L d\mathbf{n}. \tag{4.12}$$

For a Bunsen flame, the turbulent speed S_T is estimated from the flow rate supposing complete burning (so that the consumption speed is directly related to the inlet mass flow rate) [52]:

$$\rho_f S_T A_L = \rho_f S_L^{GRI3.0} A_T I_0 = \dot{m}_{in}, \tag{4.13}$$

where ρ_f is the density of fresh gas and $\dot{m}_{in}$ is the mass inflow of reactants integrated over the inflow plane A:

$$\dot{m}_{in} = \int_A \rho_f u_f dA, \tag{4.14}$$

where u_f is the inlet velocity. Therefore, assuming that the turbulent Bunsen flame consists of two turbulent flame fronts aligned with the (x,z) plane, the turbulent burning velocity is evaluated at each axial location from $N_t = 60$ instantaneous solutions according to:

$$\rho_f S_T = \frac{1}{N_t} \sum_1^{N_t} \int_{-\infty}^{\infty} \int_0^{L_z} \dot{\omega}_c .dz.dy/(2L_z). \tag{4.15}$$

The turbulent-laminar ratio of the flame area at each streamwise location is obtained by integrating the flame surface density (given by $|\nabla c|$) across the (y,z) plane from $N_t = 60$ instantaneous solutions:

$$\frac{A_T}{A_L} = \frac{1}{N_t} \sum_1^{N_t} \int_{-\infty}^{\infty} \int_0^{L_z} |\nabla c| .dz.dy/(2L_z). \tag{4.16}$$

It represents the first effect of turbulence on the flame front.

The flame wrinkling A', the burning velocity and the burning intensity I_0 are plotted in Fig. 4.37 along the streamwise direction and their averaged values are summarized in Table 4.9. The **flame wrinkling** A' predicted by the reduced 2S_CH4_BFER* and

Table 4.9 - *Global burning parameters averaged on the flame length.*

	2S_CH4_BFER	2S_CH4_BFER*	SESHADRI*	LU
Burning velocity	1.356	1.611	1.143	1.135
A'	1.23	1.54	1.34	1.41
I_0	1.18	0.741	0.855	0.79

SESHADRI* mechanisms is in a very good agreement with the LU scheme, whereas significant discrepancies are detected downstream for the 2S_CH4_BFER scheme. It should be noticed that Eq. (4.16) gives a good estimation of the flame wrinkling until the Bunsen flame presents two distinct flame fronts. The flame wrinkling is less to one where the two flame fronts meet, i.e. near the tip of the flame.

Looking at Eq. (4.10), it is clear that the **burning intensity** I_0 (Fig. 4.37b.) represents the deviation of the local consumption speed $\overline{S}_C$ to the laminar flame speed $S_L^{GRI3.0}$ due to the response of the chemical mechanism to stretch. Generally, high strain rates and curvatures are detected in the flame near the inlet which reduces the burning intensity I_0 of the flame. If it were not for the supply of hot products from the coflow, it

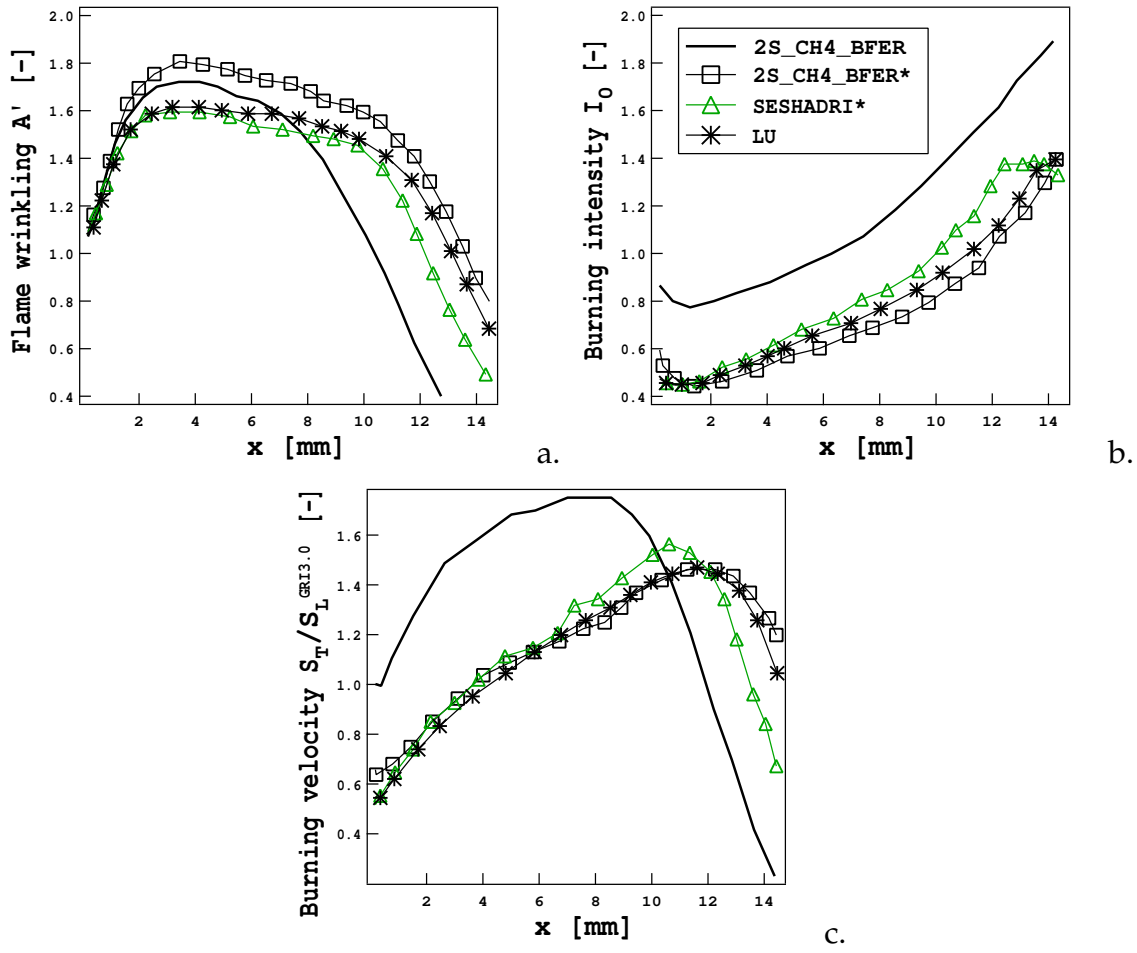

Figure 4.37 - *Mean a) flame wrinkling, b) flame burning intensity factor and c) turbulent flame speed evaluations along the axial direction of the flame. Comparison between the four reduced mechanisms: 2S_CH4_BFER (– –), 2S_CH4_BFER* (. . .), SESHADRI* (– · –); and LU (—).*

would probably extinguish. As the strain rate and the curvature decrease downstream the value of I_0 increases again. The burning intensity I_0 is greatly overestimated by the 2S_CH4_BFER scheme, since it is only slightly affected by strain rate and curvature, whereas the modified 2S_CH4_BFER* and the SESHADRI* mechanisms correctly predict it .

Since no relevant differences between reduced mechanisms have been detected in terms of the flame wrinkling, discrepancies on the **turbulent burning velocity** for the 2S_CH4_BFER are mainly due to the overestimated burning intensity I_0 (Fig. 4.37c.). The turbulent burning velocity S_T/S_L predicted by the LU scheme is less than one near the flame inlet since the high strain rate affects the flame front. The turbulent speed S_T has been divided by the flame speed $S_L^{GRI3.0}$ of an unstrained laminar flame that largely overestimates the consumption speed S_C of laminar strained flames. Since the

consumption speed predicted by the 2S_CH4_BFER scheme is not affected by strain rate, the burning velocity is generally overestimated.

As already noticed, the burning intensity is largely overestimated by the 2S_CH4_BFER scheme whereas the global burning parameters are correctly predicted by both the 2S_CH4_BFER* and SESHADRI* scheme. Results are therefore in agreement with the conclusions on laminar strained flames and on flame/vortex and flame/HIT configurations.

4.4 Conclusions

In this chapter, the performances of five different reduced mechanisms have been evaluated and compared to the thirteen-species LU scheme, used as a reference, on three different configurations with increasing complexity:

- two-dimensional flame/vortex configuration;
- three-dimensional flame interacting with a homogenous isotropic turbulent field;
- three-dimensional stationary lean premixed Bunsen flame.

In these calculations, turbulence was fully resolved (DNS approach). Different flame characteristics have been analyzed in all cases:

- **Flame thickness:** in the reaction-sheet regime, the smallest eddies are expected to thicken the preheat zone while large scale structures are expected to thin the flame through high stretch. In the flame/HIT and the Bunsen flame configurations, all mechanisms except the 2S_CH4_BFER* scheme are able to reproduce the impact of turbulence on flame thickness. The preheat zone is thickened whereas the reaction zone thickness varies with the strain rate and curvature: for higher values of strain rate, the reaction zone is thinned (in agreement with laminar results) whereas the thickness increases with curvature. Similar conclusions have been drawn for the flame/vortex interaction concerning the reaction zone, but no thickening of the preheat zone has been observed since this configuration belongs to the corrugated flamelet regime. The unrealistic behavior of the 2S_CH4_BFER* scheme, predicting a thickened reaction zone for small values of strain rate, has already been observed in laminar calculations and is probably due to the use of a high species Lewis number, $Le_k = 1.65$.
- **Global burning parameters** (consumption speed / burning intensity/ turbulent speed): these quantities highly depend on the chemical mechanism and its response to stretch. A good prediction of the burning intensity is essential since it

controls the turbulent flame and consequently, the flame length.
Generally, the consumption speed is expected to decrease when strain rate increases but the reduced mechanisms differently respond to stretch. Their behavior on turbulent flames is strictly related to laminar results: the 2S_CH4_BFER scheme is quite insensitive to stretch, but its modified version 2S_CH4_BFER* corrects this behavior. As a consequence, the Bunsen flame predicted by the 2S_CH4_BFER scheme has a too high intensity whereas better results are obtained with the 2S_CH4_BFER* mechanism. Since the JONES* scheme wrongly interacts with stretch, it has not been tested in the Bunsen flame configuration. Finally, the SESHADRI* scheme has a correct response to stretch in terms of consumption speed and as a consequence, the Bunsen flame predicted by this mechanism is similar to the LU solution.

- **Flame wrinkling:** it depends on the interaction between turbulence and flame, i.e. the combustion regime, and on the consumption speed response to strain rate. It is generally overestimated by the 2S_CH4_BFER and JONES* schemes since they overestimate the turbulent speed.

- **Flame structure:** even if the smallest eddies could interact with the preheat zone, the inner flame structure is basically conserved. The flame structure has been investigated looking at the concentration of the intermediate *CO* species highly sensitive to stretch. The turbulent flame results are similar to laminar strained flames with a maximum value of the *CO* mass fraction which decreases when strain rate increases. Only analytical schemes seem to be able to predict the *CO* mass fraction in turbulent flames.

The **computational cost** strongly depends on the number of species solved by the different mechanisms. The reduced computational cost for the Bunsen flame configuration is shown in Table 4.10. The two-step schemes and the SESHANDRI* mechanism take into account six and eight species respectively and the computational cost is drastically reduced of about 35% – 25% respectively compared to the LU calculation solving 13 species balance equations.

Table 4.10 - *Reduced computational cost needed for the 3D Bunsen flame simulation.*

2S_CH4_BFER	2S_CH4_BFER*	SESHADRI*	LU
0.625	0.625	0.722	1.0

The main conclusion is that the performances of the different schemes for turbulent flames are generally comparable to results for laminar strained flames in terms of flame structure and burning intensity. The modification of the two-step scheme (2S_CH4_BFER) in order to predict the consumption speed of laminar strained flames

has been tested. The modified 2S_CH4_BFER* scheme correctly reproduces the global burning parameters of the Bunsen flame and results are greatly improved compared to 2S_CH4_BFER solution. Using the modified mechanism, the computational cost is reduced of about 35% and the result accuracy is preserved.

Chapter 5

Impact of the reduced chemical mechanisms on LES of a lean partially premixed swirled flame

Performances of six reduced mechanisms for methane/air premixed combustion have been evaluated on laminar tests (Chapter 3) and DNS of academic and Bunsen flame configurations (Chapter 4). One of the main conclusions is that the description of some quantities such as the turbulent flame speed or the flame structure in turbulent flames strongly depend on the response to strain rate of the chemical mechanisms for a laminar strained flame. The validity of this conclusion is hereafter analyzed for an industrial partially premixed flame.

In this Chapter, the performances of the six reduced mechanisms (2S_CH4_BFER, 2S_CH4_BFER*, JONES, PETERS, SESHADRI and LU) introduced in Chapter 3 as well as the FPI_TTC* tabulation method are investigated in the experimental PRECCINSTA burner in terms of species concentrations, temperature and flame structure.

The objective here is to identify the characteristics of a reduced mechanism mostly impacting the LES of realistic turbulent flames in order to:

- be able to build from one-dimensional tests a reliable reduced scheme which correctly predicts the quantities of interest in three-dimensional configurations;
- select the mechanism offering the best compromise between CPU cost and result accuracy.

The PRECCINSTA experimental burner is an adequate configuration to reach

this objective. The behavior of this configuration, derived from an industrial design by Turbomeca, is representative of an industrial gas turbine combustor and has been widely described and studied experimentally [168, 169, 107] and numerically [133, 66, 3, 61, 111].

Two different regimes have been detected experimentally (see Table 5.1) and quite or pulsating swirled flames have been observed [107] depending on the global equivalence ratio. A comparison between the two operating points and an analysis of the thermoacustic instabilities will be proposed in Chapter 6, whereas in this Chapter, only the behavior of the stable flame is analyzed (case 2a, $\phi = 0.83$).

Table 5.1 - *Flame parameters of the experimental cases*

case	Air flow $[g/min]$	Methane flow $[g/min]$	Thermal power P_{th} $[kW]$	Global equivalence ratio $\phi[-]$
1	734.2	30.0	25.1	0.70
2a	734.2	35.9	30.0	0.83

In Section 5.1, the experimental setup of the PRECCINSTA burner is presented together with the available experimental measurements. In Section 5.2, the different numerical parameters are described, with particular attention to the new thickening sensor based on the species production/consumption rate proposed in Section 3.4. Finally in Section 5.3, results for the different reduced mechanisms and for the FPI_TTC* method are compared to the experimental data and the numerical results obtained with the reference LU mechanism. Additional analysis of the flame, such as the flame length and the turbulent flame speed, are presented and the impact of grid resolution is also discussed. Finally, an *a priori* methodology based on one-dimensional unstrained and strained laminar flames is proposed to evaluate the capability of any mechanism to reproduce the main chemical phenomena of a three-dimensional turbulent partially premixed flame.

5.1 The PRECCINSTA burner

The PRECCINSTA burner is an experimental configuration for the study of a partially premixed swirled flame. Geometry is sketched in Fig. 5.1. Air is injected into the plenum through one large air intake while methane is injected through twelve small tubes of diameter 1 *mm* directly into the swirler (Fig. 5.2) methane and air are then

mixed by the high momentum flow of the swirler and a methane/air mixture, supposed homogeneous, enters the combustion chamber.

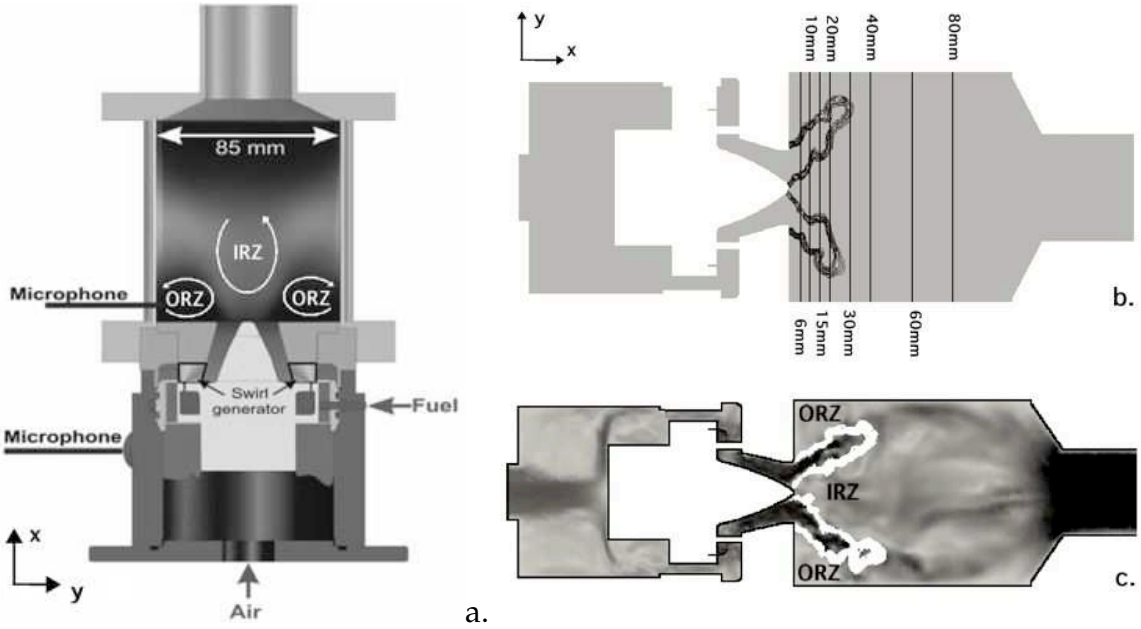

Figure 5.1 - *a) Sketch of the PRECCINSTA design. b) Visualization of the experimental measurement planes [107]. Isolines of heat release identify the reaction zone. c) Velocity field and sketch of the different zones. The white region identifies the FG/IRZ and FG/ORZ layers.*

A swirled flame with the classical conical shape, is then stabilized at the nozzle exit. Different zones may be identified in the chamber (Fig. 5.1c.):

- An **inner recirculation zone** (IRZ) located in the inner zone of the flame, characterized by the highest temperatures. The transport of combustion products by the reverse flow backward to the nozzle is the essential mechanism for flame ignition and stabilization.

- A conically-shaped **fresh gas** (FG) injection characterized by lower temperatures but high axial and radial velocities.

- Two **outer recirculation zones** (ORZ) composed of burnt gases, located close to chamber walls. Generally, their temperature is smaller than the equilibrium temperature, i.e. the IRZ temperature, due to wall heat losses. Flow velocities are usually small in this region.

- An inner **FG/IRZ layer**, separating the IRZ and fresh gases, and an outer **FG/ORZ layer**, located between the fresh gases and the ORZ. Reactions take place in these

layers which are experimentally characterized by the highest velocity fluctuations and the highest concentrations of intermediates species such as CO and H_2.

The burnt gases finally exit the chamber through the exhaust tube. The chamber dimensions are $L_x \times L_y \times L_z = 114\ mm \times 85\ mm \times 85\ mm$, where L_x, L_y and L_z are the chamber sizes in the axial, tangential and transverse directions respectively (Fig. 5.1a.).

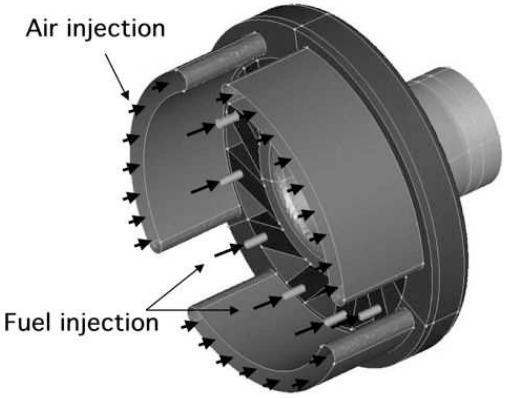

Figure 5.2 - *Details of the injector showing the twelve injections of methane and the air injection [2].*

5.1.1 Experimental measurements

Laser Raman scattering measurements are available for concentration of the major species (CH_4, CO, CO_2, H_2O, H_2, N_2 and O_2) and for temperature in vertical planes (y, z) at eight different axial positions downstream of the injector ($h = 6, 10, 15, 20, 30, 40, 60, 80\ mm$, where $h = 0\ mm$ corresponds to the exit plane of the nozzle) for at least five radial positions r (Fig. 5.1b). The systematic and statistical uncertainties are less than 4% and 2.5% respectively for temperature and less than 5% and 7% respectively for almost all species expect for CO and H_2 for which statistical uncertainty is between $20 - 50\%$ [107]. A summary of the measurement uncertainties is given in Table 5.2.

Laser Doppler Velocimetry (LDV) measurements of the velocity field were also performed. Unfortunately, the operating point corresponds to slightly different conditions ($\phi = 0.75$) for which an unstable flame was not completely silent and can not be used for a direct comparison with stable flame results.

Table 5.2 - *Summary of the measurement uncertainties [107].*

Measured quantity	Systematic uncertainty	Statistical uncertainty
Temperature	±3 – 4%	±1.5 – 2%
H_2O mole fraction	±3 – 5%	±3% (density-dependent)
O_2 mole fraction	±3 – 5%	±7% (density-dependent)
CO_2 mole fraction	±3 – 5%	±7% (density-dependent)
CO mole fraction	±5 – 10%	±20 – 50% (density-dependent)
H_2 mole fraction	±5 – 10%	±10 – 30% (density-dependent)
N_2 mole fraction	±5 – 9%	±1 – 3% (density-dependent)

5.2 The numerical setup

Numerous simulations of the PRECCINSTA configuration have been proposed [133, 66, 3, 61, 111]. Previous studies have always assumed a perfect mixing between methane and air at the nozzle exit, which simplifies the computational work: there is no need to account for the small tubes injecting methane and to resolve the mixing zone between air and methane. Instead, a perfect methane/air mixture at the global equivalence ratio $\phi = 0.83$ is directly injected in the plenum and the computational cost is reduced. Results are globally in agreement with experimental data even if the mixing is incorrectly described and difficulties in describing the near-wall zone have been detected.
Only recently, fuel/air mixing has been explicitly computed including fuel jets into the swirler in order to estimate the impact of the perfect premixing assumption on prediction of major species concentration [2], NO_x formation [138] or thermo-acoustic instabilities [62].
Therefore in the following, LES are performed without the perfect mixing assumption to better reproduce the experimental setup: dry air and pure methane are injected separately and their mixing is completely resolved in the swirler (Fig.5.3).
The same numerical setup is used for all computations to guarantee consistent comparisons of the results and to correctly identify the impact of the reduced chemical mechanisms.
In the following, each calculation is identified by the name of the chemical description used.

5.2.1 Mesh, numerical method and boundary conditions

The same numerical parameters used in [62] have been kept to perform the present LES with the different reduced mechanisms, and are summarized below.

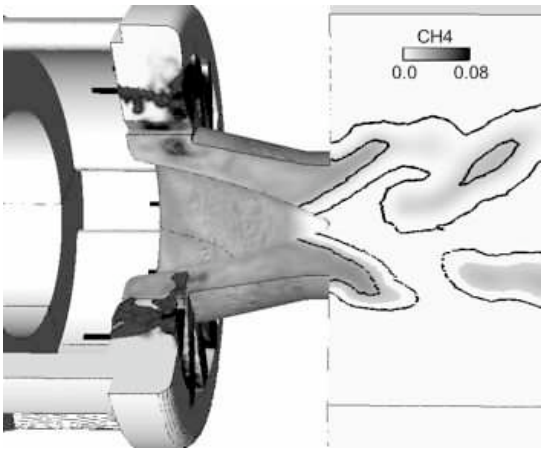

Figure 5.3 - *Details of the methane injection colored by methane mass fraction. Black iso-lines represents the heat released.*

An overview of the computational domain is presented in Fig. 5.4. As the chamber exhaust has not been acoustically characterized in the experiments, the numerical domain has been extended far downstream of the combustion chamber including a part of the outside atmosphere and imposing a non-reflective boundary condition at its outlet [133]. The full realistic geometry is meshed including the twelve methane injection holes as shown in Fig. 5.5. The mesh is unstructured and contains about five millions tetrahedral elements. The mesh is refined inside the swirler vanes in order to obtain a good description of the mixing phenomenon. There are at least five cells in radial direction for each methane injection hole, which means that the cell length is about 0.2 mm in the holes. Those cells are the smallest in the computational domain. The size of the cells where reactions presumably take place is about 1 *mm*.

A Taylor-Galerkin weighted residual central distributions scheme is used for numerical integration [45].

The inlets for methane and air and the outlet are described by Navier-Stokes Characteristic Boundary Conditions (NSCBC) [113, 142, 122] to ensure a physical representation of the acoustic wave propagation and reflection. An adiabatic no-slip condition is applied to all walls. The outlet NSCBC condition recently proposed by Granet et al. [72] is imposed on the entire outer atmosphere boundary. Dry air and pure methane flows are imposed at ambient temperature at the plenum inlet and at the swirler holes respectively, according to the experimental setup (Table 5.1). Note that there is a slight preheating in the experiments [107] and that the temperature of the fuel/air mixture varied between 320 and 380 K prior to entering the combustion chamber. Moreover during the measurements, the ambient pressure varied between 995 and 1030 mbar. These differences may have a slight influence on the results, and should be kept in mind when comparing them.

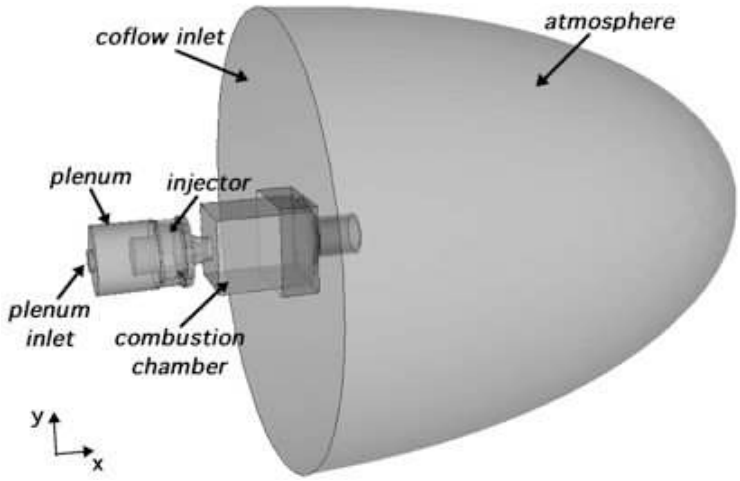

Figure 5.4 - *Sketch of the computational domain.*

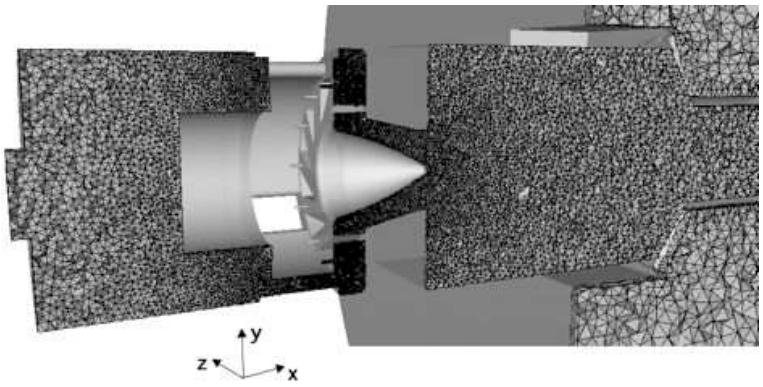

Figure 5.5 - *Computational half-domain mesh.*

An initial non-reacting calculation is performed to correctly initialize the velocity field. The species mass fractions and temperature from an equilibrium calculation are then imposed in the combustion chamber. A hyperbolic tangent function is used to obtain a smooth variation between the burnt and fresh conditions. The atmosphere is initially filled with pure N_2 at the burnt gas temperature of the injected mixture to avoid any unphysical chemical recombination between burnt gases and fresh air at the chamber exit. To maintain N_2 in the atmosphere, a coflow of N_2 is injected at the inlet of the atmosphere with low velocity (5 m/s) compared to the burnt gas velocity at the chamber exit.

The averages are collected over 35 *ms* of physical time. Scatterplots and statistical information are deduced from more than 100 instantaneous solutions collected every 0.2 *ms*. When using the FPI_TTC* method, result accuracy strongly depends on the discretization of the look-up table. In the LES of the PRECCINSTA burner, the same

dimensions of the table as for the unstrained premixed flames of Section 3.3 (i.e. 1000 points for the progress variable c^{fpi} and 2000 for the mixture fraction z^{fpi}) are used. The memory size reaches 0.064 *Go*, which could be easily handled by most of the calculators.

5.2.2 Artificially thickened flame model

The interaction between the chemical kinetics and turbulence is modeled by the DTFLES model presented in Section 3.4. There are at least two difficulties when comparing several chemistry models using the DTFLES model. First, the thermal thickness varies with the mechanism (see Table 3.9 in Section 3.2.1) and the equivalence ratio (see Fig. 3.13 in Section 3.2.1). Second, the number and the roles of reactions are different. The improved DTFLES model presented in Section is therefore used in the PRECCINSTA configuration.

The thickening sensor, identifying the zone where the thickening and the efficiency functions are applied, is based on the production/consumption rate $\dot{\omega}_{Y_c} = \dot{\omega}_{Y_{CO}} + \dot{\omega}_{Y_{CO_2}}$ to be consistent with the FPI_TTC* formulation. Using this sensor, the flame is thickened very similarly whatever the mechanism used, on both the reaction zone (where CO is produced) and the post-flame zone (where CO recombines into CO_2). Instantaneous fields of thickening function are displayed in Fig. 5.6 for the reduced mechanisms tested and the FPI_TTC* calculation. Thickening is applied locally where the flame is located (here identified by the iso-line of heat release). No thickening is applied downstream of the flame where mixture is in an equilibrium state and no reaction occurs. Moreover, the thickening function varies locally: close to the nozzle where the grid is more refined $\Delta x = 1.0$ *mm* (see Fig. 5.5), small values of the thickening function are detected ($\mathcal{F} \approx 3 - 4$) whereas the thickening function takes higher values downstream in the chamber where the mesh is coarser $\Delta x \approx 1.8$ *mm* ($\mathcal{F} \approx 12$). The thickening function correctly accounts for the cell size to guarantee at least five points in the flame front.

5.3 Analysis of results

Figure 5.7 first compares the numerical results and the experiments in terms of mean temperature field. The measurements being restricted to the region $r < 30$ *mm* due to the visualization window dimension, no experimental result is available near the walls. The overall agreement is acceptable but a detailed analysis showns non-negligible differences between the chemical modes. A small flame, rapidly reaching the equilibrium state, is obtained in the 2S_CH4_BFER and JONES cases whereas a longer flame with lower temperature in the ORZ and in the near-wall region is found in the

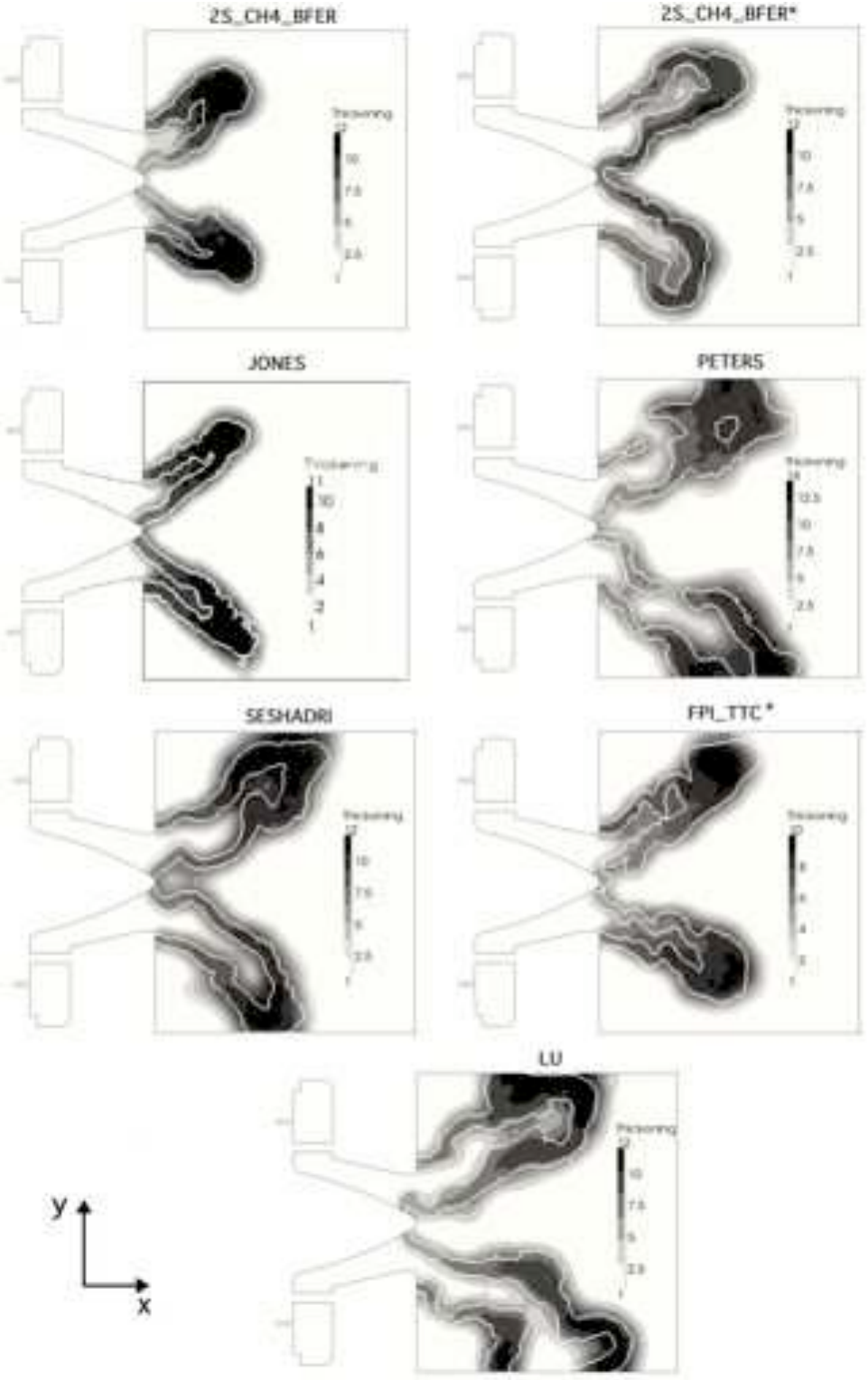

Figure 5.6 - *Instantaneous thickening function for the different chemistries. The flame position is identified by the white iso-line of heat release. Different scales are used to reproduce the thickening function of the different chemical descriptions.*

2S_CH4_BFER* simulation. The analytical schemes are better in agreement with the LU mechanism, predicting the longest flames and a recombination zone touching the wall downstream of the flame ($-40\ mm < r < -30\ mm$ and $25\ mm < h < 50\ mm$). The FPI_TTC* method shows an accurate flame length but slightly underestimates the opening angle of the flame.

In Chapters 3 and 4 it has been shown that the LU mechanism could be considered as accurate as the detailed GRI3.0 scheme. The discrepancies between the results of LU and the experiments are likely to be due to some numerical simplifications such as the combustion model, the adiabaticity assumption and the numerical discretization, but not to the chemical description. Especially, the prediction of the temperature in the ORZ as well as in the near-wall region is inaccurate when neglecting wall heat losses and radiation effect in the simulation. However, since the objective of this work is to study the impact of the chemical description on LES of turbulence complex three-dimensional flames, LU results, although biased by numerous modeling assumption, will be taken as a reference.

5.3.1 Mixing

Since methane and air are injected separately, the mixture entering the PRECCINSTA burner is not perfectly mixed and its equivalence ratio varies with time and space. Results are then impacted by the quality of the mixing prediction and the response of the chemistry to varying equivalence ratios.
The Bilger definition of the mixture fraction based on the atomic mass fraction (see Eq. (2.34) in Section 2.2) is preferred to the FPI_TTC* definition (Eq. (3.64)) for the mixture fraction z^{fpi}, which is a passive scalar only assuming unity Lewis numbers. With the Bilger definition, the mixture fraction of a stoichiometric mixture is equal to $z_{st} = 0.055$ whereas the mixture fraction corresponding to the equivalence ratio of PRECCINSTA is $z = 0.0461$.
Figure 5.8 displays the scatterplots of instantaneous temperature versus mixture fraction for the experiments and the seven chemical descriptions in four different vertical (y, z) planes ($h = 6, 15, 30$ and $80\ mm$). The correlation between temperature and mixture fraction is correctly predicted whatever the chemical description: the highest variations of mixture fraction are found in the closest plane to the nozzle exit ($h = 6\ mm$). Downstream in the chamber, the mixture fraction variations decrease as the distance to the nozzle exit increases, approaching the equilibrium. Both experimental and numerical results are characterized by a wide range of mixture fraction at injection ($h = 6\ mm$), the fresh gases represented by the points with the lowest temperature ($T \approx 320\ K$) being not perfectly premixed. At this stage, the mixture fraction distribution is correctly predicted by all mechanisms (see Fig. 5.9) although the extreme values are generally underestimated.

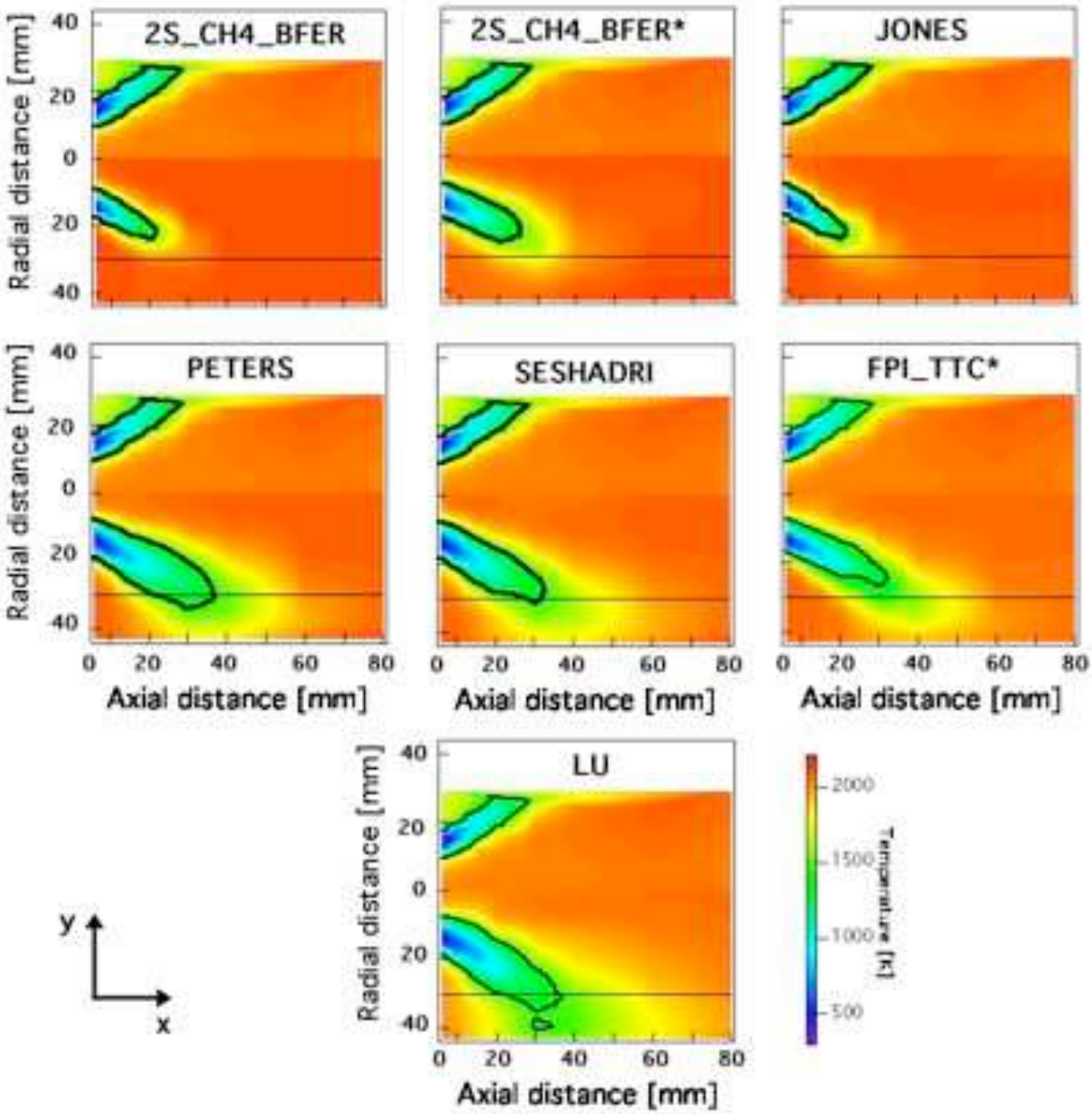

Figure 5.7 - *Mean temperature field in the* (x, y) *plane. Comparison between LES (bottom) and experiments (top) for the seven chemical models tested. Black iso-line of the progress variable* $c = 0.65$ *represents the mean flame surface position.*

Experiments show that the fresh gases are still present at $h = 15$ *mm*, which is difficult to describe for all mechanisms. At $h = 30$ *mm*, the lowest values of temperature are

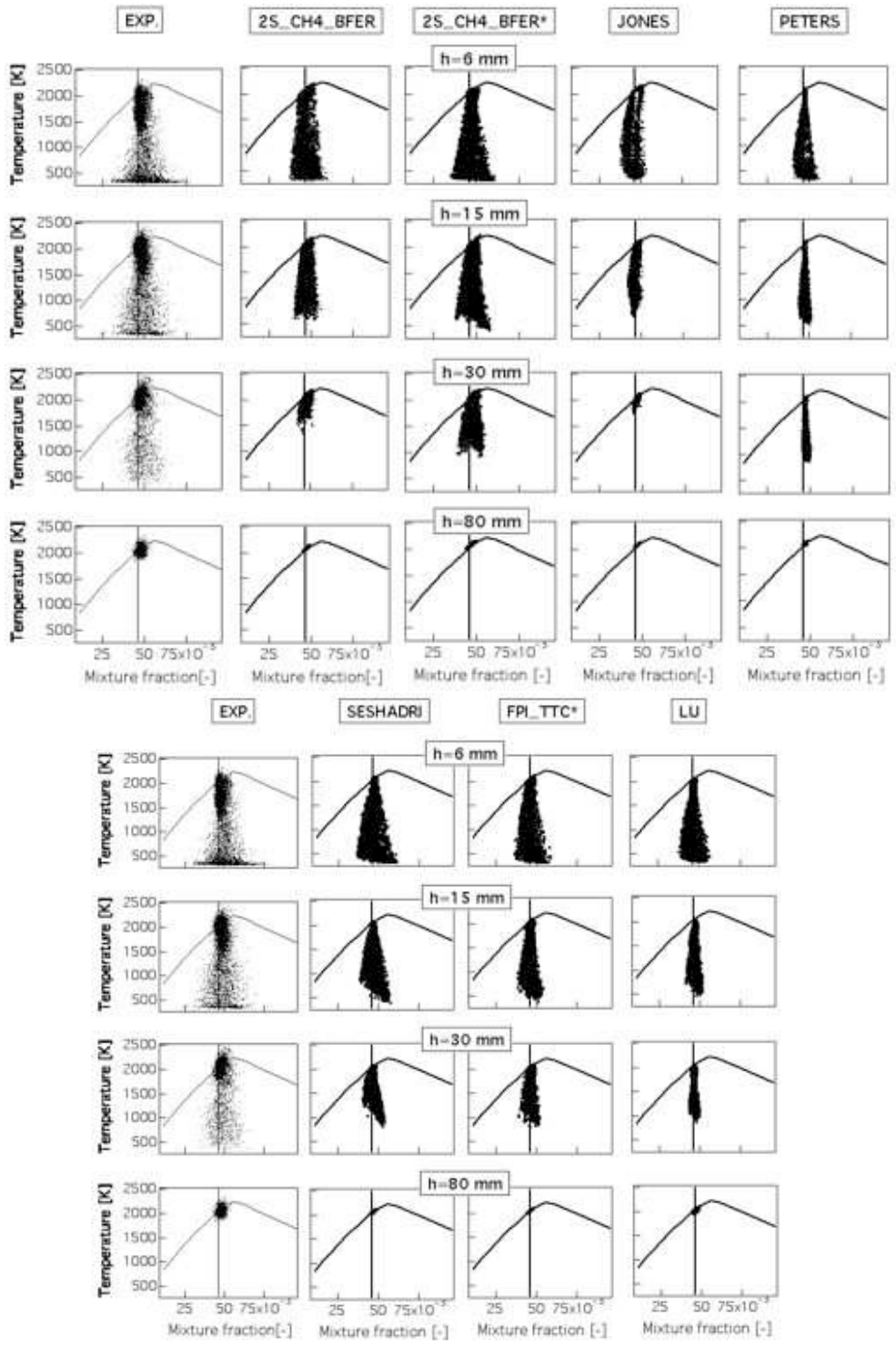

Figure 5.8 - *Scatterplot of instantaneous temperature versus mixture fraction at four measurement planes ($h = 6, 15, 30, 80$ mm). Comparison between experiments and numerical results using the seven chemical descriptions.*

not captured by the 2S_CH4_BFER and JONES schemes, agreeing with their prediction of a smaller flame which is already at equilibrium in this region. The 2S_CH4_BFER* mechanism slightly underestimates the flame length compared to the LU scheme but the correlation at $h = 30\ mm$ is correctly predicted. Close to the chamber exit ($h = 80mm$), the equilibrium state is reached for all the chemical descriptions and the variations in mixture fraction are drastically reduced.

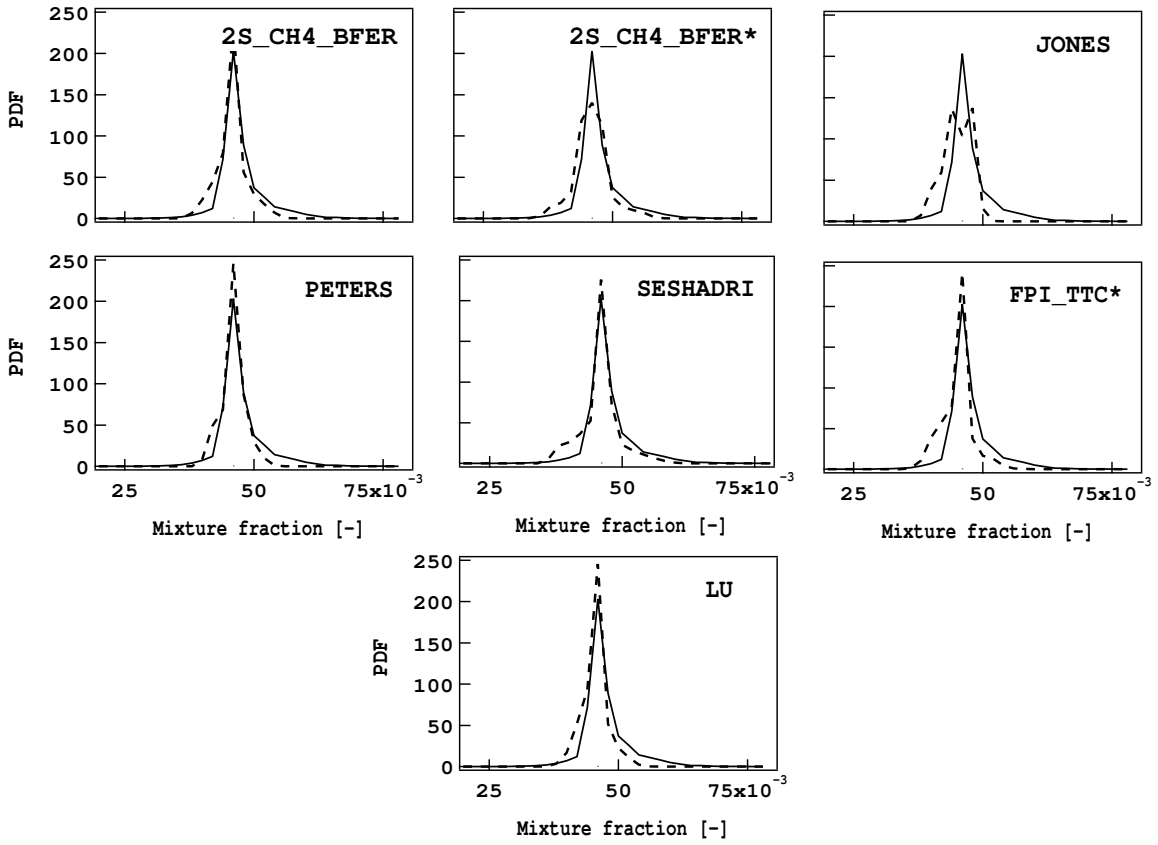

Figure 5.9 - *Mixture fraction distribution at the first measurement plane ($h = 6\ mm$): experimental data (——) and numerical results (– –) for the seven chemical descriptions.*

Performances of the different mechanisms have been evaluated for perfectly premixed combustion in DNS calculations in Chapter 4, but the mechanism behavior could be affected when simulating a partially premixed flame if it has an incorrect response to equivalence ratio variation. For example, the JONES and PETERS mechanisms are expected to fail the description of rich burning mixture since largely underestimating the laminar flame speed for premixed flames at $\phi > 1.2$ (Fig. 3.11 in Section 3.2.1).
The partial premixing is assessed integrating the probability density functions of Fig. 5.9 over the different ranges of equivalence ratio to analyze the equivalence ratio of the mixture at the first measurement plane ($h = 6\ mm$). Results are given in Table 5.3. The

maximum probability is reached at the global equivalence ratio $\phi = 0.83$ ($z = 0.461$). Globally, the agreement between the reduced chemical descriptions and the experimental results is satisfactory but some discrepancies are detected. More than 50% of the probability belongs to $z < 0.0461$ and a mixture leaner than the global equivalence ratio ($z < 0.0461$) is more likely to be seen than a richer mixture for all reduced mechanisms in contrast with experimental results. Globally more than 50% of the probability belongs to $0.79 < \phi < 0.87$, i.e. the mixture fraction variation is small and more than 90% of the points are between $\phi = 0.67$ and $\phi = 0.98$ ($0.038 < z < 0.052$). Rich mixture, i.e. $z > 0.55$, is not likely to be seen since only 3% and 8% of the mixture is rich in numerical and experimental results respectively.
As a consequence, even if the PETERS and the JONES mechanisms have an incorrect response to equivalence ratio larger than stoichiometry, results are expected not to be affected since the mixture keeps lean most of the time.

Table 5.3 - *Distribution of the mixture fraction in the plane closest to the nozzle exit (h = 6 mm). Comparison between the seven chemical descriptions.*

Equiv. ratio	Mixture fraction	**BFER**	**BFER***	**JONES**	**PETERS**	**SESH.**	**FPI_TTC***	**LU**	**EXP.**
$\phi > 1.0$	$z > 0.055$	1%	3%	0%	0.1%	3%	0.7%	0.2%	8%
$\phi < 0.83$	$z < 0.0461$	54%	52%	59%	50%	51%	61%	58%	40%
$0.79 < \phi < 0.87$	$0.044 < z < 0.048$	61%	51%	48%	65%	58%	60%	64%	57%
$0.67 < \phi < 0.95$	$0.038 < z < 0.052$	96%	93%	99%	99%	91%	96%	98%	87%

5.3.2 Mean and fluctuating quantities

The mean axial and tangential **velocity** fields are reproduced in Figs. 5.10 and 5.11 respectively at five sections downstream of the nozzle exit ($h = 1.5, 5, 15, 25$ and 35 *mm*) for all chemical descriptions. Unfortunately, no LDV measurements are available for this operating point to compare with experiments. The LU is therefore used as reference. Results for all reduced schemes are in good agreement with the predictions of LU. Only the FPI_TTC* method predicts a smaller IRZ (Fig. 5.10). This discrepancy is coherent with the smaller opening angle of the flame which has been detected on the mean temperature field in Fig. 5.7 when using the FPI_TTC* method.

For temperature and major species, Laser Raman measurements at five sections ($h = 6, 10, 20, 30$ and 60 *mm*) are used as additional information to assess the quality of the numerical results. Due to the number of schemes tested, in the following, the left side of a figure shows results for 2S_CH4_BFER (—), 2S_CH4_BFER* (– –) and JONES (·····) in comparison with experimental (◯) and LU (■) results. On the right side of each

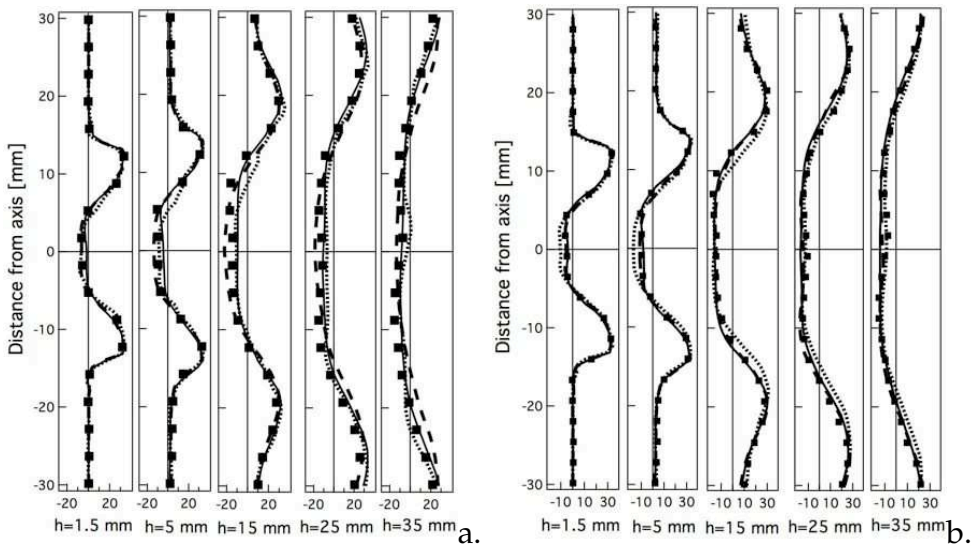

Figure 5.10 - *Mean axial velocity profiles at five sections in the chamber. The LU scheme (■) is compared to the other mechanisms: a) 2S_CH4_BFER (——), 2S_CH4_BFER* (– –) and JONES (·····) b) PETERS (——), SESHADRI (– –) and FPI_TTC* (·····).*

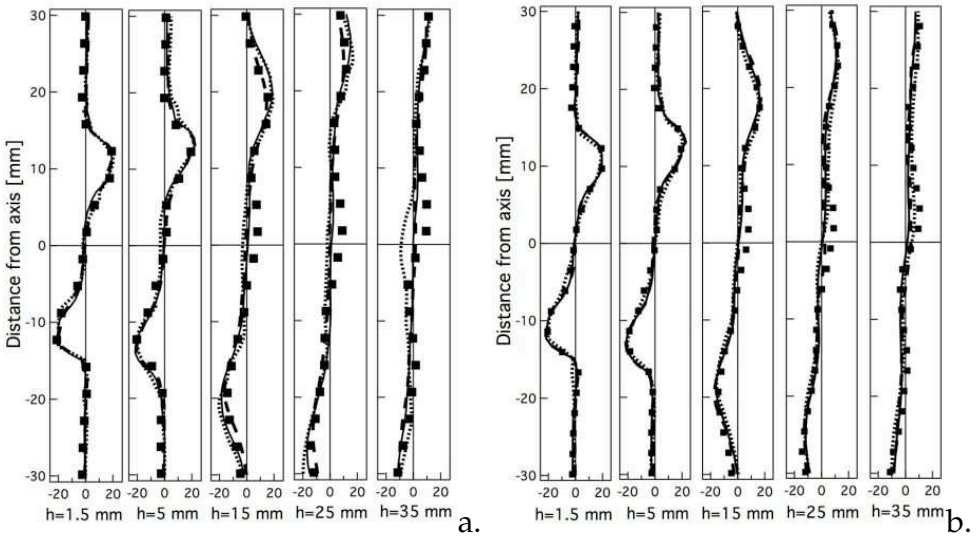

Figure 5.11 - *Mean tangential velocity profiles at five sections in the chamber. The LU scheme (■) is compared to the other mechanisms: a) 2S_CH4_BFER (——), 2S_CH4_BFER* (– –) and JONES (·····) b) PETERS (——), SESHADRI (– –) and FPI_TTC* (·····).*

figure, results for PETERS (——), SESHADRI (– –) and FPI_TTC* (·····) are presented with the experimental (◯) and LU (■) results. The agreement between simulations and experimental results is satisfactory in terms of temperature and major species profiles.

Figures. 5.12 and 5.13 show the mean and fluctuating **temperature** profiles respectively:

- in the **IRZ**: the simplest mechanisms correctly predict the temperature profiles whereas the most complex schemes (JONES, PETERS, SESHADRI) as well as the FPI_TTC* method slightly underestimate the flame extension (see results at $h = 10\ mm$ and $h = 20\ mm$ in Fig. 5.12). Moreover, the temperature fluctuations in the IRZ are slightly overestimated by the most complex chemistries (PETERS and SESHADRI) and the 2S_CH4_BFER* schemes. The same discrepancies on the IRZ width and the temperature fluctuations are found between experiments and the LU results. It seems therefore reasonable to suspect that do not results from chemistry model.

- in the **FG/IRZ layer** and the **FG** zone: the transition from burnt gases to fresh gases is correctly described in terms of mean temperature by all chemical descriptions. The FG/IRZ layer is characterized by the highest fluctuations of temperature which are well reproduced by the simplest 2S_CH4_BFER and 2S_CH4_BFER* schemes and slightly overestimated by all other schemes.

- in the **FG/ORZ layer**: temperature is correctly predicted at the first two measurement planes by all reduced schemes. On the contrary, the mean temperature is overpredicted (see $r \approx 20\ mm$ and $h = 6,10\ mm$) by the FPI_TTC* method which underestimates the opening angle of the flame. Downstream, the 2S_CH4_BFER, 2S_CH4_BFER* and JONES schemes largely overestimate the mean temperature, whereas the most complex schemes capture the correct values (see $x > 20\ mm$ at $h = 20\ mm$). This behavior seems to be related to the flame length: the simplest schemes predict a smaller flame which is already at equilibrium in this zone, whereas the analytical schemes predict a longer flame which has not yet reached its maximum temperature, agreeing with the experimental and the LU results. This zone is characterized by high temperature fluctuations which are generally correctly reproduced.

- in the **ORZ** detected only in sections $h = 6\ mm$ and $h = 10\ mm$, the temperature is greatly overestimated by all chemical descriptions including the LU scheme as wall heat losses and radiation effect are neglected. This zone is characterized by small temperature fluctuations.

The mean and fluctuations profiles of CH_4 and CO_2 mass fractions in Figs. 5.14-5.17 lead to the same conclusions: results are generally satisfactory, the profiles are correctly

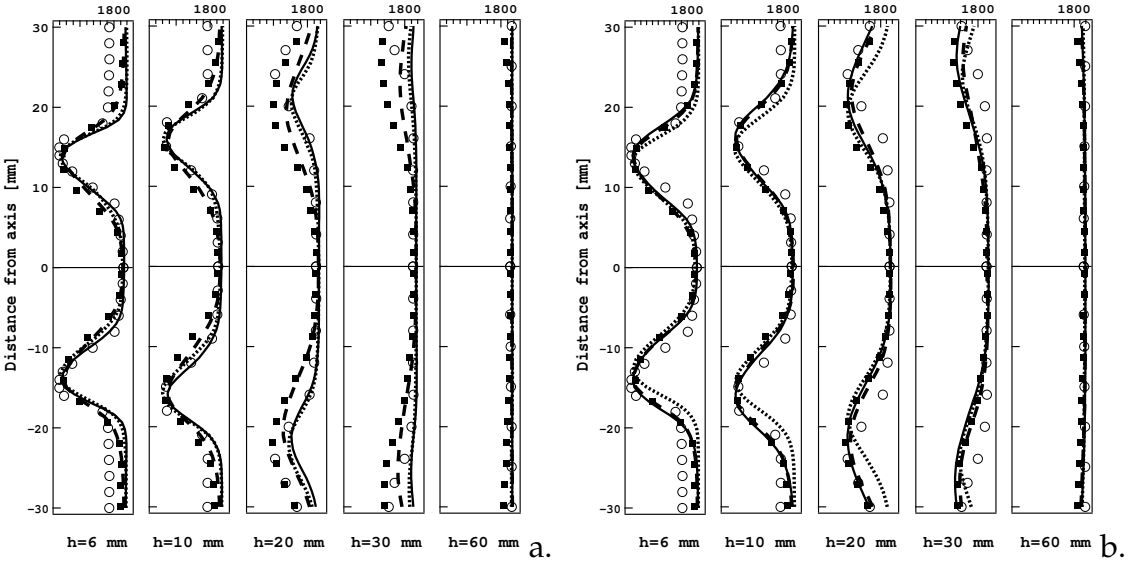

Figure 5.12 - *Mean temperature profiles at five sections in the chamber. The experimental (○) and LU (■) results are compared to numerical data for the other mechanisms: a) 2S_CH4_BFER (——), 2S_CH4_BFER*(– –) and JONES (·····) b) PETERS (——), SESHADRI (– –) and FPI_TTC* (·····).*

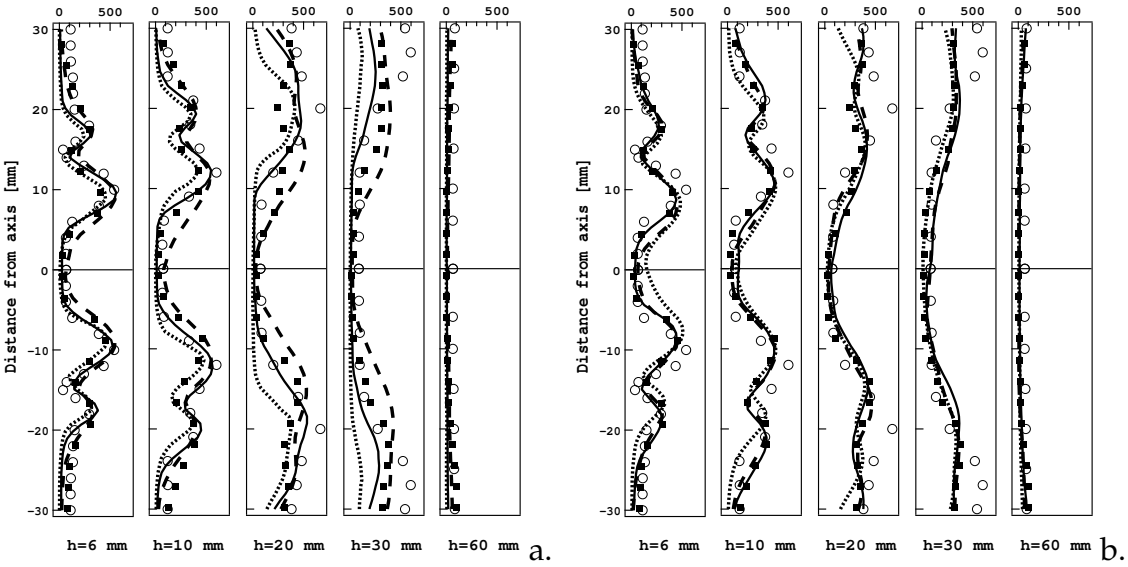

Figure 5.13 - *Fluctuating temperature profiles at five sections in the chamber. The experimental (○) and LU (■) results are compared to numerical data for the other mechanisms: a) 2S_CH4_BFER (——), 2S_CH4_BFER*(– –) and JONES (·····) b) PETERS (——), SESHADRI (– –) and FPI_TTC* (·····).*

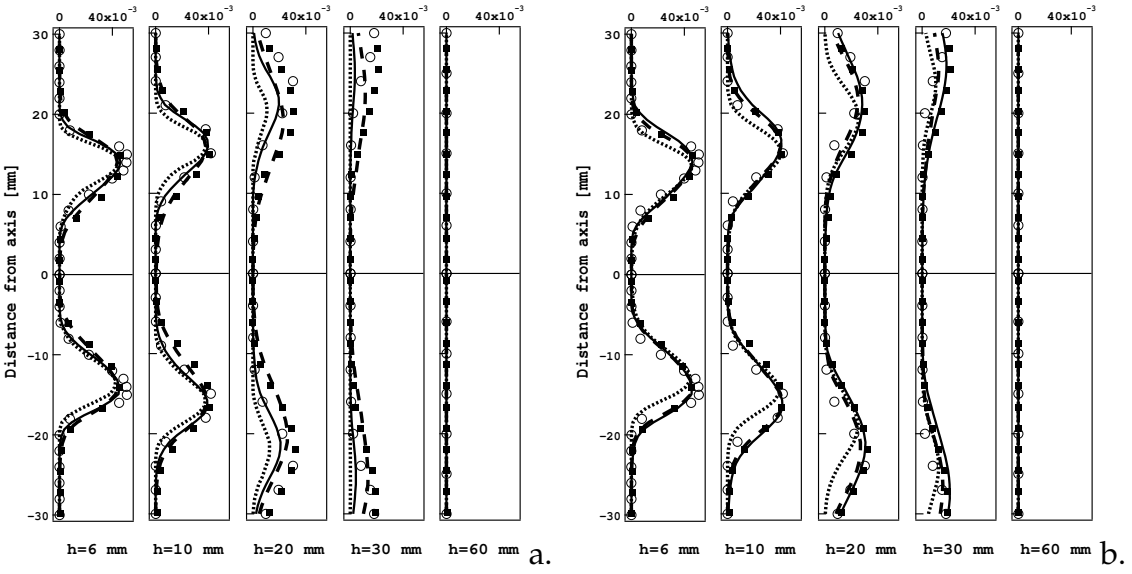

Figure 5.14 - *Mean CH_4 profiles at five sections in the chamber. The experimental (○) and LU (■) results are compared to numerical data for the other mechanisms: a) 2S_CH4_BFER (——), 2S_CH4_BFER*(– –) and JONES (·····) b) PETERS (——), SESHADRI (– –) and FPI_TTC* (·····).*

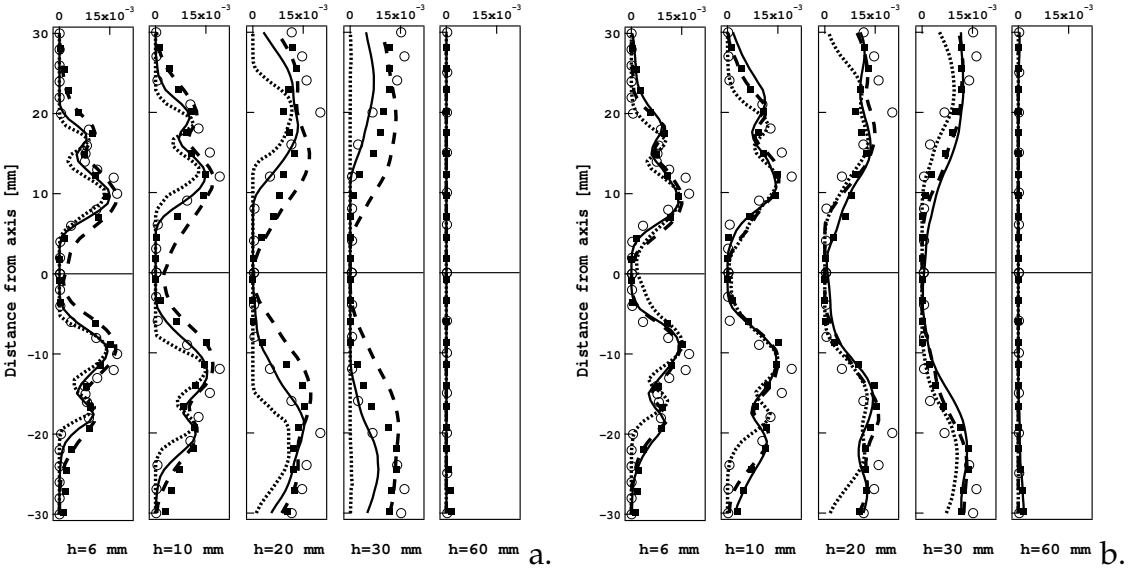

Figure 5.15 - *Fluctuating CH_4 profiles at five sections in the chamber. The experimental (○) and LU (■) results are compared to numerical data for the other mechanisms: a) 2S_CH4_BFER (——), 2S_CH4_BFER*(– –) and JONES (·····) b) PETERS (——), SESHADRI (– –) and FPI_TTC* (·····).*

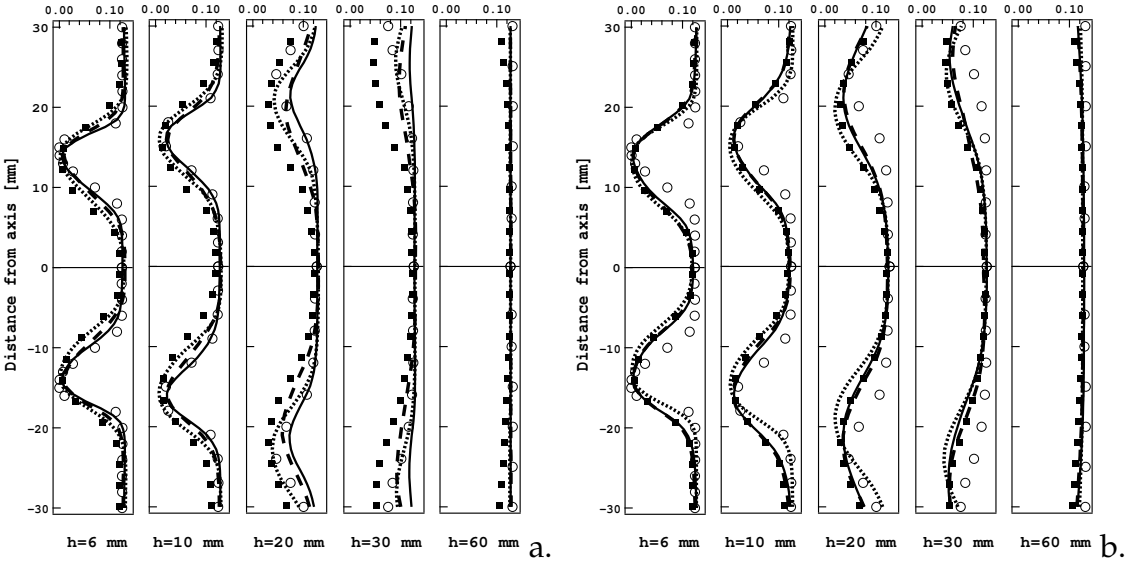

Figure 5.16 - *Mean CO_2 profiles at five sections in the chamber. The experimental (○) and LU (■) results are compared to numerical data for the other mechanisms: a) 2S_CH4_BFER (——), 2S_CH4_BFER*(– –) and JONES (·····) b) PETERS (——), SESHADRI (– –) and FPI_TTC* (·····).*

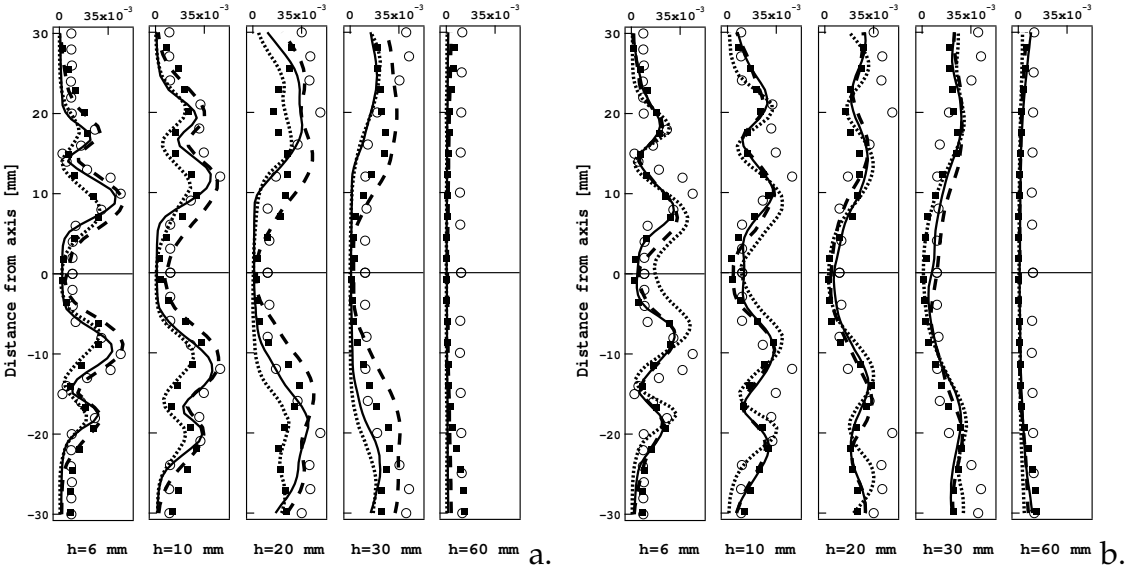

Figure 5.17 - *Fluctuating CO_2 profiles at five sections in the chamber. The experimental (○) and LU (■) results are compared to numerical data for the other mechanisms: a) 2S_CH4_BFER (——), 2S_CH4_BFER*(– –) and JONES (·····) b) PETERS (——), SESHADRI (– –) and FPI_TTC* (·····).*

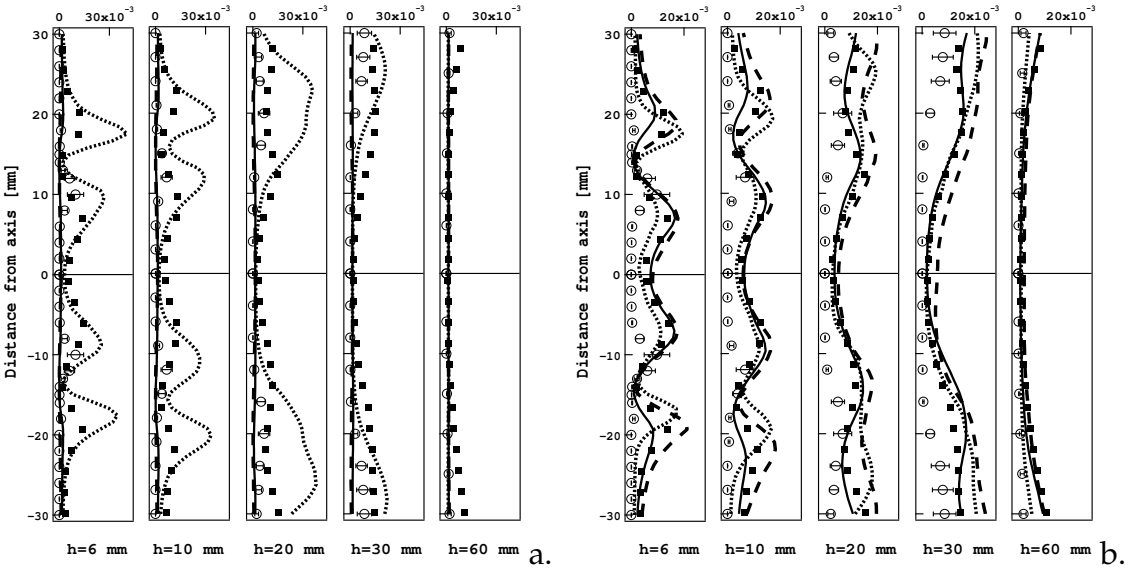

Figure 5.18 - *Mean CO profiles at five sections in the chamber. The experimental (○) and LU (■) results are compared to numerical data for the other mechanisms: a) 2S_CH4_BFER (——), 2S_CH4_BFER*(– –) and JONES (·····) b) PETERS (——), SESHADRI (– –) and FPI_TTC* (·····).*

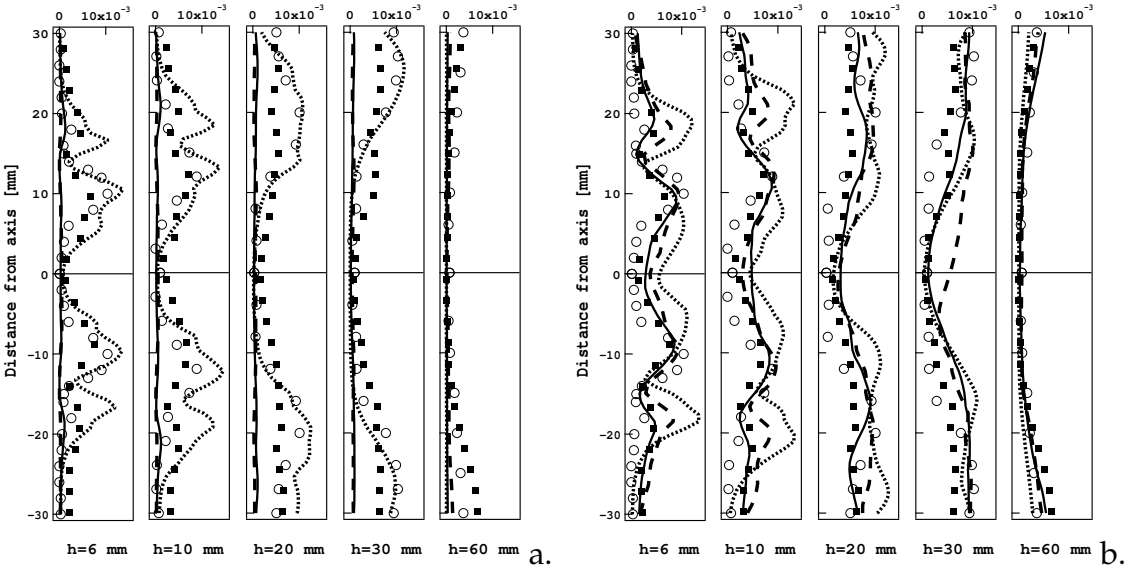

Figure 5.19 - *Fluctuating CO profiles at five sections in the chamber. The experimental (○) and LU (■) results are compared to numerical data for different mechanisms: a) 2S_CH4_BFER (——), 2S_CH4_BFER*(– –) and JONES (·····) b) PETERS (——), SESHADRI (– –) and FPI_TTC* (·····).*

reproduced and the maximum values of fluctuations are also captured. The simplest schemes (2S_CH4_BFER and JONES) are confirmed to predict a too short flame and results are not accurate at $h = 20$ mm and $x > 20$ mm where there is a recombination zone only detected by the analytical schemes. The modified 2S_CH4_BFER* scheme is globally closer to the LU mechanism compared to the original scheme but discrepancies are still detected. The FPI_TTC* species profiles are affected by the underestimation of the flame opening angle.

Being one major pollutant, the prediction of the **CO concentration** in an industrial configuration is a very important but still difficult task. Since it is one of the most radiative species, its prediction requires to estimate the radiative flux [150, 125, 5]. Moreover, the correct description of intermediate species is not straightforward even for laminar flames and adequate chemical schemes are required.
In Fig. 5.18 the mean profiles of CO species are compared to the measurements (note that the experimental error on CO was estimated at 50%) and the LU results:

- the simplest 2S_CH4_BFER and 2S_CH4_BFER* schemes greatly underestimate the CO mass fractions and their fluctuations in the reaction zone, agreeing with the one-dimensional laminar analysis (Sections 3.2.1 and 3.2.2). However, the correct level of CO concentration is recovered at equilibrium (at $h = 60$ mm).

- the JONES scheme greatly overestimates the maximum value of mean and fluctuating CO mass fractions in the reaction zone, also confirming the analysis of strained laminar flames.

- the analytical schemes (PETERS, SESHADRI) then well predict CO mass fraction (Fig. 5.18b) although it is slightly overestimated in the IRZ. Only one peak of CO is experimentally detected in the FG/IRZ layer whereas a smaller second peak of CO is predicted by LES in the FG/ORZ zone even with the LU scheme. This difference could be due to the adiabacity assumption or the mesh refinement (see Section 5.3.5). The CO fluctuations are accordingly correctly reproduced.

- results obtained with the FPI_TTC* method are very similar to the SESHADRI results. Highest values for the second peak of CO which is not experimentally recovered are obtained in the FG/ORZ zone. Fluctuations are generally overestimated compared to the analytical schemes.

Thus, the semi-global mechanisms are unable to predict the CO concentration in the reaction zone and sophisticate chemical schemes are required to estimate the mean and fluctuating profiles. The impact of both the mesh resolution (investigated in Section 5.3.5) and the adiabaticity assumption requires dedicated investigation.

5.3.3 Mean flame surface

The mean flame surface is identified by the normalized progress variable c based on the O_2 species (Eq. (3.59)) to be consistent with the one-dimensional analysis and DNS presented in Chapters 3 and 4.

From results on DNS of two- and three-dimensional flame/turbulence interaction configurations in Chapter 3, it is evident that the turbulent speed and, consequently, to the flame length of turbulent flames is strictly linked to the mechanism response to strain rate for one-dimensional laminar flames. Discrepancies on the flame length detected in Fig. 5.7 between the six reduced chemical mechanisms could be then justified and are investigated in the following in terms of turbulent flame, flame wrinkiling and the local consumption speed.

Since the flame is cylindrical, the azimuthal averages are assumed equivalent to Reynolds statistics in the (x,y) plane during a swirl period [111, 162]. This hypothesis is assumed hereafter to calculate three-dimensional burning quantities such as the turbulent speed or the flame wrinkling from two-dimensional information.

Since the flame fronts are distinct only on a small zone near the nozzle exit (Fig. 5.7), it has been preferred not to use Equation (4.16) to calculate the flame wrinkling. The unwrinkled area A_L is calculated as the surface of the mean isoline at $c = 0.65$, the mean wrinkled area A_T is obtained averaging the instantaneous surfaces of the isoline $c = 0.65$ and the flame wrinkling is given by $A' = A_T/A_L$ at each axial position (Fig. 5.20a.). Discrepancies are detected between the different mechanisms. The 2S_CH4_BFER and JONES mechanisms underestimate the flame wrinkling, which is in contrast with results obtained in the DNS calculations (Sections 4.2 and 4.3).

Wrinkling mainly depends on the interaction of the turbulence with the flame front, i.e. to the combustion regime, as well as to the chemical response to strain rate. The Kolmogorov length scale for the PRECCINSTA burner has been estimated to be $l_\mathcal{K} = 29e^{-6}m$ leading to a Karlovitz number $Ka \approx 300$ [111] which has the same order of magnitude of the Karlovitz numbers characterizing the flame/HIT and the Bunsen flame configurations. However, using the TFLES approach the flame is generally thickened in order to obtain at least five points in the front the flame, i.e. $\delta_F = 5\Delta x$ and the solved turbulent length scale is Δx leading to a solved Karlovitz number $Ka^{LES} = (5\Delta x/\Delta x)^2 = 25$. The wrinkling effect of turbulence on the flame front is consequently reduced and resolved flame lies more in the corrugated flamelet regime. The chemical time scale is also modified for each mechanisms. However, the PRECCINSTA configuration is more complex than the Bunsen flame and the identification of the reasons for the flame wrinkling discrepancies is not straightforward.

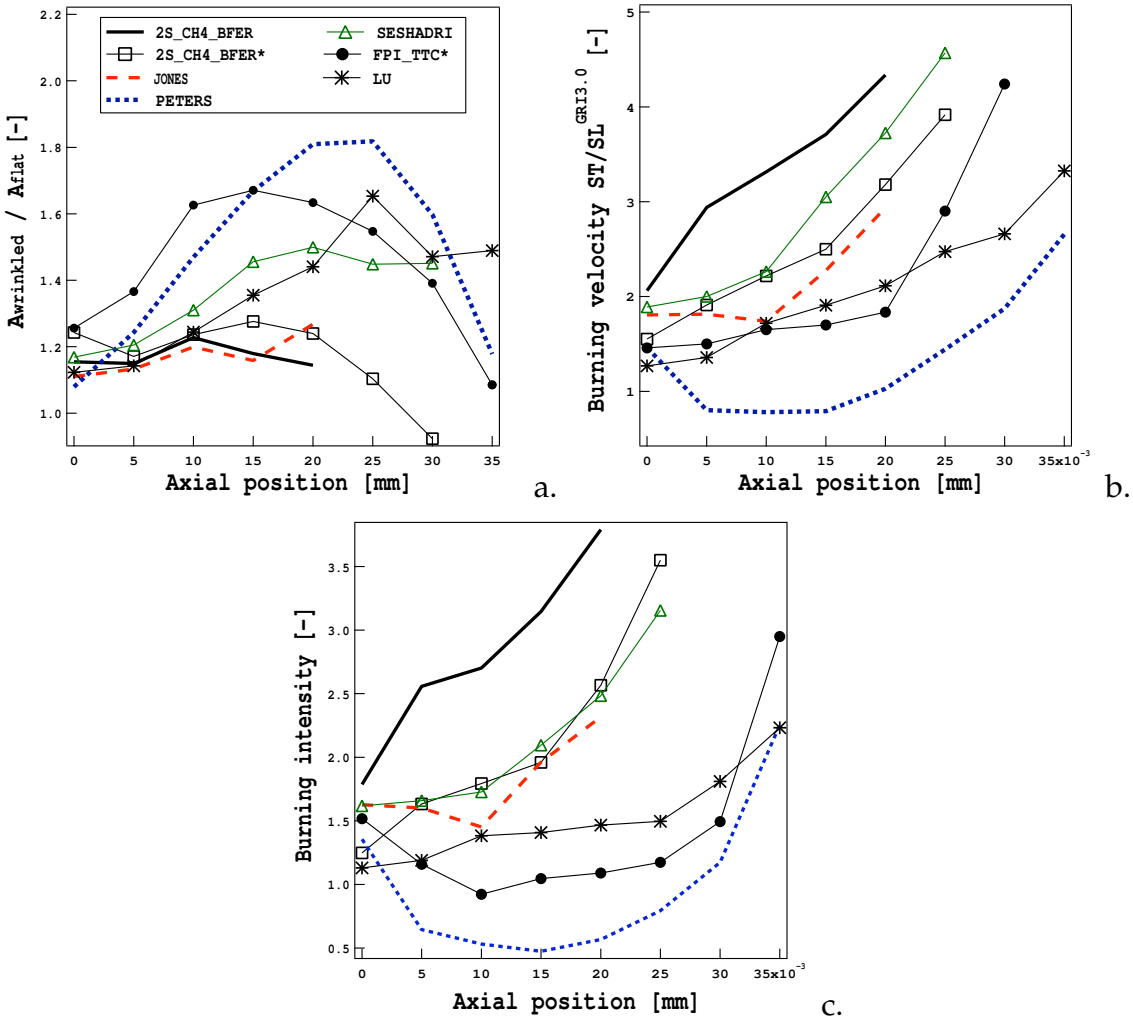

Figure 5.20 - *a) Mean flame wrinkling, b) mean turbulent speed and c) mean local flamelet consumption speed $\overline{S}_C$ as a function of the axial position in the PRECCINSTA configuration. Comparison between the seven chemical descriptions.*

The turbulent speed is calculated considering the mean consumption rate of O_2 species $\overline{\dot{\omega}}_{O_2}$ in the (x,y) plane which is integrated across the flame, i.e. along the normal to the iso-c contour identifying the flame ($c = 0.65$):

$$S_T = \frac{1}{\rho Y_{O_2}} \int \overline{\dot{\omega}}_{O_2} d\mathbf{n}. \tag{5.1}$$

To ensure not to neglect an important contribution in the $z-$direction when calculating S_T in the (x, y) plane as done in Section 4.2. Results are then averaged in the tangential $y-$direction to obtain the mean turbulent speed S_T at each axial position (Fig. 5.20c.).

The **burning intensity** I_0 in Fig. 5.20b is computed from the burning speed $S_T/S_L^{GRI3.0}$

and the flame wrinkling. Results are in agreement with the one-dimensional analysis on strained flames (Section 3.2.2): the highest values of $\overline{S}_C$ are obtained for the 2S_CH4_BFER and JONES schemes, whereas the most complex schemes (PETERS and SESHADRI) and the FPI_TTC* method predict slower values of I_0 similar to the LU mechanism. Results of the 2S_CH4_BFER* mechanism are also closer to the LU reference indicating a good behavior on strained laminar flames sufficient to give good results in LES of experimental three-dimensional flames.

Since the flame wrinkling is correctly reproduced in all cases, discrepancies on the **burning speed** $S_T/S_L^{GRI3.0}$ (Fig. 5.20c.) strongly depend on the burning intensity I_0. Results obtained with the PETERS and SESHADRI schemes as well as the FPI_TTC* method are quite similar and agree well with the reference LU mechanism. In comparison, the 2S_CH4_BFER and JONES mechanisms predict too high values of I_0 which is partially corrected by the 2S_CH4_BFER* scheme.
The different lines reproduced in Fig. 5.20c. end where the mean flame surface ends indicating the **flame length**, which is directly linked to the burning speed S_T/S_L, could be deduced for all mechanisms. The most complex schemes predict the longest flame and the lowest turbulent speed. On the contrary, the flames predicted by the 2S_CH4_BFER and JONES schemes are shorter and their burning speed S_T/S_L is larger, while the modified 2S_CH4_BFER* scheme reproduces a flame more similar to the LU flame. The analytical PETERS and SESHADRI schemes, as well as the FPI_TTC* method, reproduce the flame length and the turbulent speed better than the 2S_CH4_BFER and JONES schemes.

5.3.4 Towards pollutant emission prediction: the post-flame zone

Flames are generally composed by two different regions: a reaction zone characterized by high temperature gradient where intermediate species such as CO and H_2 are created and a post-flame zone where slow recombination reactions convert intermediates into products. The **recombination zone** plays an important role in the description of the flame temperature, pollutant concentration and NO_x production located in the near-wall zone in the PRECCINSTA burner.
To identify these zones, the production/destruction rate of CO species is a good marker: generally, CO is produced in the reaction zone whereas it recombines into CO_2 in the post-flame region.[1] In Fig. 5.21, the instantaneous reaction zone is identified by a grey iso-line and the instantaneous recombination region is highlighted by the black regions

[1]Concerning the FPI_TTC* method, it is not possible to know the contribution of $\dot{\omega}_{CO}$ to the source term $\dot{\omega}_c$ only. The reaction and the recombination zones have been estimated from the proper variable and looking at the results of unstrained premixed flames: $0.01 < c^{fpi} < 0.85$ for the flame zone and $0.85 < c^{fpi} < 0.99$ for the post-flame zone.

for all mechanisms. Results confirm the observations made for laminar premixed flame structures. The simplest 2S_CH4_BFER and 2S_CH4_BFER* schemes lead to unphysical results since the recombination zone could not be distinguished from the reaction zone. As a consequence, even if the response to stretch has been corrected for the 2S_CH4_BFER* scheme and a longer flame is predicted, the description of the near-wall zone is still incorrect since the equilibrium state is reached too quickly. A distinction between the two regions is shown for all other mechanisms. The JONES scheme correctly predicts a recombination zone surrounding the reaction zone but its location is wrong since the predicted flame length is too small. The results for PETERS, SESHADRI and FPI_TTC* mechanisms are very close to results of LU reproducing the same flame length and a recombination zone located in the near-wall region.

As already mentioned, intermediate species such as **CO** are very sensitive to stretch (Section 3.2.2).
The numerical correlation between mean CO mass fraction and mean progress variable c is represented in Fig. 5.22. Correlations of an unstrained (solid line) and two strained (dashed lines) laminar premixed flames at $a = 2000s^{-1}$ and $a = 20000s^{-1}$ are displayed to facilitate the analysis. Note that the information on strained laminar flames can not be directly used since the impact of stretch on thickened flames has not been quantified. As experimental data on CO have high uncertainties, LU results are preferred as reference. The two-step chemical schemes greatly underestimate the maximum value of CO mass fraction as expected from results of laminar flames. This is mainly due to the superposition of the reaction zone with the recombination region: the CO produced by the CH_4 oxidation reaction is instantaneously converted into CO_2 predicting no peak of CO concentration in the reaction zone. On the contrary, the JONES scheme overestimates the CO mass fraction, confirming Fig. 5.18. Results for analytical schemes are in good agreement with the LU mechanism since they take into account the fundamental reactions of CO production and destruction, and so does the FPI_TTC* method. Globally, the maximum value of CO mass fraction is lower than the value of an unstrained laminar premixed flame and the flame structure is close to the results obtained for laminar strained flames (even if the flame has been thickened). As expected, the flame structure is more similar to a strained flame than to an unstrained one. A correct description of the flame response to stretch is thus a required characteristic of a chemical mechanism if intermediate species, radicals and pollutants are of main interest since they are greatly affected by stretch.

Instantaneous fields of **H**, **O** and **OH radicals** are shown in Fig. 5.23. A correct description of these species is necessary whenever thermal-NO has to be predicted and could be used to qualitatively localize the region of NO production in the configuration. No experimental data are available for these species and the LU mechanism is again used as reference to validate the behavior of the analytical schemes and the FPI_TTC* method which are the only chemical descriptions containing information on these

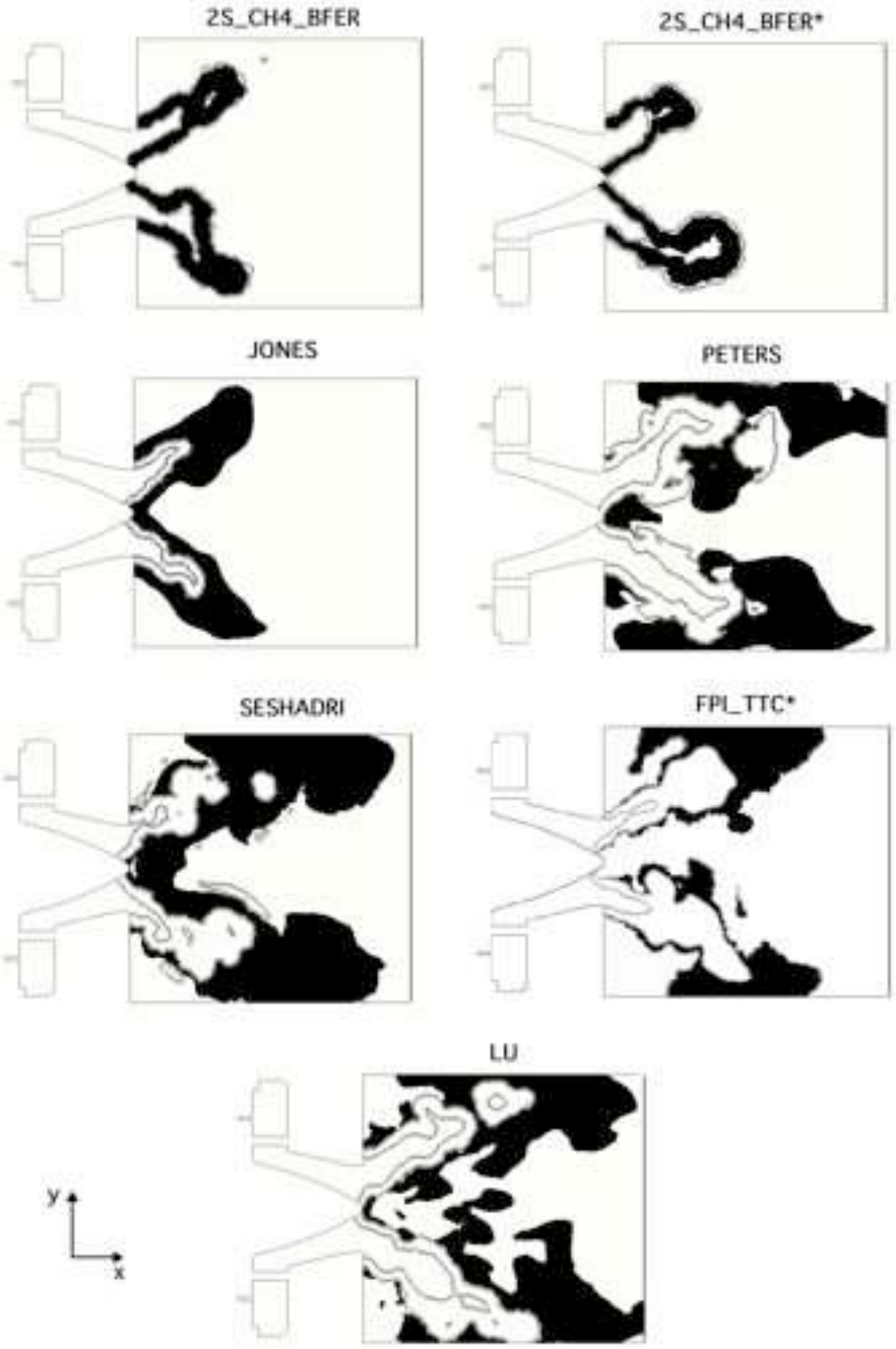

Figure 5.21 - *Instantaneous reaction zone (grey iso-line) and recombination region (black surface) for the seven chemical descriptions.*

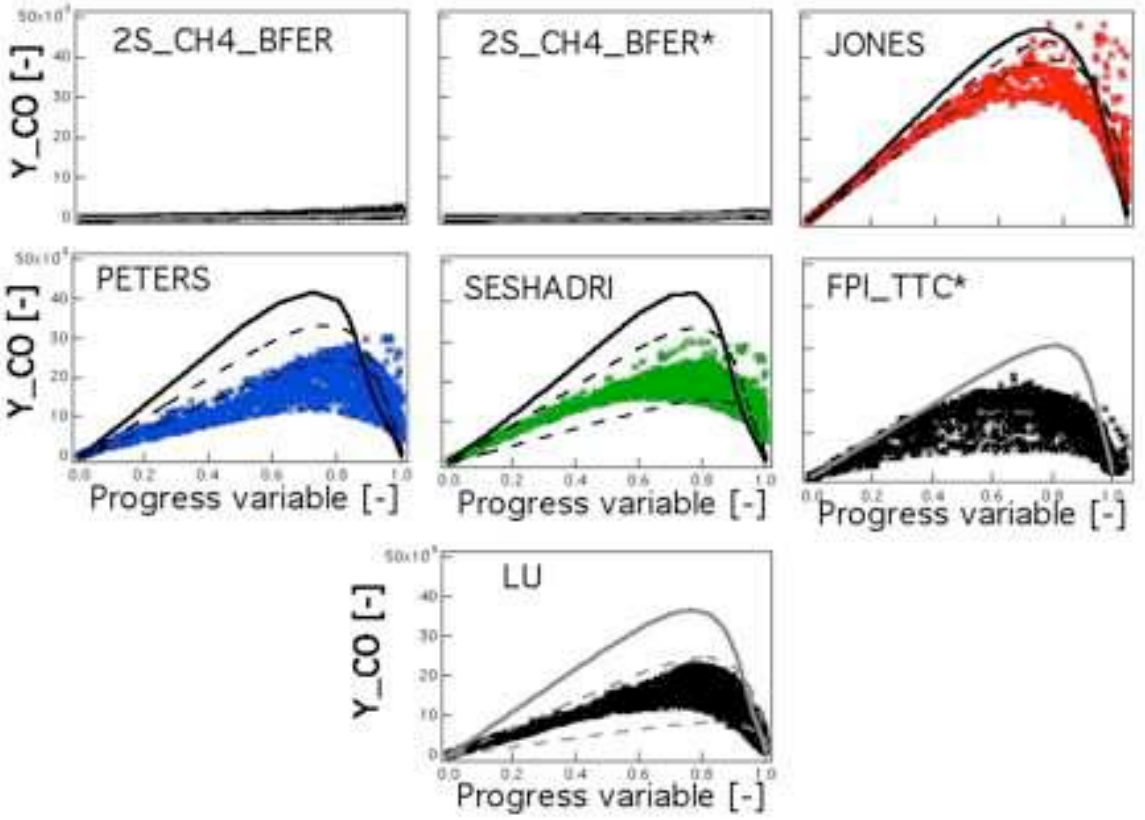

Figure 5.22 - *Correlation between mean CO mass fraction and mean progress variable c. The solid line corresponds to the correlation of an unstrained premixed laminar flame and the two dashed lines refer to strained premixed laminar flames ($a = 2000s^{-1}$ and $a = 20000s^{-1}$).*

intermediates. In the analytical schemes, only *H* species is solved whereas *O* and *OH* species are assumed in QSS, algebraic relations (Eq. (3.45)) being used to calculate them by *a posteriori* processing. Profiles for *H*, *O* and *OH* species are obtained looking at the information in the look-up table with a post-processing procedure in the FPI_TTC* method. The analytical schemes correctly localize *O*, *OH* and *H* species although the SESHADRI mechanism slightly overestimates *O* and *OH* concentrations whereas the PETERS scheme slightly underestimates them. This behavior is consistent with the analysis of laminar flames since the algebraic relations obtained for *O* and *OH* as well as the QSS assumption are not necessarily valid for turbulent flames. The solved *H* species are in agreement with the LU results. The FPI_TTC* method provides *O* and *H* species in a smaller region downstream of the flame front compared to the LU mechanism even in the near-wall zone. This information about radical species is however insufficient to assess the capacity of the different chemical descriptions to correctly reproduce the thermal *NO*. Additional measurements are required to conclude.

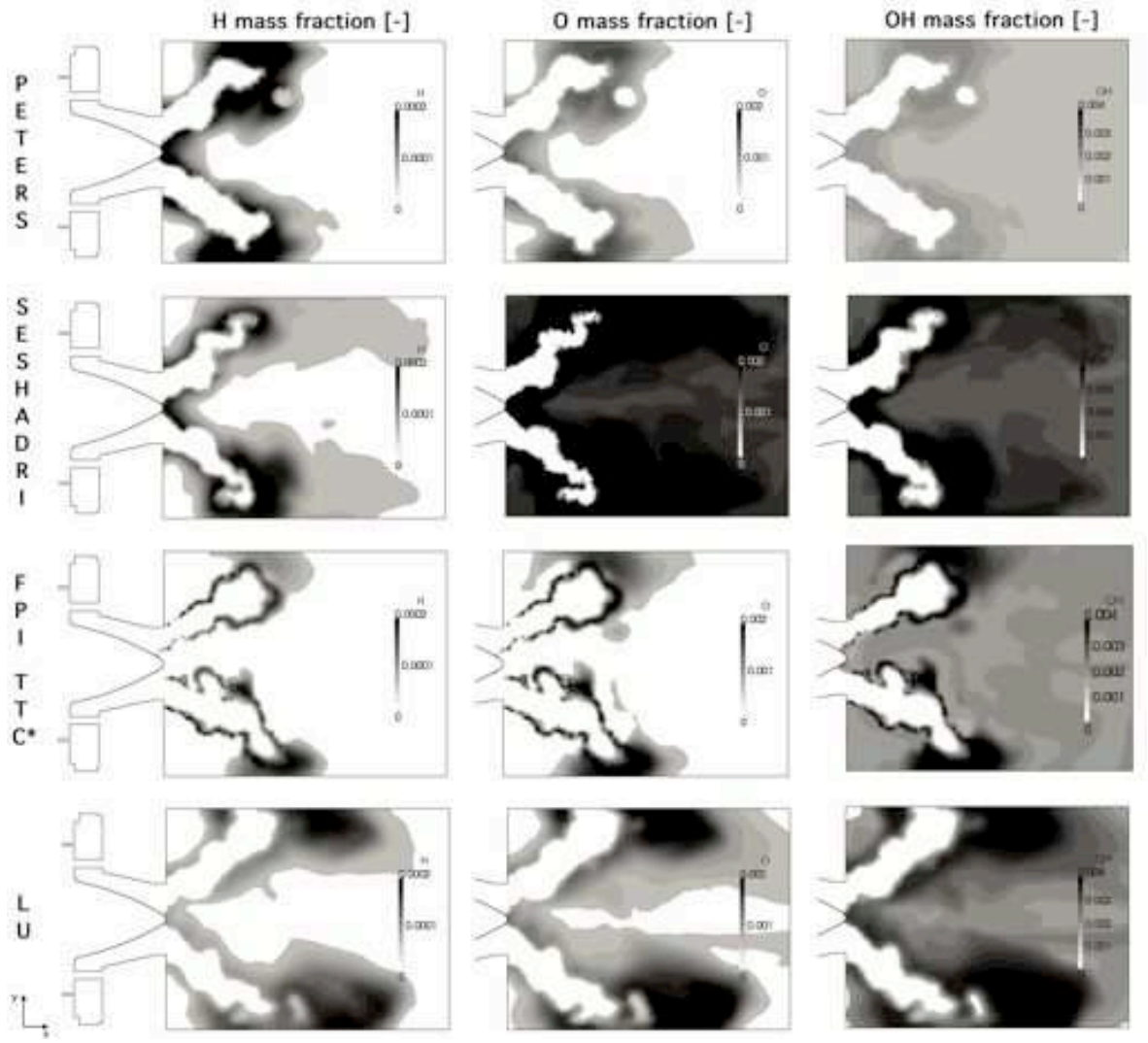

Figure 5.23 - *Instantaneous fields of H, O and OH mass fractions for the analytical schemes (PETERS, SESHADRI and LU) and the FPI_TTC* method. The LU mechanism is considered as reference.*

5.3.5 Impact of mesh refinement

The quality of numerical results strongly depends on the mesh refinement [111]. The behavior of the flame not only depends on the chemical description but also on the flow dynamics, the combustion model [76] and the mixing phenomenon in the swirler, all phenomena being very sensitive to mesh quality. Refining the mesh reduces the impact of the combustion model by reducing the thickening factor. In the following, results on a finer mesh containing 20 millions cells (referred as 'fine' mesh hereafter) are compared to the results on the 5 millions cells mesh (referred as 'coarse' mesh hereafter) for the simplest chemical scheme (2S_CH4_BFER) and the analytical PETERS mechanism. The

swirler and the chamber have been mainly refined, with a characteristic cell size which is reduced from 1 *mm* to 0.6 *mm* in the reaction zone and from 0.6 *mm* to 0.4 *mm* in the swirler. The resolution in the tube of methane injection is preserved to 0.2 *mm*. As a consequence, the thickening function takes lower values preserving five points in the flame front.

The mean temperature profiles for the 2S_CH4_BFER and PETERS schemes on both the coarse and the fine meshes are compared to experiments in Fig. 5.24. The extension of the IRZ ($h = 6$ *mm* and $h = 10$ *mm*) is better predicted on the fine mesh for both chemistries. Confirming the results on the coarse mesh (Section 5.3.2), the temperature in the FG/ORZ layer at $h = 20$ *mm* is still greatly overestimated by the 2S_CH4_BFER mechanism but accurately predicted by the PETERS scheme. The temperature in this region depends much more on the chemistry used than on the grid resolution, its description being incorrect if the chemical scheme predicts a too short flame. The temperature fluctuations are presented in Fig. 5.25 for both meshes and schemes. For the first measurement planes, fluctuations are generally higher in the reaction zone on the fine mesh whereas their values are not modified neither in the IRZ nor in the ORZ. For $h > 20$ *mm*, results for the PETERS mechanism are slightly improved reproducing the correct level of fluctuations. The mean and fluctuating profiles for *CO* species are displayed for the PETERS scheme in Fig. 5.26. As the 2S_CH4_BFER scheme predicts unphysical profiles (Section 5.3.2) and there is no improvement with increasing grid resolution, the results are not shown. Figure 5.26 shows that the PETERS scheme predicts better *CO* profiles on the fine grid and lower levels of mean *CO* are predicted in the IRZ agreeing with the experimental results. Most important, the second peak of *CO* in the FG/ORZ layer which was not reproduced by experiments is drastically reduced. Thus, the prediction of intermediate species seems to be highly dependent not only on the chemical description but also on the grid resolution: since the flame is less thickened by the TFLES method on the fine mesh, higher values of stretch could impact the flame structure.

The mesh impact on the FPI_TTC* results has not been evaluated in this work. However, a similar analysis on the PRECCINSTA burner[2] has been proposed by Moureau et al. [111] where results for *CO* on a grid composed of 2634 million cells are presented (Fig. 5.27). In this calculation, the reaction zone is characterized by a cell size of 0.1 *mm* and the flame front is completely resolved. The tabulation method predicts a second peak of *CO* in the FG/ORZ zone even higher than the peak in the FG/IRZ zone for a very well resolved LES calculation[3]. The authors explained that this discrepancy is basically

[2]A perfectly premixing has been assumed in [111]. However looking at the small variations of mixture fraction encountered for this operating point, this hypothesis does not contribute significantly to errors on *CO* mass fraction.

[3]It should be noticed that the FPI_PCM method, i.e. a different combustion model, has been used in [111]. However, the quality of the FPI tabulation method in the description of *CO* mass fraction may be considered as independent on the combustion model used in a very well resolved LES.

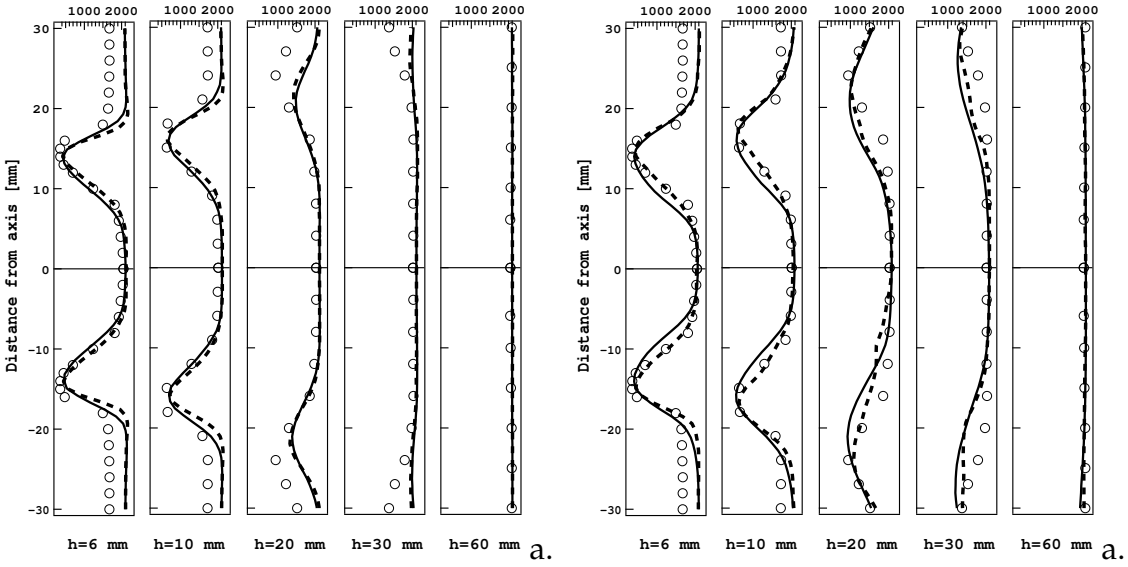

Figure 5.24 - *Mean temperature profiles at five sections in the chamber. The experimental results (○) are compared to the numerical results for two mechanisms and two grids: a) 2S_CH4_BFER - 5 mil. (——) and 2S_CH4_BFER - 20 mil. (– –) b) PETERS - 5 mil. (——) and PETERS - 20 mil. (– –).*

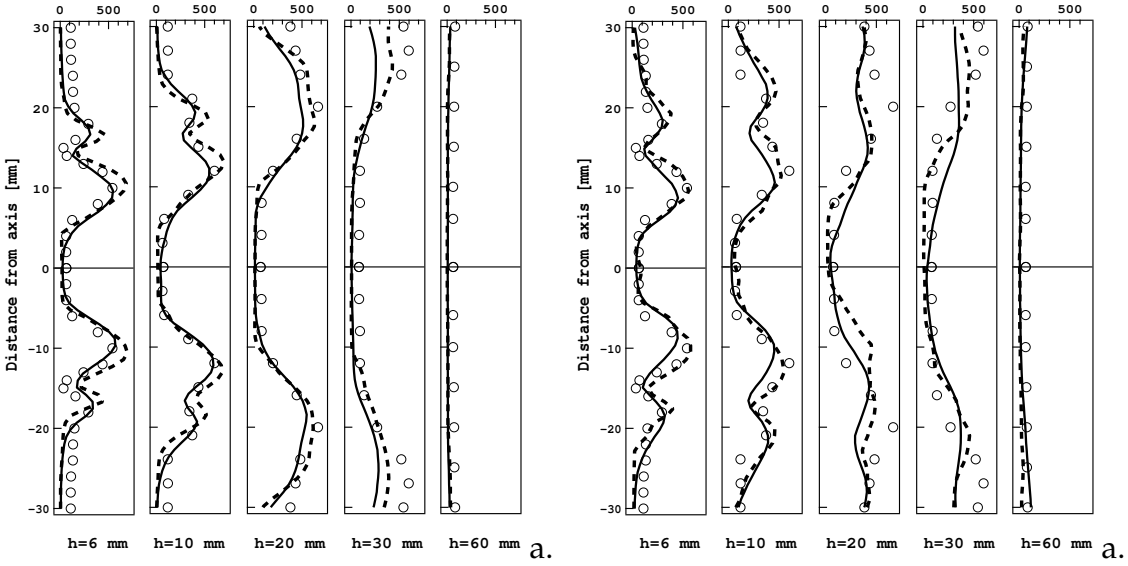

Figure 5.25 - *Fluctuating temperature profiles at five sections in the chamber. The experimental results (○) are compared to the numerical results for two mechanisms and two grids: a) 2S_CH4_BFER - 5 mil. (——) and 2S_CH4_BFER - 20 mil. (– –) b) PETERS - 5 mil. (——) and PETERS - 20 mil. (– –).*

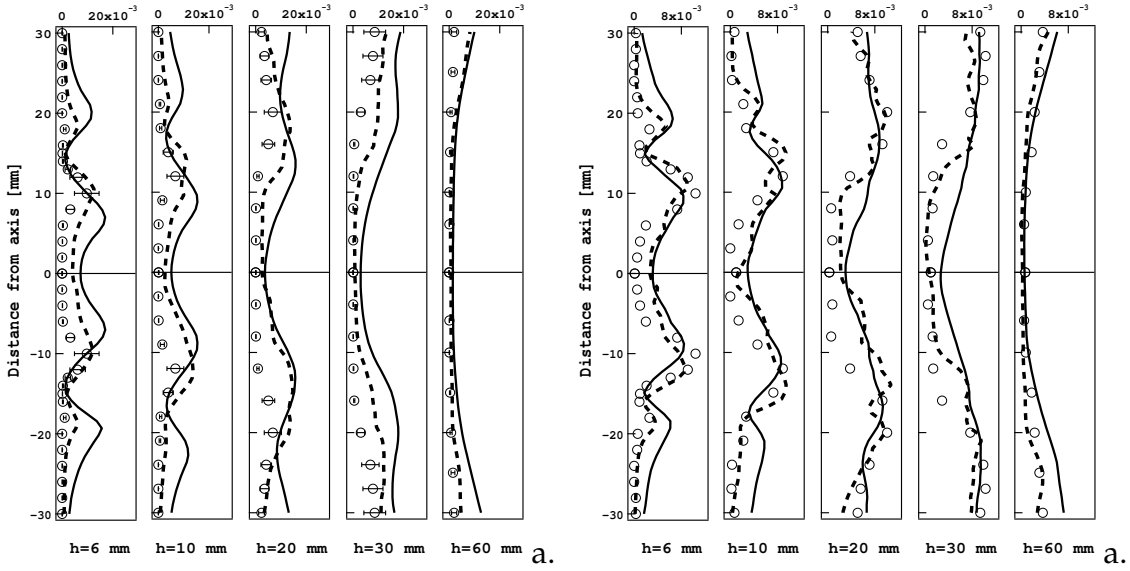

Figure 5.26 - *a) Mean and b) fluctuating CO profiles at five sections in the chamber. The experimental results (○) are compared to the numerical results for the PETERS mechanism and to grid resolutions: 5 mil. (——) and 20 mil. (– –).*

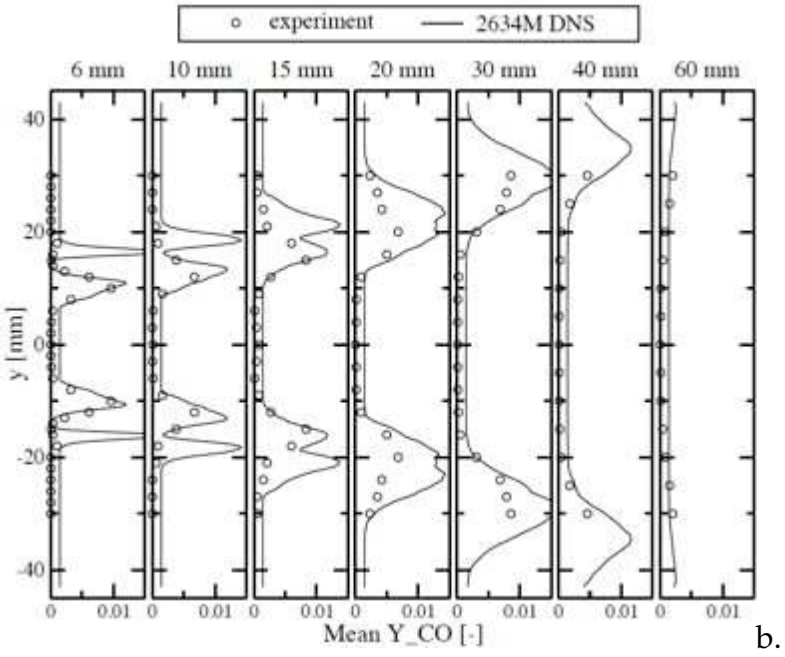

Figure 5.27 - *Mean CO profiles at seven sections in the chamber. Comparison between experiments and a very well resolved LES using the FPI_PCM method. Figure extracted from Moureau et al. [111].*

due to the adiabaticity assumption. However looking at the results of the PETERS scheme on the fine mesh, this theory seems not valid. The tabulation method is suspected to be unable to reproduce the chemical phenomena in the FG/ORZ layer which, probably, could not be described only from the information of laminar unstrained premixed flames. To verify this hypothesis, a LES using the FPI_TTC* method on the fine mesh should be performed.

5.4 General remarks and conclusions

The impact of the chemical description in a LES of a three-dimensional partially premixed flame has been analyzed in this chapter. Results for six reduced schemes and the FPI_TTC* method have been compared to experimental data and numerical results using the reference LU mechanism.
The PRECCINSTA burner is characterized by a partially premixing and the quality of the results may depend on the mechanism capability to describe the laminar flame speed on a wide range of equivalence ratio. Globally, all mechanisms correctly predict the laminar flame speed of lean laminar premixed flames but the JONES and PETERS* mechanisms overestimate the flame speed for rich mixtures. However, since more than 90% of the reacting points in PRECCINSTA has a lean composition, the errors of JONES and PETERS* schemes in describing the laminar flame speed response to equivalence ratio variations are negligible.

The simplest chemical scheme 2S_CH4_BFER satisfactorily predicts the mean profiles of temperature and major species with a low computational cost but the modified 2S_CH4_BFER* mechanism should be preferred since it improves the flame length prediction without any additional cost. Moreover, this mechanism does not require any modification for other operating points whereas all other reduced mechanisms have to be tested and corrected if the operating point changes. No major improvements are obtained when using the JONES mechanism. The analytical schemes (PETERS and SESHADRI) accurately predict the flame length, the concentration of intermediate species and the flame structure for an additional computational cost of only 15% compared to the 2S_CH4_BFER scheme (Table 5.4), but a reduced computational cost of about 20% when compared to LU. The FPI_TTC* method is fastest as it solves

Table 5.4 - *Computational time normalized by the computation time of the LES using the LU scheme.*

FPI_TTC	2S_CH4_BFER	2S_CH4_BFER*	JONES	PETERS	SESHADRI	LU
0.80	1.00	1.00	1.10	1.12	1.12	1.39

two variables instead of N species. Its results are satisfactory in terms of flame length and major species profiles although the flame opening angle is underestimated. Unfortunately, this method seems unable to predict intermediate species which are greatly affected by stretch but a more detailed analysis should be done.

With these LES results, an *a priori* methodology to evaluate the mechanism capability to predict some three-dimensional chemical phenomena has been proposed based on one-dimensional unstrained and strained laminar flames:

- a correct description of the consumption speed for laminar strained flames is necessary if the turbulent flame speed S_T and, as a consequence, the mean flame surface and its length have to be described on turbulent flames. Correcting the simplest scheme (2S_CH4_BFER) to predict the response of the laminar consumption speed to strain (2S_CH4_BFER*) results on the flame length have been improved.
- The *CO* mass fraction in the reaction zone for unstrained and strained flames has to be correctly described to predict the *CO* concentration of turbulent flames.
- The presence of a recombination zone for an unstrained flame guarantees the presence of a small temperature gradient region characterized by product formation.

All these conclusions are supposed to be valid for most hydrocarbons. On the one side, when building a new chemical scheme its requirements could be fixed compromising the computational cost, the robustness of the chemical description and the desired quality of results . On the other side, the quality of the LES results of a three-dimensional configuration could be anticipated testing the reduced mechanisms on laminar one-dimensional premixed unstrained and strained flames (Table 5.5). This procedure has been however evaluated only on premixed flames and still needs a validation for diffusion flames.

Concerning pollutant emissions, different studies are recommended. A LES of the PRECCINSTA burner should be performed on a finer mesh with the SESHADRI and the LU mechanisms in order to conclude on the possibility of accurately predicting the *CO* mass fraction. Wall heat losses and radiation effects should also be taken into account but they would required detailed measurements since they may have a strong impact on the flame stability. Finally, the possibility of reduced schemes to predict thermal-NO could be investigated using specific analytical schemes [103], fitted mechanism [139] and tabulation method [138].

Table 5.5 - *Performances of the difference reduced chemical descriptions .*

	BFER	**BFER***	**JONES***	**PETERS***	**SESHADRI***	**FPI_TTC***
Consumption speed	- - wrong lam. strained flames	+	- - wrong lam. strained flames	+ +	+ +	? to be evaluated
Flame wrinkling	- - wrong S_c	+	- - wrong S_c	+ +	+ +	+ +
Pollutants and postflame region	- - wrong lam. unstrained flames	- - wrong lam.r unstrained flames	- wrong lam. strained flames	+ +	+ +	- to be evaluated
CPU	++	++	+	-	-	++

Chapter 6

Large-Eddy Simulation of instabilities in a lean partially premixed swirled flame

The impact of the reduced mechanisms in a LES of a lean partially premixed swirled flame has been analyzed in Chapter 4. The limits of the simplest chemical description (the two-step 2S_CH4_BFER scheme) in terms of response to stretch and pollutant emissions prediction are clear but this kind of mechanism correctly describes the main features of the flow field such as velocity and temperature with a low computational cost. For these reasons, the two-step 2S_CH4_BFER scheme is expected to be able to predict the thermo-acoustic instabilities occuring in a lean-premixed (LPM) swirled combustor [80] such as PRECCINSTA. In view of the previous results, it would have been preferable to use the modified 2S_CH4_BFER* scheme, but it did not yet exist at the time when the present simulations were done.
In LPM combustion, fuel and air are premixed before entering the combustor chamber to avoid the formation of stoichiometric zones where the high flame temperature produces thermal NO_x. Since the system usually operates near the lean extinction limit, a small perturbation in equivalence ratio may produce a significant variation of the heat release which, if resonating with the chamber acoustic waves, generate unsteady flow oscillations.

The ability of LES to reproduce the combustion instabilities of the lean partially premixed swirled flame using the two-step 2S_CH4_BFER scheme has been presented in the article *"Large-Eddy Simulation of combustion instabilities in a lean partially premixed swirled flame"* by B.Franzelli, E. Riber , L. Gicquel and T. Poinsot which has been accepted with minor revision in Combustion and Flame in 2011 and is reported in the following.

6.1 Article

The article *"Large-Eddy Simulation of combustion instabilities in a lean partially premixed swirled flame"* by B.Franzelli, E. Riber , L. Gicquel and T. Poinsot, accepted with minor revision in Combustion and Flame in 2011, is reported in the following.

Introduction

The instabilities of swirled turbulent flows have been the subject of intense research in the last ten years. One important issue has been to identify the possibilities offered by simulation and especially Large Eddy Simulation (LES) to predict self-excited combustion oscillations. The specific example of swirled combustors where flames couple with acoustic modes has received significant attention [50, 146, 64, 139] because such oscillations are often found in real gas turbines [96, 124]. An important question in swirled unstable flames is the effect of mixing on stability. In most real systems, combustion is not fully premixed and even in laboratories, very few swirled flames are truly fully premixed. The effects of equivalence ratio fluctuations on flame stability in combustors have been known for a long time [95, 147]: changes in air inlet velocity induce variations of the flow rate through the flame but may also induce mixing fluctuations and the introduction into the combustion zone of non-constant equivalence ratio pockets. These pockets create unsteady combustion and can generate instabilities.

In many experiments, LES is performed assuming perfect mixing mainly because the computational work is simpler: there is no need to mesh the fuel injection holes or to resolve the zone where these jets mix with air. However, this assumption totally eliminates fluctuations of equivalence ratio as a mechanism of instability, thereby limiting the validity of the LES. One specific example of such limitations is reported in the experiment of [168, 169, 107] which has been computed by multiple groups [133, 66, 61, 111, 3]. This methane/air swirled combustor was especially built to study combustion instabilities in such systems and for all computations up to now, perfect mixing has been assumed by LES experts because methane was injected in the swirler, far upstream of the combustor, suggesting that perfect mixing is achieved before the combustion zone. Interestingly, all computations performed with perfect mixing assumptions have failed to predict the unstable modes observed in the experiments. Moreover, recent Laser Raman scattering measurements [107] show that mixing is not perfect in the chamber and suggest that incomplete mixing could be the source of the instability observed for a mean operating equivalence ratio smaller than $\phi = 0.75$.

The objective of the present work is to use LES to investigate the effects of mixing for this laboratory-scale combustor. The unstructured grid is sufficiently fine to resolve the methane jets and perform both perfectly premixed and real methane injection

simulations. Comparing these simulations to experimental results provides a clear description of the effects of the perfectly premixed assumption. Results show that resolving the mixing of methane and air allows to obtain better mean flow statistics, more realistic Probability Density Functions (pdf) of mixing within the combustor and most importantly, to predict when the combustor becomes unstable. Section 6.1.1 presents the experimental setup and discusses the most important experimental results. Section 6.1.2 describes the numerical setup used for the LES (chemical scheme, mesh, boundary conditions). Section 6.1.3 presents the results for a 'quiet' flame at equivalence ratio $\phi = 0.83$ and a 'pulsating' flame at $\phi = 0.7$. LES results for the two regimes are compared to experimental data in terms of mean and root mean square (RMS) temperature, species and velocity fields, unsteady activity, and pdf of mixture fraction. Even though a further improved LES of the experiment would involve many other ingredients (a finer mesh, more precise chemical schemes, radiation model, wall heat loss description), present results demonstrate that a proper LES of this configuration must include the methane jets and can not be performed with a fully perfect mixing assumption.

6.1.1 The swirled premixed burner configuration

The target experimental burner has been widely described and studied experimentally [168, 169, 107] but also numerically [133, 66, 61, 111, 3]. It is derived from an industrial design by Turbomeca and its behaviour is representative of an industrial gas turbine combustor. Two different regimes have been detected experimentally in this swirled combustor: a 'quiet' and a 'pulsating' flame.

The combustor can be divided into four distinct parts (Fig. 6.1). The first part is the plenum, where dry air at ambient temperature is injected through one large hole. The second part is the injector, where the air flow is swirled by twelve radial veins. Methane is injected into the air flow through twelve small holes (one for each vane) of 1 mm diameter within the radial swirler. The high momentum flow of the swirler is supposed to ensure a good mixing of air and fuel before the nozzle exit. The exit plane of the nozzle is defined as $h = 0$ for all measurements. The third part of the configuration is the combustion chamber which has a square cross subsection (85×85 mm^2) and is equipped with 1.5 mm thick quartz walls to enable optical measurements. The fourth part is a converging duct which connects the combustor to the atmosphere.

Two different regimes have been experimentally observed [107]:

- Case 1: For a global equivalence ratio of $\phi = 0.7$, an unsteady pulsating flame is detected at a frequency $f = 290$ Hz.

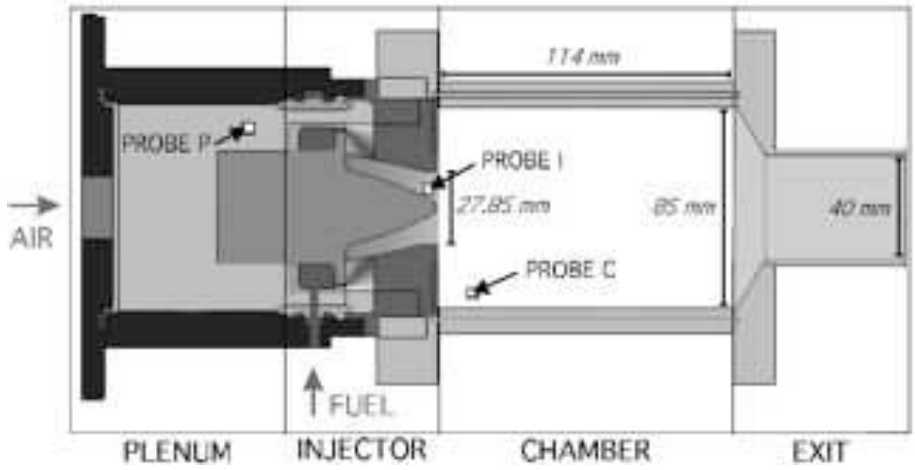

Figure 6.1 - *Schematic of the experimental burner design [168, 169, 107]. Probe P is located in the plenum at h = −70 mm. Probe I is located in the injector before the swirler exit (h = −5 mm) and probe C is in the chamber at h = 10 mm.*

- Case 2a: For a global equivalence ratio of $\phi = 0.83$, a quiet and stable flame is observed in the combustion chamber.

For both cases, Laser Doppler Velocimetry (LDV) measurements of the velocity field were performed in vertical planes located at five different axial subsections (h = 1.5, 5, 15, 25 and 35 *mm*) and along the radial direction. Note that the LDV measurements for the 'quiet' flame correspond to slightly different conditions (case 2b in Table 6.1), *i.e.* a global equivalence ratio of $\phi = 0.75$, and they are not useful for a direct comparison with the numerical results. Systematic and statistical uncertainties are less than 0.5% and 2% respectively [107]. The burner operating conditions of all cases are summarized in Table 6.1.
Laser Raman scattering is used in both cases 1 and 2a to obtain quantitative measurements of major species ($CH_4, O_2, N_2, CO, CO_2, H_2O$ and H_2) and temperature in vertical planes at eight different subsections downstream of the injector (h = 6, 10, 15, 20, 30, 40, 60 and 80 *mm*). The systematic and statistical uncertainties are less than 4% and 2.5% respectively for temperature and less than 5% and 7% respectively for almost all species [107]. For CO and H_2, the statistical uncertainty is between 20 − 50%.

Raman measurements were analyzed [107] in front of the swirler exit to characterize methane/air mixing in the Inner Recirculation Zone (IRZ) and evaluate equivalence ratio fluctuations that can be a source of combustion instabilities. Although the fuel injection was designed to provide an efficient mixing between air and fuel at the chamber inlet, a comparison between the 'quiet' and the 'pulsating' flame suggests

that mixing in the chamber is not perfect and that the fluctuations of equivalence ratio can be the source of the instabilities. Figure 6.2 displays the experimental correlation between temperature and mixture fraction (noted z and based on Bilger's definition [16]) for the 'quiet' ($\phi = 0.83$) and the 'pulsating' ($\phi = 0.7$) cases. The mixture fraction distribution suggests that mixing is not perfect and that its variation is bigger for the 'pulsating' flame at $\phi = 0.7$. Experiments also suggest that this fluctuation is linked to an oscillation of the methane supply [107]. One conclusion is thus that this oscillation generates a variation of combustion intensity, which in turn triggers the pressure oscillation. This effect is higher at $\phi = 0.7$ than at $\phi = 0.83$.
As a consequence, describing mixing before the nozzle exit is necessary to predict the instabilities when performing LES. The hypothesis of perfect premixing used in all previous simulations of this burner seems to be too restrictive and the evaluation of its impact is analyzed with LES in the following subsections.

Table 6.1 - *Flame parameters of the experimental cases. The mixture fraction is based on the Bilger [16] definition.*

Experimental case	**1**	**2a**	**2b**
Air flow rate $[g/min]$	734.2	734.2	734.2
Methane flow rate $[g/min]$	30.0	35.9	32.3
Thermal power $[kW]$	25.1	30.0	27.0
Equivalence ratio $[-]$	0.70	0.83	0.75
Mixture fraction $[-]$	0.0391	0.0463	0.0418

6.1.2 Large Eddy simulation for gas turbines

Four different simulations (Table 6.2) have been performed to study the impact of mixing on the instabilities.
Cases A and C correspond to the 'quiet' and 'pulsating' flames, for which perfect premixing is assumed in LES: a perfectly premixed mixture of methane and dry air at the studied equivalence ratio is injected directly in the plenum (no fuel is injected through the twelve holes in the swirler). In cases B and D, respectively corresponding to the 'quiet' and 'pulsating' flames, LES are computed without the perfect mixing assumption and match exactly the experimental setup: dry air is injected in the plenum and mixes in the swirler with the methane injected through the twelve injection holes. To allow a direct comparison of all simulations, all cases are calculated on the same mesh and with the same numerical parameters.

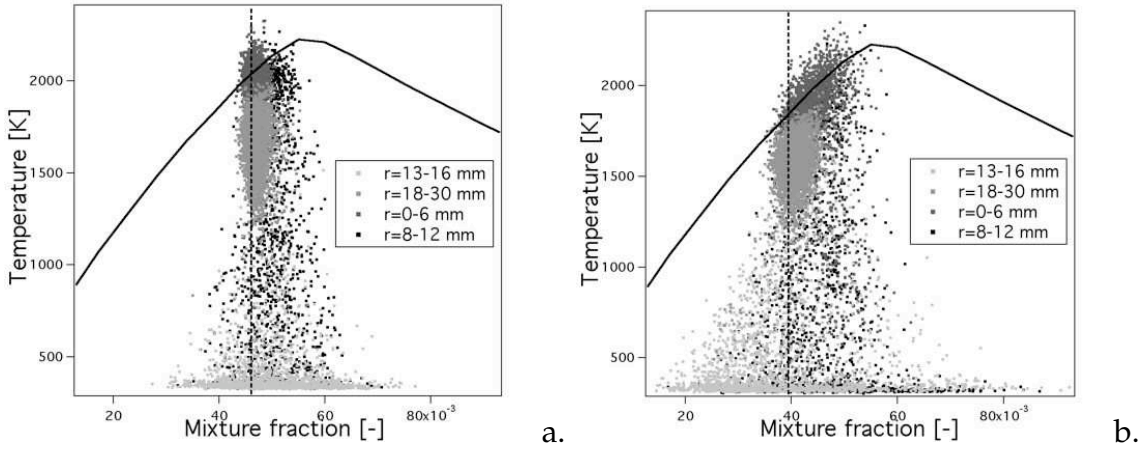

Figure 6.2 - *Correlation between temperature and mixture fraction at subsection h = 6 mm for a., the 'quiet' flame (case 2a in Table 6.1) and b., the 'pulsating' flame (case1). Symbols represent single-shot Raman measurements at different radial positions. The solid line shows the equilibrium temperature whereas the vertical dashed line indicates the global mixture fraction (experimental data from [107]).*

The 2S_CH4_BFER mechanism for premixed methane/air flames

The LES are performed using a two-step reduced scheme for laminar premixed methane/air flames called 2S_CH4_BFER. It contains six species (CH_4, O_2, N_2, CO, CO_2 and H_2O) and has been built using the methodology described in [63] for premixed kerosene-air flames.
Simple models for transport and thermodynamic properties are used. A constant Prandtl number $Pr_o = \mu c_P/\lambda$ is assumed, where c_P is the gas mixture specific heat capacity at constant pressure, λ is the gas mixture thermal conductivity, and μ is the gas mixture dynamic viscosity following a power law:

$$\mu(T) = \mu_o \left(\frac{T}{T_o}\right)^{\alpha} . \tag{6.1}$$

The Prandtl number $Pr_o = 0.7$ and the reference dynamic viscosity $\mu_o = 1.8405\ 10^{-5}\ kg/m/s$ result from the GRI 3.0 detailed mechanism [65] involving 53 species and 341 reactions. They correspond to the Prandtl number and dynamic viscosity in the burnt gases at the reference temperature $T_o = 300K$ whereas the exponent $\alpha = 0.6759$ enables to fit the temperature dependency of the dynamic viscosity over the whole range of temperature at atmospheric pressure [124]. Moreover, the unity Lewis number assumption for all species is used, which does not affect much the laminar flame structure for light fuels [63] and is consistent with the other simplifications used for molecular transport and thermodynamic data.

Table 6.2 - *Main characteristics of the numerical cases.*

Numerical case	**A**	**B**	**C**	**D**
Corresponding experimental case	2a	2a	1	1
Experimental behaviour	Stable	Stable	Unstable	Unstable
Mixing	Perfect	Non-perfect	Perfect	Non-perfect
Equivalence ratio [−]	0.83	0.83	0.7	0.7
Plenum composition	Air+CH_4	Air	Air+CH_4	Air
Plenum flow rate [g/min]	734.2	734.2	734.2	734.2
Holes composition	-	CH_4	-	CH_4
Holes flow rate [g/min]	-	35.9	-	30.0
Numerical behaviour	Stable	Stable	Stable	Unstable

The 2S_CH4_BFER scheme is based on the two following reactions:

$$CH_4 + 1.5\ O_2 \quad => \quad CO + 2\ H_2O \tag{6.2}$$

$$CO + 0.5\ O_2 \quad <=> \quad CO_2\ , \tag{6.3}$$

where the forward reaction rates for reactions (6.2) and (6.3) are written as:

$$k_{f,1} = A_1\ f_1(\phi)\ T^{\beta_1} e^{(-E_{a,1}/RT)}\ [CH_4]^{n_{CH_4}}\ [O_2]^{n_{O_2,1}}\ , \tag{6.4}$$

$$k_{f,2} = A_2\ f_2(\phi)\ T^{\beta_2} e^{(-E_{a,2}/RT)}\ [CO]^{n_{CO}}\ [O_2]^{n_{O_2,2}}\ , \tag{6.5}$$

where A_k is the pre-exponential factor, $E_{a,k}$ the activation energy, β_k the temperature exponent of reaction k and $n_{j,k}$ the reaction exponent for species j in reaction k. The subscripts 1 and 2 respectively denote the methane oxidation and the $CO - CO_2$ equilibrium reactions. The reaction parameters are summarised in Table 6.3.

Table 6.3 - *Activation energy E_a, temperature exponent β, pre-exponential factor A and reaction exponents n_k used for the 2S_CH4_BFER mechanism. Units are: mol, s, cm^3 and cal/mol.*

	CH_4 oxidation		CO-CO_2 equilibrium	
Activation energy	3.55×10^4		1.2×10^4	
Temperature exponent	0.0		0.8	
Pre-exponential factor	4.9×10^9		2×10^8	
Reaction exponents (-)	n_{CH_4}	0.50	n_{CO}	1.00
	$n_{O_2,1}$	0.65	$n_{O_2,2}$	0.50

The reaction exponents $n_{j,k}$ have been chosen following [124] so that the obtained pressure exponent $\alpha_P = (n_{CH_4} + n_{O_2} - 2)/2$ is almost equal to the mean value over the

whole range of pressure, temperature and equivalence ratio considered: $\alpha_P = -0.425$. Note that this pressure dependent coefficient is not constant [172], varying from $\alpha_P = -0.53$ for $T_f = 300\ K$ and $P = 10\ atm$, to $\alpha_P = -0.29$ at $T_f = 700\ K$ and $P = 3\ atm$ using the GRI 3.0 mechanism.
The first reaction controls the flame speed and the autoignition time. The second reaction represents the $CO - CO_2$ equilibrium and is necessary to predict the flame temperature in the burnt gases for rich mixtures.
The two pre-exponential factors are adjusted by two correction functions depending on local equivalence ratio: f_1 allows to decrease the laminar flame speed for rich flames, bringing the flame speed to the GRI 3.0 mechanism values whereas f_2 is calibrated to adjust the thickness of the post-flame zone and to quickly reach the equilibrium state. The two correction functions are given by:

$$f_1(\phi) = \frac{2}{\left[1 + \tanh\left(\frac{\phi_{0,1}-\phi}{\sigma_{0,1}}\right)\right] + B_1\left[1 + \tanh\left(\frac{\phi-\phi_{1,1}}{\sigma_{1,1}}\right)\right] + C_1\left[1 + \tanh\left(\frac{\phi-\phi_{2,1}}{\sigma_{2,1}}\right)\right]}, \quad (6.6)$$

$$\begin{aligned} f_2(\phi) &= \frac{1}{2}\left[1 + \tanh\left(\frac{\phi_{0,2} - \phi}{\sigma_{0,2}}\right)\right] + \frac{B_2}{2}\left[1 + \tanh\left(\frac{\phi - \phi_{1,2}}{\sigma_{1,2}}\right)\right] \\ &+ \frac{C_2}{2}\left[1 + \tanh\left(\frac{\phi - \phi_{2,2}}{\sigma_{2,2}}\right)\right] \times \left[1 + \tanh\left(\frac{\phi_{3,2} - \phi}{\sigma_{3,2}}\right)\right], \end{aligned} \quad (6.7)$$

where the coefficients are summarized in Table 6.4.

To validate the 2S_CH4_BFER scheme, calculations of premixed laminar methane/air

Table 6.4 - *Coefficients for the two correction functions f_1 and f_2 in the 2S_CH4_BFER scheme.*

	$\phi_{0,j}$	$\sigma_{0,j}$	B_j	$\phi_{1,j}$	$\sigma_{1,j}$	C_j	$\phi_{2,j}$	$\sigma_{2,j}$	$\phi_{3,j}$	$\sigma_{3,j}$
$j = 1$	1.1	0.09	0.37	1.13	0.03	6.7	1.6	0.22	-	-
$j = 2$	0.95	0.08	$2.5\ 10^{-5}$	1.3	0.04	0.0087	1.2	0.04	1.2	0.05

flames were performed using CANTERA [71] for three different values of fresh gas temperature ($T_f = 300, 500, 700K$) and pressure ($P = 1, 3, 10\ atm$). Ten equivalence ratios have been tested, from $\phi = 0.6$ to $\phi = 1.5$.

For the whole range of pressure and fresh gas temperature, the 2S_CH4_BFER scheme reproduces well the laminar flame speed in comparison with the GRI 3.0 mechanism (Fig. 6.3). The largest discrepancies occur for $T_f = 300\ K$, $P = 10\ atm$ (up to 32%) and $T_f = 700\ K$, $P = 3\ atm$ (up to 19%) due to the variations of the pressure dependency coefficient observed at these conditions. The temperature dependency is

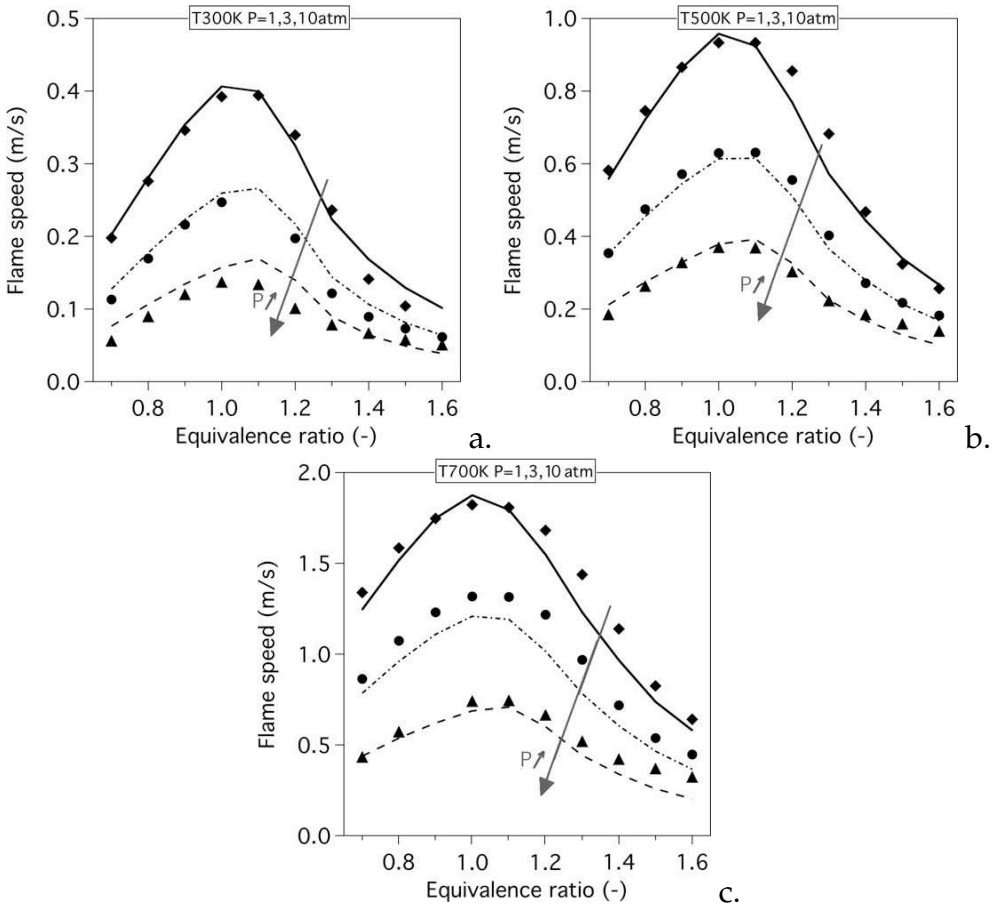

Figure 6.3 - *Laminar flame speed versus equivalence ratio at fresh gas temperature T_f = 300K (a.), 500K (b.) and 700K (c.). Comparison between 2S_CH4_BFER scheme (P = 1 atm: ——, P = 3 atm: —·—·—, P = 10 atm: – – –) and GRI 3.0 detailed mechanism (P = 1 atm: ♦, P = 3 atm: •, P = 10 atm: ▲).*

well preserved. Focusing on the experimental burner studied in this work, the results at ambient pressure and temperature are very close to the GRI 3.0 mechanism.

In Fig. 6.4, the adiabatic temperature obtained at $T_f = 300\ K$ and $P = 1\ atm$ with the 2S_CH4_BFER scheme is plotted versus equivalence ratio and compared to equilibrium values using the 6 species involved in the reduced scheme and the 53 species involved in the GRI 3.0 mechanism. The agreement is very good up to $\phi = 1.4$, as expected when using two-step chemical schemes [63]. This shows also that the scheme should perform well in the targeted burner where experiments indicate that the local equivalence ratio in the chamber never exceeds $\phi = 1.4$ ($z \simeq 0.08$ in Fig. 6.2).

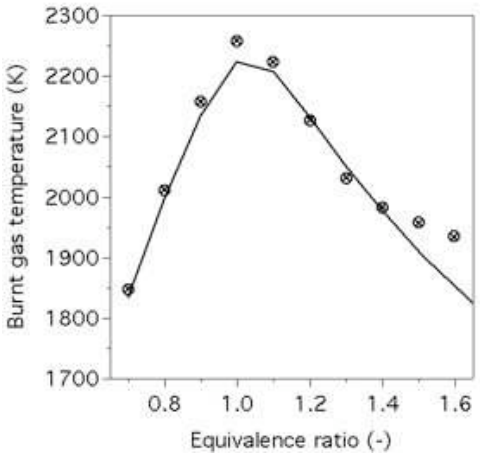

Figure 6.4 - *Burnt gas temperature versus equivalence ratio. Comparison between GRI3.0 mechanism (——), equilibrium results (×) and 2S_CH4_BFER scheme (○) at pressure $P = 1$ atm and fresh gas temperature $T_f = 300$ K.*

The numerical setup

A compressible LES code [139, 133, 46, 83, 144, 149, 131, 68, 113, 157, 143, 23, 145] is used to solve the Navier-Stokes equations on hybrid (structured and unstructured) grids with real thermo-chemistry. A Taylor-Galerkin weighted residual central distribution scheme is used for the numerical integration [113, 45, 47]. It is a finite element based scheme, providing third-order accuracy in time and space on unstructured meshes. The interaction between chemical kinetics and turbulence is modeled by the Dynamically Thickened Flame (DTFLES) model [46]. Following the theory of laminar premixed flames [173], the flame speed s_L^o and the flame thickness δ_L^o may be expressed as:

$$s_L^o \propto \sqrt{\lambda A} \quad \text{and} \quad \delta_L^o \propto \frac{\lambda}{s_L^o} = \frac{\lambda}{A}\,, \tag{6.8}$$

where λ is the thermal diffusivity and A is the pre-exponential constant. Increasing the thermal diffusivity by a factor F, the flame speed is kept unchanged if the pre-exponential factor is decreased by the same factor [33]. This operation leads to a flame thickness which is multiplied by F and easy to resolve on a coarse mesh. Additional information needs however to be supplied so as to properly reproduce the effect of the subgrid-scale interaction between turbulence and chemistry [7, 93], which is the intent of the so-called efficiency function [46]. If F is applied everywhere in the computational domain, the model is limited to perfectly premixed combustion. In this work, a modified version called DTFLES is used to apply the factor F in the flame front only [93].

The computational domain (Fig. 6.5) extends downstream of the combustion

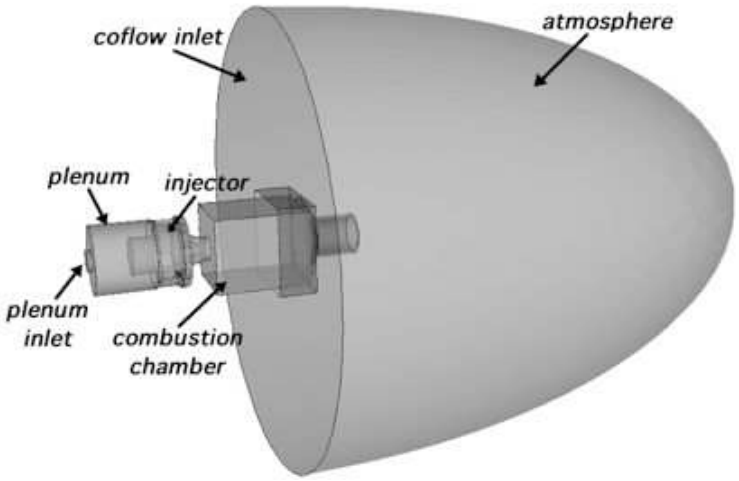

Figure 6.5 - *Schematic of the computational domain.*

chamber to take into account a part of the outside atmosphere. Indeed since the acoustic impedance at the chamber exit is unknown, a solution proposed in [133] is to extend the grid far enough downstream of the chamber exit to be able to impose a non-reflecting outlet boundary condition at atmospheric pressure. The full geometry is meshed including the twelve holes located upstream of the swirler.The mesh shown in Fig. 6.6a is unstructured and contains five million tetrahedral elements. It is refined inside the swirler veins to capture mixing. There are at least five cells in the radial direction of each methane injection hole, which means that the characteristic cell length is about 0.2 *mm* in this region. Those cells are the smallest of the computational

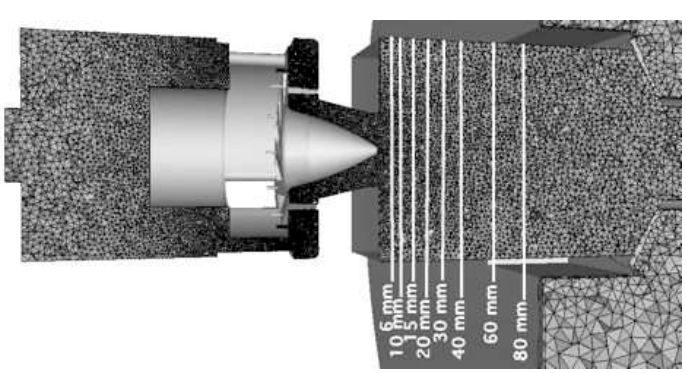

a.

b.

Figure 6.6 - *a) Computational half-domain mesh. b)Detail of the twelve computational holes upstream of the swirler for the methane injection (LES's numerical cases B and D in Table 6.2). Instantaneous iso-surface of methane mass fraction equal to 0.5.*

domain. The characteristic size of the cells where reactions take place is about 1 *mm*: a local thickening factor of ten is sufficient to obtain at least five points in the flame front.

The inlets (air and fuel) and the outlet are described by Navier-Stokes Characteristic Boundary Conditions (NSCBC) [123, 113, 72]. An adiabatic no-slip condition is applied for all walls. All simulations are performed on the same mesh and with the same numerical parameters: only the boundary condition specifications vary. If the perfect mixing assumption is applied (cases A and C), the fuel injection holes are considered as walls and a perfectly premixed methane/air mixture is injected at the plenum inlet (the composition of the mixture varies accordingly to the equivalence ratio analyzed). Otherwise (cases B and D), dry air is imposed at the plenum inlet and pure methane at the swirler holes, as evidenced by an instantaneous iso-surface of CH_4 species mass fraction equal to 0.5 in Fig. 6.6b.

At the inlet of the plenum and the methane injections, mass flow is imposed (Table 6.2). Fresh gases are injected at 320 K for all simulations[1].

6.1.3 Results and discussions

The 'quiet' flame - $\phi = 0.83$

At $\phi = 0.83$ (case 2a), the burner is experimentally characterized by a quiet flame stabilized at the nozzle exit. Two different numerical simulations have been performed for this operating point:

- Case A: Previous LES for this operating point [133, 66, 61, 111] have correctly reproduced a quiet flame when injecting a perfectly premixed mixture at the inlet. Similar conclusions are reached here.
- Case B: In this case, methane and air are injected separately. Figure 6.7a. shows the numerical correlation between temperature and mixture fraction which corresponds to the experimental results of Figure 6.2a., in the first subsection downstream of the nozzle exit ($h = 6$ *mm*) for different radial positions. Light-grey samples are collected at $r = 13-16$ *mm* close to the injection of fresh gases into the chamber where the temperature is low and the mixture fraction variance is maximum.Even if the experimental extreme values of mixture fraction ($z_{min} \approx 0.03$ and $z_{max} \approx 0.07$) are not captured by LES, the mixture fraction distribution is correctly

[1]In the experiments, the inlet fuel/air mixture temperature varies between 320 and 380 K. Likewise, the ambient pressure varies between 995 and 1030 mbar. These differences could have a moderate effect on the results.

reproduced (Figure 6.7b.). The reaction zone is roughly represented by the black symbols ($r = 8 - 12$ *mm*) in Fig. 6.7a.: it is a region of intermittency between fresh and burnt gases. The charcoal-grey symbols in Fig. 6.7a. correspond approximately to the IRZ. It is almost an equilibrium state: the temperature reaches

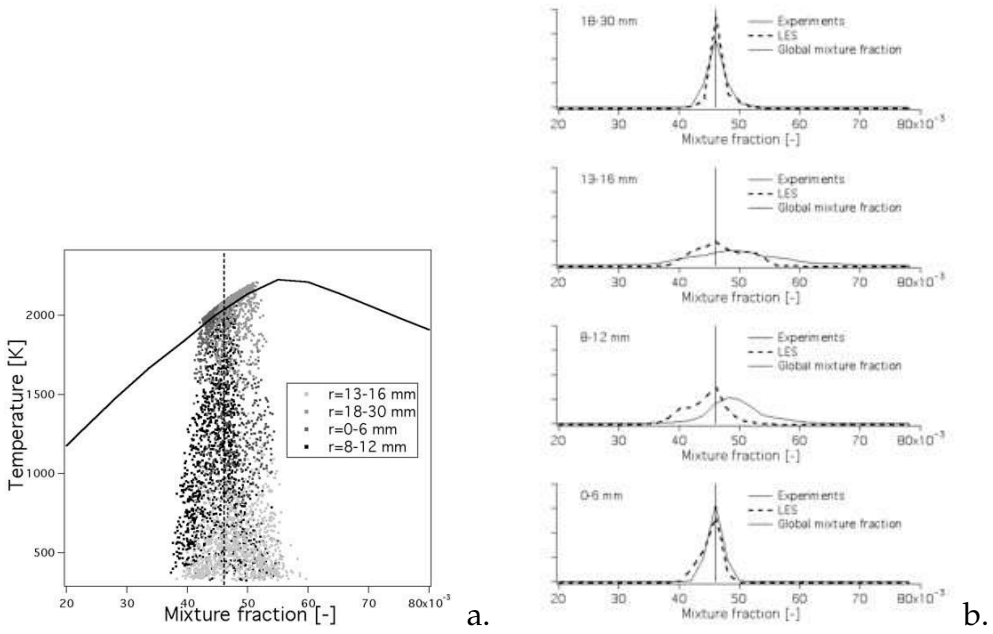

Figure 6.7 - *a. Numerical correlation between temperature and mixture fraction for the 'quiet' flame ($\phi = 0.83$) at $h = 6$ mm (case B). b. Experimental (case 2a - solid line) and numerical (case B - dashed line) mixture fraction distribution at $h = 6$ mm for the 'quiet' flame ($\phi = 0.83$). The global mixture fraction is indicated by the vertical line.*

the adiabatic value and the equivalence ratio is close to the mean value of the combustor ($\bar{z} = 0.0463$). Both the reaction zone and the IRZ are correctly reproduced by the simulation. Discrepancies between experimental and numerical results are mainly detected in the Outer Recirculation Zone (ORZ) corresponding to $r = 18 - 30$ *mm* (mid-grey symbols): the temperature is overestimated most likely because heat losses at the chamber walls and radiation effects are not taken into account. Nevertheless, the flame structure is well characterized and the mixing between fresh air and methane is correctly described. Figure 6.8a. compares the scatterplots of computed temperature versus mixture fraction with the experimental results at three subsections further in the combustion chamber ($h = 15, 30$ and 80 *mm*). As the distance from the swirler exit increases, the mixture fraction variations are reduced and the local gas state approaches equilibrium. Note that LES has some difficulties capturing the presence of fresh gases at $h = 15$ *mm* and predicts a slightly shorter flame. Nevertheless, the experimental mixture fraction

distribution is correctly reproduced by the computations (Fig. 6.8b.).

Figure 6.9a. compares the mean temperature profiles at five different subsections in the chamber obtained numerically with (case B) and without (case A) the perfect premixing hypothesis (solid line and dashed line respectively) with the experimental results (symbols). The simulations correctly reproduce the IRZ and the reaction zone. The temperature in the ORZ is overestimated since wall heat losses and radiation effects are not taken into account. Mean profiles reveal no significant differences between the two LES. Figure 6.9b. compares numerical and experimental temperature fluctuation profiles. When air and methane are injected separately, the flame oscillations are slightly increased and the temperature fluctuations are better described in the reaction zone. Nevertheless, the fluctuations within the ORZ and IRZ are still underestimated due to the adiabatic hypothesis. Mean and RMS profiles of CO_2 provide similar levels of agreement with experiments (Fig. 6.10). The description of CO_2 fluctuations is slightly improved when injecting methane and air separately (case B) but no relevant difference between the numerical results is detected in the mean profiles. For CO, the situation is different: Fig. 6.11 compares LES mean profiles of CO with experimental results for which error bars are introduced. Although both simulations greatly underestimate the levels of CO species, it is difficult to conclude since experimental results show an error bar of about 50%. All other species are correctly described and the quality of the results is similar to that of CO_2 (not shown).

The 'pulsating' flame - $\phi = 0.7$

The burner has never been computed for an equivalence ratio of $\phi = 0.7$, which corresponds to a 'pulsating' flame oscillating around its mean position located in the near field of the nozzle exit. Figure 6.12 displays the temporal evolution of heat release, mixture fraction and pressure fluctuations before the exit nozzle (probe I in Fig. 6.1) for the two numerical simulations performed at this operating point:

- Case C: Assuming perfect premixing, no variation of the mixture fraction is detected and oscillations of pressure are small at probe I. Heat release localizes the reaction zone and consequently, the flame position. In this case, it is constantly equal to zero: a quiet flame is stabilized at the nozzle in contrast to the experimental results.
- Case D: When methane and air are injected separately, higher pressure oscillations are observed before the nozzle exit (Fig. 6.12c.). High heat release fluctuations are detected at probe I (Fig. 6.12a.), which indicates a pulsating flame and supports the experimental observation that the fluctuations in equivalence ratio at the nozzle are the cause of the thermo-acoustic instabilities.

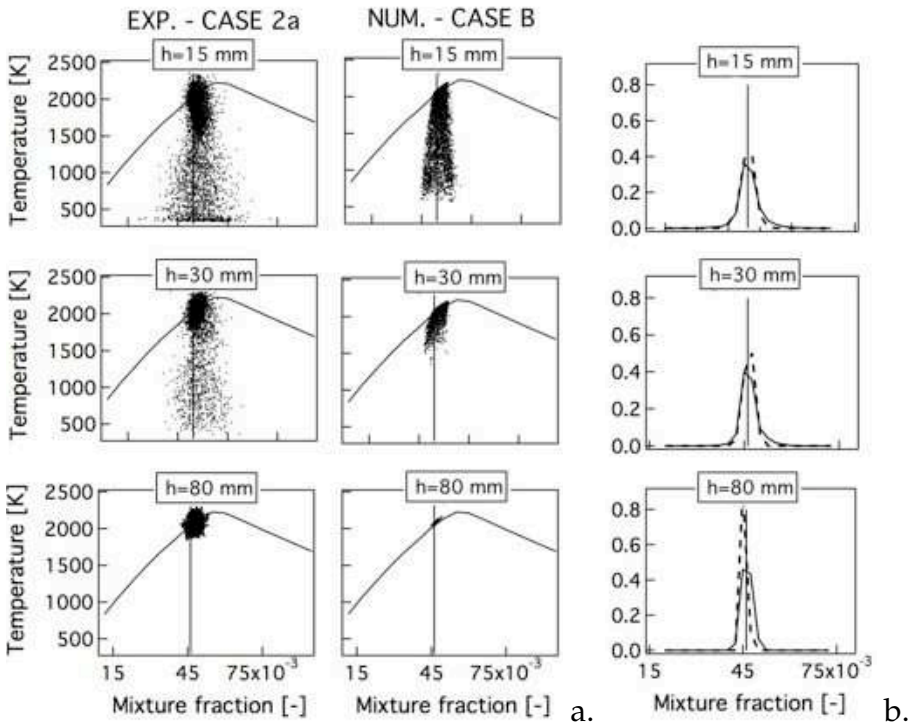

Figure 6.8 - *a. Experimental (case 2a) and numerical (case B) correlation between temperature and mixture fraction for the 'quiet' flame ($\phi = 0.83$) at $h = 15, 30$ and 80 mm. b. Experimental (case 2a - solid line) and numerical (case B - dashed line) distribution of the mixture fraction at $h = 15, 30$ and 80 mm for the 'quiet' flame.*

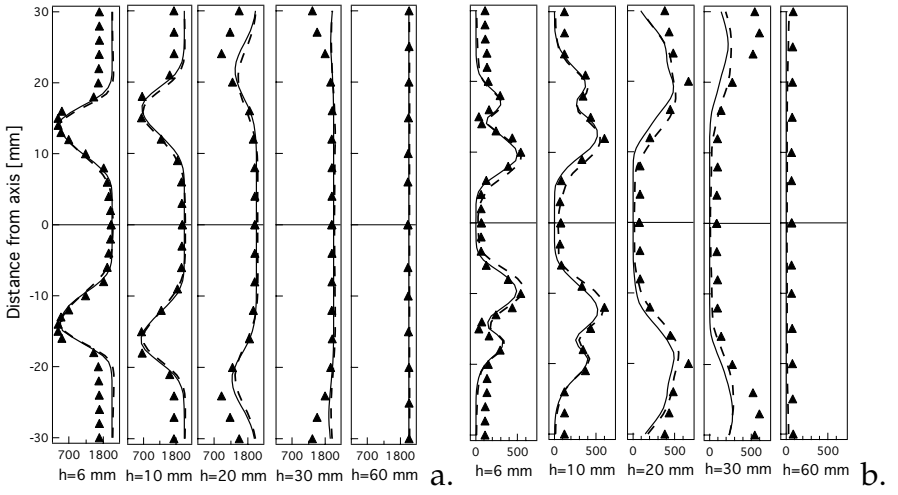

Figure 6.9 - *a. Mean and b. RMS temperature profiles for the 'quiet' flame ($\phi = 0.83$) at five subsections in the chamber. The experimental results (symbols) are compared to numerical data: perfect premixed (case C - solid line) and non perfect premixed simulation (case D - dashed line).*

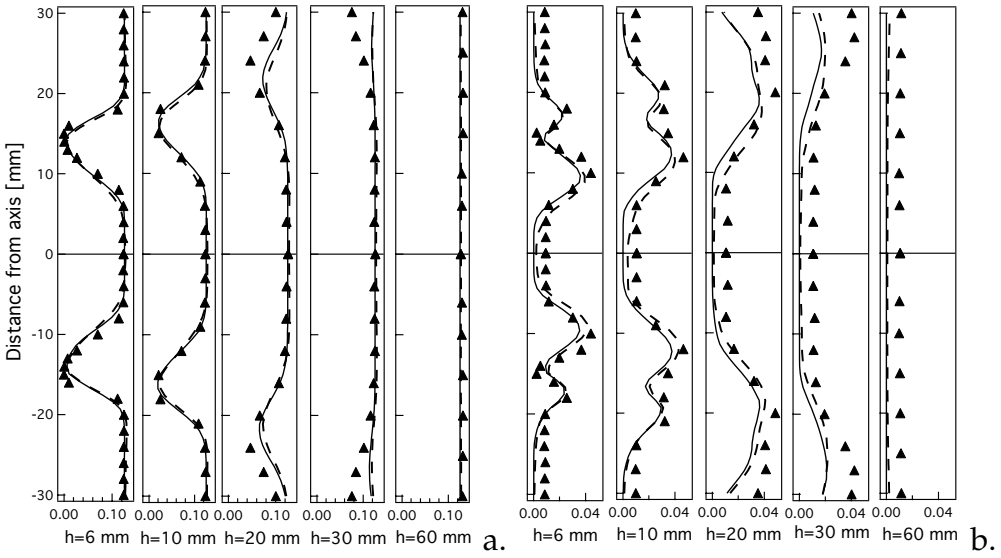

Figure 6.10 - *a. Mean and b. RMS CO_2 profiles for the 'quiet' flame (ϕ = 0.83) at five subsections in the chamber. The experimental results (symbols) are compared to numerical data: perfect premixed (case C - solid line) and non perfect premixed simulation (case D - dashed line).*

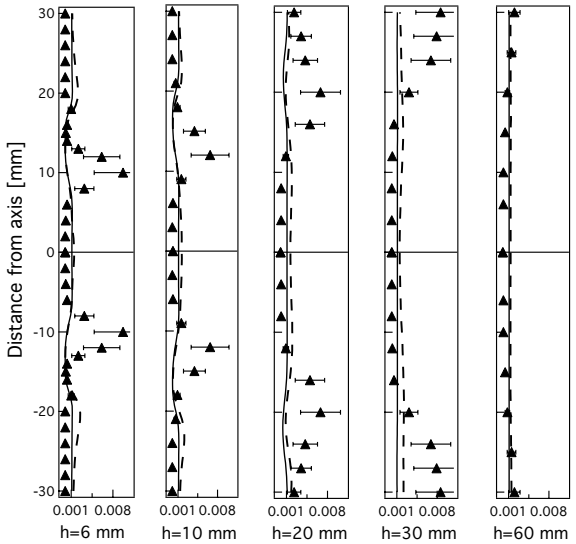

Figure 6.11 - *Mean CO species profiles for the 'quiet' flame (ϕ = 0.83) at five subsections in the chamber. The experimental results (symbols) are compared to numerical results: perfectly premixed simulation (case A - solid line) and non perfectly premixed simulation (case B - dashed line).*

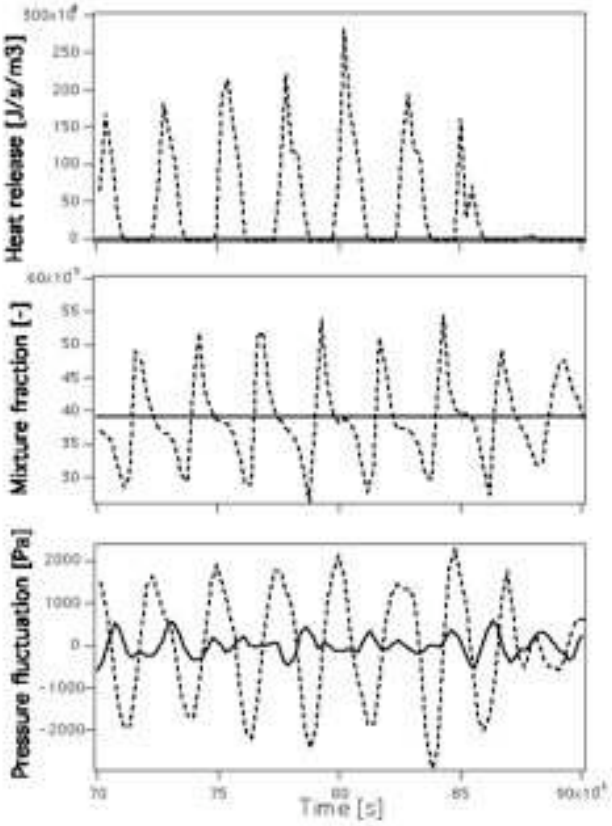

Figure 6.12 - *Temporal evolution of the heat release (a.), mixture fraction (b.) and pressure (c.) at probe I for the 'pulsating' flame ($\phi = 0.7$). Comparison between perfectly premixed simulation (case C - solid line) and non perfectly premixed simulation (case D - dashed line).*

LES and experiments are compared at the first subsection downstream of the nozzle exit ($h = 6\,mm$) in terms of correlation between temperature and mixture fraction (Fig. 6.13a.) and distribution of mixture fraction (Fig. 6.13b.). These figures can be compared to Figs. 6.7a. and 6.7b. respectively for the 'quiet' flame (case B): obviously, case D exhibits much higher unmixedness and temperature variations. The experimental distribution of mixture fraction is correctly reproduced even if the experimental extreme values of mixture fraction, $z_{min} \approx 0.015$ and $z_{max} \approx 0.08$ respectively, are not captured (Fig. 6.13). Within the chamber ($h = 15, 30$ and $80\ mm$), the scatterplots of temperature versus mixture fraction also match experimental results (Fig. 6.14a.) and the mixture fraction distribution is correctly estimated (Fig. 6.14b.).

The mean profiles obtained for case D correspond to a pulsating situation. Velocity has been measured for this case and LES profiles of the mean velocity components

(axial, radial and tangential) can be compared to LDV measurements at five subsections downstream of the injector (in Fig. 6.15 only axial and radial velocities are represented). Three different regions can be detected looking at the mean axial velocity: the injection of fresh gases generates a conically-shaped flow characterized by high axial and radial velocity values; a reverse flow is detected in the IRZ and the ORZ is characterized by low velocities. Profiles are generally improved for case D: the opening of fresh gas injection is correctly captured and the negative velocity values that characterize the IRZ reach approximately 20 m/s at $h = 1.5$ mm as measured experimentally.

The mean temperature profiles for cases C and D are compared to the experimental results in Fig. 6.16a. The agreement between numerical and experimental results is generally good. The temperature of the IRZ and the reaction region are better described by the non perfectly-premixed LES (case D). Again, temperature profiles are overestimated in the ORZ. The perfect premixing hypothesis (case C) has a strong effect on the temperature fluctuations (Fig. 6.16b.). Since LES for case C leads to a quiet flame and does not capture the instability, the temperature fluctuations are greatly underestimated, whereas case D correctly predicts them. This difference is more evident in the IRZ than in other regions and clearly shows the importance of computing mixing if the objective is to capture unstable modes.

Finally, the mean and RMS profiles of CO_2 (Fig. 6.17) lead to the same conclusions: mean CO_2 profiles are slightly improved when assuming non perfect premixing, but the RMS profiles are much better captured when the methane jets are calculated (case D). All other species profiles (not shown) confirm these results except CO for which experimental uncertainties are high.

Time evolutions of the fluctuations of total heat release q and chamber pressure p_C (probe C in Fig. 6.1) are shown in Fig 6.18a for case D. Heat release and pressure oscillate at the same frequency, suggesting that the instability in case D is fed by a flame/acoustics coupling. The associated flapping frequency is found equal to $f_{num} \approx 390$ Hz for case D, when the experimental value f_{exp} is close to 290 Hz. This discrepancy could be due to the acoustic impedance at the fuel injection which was not characterized experimentally and arbitrarily imposed in LES.
Despite this limitation, a phase-averaged description of LES dynamics is proposed in the following. For the analysis, the pressure drop ΔP (between probes P and C in Fig. 6.1) and the pressure in the plenum P_P (probe P) are displayed in Fig. 6.18b for case D. As these two signals are almost in phase, the plenum pressure can be considered as a proper signal to perform phase-averaging analysis in the chamber. To compare with the experiments, numerical results are sampled at four phases of the pressure P_P over 20 cycles of the LES results: the minimum, maximum and medium values (reference points named as *ph1*, *ph5*, *ph3* and *ph7* in [107], see Fig. 6.18b).

The feedback loop of the self-sustained pulsation can only be presumed in the experiments since no data is available for the swirler. But in LES, it can be visualized by displaying phase-locked instantaneous velocity fields (Fig. 6.19a.) and CH_4 fields (Fig. 6.19b.) of the 'pulsating' flame. When ΔP is small (phase *ph1*), the axial velocity in the swirler is low (Fig. 6.19a.). The methane jets are injected in a low velocity air stream. They are not deviated significantly and impact the wall of the chamber. Fuel accumulates in the swirler (phase *ph*1 in Fig. 6.19b.). At phase *ph3*, the air velocity is still low, the fuel mass fraction is maximum in the swirler and a lean mixture enters the chamber. When ΔP is maximum (phase *ph5*), the axial velocity within the swirler is high. The methane jets do not impact walls and the fuel accumulated in the swirler is pushed towards the chamber. It enters the chamber at phase *ph7* (Fig. 6.19b.).

The time evolution of the axial velocity and mixture fraction near the exit nozzle (probe *I* in Fig. 6.1) together with the pressure drop are displayed in Fig. 6.20. LES supports experimental conclusions: the velocity field in the swirler oscillates when the pressure drop pulsates and rich gas pockets are periodically pushed into the chamber [175].

6.1.4 Conclusions

This study has provided a systematic comparison of mean and RMS fields obtained experimentally and by LES in the swirled methane/air experimental combustor [168, 169, 107]. LES have been performed with a compressible solver to capture self-excited modes. Methane injection was either simplified by assuming perfect premixing upstream of the swirler or fully resolved by meshing all methane injectors and computing the mixing between air and methane within the swirler. Results demonstrate that assuming that the methane/air flow entering the chamber is perfectly premixed has a limited influence for the stable regime at $\phi = 0.83$: the mean and RMS fields obtained with or without perfect mixing assumptions are very close and agree well with experimental data. However, a strong effect of the perfect mixing assumption is observed on the unstable regime at $\phi = 0.7$: LES with perfectly premixed mixture remains stable while LES where the methane jets are resolved leads to a self-excited mode. The velocity pulsates and the fuel periodically accumulates within the swirler before entering the chamber and burning in a very unsteady mode. This result confirms the experimental study of Meier *et al.* [107] who indicates that insufficient mixing is probably the source of the unstable mode observed at $\phi = 0.7$. The details of the exact mechanism controlling the instability mechanism itself were not identified yet but results demonstrate that both compressibility and methane/air mixing must be included in future codes trying to reproduce this type of unstable modes.

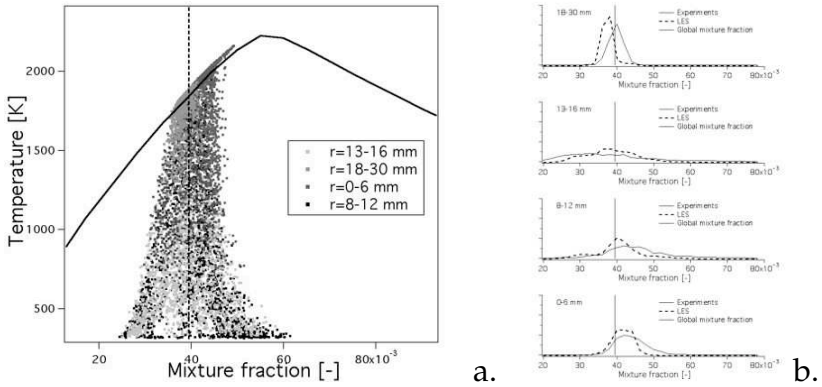

Figure 6.13 - *a. Numerical correlation between temperature and mixture fraction for the 'pulsating' flame ($\phi = 0.7$) at $h = 6$ mm (case D). b. Experimental (case 1 - solid line) and numerical (case D - dashed line) distribution of mixture fraction at $h = 6$ mm for the 'pulsating' flame ($\phi = 0.7$). The global mixture fraction is indicated by the vertical line.*

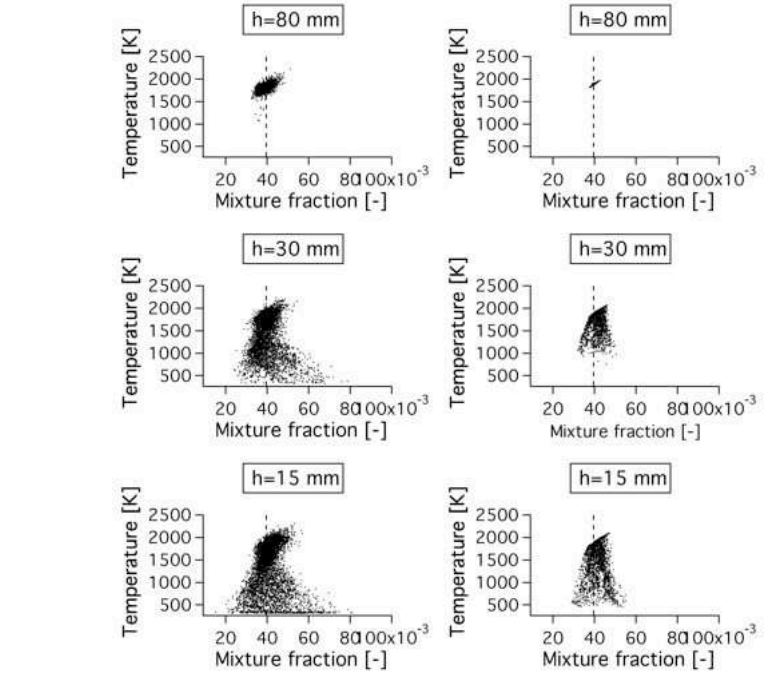

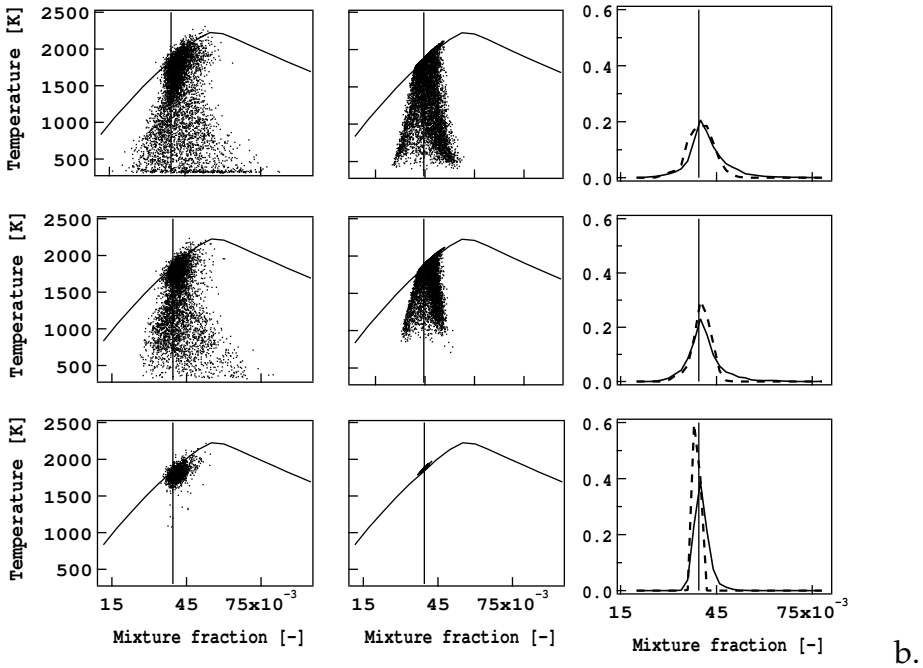

Figure 6.14 - *a. Experimental (case 1) and numerical (case D) correlation between temperature and mixture fraction for the 'pulsating' flame ($\phi = 0.7$) at $h = 15, 30$ and 80 mm. b. Experimental (case 1 - solid line) and numerical (case D - dashed line) distribution of mixture fraction at $h = 15, 30$ and 80 mm for the 'pulsating' flame.*

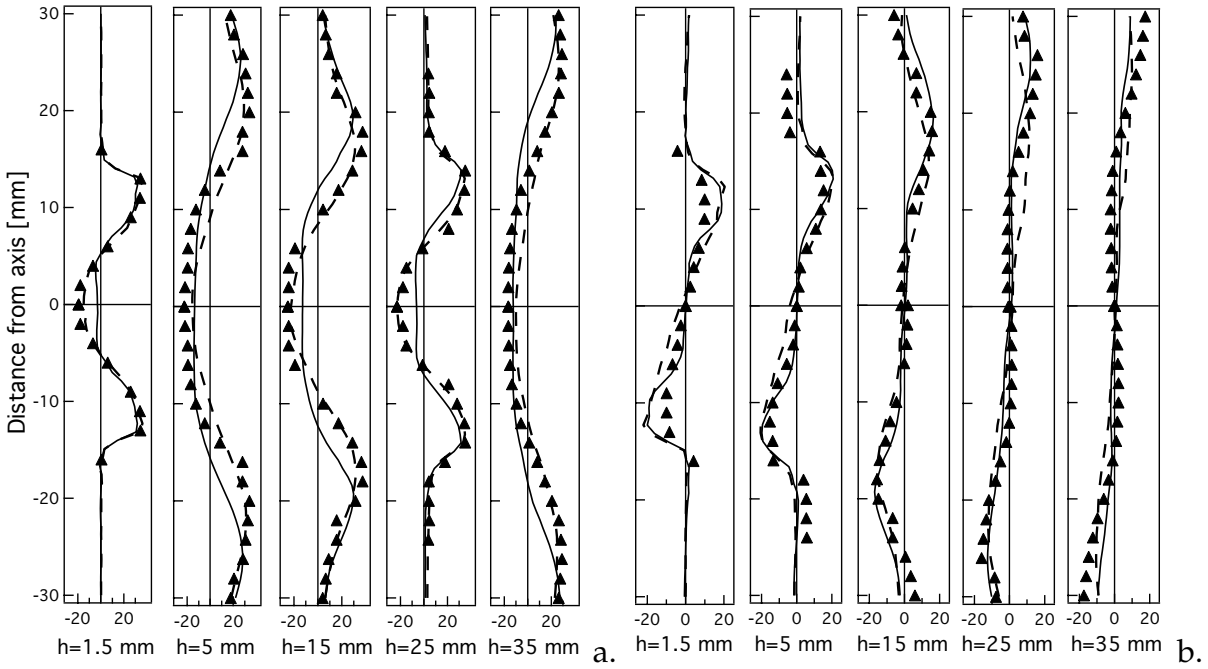

Figure 6.15 - *Mean a. axial and b. radial velocity profiles for the 'pulsating' flame ($\phi = 0.7$) at five subsections in the chamber. The experimental results (symbols) are compared to numerical results: perfectly premixed simulation (case C - solid line) and non perfectly premixed simulation (case D - dashed line).*

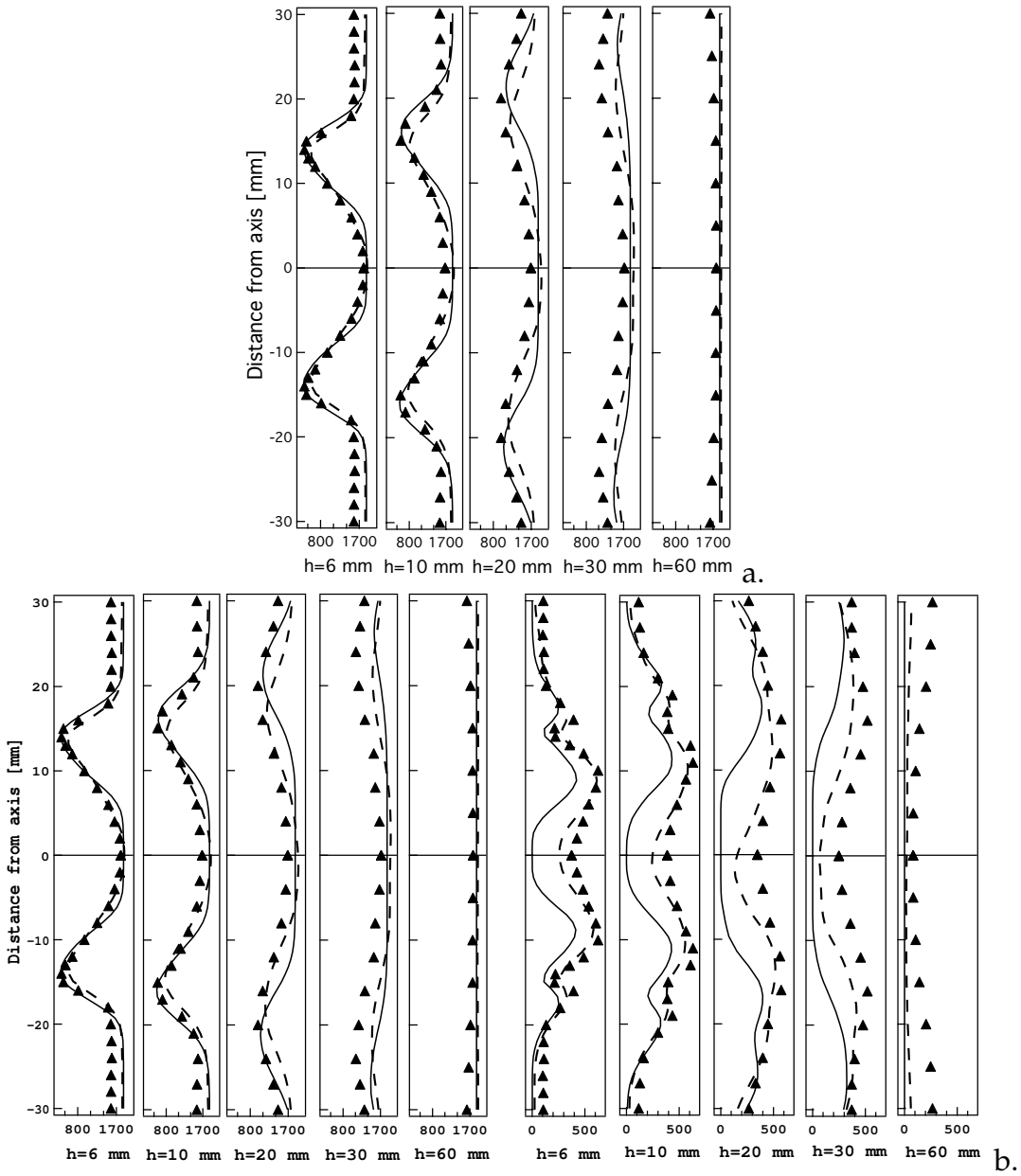

Figure 6.16 - *a. Mean and b. RMS temperature profiles for the 'pulsating' flame ($\phi = 0.7$) at five subsections in the chamber. The experimental results (symbols) are compared to numerical data: perfect premixed (case C - solid line) and non perfect premixed simulation (case D - dashed line).*

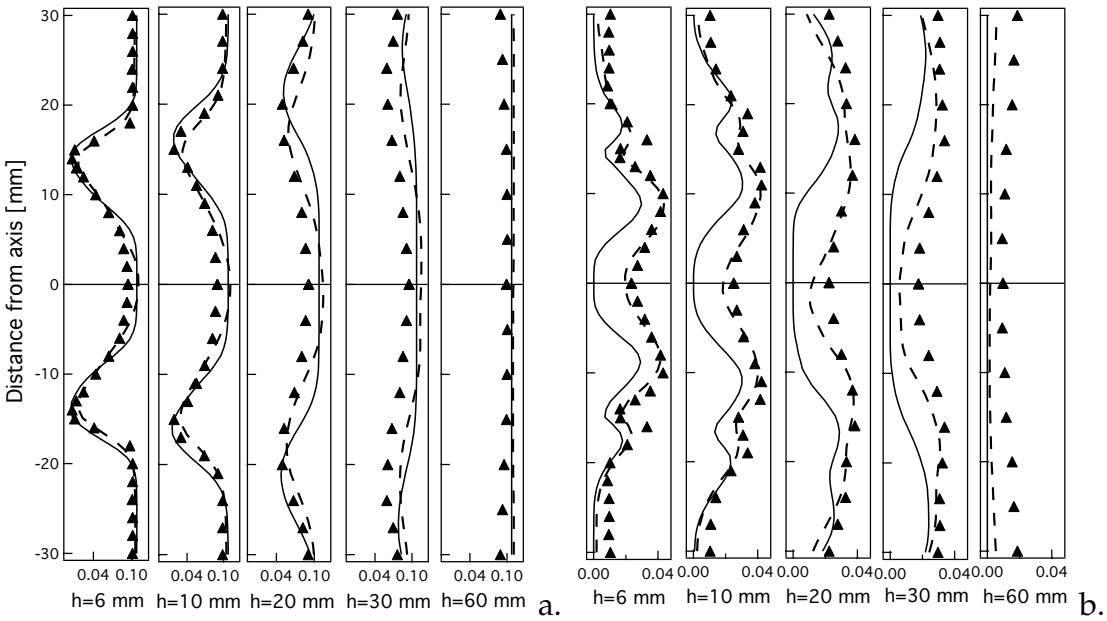

Figure 6.17 - *a. Mean and b. RMS CO_2 profiles for the 'pulsating' flame ($\phi = 0.7$) at five subsections in the chamber. The experimental results (symbols) are compared to numerical data: perfect premixed (case C - solid line) and non perfect premixed simulation (case D - dashed line).*

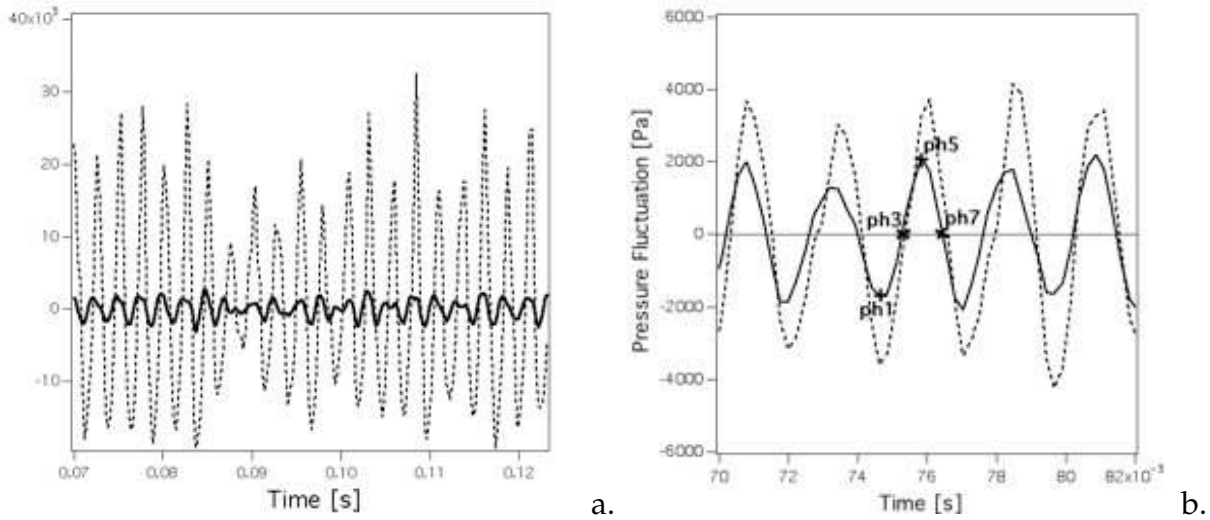

Figure 6.18 - *a) Temporal evolution of the fluctuations of chamber pressure p_C (solid line, probe C in Fig. 6.1) and total heat release q (dashed line) for the 'pulsating' flame (case D). b) Temporal evolution of the plenum pressure P_P at probe P in Fig. 6.1 (solid line) and the pressure drop ΔP (dashed line) between plenum and chamber (probe C in Fig. 6.1) for the 'pulsating' flame (case D).*

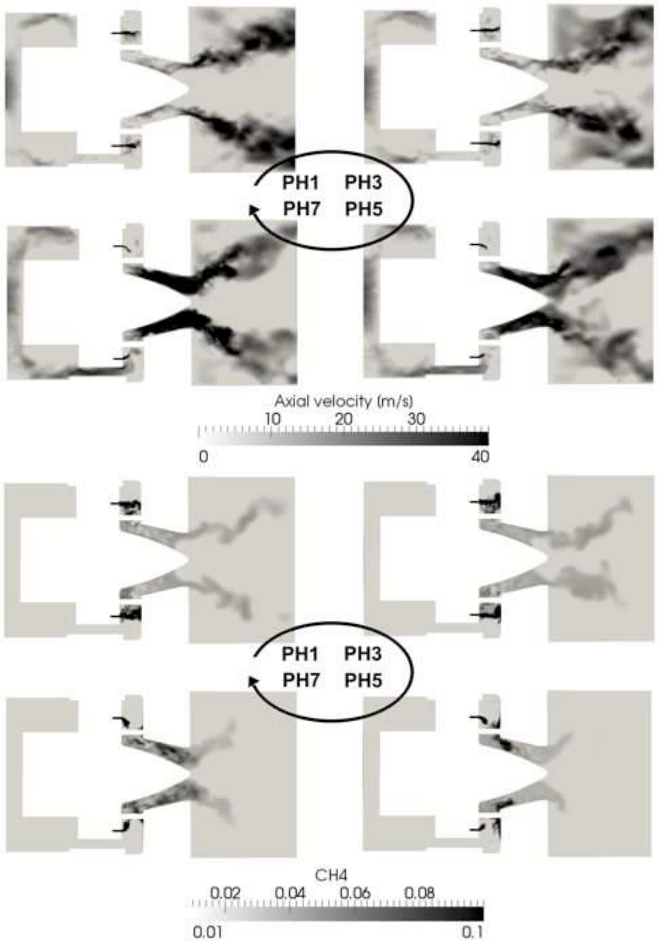

Figure 6.19 - *Phase-locked instantaneous fields of a. axial velocity and b. CH_4 mass fraction for four different phases ph1, ph2, ph3 and ph4 for the 'pulsating' flame (ϕ = 0.7, case D).*

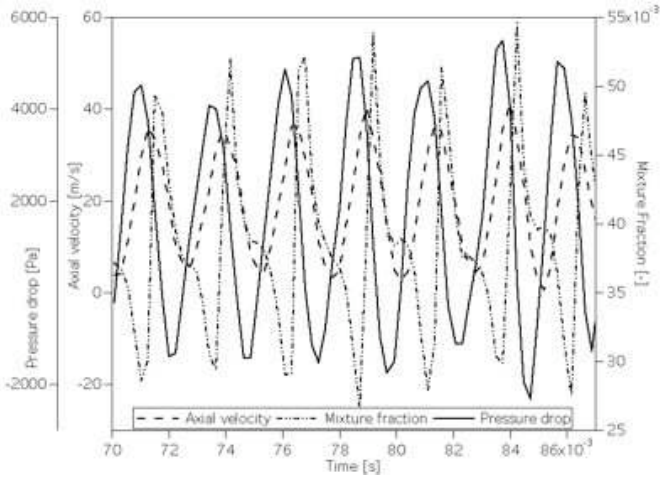

Figure 6.20 - *Temporal evolution of the pressure drop (solid line), axial velocity (dashed line) and mixture fraction (dotted-dashed line) in the swirler (probe I) for the 'pulsating' flame (ϕ = 0.7, case D).*

General conclusions

In the last years the need for simulations based on reliable chemistries has considerably increased to meet the restrictions on pollutant emissions of aeronautical burners. However, more and more complex configurations are investigated and simplification of the chemical description is commonly used to drastically reduce the computational cost. Reliable and computationally affordable chemical descriptions are therefore a key issue for the development of aeronautical engines. If reduced and tabulated chemistries have already been proposed, they should be carefully used when simulating turbulent three-dimensional complex flames, as they are generally developed in the context of laminar flames.

In the present work, simplified chemical descriptions have been proposed and their performances have been evaluated in Direct Numerical Simulations and Large Eddy Simulations of three-dimensional complex turbulent premixed flames, in an attempt to find the best compromise between CPU cost and accuracy.

The methodology developed to build a reduced chemistry valid over a wide range of initial temperature, pressure and equivalence ratio has proved very efficient for both kerosene [63] and methane. Fitting their Arrhenius parameters allow to capture the main flame characteristics such as flame speed and burnt gas temperature. However this is not sufficient to guarantee a good behavior in turbulent flames. Next step has been to study laminar unstrained and strained methane/air premixed flames. A modified version, 2S_CH4_BFER*, has been proposed to improve results for strained flames. Four other reduced mechanisms have been studied: the four-step fitted JONES mechanism [82], the analytical PETERS [116] and the SESHADRI [39] and the LU schemes [98], in comparison with the detailed GRI3.0 mechanism. Performances were evaluated in terms of consumption speed, flame structure, flame thickness, prediction of CO and radical species. As can be expected, higher complexity of the mechanism leads to better accuracy of results but also to higher computational costs. The challenge is to find the best compromise. Results may be summarized as follows:

- the agreement between LU and GRI3.0 results is excellent. Consequently the LU scheme has been used as reference in the DNS and LES calculations in Chapters 4 and 5.
- the two-step 2S_CH4_BFER scheme correctly reproduces laminar flame speed and burnt gas temperature for unstrained flames;
- details on the structure of unstrained flames are gained using the JONES scheme;
- a good description of the consumption speed response to strain rate requires a modification of 2S_CH4_BFER, using non-unity Lewis number (2S_CH4_BFER*).
- a good description of the flame structure response to strain rate is obtained only using the analytical schemes ;

To complete the comparison between the different chemical descriptions, the FPI_TTC approach has been also evaluated on unstrained premixed flames but a validation is still required for strained flames.
The coupling with turbulent combustion modeling has been finally addressed as a generalization of the artificially thickened flame method to multi-reactions chemistry and partially premixed flames.

Finally all previous chemistry models have been evaluated in unsteady turbulent combustion simulations.
In Chapter 4, DNS of both a two-dimensional interaction of a pair of vortices with a flame and a three-dimensional flame interacting with a homogenous isotropic turbulent field, lead to the following conclusions:

- consumption speed strongly varies with strain rate but also with curvature. The prediction of this quantity strongly depends on the kinetic scheme and is qualitatively in agreement with results from laminar strained flames.
- same conclusion is obtained for the description of the flame structure and, in particular, of the mass fraction of intermediate species such as CO which are strongly affected by strain rate. Only the analytical schemes are able to reproduce the LU results, as simpler ones fail in predicting CO and do not include other radicals;
- the flame thickening is less sensitive to the chemical mechanism and it generally depends on the combustion regime.

From these preliminary conclusions, four different mechanisms have been selected to perform the DNS of a three-dimensional perfectly premixed Bunsen flame and the LU

mechanism being used as a reference [137]: the 2S_CH4_BFER scheme representing the cheapest fitted scheme, its modified version 2S_CH4_BFER* and the SESHADRI* scheme representing the most accurate reduced mechanism. The flame thickening and the flame wrinkling are generally reproduced by all mechanisms since they are mostly governed by the interaction between turbulence and flame front, i.e. the combustion regime. On the contrary, discrepancies are shown on the global burning parameters such as the turbulent speed or the burning intensity. These quantities are strictly linked to the flame response to strain of the three mechanisms: the 2S_CH4_BFER scheme largely overestimates the consumption speed as it is almost insensitive to strain rate, whereas correct values are obtained with both the 2S_CH4_BFER* and the SESHADRI* schemes.

In Chapter 5, the different chemical descriptions are tested in LES of the swirled partially premixed flame of the experimental PRECCINSTA burner using the artificially thickened flame method. All mechanisms predict a correct laminar flame speed at least for lean mixtures and are suitable for LES of PRECCINSTA since 90% of the reacting points have a lean composition. Results for five different reduced schemes and the FPI_TTC* method have been compared to experimental data and numerical results obtained with the reference LU mechanism:

- the cheapest two-step scheme correctly predicts the mean profiles of temperature and major species as well as their fluctuations. As expected, the modified 2S_CH4_BFER* version improves the description of the flame length for the same computational cost;
- the JONES scheme presents the same accuracy as the two-step schemes, but for a higher computational cost;
- results for analytical schemes are in good agreement with the reference LU results in terms of flame length and flame structure. The flame is correctly characterized by a thin reaction zone and a wider recombination region in the near-wall zone. All these improvements are mainly due to the correct description of consumption speed, flame structure and species concentrations for strained laminar flames. No relevant discrepancies have been detected between the SESHADRI and the LU mechanisms but 20% of computational time could be saved using the SESHADRI scheme;
- the FPI_TTC* method is the least expensive chemical description and presents satisfactory results in terms of flame length and major species profiles even if the flame opening angle is underestimated;
- results for *CO* mass fractions are qualitatively in agreement with experimental data when using analytical schemes but they are expected to be improved using a finer mesh or introducing wall heat losses and radiation. Again, a good

description of CO mass fraction on laminar strained flames seems necessary if its concentration has to be predicted in complex industrial configurations. For the same results, CO mass fractions seem to be overestimated by the JONES and the FPI_TTC descriptions, but more accurate analysis on strained flames with the tabulation method are still required;

- instantaneous fields of H, O and OH radical species have also been analyzed since a correct description of these species is necessary to correctly reproduce the Zel'dovich mechanism for the prediction of thermal-NO. Compared to LU results, the analytical schemes correctly localize radical species but their concentration is only qualitatively reproduced. Before concluding on the possibility to use analytical schemes to predict of thermal-NO, the impact of errors of the radical concentration on NO_x prediction has to be evaluated;

- the generalization of the thickened flame method has been validated for both reduced chemistries and tabulation methods.

Even if the simplest 2S_CH4_BFER scheme has an incorrect response to stretch and could not be used to predict pollutant emissions, it correctly describes the main features of the flow field such as velocity field and temperature profiles with a low computational cost. In Chapter 6, results presented in the article *"Large-Eddy Simulation of combustion instabilities in a lean partially premixed swirled flame"* by B.Franzelli, E. Riber, L. Gicquel and T. Poinsot has been reported. The ability of LES to reproduce the combustion instabilities of a lean partially premixed swirled flame has been assessed even using the two-step 2S_CH4_BFER scheme.

This work shows that there is no "perfect" scheme performing well on all criteria, and that the choice of a reduced chemistry must be first driven by the quantities of interest in the simulation. Then the best compromise between CPU cost and result accuracy must be made.
Therefore, an *a priori* methodology to evaluate the mechanism performances is necessary, and it is shown here that it can be based on one-dimensional unstrained and strained laminar flames:

- the burning intensity and, as a consequence, the mean flame surface as well as its length are linked to the response of consumption speed to strain rate for laminar strained flames.

- The CO mass fraction in the reaction zone for unstrained and strained flames has to be correctly described to predict the CO concentration of turbulent flames.

- Reproducing the recombination zone of an unstrained flame guarantees the presence of a small temperature gradient region characterized by products and pollutant formation.

Table 6.5 - *Performances of the reduced chemical descriptions.*

	BFER	**BFER***	**JONES***	**PETERS***	**SESHADRI***	**FPI_TTC***	LU
Consumption speed	- -	+	- -	+ +	+ +	+	+ +
Flame wrinkling	- -	+	- -	+ +	+ +	+ +	++
Pollutants	- -	- -	-	+ +	+ +	-	++
Postflame region	- -	- -	-	+ +	+ +	-	++
CPU	++	++	+	-	-	++	- -

Table 6.5 summarizes the results of such a procedure for the schemes studied in this work. If the objective is to study pollutants and radicals, analytical schemes have to be preferred. If the objective is to capture flame length and consumption, two-step schemes such as 2S_CH4_BFER* are good candidates. Tabulated methods were not fully evaluated here but they represent an interesting alternative and should be further investigated.

All these conclusions are supposed to be valid for most hydrocarbons. However, this procedure has been evaluated only on premixed flames and still needs a validation for diffusion flames.
In a long term perspective, it can be expected that supercomputer developments will allow to use more and more accurate analytical schemes including information about radicals for an affordable CPU cost in complex industrial configurations. However in the short term perspective, the computational cost will not be affordable and new approaches are necessary. The main weakness of reduced schemes is the lack of description of intermediate species. Using a tabulated method all information on radical and intermediate species are available into the look-up table, but their application to complex industrial configurations is not straightforward mainly because evaporation of spray and cooling effects induce non-negligible heat losses which should be accounted for. Hybrid methods combining reduced/tabulated chemistry could be an interesting approach to predict soot emissions or radiation.

Bibliography

[1] S. F. Ahmed, R. Balachandran, T. Marchione, E. Mastorakos, Spark ignition of turbulent nonpremixed bluff-body flames, Combust. Flame 151 (1-2) (2007) 366–385.

[2] G. Albouze, Simulation aux grandes échelles des écoulements réactif non prémélangés, Phd thesis, INP Toulouse (2009).

[3] G. Albouze, L. Gicquel, T. Poinsot, Chemical kinetics modeling and LES combustion model effects on a perfectly premixed burner, Comptes Rendus Mécanique 337 (2009) 318–328.

[4] S. Aly, H. Salem, Prediction of premixed laminar flame characteristics commercial kerosene fuel, Fuel 68 (9) (1989) 1203–1209.

[5] J. Amaya, Unsteady coupled convection, conduction and radiation simulations on parallel architectures for combustion applications, Phd thesis, INP Toulouse (2010).

[6] M. S. Anand, S. B. Pope, Calculations of premixed turbulent flames by PDF methods, Combust. Flame 67 (2) (1987) 127–142.

[7] C. Angelberger, F. Egolfopoulos, D. Veynante, Large Eddy Simulations of chemical and acoustic effects on combustion instabilities, Flow, Turb. and Combustion 65 (2) (2000) 205–22.

[8] C. Angelberger, D. Veynante, F. Egolfopoulos, T. Poinsot, Large Eddy Simulations of combustion instabilities in premixed flames, in: Proc. of the Summer Program, Center for Turbulence Research, NASA Ames/Stanford Univ., 1998, pp. 61–82.

[9] P. Auzillon, Filtrage de flamme et combustion turbulente. Application à l'aéronautique, Phd thesis, Ecole Centrale Paris (2011).

[10] P. Auzillon, B. Fiorina, R. Vicquelin, N. Darabiha, O. Gicquel, D. Veynante, Modeling chemical flame structure and combustion dynamics in LES, Proc. Combust. Inst. 33 (1) (2011) 1331–1338.

[11] R. S. Barlow, Laser diagnostics and their interplay with computations to understand turbulent combustion, Proc. Combust. Inst. 31 (1) (2007) 49–75.

[12] R. S. Barlow, J. H. Frank, Effects of turbulence on species mass fractions in methane/air jet flames, Proc. Combust. Inst. 27 (1) (1998) 1087–1095.

[13] M. Baum, T. J. Poinsot, D. C. Haworth, Numerical simulations of turbulent premixed H2/O2/N2 flames with complex chemistry, in: Proc. of the Summer Program, Center for Turbulence Research, NASA Ames/Stanford Univ., 1992, pp. 345–366.

[14] M. Baum, T. J. Poinsot, D. C. Haworth, N. Darabiha, Direct numerical simulations of H2/O2/N2 flames with complex chemistry in two-dimensional turbulent flows, J. Fluid Mech. 281 (1994) 1–32.

[15] R. W. Bilger, S. B. Pope, K. N. C. Bray, J. F. Driscoll, Paradigms in turbulent combustion research, Proc. Combust. Inst. 30 (1) (2005) 21–42.

[16] R. W. Bilger, B. Yip, M. B. Long, A. R. Masri, An atlas of QEDR flame structures, Combust. Sci. Tech. 72 (4-6) (1990) 137–155.

[17] R. J. Blint, The relationship of the laminar flame width to flame speed, Combust. Sci. Tech. 49 (1-2) (1986) 79–92.

[18] M. Boger, D. Veynante, H. Boughanem, A. Trouvé, Direct Numerical Simulation analysis of flame surface density concept for Large Eddy Simulation of turbulent premixed combustion, Proc. Combust. Inst. 27 (1) (1998) 917–925.

[19] B. Böhm, J. Brübach, C. Ertem, A. Dreizler, Experiments for combustion-LES validation, Flow, Turb. and Combustion 80 (4) (2007) 507–529.

[20] P. Boivin, C. Jiménez, A. Dauptain, B. Cuenot, Large Eddy Simulation of a supersonic hydrogen-air jet using reduced chemistry, in: 13th International Conference on Numerical Combustion, Corfu, Greece, 2011.

[21] P. Boivin, C. Jiménez, A. L. Sanchez, F. A. Williams, An explicit reduced mechanism for H2-air combustion, Proc. Combust. Inst. 33 (1) (2011) 517–523.

[22] J. Borken-Kleefeld, T. Berntsen, J. Fuglestvedt, Specific climate impact of passenger and freight transport, Environ. Sci. Technol. 44 (15) (2010) 5700–5706.

[23] G. Boudier, L. Y. M. Gicquel, T. Poinsot, D. Bissières, C. Bérat, Comparison of LES, RANS and experiments in an aeronautical gas turbine combustion chamber, Proc. Combust. Inst. 31 (2) (2007) 3075–3082.

[24] G. Boudier, L. Y. M. Gicquel, T. Poinsot, D. Bissières, C. Bérat, Effect of mesh resolution on large eddy simulation of reacting flows in complex geometry combustors, Combust. Flame 155 (1-2) (2008) 196–214.

[25] H. Boughanem, Evaluation des termes de transport et de dissipation de surface de flamme par simulation numérique directe de la combustion turbulente, Phd thesis, Université de Rouen (1998).

[26] H. Boughanem, A. Trouvé, The domain of influence of flame instabilities in turbulent premixed combustion, Proc. Combust. Inst. 27 (1) (1998) 971–978.

[27] K. N. C. Bray, R. S. Cant, Some applications of kolmogorov's turbulence research in the field of combustion, Proc. R. Soc. Lond. A . A.N. Kolmogorov Special Number 434 (1890) (1991) 217–240.

[28] K. N. C. Bray, J. B. Moss, A closure model for the turbulent premixed flame with sequential chemistry, Combust. Flame 30 (1977) 125–131.

[29] J. Buckmaster, G. Ludford, Theory of laminar flames, Cambridge University Press, 1982.

[30] M. Bui-Pham, K. Seshadri, F. A. Williams, The asymptotic structure of premixed methane-air flames with slow CO oxidation, Combust. Flame 89 (3-4) (1992) 343–362.

[31] A. Buschmann, F. Dinkelacker, T. Schafer, M. Schafer, J. Wolfrum, Measurement of the instantaneous detailed flame structure in turblent premixed combustion, Proc. Combust. Inst. 26 (1) (1996) 437–445.

[32] W. Bush, F. Fendell, Asymptotic analysis of laminar flame propagation for general Lewis numbers, Combust. Sci. Tech. 1 (1970) 421–428.

[33] T. D. Butler, P. J. O'Rourke, A numerical method for two-dimensional unsteady reacting flows, Proc. Combust. Inst. 16 (1977) 1503–1515.

[34] R. R. Cao, S. B. Pope, The influence of chemical mechanisms on pdf calculations of nonpremixed piloted jet flames, Combust. Flame 143 (1) (2005) 450–470.

[35] N. Chakraborty, S. Cant, Unsteady effects of strain rate and curvature on turbulent premixed flames in an inflow-outflow configuration, Combust. Flame 137 (1-2) (2004) 129–147.

[36] F. Charlette, D. Veynante, C. Meneveau, A power-law wrinkling model for LES of premixed turbulent combustion: Part I - non-dynamic formulation and initial tests, Combust. Flame 131 (1-2) (2002) 159–180.

[37] J. H. Chen, A. Choudhary, B. de Supinski, M. DeVries, E. R. Hawkes, S. Klasky, W. K. Liao, K. L. Ma, J. Mellor-Crummey, N. Podhorszki, R. Sankaran, S. Shende, C. S. Yoo, Terascale direct numerical simulations of turbulent combustion using S3D, Computational Science & Discovery 2 (2009).

[38] J. Y. Chen, A general procedure for constructing reduced reaction mechanisms with given independent relations, Combust. Sci. Tech. 57 (1988) 89–94.

[39] J. Y. Chen, R. W. Dibble, Applications of reduced chemical mechanisms for the prediction of turbulent nonpremixed methane jet flames, in: M. D. Smooke (ed.), Reduced Chemical Mechanisms and Asymptotic Approximations for Methane-Air Flames, vol. 384, Springer-Verlag, New York, 1991, pp. 193–226.

[40] J. Y. Chen, T. Kaiser, W. Kollmann, Transient behavior of simplified reaction mechanisms for methane nonpremixed combustion, Combust. Sci. Tech. 92 (1993) 313–347.

[41] K. S. Chen, J. Y. Hwang, Experimental study on the mixing of one- and dual-line heated jets with a cold crossflow in a confined channel, AIAA Journal 29 (3) (1991) 353–360.

[42] Y. Chen, R. Bilger, Experimental investigation of three dimensional flame front structure in premixed turbulent combustion-II, Combust. Flame 138 (1-2) (2004) 155–174.

[43] R. K. Cheng, I. G. Shepherd, The influence of burner geometry on premixed turbulent flame propagation, Combust. Flame 85 (1-2) (1991) 7–26.

[44] P. Clavin, Dynamic behavior of premixed flame fronts in laminar and turbulent flows, Prog. Energy Comb. Sci. 11 (1) (1985) 1–59.

[45] O. Colin, Simulations aux grandes échelles de la combustion turbulente prémélangée dans les statoréacteurs, Phd thesis, INP Toulouse (2000).

[46] O. Colin, F. Ducros, D. Veynante, T. Poinsot, A thickened flame model for large eddy simulations of turbulent premixed combustion, Phys. Fluids 12 (7) (2000) 1843–1863.

[47] O. Colin, M. Rudgyard, Development of high-order Taylor-Galerkin schemes for unsteady calculations, J. Comput. Phys. 162 (2) (2000) 338–371.

[48] P. Dagaut, M. Cathonnet, The ignition, oxidation and combustion of kerosene: A review of experimental and kinetic modeling, Prog. Energy Comb. Sci. 32 (1) (2006) 48–92.

[49] L. P. H. de Goey, J. A. van Oijen, H. Bongers, G. R. A. Groot, New flamelet based reduction methods: the bridge between chemical reduction techniques and flamelet methods, in: European Combustion Meeting, Orléans (France), 2003.

[50] F. di Mare, W. Jones, K. Menzies, Large-Eddy Simulation of a model gas turbine combustor, Combust. Flame 137 (2004) 278–294.

[51] C. Dopazo, L. Valino, F. Fuego, Statistical description of the turbulent mixing of scalar fields, Int. J. Modern Physics B 11 (1997) (25).

[52] J. F. Driscoll, Turbulent premixed combustion: Flamelet surface and its effect on turbulent burning velocities, Prog. Energy Comb. Sci. 34 (1) (2008) 91–134.

[53] L. Duchamp de Lageneste, H. Pitsch, Progress in Large Eddy Simulation of premixed and partially-premixed turbulent combustion, in: Annual Research Briefs , Center for Turbulence Research, NASA Ames/Stanford Univ., 2001, pp. 97–107.

[54] F. Ducros, F. Nicoud, T. Poinsot, Wall-adapating local eddy-viscosity models for simulations in complex geometries, in: ICFD, M. J. Baines, 1998, pp. 293–300.

[55] L. Elliott, D. B. Ingham, A. G. Kyne, N. S. Mera, M. Pourkashanian, C. W. Wilson, Genetic algorithms for optimisation of chemical kinetics reaction mechanisms, Prog. Energy Comb. Sci. 30 (3) (2004) 297–328.

[56] E. Fernandez-Tarrazo, A. Sanchez, A. Linan, F. Williams, A simple one-step chemistry model for partially premixed hydrocarbon combustion, Combust. Flame 147 (1-2) (2006) 32–38.

[57] V. Fichet, Modélisation de la combustion du gaz naturel par réseaux de réacteurs avec cinétique chimique détaillée, Ph.D. thesis, Ecole Centrale Paris (2008).

[58] S. A. Filatyev, J. F. Driscoll, C. D. Carter, J. M. Donbar, Measured properties of turbulent premixed flames for model assessment, including burning velocities, stretch rates and surface densities, Combust. Flame 141 (1-2) (2005) 1–21.

[59] B. Fiorina, R. Baron, O. Gicquel, D. Thévenin, S. Carpentier, N. Darabiha, Modelling non-adiabatic partially premixed flames using flame-prolongation of ILDM, Combust. Theory and Modelling 7 (2003) 449–470.

[60] B. Fiorina, O. Gicquel, D. Veynante, Turbulent flame simulation taking advantage of tabulated chemistry self-similar properties, Proc. Comb. Institute 32 (2) (2009) 1687–1694.

[61] B. Fiorina, R. Vicquelin, P. Auzillon, N. Darabiha, O. Gicquel, D. Veynante, A filtered tabulated chemistry model for LES of premixed combustion, Combust. Flame 157 (3) (2010) 465–475.

[62] B. Franzelli, E. Riber, L. Y. Gicquel, T. Poinsot, Large Eddy Simulation in combustion instabilities of a lean partially premixed swirled flame, Combust. Flame (2011) doi:10.1016/j.combustflame.2011.08.004.

[63] B. Franzelli, E. Riber, M. Sanjosé, T. Poinsot, A two-step chemical scheme for kerosene–air premixed flames , Combust. Flame 157 (7) (2010) 1364–1373.

[64] M. Freitag, J. Janicka, Investigation of a strongly swirled premixed flame using LES, Proc. Combust. Inst. 31 (1) (2007) 1477–1485.

[65] F. Frenklach, H. Wang, C. L. Yu, M. Goldenberg, C. T. Bowman, R. K. Hanson, D. F. Davidson, E. J. Chang, G. P. Smith, D. M. Golden, W. C. Gardiner, V. Lissianski, http://www.me.berkeley.edu/gri_mech.

[66] J. Galpin, A. Naudin, L. Vervisch, C. Angelberger, O. Colin, P. Domingo, Large Eddy Simulation of a fuel-lean premixed turbulent swirl-burner, Combust. Flame 155 (1-2) (2008) 247–266.

[67] M. Germano, U. Piomelli, P. Moin, W. Cabot, A dynamic subgrid-scale eddy viscosity model, Phys. Fluids 3 (7) (1991) 1760–1765.

[68] A. Giauque, L. Selle, T. Poinsot, H. Buechner, P. Kaufmann, W. Krebs, System identification of a large-scale swirled partially premixed combustor using LES and measurements, J. Turb. 6 (21) (2005) 1–20.

[69] O. Gicquel, N. Darabiha, D. Thévenin, Laminar premixed hydrogen/air counterflow flame simulations using flame prolongation of ILDM with differential diffusion, Proc. Combust. Inst. 28 (2) (2000) 1901–1908.

[70] R. G. Gilbert, K. Luther, J. Troe, Theory of thermal unimolecular reactions in the Fall-off range. II. Weak collinsion rate constants, Ber. Bunsenges. Phys. Chem. 87 (2) (1983) 169–177.

[71] D. G. Goodwin, Cantera C++ Users Guide, http://sourceforge.net/projects/cantera (2002).

[72] V. Granet, O. Vermorel, T. Leonard, L. Gicquel, T. Poinsot, Comparison of non-reflecting outlet boundary conditions for compressible solvers on unstructured grids, Am. Inst. Aeronaut. Astronaut. J. 48 (10) (2010) 2348–2364.

[73] X. J. Gu, M. Z. Haq, M. Lawes, R. Woolley, Laminar burning velocity and Markstein lengths of methane-air mixtures, Combust. Flame 121 (1-2) (2000) 41–58.

[74] E. R. Hawkes, S. R. Cant, A flame surface density approach to Large Eddy Simulation of premixed turbulent combustion, in: 28th Symp. (Int.) on Combustion, The Combustion Institute, Pittsburgh, 2000, pp. 51–58.

[75] B. S. Haynes, H. G. Wagner, Soot formation, Prog. Energy Comb. Sci. 7 (4) (1981) 229–273.

[76] F. E. Hernandez-Pérez, F. T. C. Yuen, C. P. T. Groth, O. L. Gülder, LES of a laboratory-scale turbulent premixed bunsen flame using FSD, PCM-FPI and thickened flame models, Proc. Combust. Inst. 33 (1) (2011) 1365–1371.

[77] R. Hilbert, F. Tap, H. El-Rabii, D. Thévenin, Impact of detailed chemistry and transport models on turbulent combustion simulations, Prog. Energy Comb. Sci. 30 (1) (2004) 61–117.

[78] M. Hilka, D. Veynante, M. Baum, T. Poinsot, Simulation of flame vortex interactions usind detailed and reduced chemical kinetics, in: 10th Symp. on Turbulent Shear Flows, Penn State, 1995, pp. 19–19.

[79] J. Hirschfelder, C. Curtis, B. Bird, Molecular Theory of Gases and Liquids, 1954th ed., John Wiley & Sons, New York, 1954.

[80] Y. Huang, V. Yang, Dynamics and stability of lean-premixed swirl-stabilized combustion, Prog. Energy Comb. Sci. 35 (4) (2009) 293–364.

[81] H. G. Im, J. H. Chen, Structure and propagation of triple flames in partially premixed hydrogen-air mixture, Combust. Flame 119 (4) (1999) 436–454.

[82] W. P. Jones, R. P. Lindstedt, Global reaction schemes for hydrocarbon combustion, Combust. Flame 73 (3) (1988) 222–233.

[83] A. Kaufmann, F. Nicoud, T. Poinsot, Flow forcing techniques for numerical simulation of combustion instabilities, Combust. Flame 131 (4) (2002) 371–385.

[84] R. J. Kee, F. M. Rupley, E. Meeks, A. Miller, Chemkin-III: A FORTRAN chemical kinetics package for the analysis of gas-phase chemical and plasma kinetics, Tech. Rep. SAND96-8216, Sandia National Laboratories (1996).

[85] A. P. Kelley, W. Liu, Y. X. Xin, A. J. Smallbone, C. K. Law, Laminar flame speeds, non premixed-stagnation ignition and reduced mechanisms in the oxidation of iso-octane, Proc. Combust. Inst. 33 (1) (2011) 501–508.

[86] A. Kempf, LES validation from experiments, Flow, Turb. and Combustion 80 (3) (2008) 351–373.

[87] C. A. Kennedy, M. H. Carpenter, Several new numerical methods for compressible shear-layer simulations, Appl. Num. Math 14 (4) (1994) 397–433.

[88] C. A. Kennedy, M. H. Carpenter, Low-storage, explicit Runge-Kutta schemes for the compressible Navier-Stokes equations, Appl. Num. Math 35 (3) (2000) 117–219.

[89] H. Kobayashi, T. Tamura, T. M. T. N. F. A. Williams, Burning velocity of turbulent premixed flames in an high pressure environment, Proc. Combust. Inst. 26 (1996) 389–396.

[90] K. Kuo, Principles of Combustion, John Wiley, New York, 1986.

[91] C. K. Law, Combustion Physics, Cambridge University Press, Moscow, 2006.

[92] J. P. Légier, Simulations numériques des instabilités de combustion dans les foyers aéronautiques, Phd thesis, INP Toulouse (2001).

[93] J. P. Légier, T. Poinsot, D. Veynante, Dynamically thickened flame LES model for premixed and non-premixed turbulent combustion, in: Proc. of the Summer Program, Center for Turbulence Research, NASA Ames/Stanford Univ., 2000, pp. 157–168.

[94] S. C. Li, F. A. Williams, K. Gebert, A simplified, fundamentally based method for calculating nox emissions in lean premixed combustors, Combust. Flame 119 (3) (1999) 367–373.

[95] T. Lieuwen, H. Torres, C. Johnson, B. Zinn, A mechanism of combustion instability in lean premixed gas turbine combustors, Journal of Engineering for Gas Turbines and Power 123 (1) (2001) 182–189.

[96] T. Lieuwen, V. Yang, Combustion instabilities in gas turbine engines. operational experience, fundamental mechanisms and modeling, in: Prog. in Astronautics and Aeronautics AIAA, vol. 210, 2005.

[97] F. A. Lindemann, Discussion on "the radiation theory of chemical action", Trans. Faraday Soc. 17 (1922) 588–606.

[98] T. Lu, C. K. Law, A criterion based on computational singular perturbation for the identification of quasi steady state species: A reduced mechanism for methane oxidation with NO chemistry, Combust. Flame 154 (4) (2008) 761–774.

[99] T. F. Lu, C. K. Law, A directed relation graph method for mechanism reduction, Proc. Comb. Institute 30 (1) (2005) 1333–1341.

[100] J. Luche, Elaboration of reduced kinetic models of combustion. Application to a kerosene mechanism, Ph.D. thesis, LCSR Orléans (2003).

[101] J. Luche, M. Reuillon, J. C. Boettner, M. Cathonnet, Reduction of large detailed kinetic mechanisms: application to kerosene / air combustion, Combust. Sci. Tech. 176 (2004) 1935–1963.

[102] U. Maas, S. B. Pope, Simplifying chemical kinetics: intrinsic low-dimensional manifolds in composition space, Combust. Flame 88 (3-4) (1992) 239–264.

[103] H. P. Mallampalli, T. H. Fletcher, J. Y. Chen, Evaluation of CH4/NOx global mechanisms used for modeling lean premixed turbulent combustion of natural gas, in: Fall Meeting of the Western States Section of the Combustion Institute, vol. Paper 96F-098, 1996.

[104] T. Mantel, J. M. Samaniego, C. T. Bowman, Fundamental mechanisms in premixed turbulent flame propagation via vortex-flame interactions - part II: numerical simulation, Combust. Flame 118 (4) (1999) 557–582.

[105] C. Martin, Etude énergétique des instabilités thermo-acoustiques et optimisation génétique des cinétiques réduites, Phd thesis, INP Toulouse (2005).

[106] A. Massias, D. Diamantis, E. Mastorakos, D. A. Goussis, An algorithm for the construction of global reduced mechanisms with CSP data, Combust. Flame 117 (4) (1999) 685–708.

[107] W. Meier, P. Weigand, X. R. Duan, R. Giezendanner-Thoben, Detailed characterization of the dynamics of thermoacoustic pulsations in a lean premixed swirl flame, Combust. Flame 150 (1-2) (2007) 2–26.

[108] C. Meneveau, T. Poinsot, Stretching and quenching of flamelets in premixed turbulent combustion, Combust. Flame 86 (4) (1991) 311–332.

[109] J. A. Miller, C. T. Bowman, Mecanism and modeling of nitrogen chemistry in combustion, Prog. Energy Comb. Sci. 15 (4) (1989) 287–338.

[110] P. Moin, K. D. Squires, W. Cabot, S. Lee, A dynamic subgrid-scale model for compressible turbulence and scalar transport, Phys. Fluids A 3 (11) (1991) 2746–2757.

[111] V. Moureau, P. Domingo, L. Vervisch, From Large-Eddy Simulation to Direct Numerical Simulation of a lean premixed swirl flame: Filtered Laminar Flame-PDF modeling, Combust. Flame 158 (7) (2011) 1340–1357.

[112] V. Moureau, B. Fiorina, H. Pitsch, A level set formulation for premixed combustion LES considering the turbulent flame structure, Combust. Flame 156 (4) (2009) 801–812.

[113] V. Moureau, G. Lartigue, Y. Sommerer, C. Angelberger, O. Colin, T. Poinsot, Numerical methods for unsteady compressible multi-component reacting flows on fixed and moving grids, J. Comput. Phys. 202 (2) (2005) 710–736.

[114] F. Nicoud, H. B. Toda, O. Cabrit, S. Bose, J. Lee, Using singular values to build a subgrid-scale model for Large Eddy Simulations, Phys. Fluids ,*accepted*.

[115] C. Pantano, Direct simulation of non-premixed flame extinction in a methane-air jet with reduced chemistry, J. Fluid Mech. 514 (2004) 231–270.

[116] N. Peters, Numerical and asymptotic analysis of systematically reduced reaction schemes for hydrocarbon flames, in: R. Glowinsky, B. Larrouturou, R. Temam (eds.), Numerical simulation of combustion phenomena, vol. 241, Springer-Verlag, Berlin, 1985, pp. 90–109.

[117] N. Peters, Turbulent Combustion, Cambridge University Press, 2000.

[118] N. Peters, R. Kee, The computation of stretched laminar methane-air diffusion flames using a reduced four-step mechanism, Combust. Flame 68 (1) (1987) 17–29.

[119] H. Pitsch, A consistent level set formulation for Large Eddy Simulation of premixed turbulent combustion, Combust. Flame 143 (4) (2005) 587–598.

[120] H. Pitsch, H. Steiner, Large Eddy Simulation of a turbulent piloted methane/air diffusion flame (sandia flame D), Phys. Fluids 12 (2000) 2541–2554.

[121] T. Poinsot, T. Echekki, M. G. Mungal, A study of the laminar flame tip and implications for premixed turbulent combustion, Combust. Sci. Tech. 81 (1-3) (1992) 45–73.

[122] T. Poinsot, D. Haworth, DNS and modelling of the interaction between turbulent premixed flames and walls, in: Proc. of the Summer Program, Center for Turbulence Research, NASA Ames/Stanford Univ., 1992, pp. 307–324.

[123] T. Poinsot, S. Lele, Boundary conditions for direct simulations of compressible viscous flows, J. Comput. Phys. 101 (1) (1992) 104–129.

[124] T. Poinsot, D. Veynante, Theoretical and Numerical Combustion, R.T. Edwards, 2nd edition, 2005.

[125] D. Poitou, Modélisation du rayonnement dans la simulation aux grandes échelles de la combustion turbulente, Phd thesis, Ecole des Mines d'Albi (2009).

[126] S. B. Pope, Computationally efficient implementation of combustion chemistry using in situ adaptive tabulation, Combust. Theory and Modelling 1 (1) (1997) 41–64.

[127] S. B. Pope, Turbulent flows, Cambridge University Press, 2000.

[128] G. Ribert, O. Gicquel, N. Darabiha, D. Veynante, Tabulation of complex chemistry based on self-similar behaviour of laminar premixed flames, Combust. Flame 146 (4) (2006) 649–664.

[129] J. Riley, Review of Large Eddy Simulation of non-premixed turbulent combustion, J. Fluids Eng. 128 (2) (2006) 209–215.

[130] A. Roux, L. Y. M. Gicquel, S. Reichstadt, N. Bertier, G. Staffelbach, F. Vuillot, T. J. Poinsot, Analysis of unsteady reacting flows and impact of chemistry description in Large Eddy Simulations of side-dump ramjet combustors, Combust. Flame 157 (1) (2010) 176–191.

[131] A. Roux, L. Y. M. Gicquel, Y. Sommerer, T. J. Poinsot, Large eddy simulation of mean and oscillating flow in a side-dump ramjet combustor, Combust. Flame 152 (1-2) (2008) 154–176.

[132] S. Roux, M. Cazalens, T. Poinsot, Influence of outlet boundary condition for large eddy simulation of combustion instabilities in gas turbine, J. Prop. Power 24 (3) (2008) 541–546.

[133] S. Roux, G. Lartigue, T. Poinsot, U. Meier, C. Bérat, Studies of mean and unsteady flow in a swirled combustor using experiments, acoustic analysis and large eddy simulations, Combust. Flame 141 (1-2) (2005) 40–54.

[134] C. J. Rutland, A. Trouvé, Pre-mixed flame simulations for non-unity Lewis numbers, in: Proc. of the Summer Program, Center for Turbulence Research, NASA Ames/Stanford Univ., 1990, pp. 299–309.

[135] A. L. Sánchez, A. Lépinette, M. Bollig, A. Linán, B. Lázaro, The reduced kinetic description of lean premixed combustion, Combust. Flame 123 (4) (2000) 436–464.

[136] R. Sankaran, E. R. Hawkes, J. H. Chen, T. Lu, C. K. Law, Structure of a spatially developing turbulent lean methane-air Bunsen flame, Proc. Combust. Inst. 31 (1) (2007) 1291–1298.

[137] R. Sankaran, E. R. Hawkes, C. S. Yoo, J. H. Chen, T. Lu, C. K. Law, Direct numerical simulation of stationary lean premixed methane-air flames under intense turbulence, in: 5th US combustion Meeting, 2007.

[138] J. Savre, Simulation numérique instationnaire de la combustion turbulente au sein de foyers aéronautiques at prédiction des émissions polluantes, Phd thesis, INSA Rouen (2010).

[139] P. Schmitt, T. J. Poinsot, B. Schuermans, K. Geigle, Large Eddy Simulation and experimental study of heat transfer, nitric oxide emissions and combustion instability in a swirled turbulent high pressure burner, J. Fluid Mech. 570 (2007) 17–46.

[140] T. Schönfeld, M. Rudgyard, Steady and unsteady flows simulations using the hybrid flow solver AVBP, AIAA Journal 37 (11) (1999) 1378–1385.

[141] R. Seiser, U. Niemann, K. Seshadri, Experimental study of combustion of n-decane and JP-10 in non-premixed flows, Proc. Combust. Inst. 33 (1) (2011) 1045–1052.

[142] L. Selle, Simulation aux grandes échelles des interactions flamme-acoustique dans un écoulement vrillé, Phd thesis, INP Toulouse (2004).

[143] L. Selle, L. Benoit, T. Poinsot, F. Nicoud, W. Krebs, Joint use of compressible Large Eddy Simulation and Helmoltz solvers for the analysis of rotating modes in an industrial swirled burner, Combust. Flame 145 (1-2) (2006) 194–205.

[144] L. Selle, G. Lartigue, T. Poinsot, R. Koch, K. U. Schildmacher, W. Krebs, B. Prade, P. Kaufmann, D. Veynante, Compressible Large Eddy Simulation of turbulent combustion in complex geometry on unstructured meshes, Combust. Flame 137 (4) (2004) 489–505.

[145] A. Sengissen, A. Giauque, G. Staffelbach, M. Porta, W. Krebs, P. Kaufmann, T. Poinsot, Large eddy simulation of piloting effects on turbulent swirling flames, Proc. Combust. Inst. 31 (2) (2007) 1729–1736.

[146] A. Sengissen, J. F. V. Kampen, R. Huls, G. Stoffels, J. B. W. Kok, T. Poinsot, LES and experimental studies of cold and reacting flows in a swirled partially premixed burner with and without fuel modulation, Combust. Flame 150 (1-2) (2007) 40–53.

[147] S. Sheekrishna, S. Hemchandra, T. Lieuwen, Premixed flame response to equivalence ratio perturbations, Combust. Theory and Modelling 14 (5) (2010) 681–714.

[148] J. Simmie, Detailed chemical kinetic models for the combustion of hydrocarbon fuels, Prog. Energy Comb. Sci. 29 (6) (2003) 599–634.

[149] Y. Sommerer, D. Galley, T. Poinsot, S. Ducruix, F. Lacas, D. Veynante, Large Eddy Simulation and experimental study of flashback and blow-off in a lean partially premixed swirled burner, J. Turb. 5.

[150] A. Soufiani, J. Taine, High temperature gas radiative propriety parameters of statistical narrow-band model for H_2O, CO_2 and CO and correlated-k model for H_2O and CO_2, Technical note in International Journal of Heat and mass transfer 40 (1997) 987–991.

[151] G. Staffelbach, Simulation aux grandes échelles des instabilités de combustion dans les configurations multi-brûleurs, Phd thesis, INP Toulouse (2006).

[152] O. Stein, A. Kempf, LES of the Sydney swirl flame series: a study of vortex breakdown in isothermal and reacting flows., Proc. Combust. Inst. 31 (2) (2007) 1755–1763.

[153] H. Tennekes, J. L. Lumley, A first course in turbulence, M.I.T. Press, Cambridge, 1972.

[154] A. S. Tomlin, T. Turànyi, M. J. Pilling, Chapter 4: Mathematical tools for the construction, investigation and reduction of combustion mechanisms, vol. 35, Elsevier, 1997.

[155] A. Triantafyllidis, E. Mastorakos, R. L. G. M. Eggels, Large Eddy Simulations of forced ignition of a non-premixed bluff-body methane flame with Conditional Moment Closure, Combust. Flame 156 (12) (2009) 2328–2345.

[156] K. Truffin, Simulation aux grandes échelles et identification acoustique des turbines à gaz en régime partiellement prémélangé, Phd thesis, INP Toulouse (2005).

[157] K. Truffin, T. Poinsot, Comparison and extension of methods for acoustic identification of burners, Combust. Flame 142 (4) (2005) 388–400.

[158] T. Turanyi, Reduction of large mechanisms, New J. Chem. 14 (11) (1990) 795–803.

[159] C. M. Vagelopoulos, F. Egolfopoulos, Direct experimental determination of laminar flame speeds, in: 27th Symp. (Int.) on Combustion, No. 1, The Combustion Institute, Pittsburgh, 1998, pp. 513–519.

[160] J. A. van Oijen, F. A. Lammers, L. P. H. de Goey, Modeling of premixed laminar flames using flamelet generated manifolds, Combust. Sci. Tech. 127 (3) (2001) 2124–2134.

[161] D. Veynante, B. Fiorina, P. Domingo, L. Vervisch, Using self-similar properties of turbulent premixed flames to downsize chemical tables in high-performance numerical simulations, Combust. Theory and Modelling 12 (6) (2008) 1055–1088.

[162] D. Veynante, G. Lodato, P. Domingo, L. Vervisch, E. Hawkes, Estimation of three-dimensional flame surface densities from planar images in turbulent premixed combustion, Exp. Fluids 49 (1) (2010) 267–278.

[163] R. Vicquelin, Tabulation de la cinétique chimique pour la modélisation et la simulation de la combustion turbulente., Phd thesis, Ecole centrale Paris (2010).

[164] R. Vicquelin, B. Fiorina, S. Payet, N. Darabiha, O. Gicquel, Coupling tabulated chemistry with compressible CFD solvers, Proc. Combust. Inst. 33 (1) (2011) 1481–1488.

[165] J. Warnatz, Concentration-, pressure-, and temperature-dependence of the flame velocity in hydrogen-oxygen-nitrogen mixtures, Combust. Sci. Tech. 26 (1981) 203–213.

[166] J. Warnatz, U. Mass, R. W. Dibble, Combustion: Physical and Chemical Fundamentals, Modeling and Simulation, Experiments, Pollutant formation, Springer, 4th edition, 2006.

[167] J. Warnatz, N. Peters, Stretch effects in plane premixed hydrogen air flames, Tech. Rep. SAND-84-8220, Sandia National Laboratories (1984).

[168] P. Weigand, X. R. Duan, W. Meier, U. Meier, M. Aigner, C. Bérat, Experimental investigations of an oscillating lean premixed CH_4/air swirl flame in a gas turbine model combustor, in: European Combustion Meeting, 2005.

[169] P. Weigand, W. Meier, X. R. Duan, M. Aigner, Laser based investigations of thermo-acustic instabilities in a lean premixed gas turbine model combustor, in: Proceedings of GT2006 ASME Turbo Expo 2006: Power for Land, Sea and Air, Barcelona (Spain), May 8-11, 2007.

[170] H. G. Weller, G. Tabor, A. D. Gosman, C. Fureby, Application of a flame-wrinkling LES combustion model to a a turbulent mixing layer, in: 27th Symp. (Int.) on Combustion, No. 1, The Combustion Institute, Pittsburgh, 1998, pp. 899 – 907.

[171] C. Westbrook, F. Dryer, Simplified reaction mechanism for the oxidation of hydrocarbon fuels in flames, Combust. Sci. Tech. 27 (1-2) (1981) 31–43.

[172] C. K. Westbrook, F. L. Dryer, Prediction of laminar flame properties of methanol-air mixtures, Combust. Flame 37 (1980) 171–192.

[173] F. A. Williams, Combustion Theory, Benjamin Cummings, Menlo Park, CA, 1985.

[174] F. A. Williams, San Diego Mechanism, http://maeweb.ucsd.edu/c̆ombustion/cermech (2005).

[175] P. Wolf, G. Staffelbach, A. Roux, L. Gicquel, T. Poinsot, V. Moureau, Massively parallel LES of azimuthal thermo-acoustic instabilities in annular gas turbines, C. R. Acad. Sci. Mécanique 337 (6-7) (2009) 385–394.

Acknowledgements

Mon aventure chez les cousins transalpins n'aurait pas pu se passer mieux de ce que j'ai vécu pendant les dernières trois années au laboratoire CERFACS de Toulouse...

Avant tout, il faut vraiment que je remercie ma directrice de thèse *Bénédicte Cuenot*. Elle m'a donné la possibilité de faire une thèse au CERFACS et, en me laissant en totale liberté, elle a su me diriger vers le bon chemin avec idées et observations qui ont apportée une contribution énorme à cette thèse..mais surtout comment ne pas penser aux pique-niques d'été chez elle ou à l'apéritif Zonta pendant lequel elle a inventé la désormais célèbre phrase: "Benedetta, celle au pantalon vert!".
Ensuite, *Thierry Poinsot*..jamais content, jamais satisfait des résultats, mais c'est une technique pour vous faire travailler, il faut pas y croire!!!..Deux petits conseils pour les futurs thésards: n'essayez pas de le convaincre que vos résultats sont correctes et la théorie est fausse et, surtout, ne repondez jamais à une de ces mails le samedi matin si vous voulez passer un weekend de repos..
I would like to thank all the members of the jury to have dedicated time to read my manuscript and come in Toulouse expressly for my defense. It has been a great honor for me to have the opportunity to share my work with you. I really thank *Professor Heinz Pitsch* and *Professor Olivier Gicquel* for their observations and remarks, *Professor William Jones* to have hosted me in his team at the Imperial College in London (I had a great time, thank you so much), *Dr. Edward Richardson* to have helped me so much with the Bunsen flame when he really had no time to do it, *Professor Jean-François Pauwels* to have accepted the "two-step side of the chemistry" and *Dr. Anthony Roux* for not having asking me some tricky questions.
Et il ne faut surtout pas oublier ceux qui ont fait vraiment la différence: *Eleonore Riber*, le ER du mythique BFER-team, la "mini-boss" qui m'a énormément aidé entre une pause café et une photo stupide sur Photo Booth. Je suis terriblement fière de pouvoir dire d'avoir été sa première "UNOFFICIAL" thésarde. Et ce n'est pas fini.. *Olivier Vermorel*, celui qui connait la réponse à n'importe quel question sur AVBP, mon co-directeur qui tout a essayé afin de se libérer de moi. Oliv', Ele, n'essayez pas de sous-louer ma petite chambre chez vous..Je vais être de retour bientôt! Les *colocs*..Asier et Giac, ma toute première famille française (même si "François était tellement mieux!!")..JeanMatthieu

et Thomas, les colocs râleurs avec lesquels j'ai partagé des moments de pur bonheur comme les petits-déjeuners du samedi matin, les kebabs, le NCIS du vendredi soir ou la terrible soirée au cinéma à voir Twilight (et Thomas, il a même aimé le film)..Maité, la princesse catalane qui a tout essayé pour me rendre sportive et qui finalement s'est retrouvé sur le canapé à regarder "Grand frère, Pascal", et Geoffroy (pour ces solos en guitare le matin, la sauce-tomate bien aillée et le voyage en métro déguisés pour Halloween). Les *collègues de bureau*..Alban, Mauro, Marta ("Marta, ehi Marta, try to do this..GNAGNAGNA"), Jorge ("mon problème, c'est que je n'arrive pas à me concentrer quand on me parle..") et ces anecdotes improbables trouvés sur Internet, Geoffroy et le "pauvre" Matthias (le GGG du Cerfacs ..Ce fut un vrai plaisir partager avec vous le bureau, Monsieur Kraushaarahaaraa). Les *collègues de couloir*..Elsa (et ses histoires sur Bubus), Camillo (pour le moment de folie), Felix, JeanMatthieu, Victor ("Maudit Victor") et Patricia (pour les merveilleuses vacances à Madrid et le salamencho), Alex ("Newfighter"), Antoine, Laurent, Roberto ("Va' pensieroooo.."), Alex E., Thomas P., Anthony (et sa femme Marina) et JeanPhilippe.. Les *petits jeunes*..Julien, Pierre, Greg et Manqi (pas encore arrivée, mais elle va tout déchiré). Les *anciennes thèsards*.. Olivier C. (pour les journées à Londres et les bonbons), Guillhem (pour avoir été le premier français a trouver le courage de me parler), Thomes S., Matthieu B. (celui qui m'a initié aux flammes 1D) et les *thèsards des autres laboratoires*..Pierre de Ecole Centrale Paris, Nakul, Konna, Francesco, Alessio, Iro, Regina e Claudio dell'Imperial College London. Enfin, l'équipe de secours contre tous les problèmes de bureaucratie, d'informatique, d'organisation ou de depressione..Marie (pour m'avoir dépanné et conseillé), Nicole, Severine (avec tes papiers tu m'as sauvé la vie plusieurs fois!!), Michèle et Chantal (le dream-team du secrétariat), Isabelle, Gérard, Fabrice, Patrick et Nicolas (il est où le but de Blue Gene que on m'avait promis?)..MERCI MERCI MERCI et encore MERCI!
E alla fine di tutto si riparte dall'inizio..un immenso grazie alla mia famiglia..per la bella sorpresa, per il super rinfresco (echi della sua magnificenza sono arrivati fino a Parigi) e per essermi stati accanto in questa avventura senza capire una sola acca di ciò che faccio..e, sempre, comunque e dovunque, a *Roberto*..che senza alcun minimo dubbio dovrebbe ricevere il dottorato insieme a me per il suo impegno, la sua pazienza e il suo supporto..senza di lui, questi ultimi tre anni non sarebbero stati che tre lunghi anni di dottorato..

Partie en français

Contexte de l'étude

2,2 milliards de passagers voyagent chaque année grâce au transport aérien et son activité génère au total près de 32 millions d'emplois. Son impact économique a été estimé à 3.560 milliards d'euros[2]. Malheureusement, la combustion de carburants de nature fossile communément utilisés dans les foyers aéronautiques a un impact néfaste sur le climat puisqu'elle génère également des émissions polluantes :

- Les **oxydes de carbone** comme le monoxyde de carbone CO d'une part, à l'origine d'intoxications et de maladies mortelles (problèmes cardiovasculaires et ischémies) chez l'homme, et le dioxyde de carbone CO_2 d'autre part, reconnu comme gaz à effet de serre;
- Les **oxydes d'azote** comme le monoxyde d'azote NO, le dioxyde d'azote NO_2 plus connus sous le nom de NO_x ainsi que le protoxyde d'azote qui est un puissant gaz à effet de serre. Les oxydes d'azote sont en partie responsables des pluies acides et de la formation de l'ozone dans les basses couches de l'atmosphère;
- Les **oxydes de soufre** comme le dioxyde de soufre SO_2 et le trioxyde de soufre SO_3 qui sont également responsables des pluies acides. Ces particules fines sont émises dans l'air et sont un facteur de risques sanitaires;
- Les **suies** qui forment un ensemble de composés chimiques avec un impact très néfaste sur la santé. Elles résultent d'une combustion incomplète due soit à des basses températures, soit à une trop forte inhomogénéité du mélange.

Le Conseil consultatif pour la recherche aéronautique européenne (ACARE pour Advisory Council for Aeronautics Research in Europe en anglais) est composé de représentants des états membres de l'Europe, de la Commission Européene et d'autres

[2]Rapport final des activitées du project QUANTIFY (Quantifying the Climate Impact of Global and European Transport Systems)(http://www.ip-quantify.eu).

acteurs importants du milieu aéronautique comme les industries aéronautiques, les compagnies de transport et les aéroports. Depuis 2001, l'ACARE établit la ligne de conduite à suivre pour le développement de technologies aéronautiques dans l'Union Européenne. L'objectif est de développer des technologies plus performantes et plus rentables tout en préservant l'environnement et la sécurité des passagers. Trois différents axes de développement ont été identifiés dans l'addendum de 2008 au "Strategic Research Agenda" :

- **Environnement** : l'impact du transport aéronautique sur l'environnement est relativement faible comparé au transport routier (avec un effet sur l'augmentation de la température terrestre quatre fois plus petit [22]) et seulement l2% du CO_2 produit par l'homme provient du transport aérien. Cependant, les émissions polluantes des foyers aéronautiques doivent être contrôlées dans la mesure où le transport aérien augmente d'un facteur 4 à 5% par an et que les émissions polluantes contribuent plus fortement au changement climatique lorsqu'elles sont émises en altitude.

  Le développement de nouvelles technologies est une thématique primordiale puisqu'elle englobe le changement climatique, les nuisances acoustiques et la qualité de l'air. Les objectifs environnementaux fixés par l'ACARE pour l'année 2020 sont :

  - une réduction des émissions de CO_2 de 50% par passager et par kilomètre, en supposant que le kérosène restera le carburant principal;
  - une réduction des nuisances sonores de moitié par rapport à son niveau actuel;
  - une réduction des émissions de NO_x de 80%;
  - une réduction des autres émissions: suies, CO, etc.;
  - une minimisation de l'impact industriel sur l'environnement.

- **Carburants alternatifs** : la demande d'énergie est en constante augmentation compte tenu de la croissance de la population mondiale et du développement des économies, alors que les réserves mondiales de pétrole s'amenuisent. L'utilisation de carburants alternatifs dans l'aviation n'est pas encore nécessaire, mais une étude des principales caractéristiques des nouveaux carburants est indispensable si on veut préparer et adapter les foyers aéronautiques aux carburants alternatifs. De plus, leur impact environnemental doit être identifié avant de pouvoir les utiliser.

- **Sûreté** : des mesures pour augmenter la sécurité des aéroports ont été proposées.

Les études numériques des foyers aéronautiques contribuent au développement des nouvelles technologies qui peuvent permettre de réduire les émissions de CO_2

et de NO_x, comme ciblé par l'ACARE. Comprendre les phénomènes de **combustion turbulente** qui se produisent dans une chambre de combustion comme la production de polluants par exemple est une étape fondamentale pour minimiser l'impact environnemental et assurer la sécurité des foyer aéronautiques utilisant des carburants alternatifs.

La combustion turbulente est caractérisée par de nombreux phénomènes : dynamique du spray et écoulements diphasiques, rayonnement et pertes thermiques, interaction flamme-acoustique, etc. Cependant de manière très simplifiée, la combustion turbulente ne décrit que l'interaction d'un écoulement turbulent avec une flamme. La prédiction de ces phénomènes n'est donc vraiment utile que si la turbulence et la chimie sont reproduites correctement. Par conséquent, la modélisation des phénomènes chimiques et de leurs interactions avec la turbulence est aujourd'hui encore l'une des problématiques majeures de la théorie de la combustion.

Objectifs de la thèse

Différents mécanismes cinétiques détaillés pour la combustion de la plupart des carburants ont été développées en tenant compte de centaines d'espèces et de milliers de réactions [148]. Ces mécanismes reproduisent fidèlement de multiples aspects de la flamme sur une vaste plage de conditions opératoires, tels que la structure de flamme monodimensionnelle, la composition d'un gaz dans un réacteur et le retard d'allumage. Malheureusement, l'utilisation de ces mécanismes dans des simulations de combustion turbulente est impossible pour deux raisons :

- **Difficultés théoriques** : dans la plupart des modèles de combustion, le couplage entre la turbulence et la combustion est décrit en comparant le temps turbulent au temps chimique. Ce couplage n'est pas évident puisque les mécanismes détaillés sont caractérisés par des temps chimiques très différents (l'oxydation du carburant est décrite par des réactions rapides, les NO_X sont en revanche générés par des réactions très lentes).
- **Coût calcul** : le temps de calcul augmente drastiquement avec le nombre d'espèces résolues. De plus, les mécanismes détaillés sont très raides et nécessitent l'utilisation d'algorithmes numériques spécifiques afin d'éviter des pas de temps trop petits.

Deux approches ont été proposées pour contourner ce problème :

- **Chimies réduites** : simplifications de schémas détaillés afin d'obtenir une description correcte du comportement chimique en utilisant moins d'espèces et de réactions. Elles peuvent être classées en deux grandes familles :

  - Mécanismes globaux ou semi-globaux ajustés [171, 63, 144] : ils sont construits pour reproduire correctement certaines quantités globales pour les flammes laminaires telles que la vitesse de flamme ou la composition du gaz à l'équilibre. Ces mécanismes sont faciles à construire pour qu'ils soient valables sur une large gamme de conditions initiales, et leur implémentation dans un code de mécanique des fluides numérique (ou CFD en anglais) est à la fois directe et robuste. En revanche, seules les quantités globales sont correctement reproduites et ces schémas ne contiennent aucune information sur les espèces intermédiaires ou les radicaux. Dans ce manuscrit, deux mécanismes ajustés ont été considérés : le mécanisme à deux étapes 2S_CH4_BFER [63] et le schéma à quatre étapes JONES [82]. Une version modifiée pour le mécanisme à deux étapes est également proposée (2S_CH4_BFER*), afin de mieux reproduire les comportements des flammes laminaires étirées.
  - Mécanismes analytiques [116, 41, 40, 103, 21] : ils ont été proposés pour inclure plus de détails tels que la structure de flamme ou le retard d'allumage. Une compréhension détaillée des phénomènes chimiques est nécessaire si l'on veut correctement éliminer les étapes chimiques qui sont négligeables pour décrire le phénomène d'intérêt. Ce type de mécanisme offre un aperçu physique des processus chimiques et décrit correctement quelques espèces intermédiaires. Malheureusement, leur implémentation et leur utilisation dans un code de CFD n'est pas immédiate car ils sont caractérisés par des relations algébriques qui sont difficiles à traiter. Leur coût calcul est plus élevé que ceux des schémas globaux. Trois différents mécanismes analytiques sont utilisés dans ce manuscrit : le schéma PETERS [116] à huit espèces, le mécanisme SESHADRI [39] qui est plus complexe mais qui comprend lui aussi huit espèces et le schéma LU [98] à treize espèces qui reproduit correctement le comportement du schéma détaillé GRI3.0 [65] pour des flammes méthane/air.

- **Chimie tabulée**: technique basée sur l'idée que les variables d'un mécanisme cinétique ne sont pas indépendantes. La structure d'un flamme est alors étudiée en fonction de quelques variables comme la température ou la fraction de mélange qui sont utilisées pour construire une base de données pour la flamme [102, 69, 160, 49]. Tous les intermédiaires et radicaux sont disponibles pendant le calcul mais leur concentration dépend des informations mémorisées dans la base de donnés et par conséquent, du prototype de flamme qui a été choisi pour construire la table. La gestion de la table est difficile lorqu'on travaille sur des configurations industrielles complexes pour plusieurs raisons :

  - ses dimensions augmentent rapidement avec le nombre de paramètres qui ont été choisis pour tabuler la flamme. Des méthodes basées sur l'auto-

similarité de flammes [128, 161, 60] ou sur des algorithmes génétiques de réduction des dimensions de la table [126] ont été proposées afin de surmonter ce problème;

– le choix de la flamme prototype pour créer la table peut être compliqué quand le régime de combustion n'est pas connu.

La méthode FPI_TTC [164] utilisée dans ce manuscrit appartient à la famille des chimies tabulées.

Les besoins en simulations basées sur des chimies fiables ont augmenté continuellement ces dernières années [77] vu les restrictions ACARE sur les émissions de polluants. Par conséquent, ces descriptions chimiques simplifiées doivent être utilisées avec précaution quand on simule des flammes turbulentes complexes pour deux raisons :

- certaines informations ont été négligées afin de réduire le coût calcul et la qualité des résultats peut en être affectée;
- toutes les méthodes de réduction ont été développées et évaluées dans des configurations laminaires et leurs performances dans des configurations turbulentes n'ont pas encore été complètement évaluées.

L'impact d'une chimie simplifiée a été étudié dans de nombreuses configurations académiques [13, 14, 77] et les résultats dans des géométries complexes [130, 155, 20] ont confirmé l'importance d'une bonne description chimique. Néanmoins, les caractéristiques nécessaires à un mécanisme simplifié pour décrire correctement les flammes turbulentes n'ont pas encore été identifiées.

L'évaluation de l'impact d'une description chimique simplifiée sur des flammes turbulentes prémélangées est l'objectif principal de cette thèse, en étudiant la concentration des espèces, la température, la structure de la flamme, son épaisseur, sa position et sa réponse à la turbulence ainsi que la prédiction des émissions polluantes.

Les deux objectifs principaux de cette thèse sont :

- **le développement d'une méthodologie pour construire des schémas simplifiés** qui prédisent correctement la vitesse de flamme, la composition et la température des gaz brulés sur une large gamme de pression, température initiale et richesse.
- **l'identification des caractéristiques fondamentales d'un mécanisme simplifié pour simuler avec précision les flammes turbulentes** dans des configurations industrielles complexes.

Pour les carburants utilisés dans les foyers aéronautiques comme le JET-A, le JP10 et éventuellement les biocarburants [48, 141, 100, 101], la construction de bases de données expérimentales et de schémas détaillés est actuellement en cours. Pour cette raison, l'analyse de cette thèse a été conduite sur le méthane pour lequel on dispose d'une large base de données expérimentales et de différents schémas détaillés. Les conclusions de ce travail sont cependant supposées valables pour la plupart des hydrocarbures et peuvent être utilisées pour le développement de nouveaux schémas simplifiés pour le kérosène et les carburants alternatifs par exemple.

Les performances des différentes descriptions chimiques sont évaluées pour deux approches différentes de la simulation des écoulements turbulents : la Simulation Numérique Directe ("Direct Numerical Simulation" - DNS) et la Simulation aux Grandes Echelles (" Large Eddy Simulation" - LES). La Simulation Numérique Directe résout explicitement toutes les échelles turbulentes spatiales et temporelles mais son utilisation est généralement limitée à des configurations académiques simplifiées dû à son coût calcul considérable. Avec la Simulation aux Grandes Echelles, le coût calcul est réduit, les équations de l'écoulement étant filtrées de façon à résoudre explicitement les grandes échelles turbulentes et à modéliser les plus petites échelles turbulentes.

Plan de la thèse

Le manuscrit se divise en trois parties :

- Partie 1 : Caractérisation générale de la combustion turbulente
  - Les outils nécessaires pour la simulation de la combustion turbulente sont présentés dans le **Chapitre 1**. Les équations de conservation sont généralisées pour des écoulements réactifs et les différents régimes de combustion sont définis. Les différentes simplifications pour la description cinétique dans les écoulements turbulents, i.e. chimie réduite et méthodes de tabulation, sont présentées avec les codes de calcul utilisés dans cette thèse.
- Partie 2 : Modélisation de la chimie pour la combustion prémélangée turbulente
  - Les principales caractéristiques des flammes laminaires prémélangées sont présentées dans le **Chapitre 2** en se concentrant sur l'impact de l'étirement et des propriétés de transport simplifiées sur la structure de la flamme.
  - Dans le **Chapitre 3**, la chimie d'une flamme prémélangée méthane/air est analysée. La chaîne de réactions de l'oxydation du méthane est expliquée et une méthodologie générale pour construire des mécanismes à deux étapes est proposée. Ce type de construction permet de prédire correctement la vitesse de flamme et l'état d'équilibre sur une vaste gamme de conditions initiales et

peut être appliqué facilement à d'autres carburants comme le kérosène [63]. Les réponses de six différents mécanismes (2S_CH4_BFER, 2S_CH4_BFER*, JONES, PETERS, SESHADRI, LU) à des flammes prémélangées non étirées ou étirées sont comparées pour les deux points de fonctionnement des géométries analysées dans la troisième partie de la thèse (PRECCINSTA et BUNSEN). Afin d'obtenir une analyse détaillée du comportement des différents types de description chimique, la méthode de tabulation FPI_TTC est évaluée dans des flammes prémélangées non étirées. Finalement, le couplage avec la combustion turbulente est étudié en généralisant le modèle de flamme épaissie (Artificially Thickened Flame Model) aux cinétiques multi-étapes et aux flammes partiellement prémelangées.

- Partie 3 : Validation et impact des cinétiques dans des simulations numériques de flammes turbulentes instationnaires

  – Dans le **Chapitre 4**, la réponse des différents mécanismes à l'étirement est analysée dans deux configurations académiques en utilisant l'approche DNS : l'interaction d'une flamme avec une paire de tourbillons d'une part, et une turbulence homogène isotrope d'autre part. A partir de ces résultats préliminaires, les mécanismes les plus performants sont retenus et utilisés dans une Simulation Numérique Directe de la flamme prémélangée de BUNSEN calculée par Sankaran [137].

  – Dans le **Chapitre 5**, les différentes descriptions chimiques (mécanismes ajustés, schémas analytiques et méthode de tabulation) sont également testées dans des LES du brûleur expérimental PRECCINSTA (Prediction and control of combustion instabilities for industrial gas turbines [107]) en utilisant le modèle de flamme épaissie. Des mesures expérimentales sont disponibles pour la température et les fractions massiques des espèces majoritaires. Elles sont utilisées pour évaluer la capacité des différents mécanismes à prédire la structure d'une flammée swirlée partiellement prémélangée.

  – Finalement dans le **Chapitre 6**, des LES du brûleur PRECCINSTA sont réalisées pour analyser la réponse du mécanisme le plus simple (2S_CH4_BFER) aux instabilités thermo-acoustiques. Le brûleur est en effet caractérisé par un comportement acoustique qui diffère selon la richesse globale du mélange : pour une certaine richesse, la flamme se stabilise dans la chambre, mais pour une richesse plus faible la flamme oscille autour de l'injection de gaz frais dans la chambre.

Trois différents codes ont été utilisés pour les différentes simulations numériques. Les flammes laminaires monodimensionnelles ont été calculées avec CANTERA [71]. Les DNS de la flamme de BUNSEN ont été réalisées avec le code S3D développé au

CRF/SANDIA [37]. Les LES du brûleur PRECCINSTA ont été calculées avec le code AVBP développé au CERFACS/IFPEnergies Nouvelles [140].
Cette thèse a été financée par l'Union Européen dans le cadre du projet ECCOMET (Efficient and Clean Combustion Experts Training-FP6-Marie Curie Actions).

Conclusions générales

La présente étude s'est consacrée à l'analyse de l'impact de descriptions chimiques simplifiées dans des Simulations Numériques Directes et des Simulations aux Grandes Echelles de flammes prémélangées turbulentes tridimensionnelles.

Une introduction à la combustion prémélangée turbulente est présentée dans le Chapitre 1. Dans le régime de flamelettes, le front de flamme turbulente est modélisé localement par une flamme laminaire qui est déformée et étirée par l'écoulement turbulent. Pour cette raison, les flammes laminaires prémélangées ont été caractérisées pour différentes conditions initiales et pour différents étirements dans le Chapitre 2.

Une méthodologie pour construire un mécanisme à deux étapes qui prédit correctement la vitesse de flamme et la composition des gaz brûlés d'une flamme méthane/air prémélangée sur une vaste gamme de conditions initiales est propose dans le Chapitre 3. Cette méthodologie a été appliquée avec succès sur des flammes kérosène/air comme illustré dans l'article: "B. Franzelli, E. Riber, M. Sanjosé and T. Poinsot,*A two-step chemical scheme for kerosene-air premixed flames*, Combustion and Flame 157 (7), pp.1364-1373 (2010)". Une modification pour le mécanisme à deux étapes a été proposée pour reproduire correctement la vitesse de consommation des flammes laminaires prémélangés etirées étirées.
Les performances des différents mécanismes réduits pour des flammes laminaires sans et avec étirement ont été évaluées ensuite:

- Les mécanismes ajustés à deux étapes (2S_CH4_BFER et 2S_CH4_BFER*) reproduisent correctement la vitesse de flamme laminaire et la composition de l'état d'équilibre mais la structure de flamme n'est pas correctement prédite. En corrigeant le nombre de Lewis pour toutes les espèces, des meilleures résultats sur la vitesse de consommation des flammes étirées peuvent être obtenus;

- Le mécanisme ajusté à quatre étapes (JONES) permet de mieux décrire la structure d'une flamme non-étirée;

- Seuls les mécanismes analytiques (PETERS et SESHADRI) décrivent correctement la réponse de la flamme à l'étirement en termes de vitesse de consommation et de structure de flamme;

- L'accord entre les mécanisme analytique le plus complexe etudié dans cette étude (LU) et le schéma détaillé (GRI3.0) est excellent et le mécanisme de Lu & Law est utilisé comme référence dans les calculs DNS et LES;

- Le comportement de la méthode de tabulation FPI_TTC n'a été validé que sur des flammes non étirées et une étude plus approfondie sur des flammes étirées est nécessaire.

Dans le Chapitre 4, l'impact des chimies réduites a en premier lieu été validé dans des DNS d'une flamme qui intéragit avec une paire de tourbillons et avec une turbulence homogène isotrope :

- Les principalles différences ont été détectées pour la vitesse de consommation qui varie fortement en fonction de l'étirement et de la courbure. La prédiction de cette quantité dépend de la chimie utilisée et elle est globalement en accord avec les résultats pour des flammes laminaires étirées.

- Les mêmes conclusions ont été tirées pour la structure de flamme représentée par la fraction massique de l'espèce *CO*. Seuls les schémas analytiques reproduisent le comportement du mécanisme de référence (LU).

- l'épaississement de la flamme dépend très faiblement du mécanisme utilisé et est d'avantage lié au régime de combustion.

A partir des conclusions préliminaires sur ces deux configurations académiques, trois mécanismes ont été retenus pour simuler la flamme de Bunsen et comparer les résultats avec le mécanisme de référence (LU). Le schéma 2S_CH4_BFER est le mécanisme ajusté le moins coûteux, le 2S_CH4_BFER* est une version modifiée pour améliorer la réponse à l'etiremente, et le mécanisme SESHADRI* est le schéma analytique le plus performant:

- L'épaississement et la déformation de la flamme sont reproduits par les mécanismes ajustés et le schéma analytique dans la mesure où ils sont principalement contrôlés par le régime de combustion turbulente.

- La vitesse turbulente dépend de la vitesse de consommation locale qui est gouvernée par le mécanisme cinétique. Comme le mécanisme ajusté 2S_CH4_BFER surestime la vitesse de consommation dans des flammes laminaires étirées, la vitesse turbulente est largement surestimée. Les résultats des mécanismes 2S_CH4_BFER* et SESHADRI sont en bon accord avec le schéma de référence LU.

Une bonne description des flammes laminaires non étirés n'est pas suffisante et les performances des mécanismes réduits doivent être évaluées sur des flammes étirées afin de prédire correctement la longueur de flamme et la vitesse turbulente.

Dans le cinquième chapitre, les différentes descriptions chimiques ont été étudiées dans une Simulation aux Grandes Echelles du brûleur industriel PRECCINSTA en utilisant la généralisation du modèle de flamme épaissie à des chimies multi-étapes et des flammes partiallement prémélangées:

- Le mécanisme ajusté à deux étapes prédit correctement les profils moyens et les fluctuations de température et d' espèces majoritaires. Comme attendu, le schéma modifié (2S_CH4_BFER*) décrit mieux la longueur de la flamme pour le même coût calcul. Les résultats obtenus avec le mécanisme ajusté à quatre étapes ne sont pas meilleurs pour un coût plus élevé. L'accord entre les mécanismes analytiques, le schéma de référence et les résultats expérimentaux est satisfaisant. En utilisant un mécanisme analytique (SESHADRI), la qualité des résultats est préservée et le coût est réduit d'environ 20% comparée au mécanisme de LU. La méthode de chimie tabulée FPI_TTC est la moins couteuse et l'accord avec les résultats expérimentaux est satisfaisant même si l'angle d'ouverture de la flamme est surestimé.

- La possibilité de prédire les émissions polluantes a été estimée en analysant la fraction massique de l'espèce *CO* dans la zone de réaction. Les résultats sont en accord avec le comportement des différents mécanismes sur des flammes étirées. Par conséquence, seuls les mécanismes analytiques permettent de reproduire correctement la concentration de *CO* même si les résultats sont sensés s'améliorer en introduisant les pertes thermiques aux parois et en raffinant le maillage.

- Une bonne description des radicaux *H*, *O* and *OH* est nécessaire afin de reproduire correctement la concentration de *NO* thermique via le mécanisme de Zel'dovich. Les mécanismes analytiques arrivent à les reproduire de façon qualitative mais une analyse plus approfondie de l'impact des erreurs dans la description des radicaux sur la prédiction de *NO* est nécessaire avant de pouvoir conclure.

- La généralisation de la méthode de flamme épaissie à des chimies multi-étapes et des flammes partiallément prémélangées a été validée à la fois pour des mécanismes cinétiques réduits et pour des méthodes de tabulation.

Dans le dernier chapitre, le mécanisme à deux étapes 2S_CH4_BFER a été utilisé pour prédire les instabilités thermo-acoustiques du brûleur PRECCINSTA comme montré dans l'article: B.Franzelli, E. Riber , L. Gicquel and T. Poinsot,"*Large-Eddy Simulation of combustion instabilities in a lean partially premixed swirled flame*" accepté dans le journal

Combustion and Flame (2011) avec corrections mineures. Avant de choisir la description chimique à utiliser, il faut toujours identifier les quantités d'intérêt à façon de trouver le meilleur compromis entre coût calcul et qualité des résultats.

Une méthodologie pour évaluer *a priori* la capacité d'un mécanisme à prédire correctement des phénomènes chimiques tridimensionnels a été identifiée en se basant sur les résultats des flammes laminaires monodimensionnelles :

- la vitesse turbulente et la longueur d'une flamme turbulente sont liées à la réponse d'un mécanisme à l'étirement en termes de vitesse de consommation pour des flammes laminaires.
- la fraction massique de *CO* dans la région de réaction peut être correctement prédite seulement si le mécanisme décrit sa concentration pour des flammes laminaire étirées.
- une description correcte de la zone de recombinaison d'une flamme laminaire est nécessaire afin de prédire la région à faible gradient de température caractérisée par la production d'espèces polluantes pour des flammes turbulentes.

Les conclusions obtenues dans cette étude ne sont valables que pour des flammes prémélangées mais elles sont supposées valides pour la plupart des hydrocarbures. Les comportements des mécanismes cinétiques réduits doivent à présént être évalués dans des flammes de diffusion. Par ailleurs, une analyse plus approfondie de la méthode de tabulation FPI_TTC sur des flammes étirées est nécessaire.